

**SYNTHESIS, CHARACTERIZATION, AND ENZYMATIC DEGRADATION OF  
NITROGEN-DOPED CARBON NANOMATERIALS**

by

**Yong Zhao**

B.S. Chemical Physics, University of Science and Technology of China, 2008

Submitted to the Graduate Faculty of  
The Dietrich School of Arts and Sciences in partial fulfillment  
of the requirements for the degree of  
Doctor of Philosophy

University of Pittsburgh

2014

UNIVERSITY OF PITTSBURGH  
THE DIETRICH SCHOOL OF ARTS AND SCIENCES

This dissertation was presented

by

Yong Zhao

It was defended on

May 23rd, 2014

and approved by

Paul Floreancig, Professor, Department of Chemistry

Haitao Liu, Assistant Professor, Department of Chemistry

Valerian E. Kagan, Professor, Department of Environmental and Occupational Health

Committee Chair: Alexander Star, Associate Professor, Department of Chemistry

Copyright © by Yong Zhao

2014

# **SYNTHESIS, CHARACTERIZATION, AND ENZYMATIC DEGRADATION OF NITROGEN-DOPED CARBON NANOMATERIALS**

Yong Zhao, PhD

University of Pittsburgh, 2014

Carbon nanomaterials, especially the  $sp^2$  carbon allotropes such as carbon nanotubes (CNTs) and graphene, have gathered extensive research interest in the recent decades. Structurally, CNTs represent one dimensional (1D) tubes with single- or multiple-layer graphitic sidewalls; and graphene is two dimensional (2D) one-atom-thick  $sp^2$  carbon sheets. With their remarkable intrinsic physical, chemical, and electronic properties, carbon nanomaterials have revolutionary potential to make impact on various existing technologies in many fields from construction and energy to electronics and biomedicine. Current research activities are focused on harnessing the desired properties of carbon nanomaterials for practical applications by their rational functionalization.

Among different covalent or noncovalent chemical functionalization schemes, heteroatom doping into the graphitic lattice most fundamentally alters the intrinsic properties of carbon nanomaterials. Nitrogen-doped CNTs are the most studied doped carbon nanomaterials due to their excellent electrochemical catalytic activity toward oxygen reduction reaction (ORR). Moreover, nitrogen-doping in multiwalled carbon nanotubes (MWCNTs) results in hollow compartments resembling stacked cups. These nanocups, termed as nitrogen-doped carbon nanotube cups (NCNCs), may find potential applications as drug delivery carriers. We managed to efficiently separate individual nanocups from their stacks through chemical and physical separation methods. By functionalizing separated NCNCs with gold nanoparticles (GNPs), the

nanocups can be effectively corked by GNPs on the cup opening. The GNP-corked NCNCs form self-enclosing nanocontainers with potential applications as drug delivery nanocarriers.

The increasing use of carbon nanomaterials in biological and industrial applications inevitably raises the risk of exposure to humans and the environment with potential toxicological and ecological issues. This research dissertation also studies the enzymatic degradation of carbon nanomaterials as a potential remedy measure to mitigate their negative impacts. Following previous studies on the enzymatic degradation of single-walled carbon nanotubes (SWCNTs) by horseradish peroxidase (HRP), we studied HRP degradation of MWCNTs and its underlying mechanism. Furthermore, by using a more potent peroxidase, myeloperoxidase (MPO), we found that MPO triggers the opening of the GNP-corked NCNCs and catalyzes the subsequent degradation of the NCNC shells. These findings allude to potential biological pathways of drug release and degradative clearance of the GNP-corked NCNCs in therapeutic applications.

## TABLE OF CONTENTS

<b>TITLE PAGE .....</b>	<b>I</b>
<b>ABSTRACT.....</b>	<b>IV</b>
<b>PREFACE.....</b>	<b>XXVII</b>
<b>1.0 INTRODUCTION.....</b>	<b>1</b>
<b>1.1 OVERVIEW.....</b>	<b>1</b>
<b>1.1.1 Synthesis of Carbon Nanotubes.....</b>	<b>4</b>
<b>1.1.2 Applications of Carbon Nanotubes .....</b>	<b>6</b>
<b>1.1.3 Functionalization of Carbon Nanotubes.....</b>	<b>7</b>
<b>1.2 CHARACTERIZATION OF CARBON NANOMATERIALS .....</b>	<b>9</b>
<b>1.2.1 Transmission Electron Microscopy .....</b>	<b>10</b>
<b>1.2.2 Scanning Electron Microscopy .....</b>	<b>11</b>
<b>1.2.3 Atomic Force Microscopy .....</b>	<b>12</b>
<b>1.2.4 Absorption Spectroscopy .....</b>	<b>13</b>
<b>1.2.5 Raman Spectroscopy .....</b>	<b>14</b>
<b>1.2.6 X-ray Photoelectron Spectroscopy .....</b>	<b>15</b>
<b>1.3 NITROGEN-DOPED CARBON NANOTUBES .....</b>	<b>17</b>
<b>1.3.1 Synthesis of Nitrogen-doped Carbon Nanotubes.....</b>	<b>17</b>
<b>1.3.2 Purification of As-synthesized N-doped Carbon Nanotubes .....</b>	<b>20</b>

1.3.3	Morphology, Structure, and Growth Mechanism of Nitrogen-doped Carbon Nanotubes .....	22
1.3.4	Potential Applications of N-doped Carbon Nanotubes .....	25
1.3.5	Separation and Manipulation of Individual Nanocups from N-doped Carbon Nanotubes .....	27
1.4	ENZYMATIC DEGRADATION OF CARBON NANOMATERIALS .....	28
1.4.1	Toxicity and Environmental Impact of Carbon Nanotubes .....	29
1.4.2	Peroxidases and Mechanism of Enzymatic Oxidation .....	31
1.4.2.1	Horseradish Peroxidase .....	31
1.4.2.2	Myeloperoxidase.....	33
1.4.3	In vitro Degradation of Carbon Nanomaterials .....	34
1.4.3.1	Degradation by HRP outside Living Systems.....	34
1.4.3.2	Degradation of Carbon Nanotubes by hMPO in vitro .....	35
1.4.3.3	Degradation of Carbon Nanotubes in vivo .....	36
2.0	SYNTHESIS, CHARACTERIZATION, AND GNP-CORKING OF NITROGEN-DOPED CARBON NANOTUBE CUPS .....	39
2.1	CHAPTER PREFACE .....	39
2.2	CORKING CARBON NANOTUBE CUPS WITH GOLD NANOPARTICLES .....	40
2.2.1	Preface .....	40
2.2.2	Introduction .....	41
2.2.3	Materials and Methods .....	43
2.2.3.1	Growth of NCNCs via chemical vapor deposition (CVD).....	43

2.2.3.2	Mechanical separation of as-synthesized NCNCs .....	44
2.2.3.3	Decoration of NCNCs with gold nanoparticles .....	44
2.2.4	Results and Discussion .....	44
2.2.5	Conclusions.....	62
2.2.6	Acknowledgement.....	63
2.3	<b>SYNTHESIS AND FUNCTIONALIZATION OF NITROGEN-DOPED CARBON NANOTUBE CUPS WITH GOLD NANOPARTICLES AS CORK STOPPERS .....</b>	<b>64</b>
2.3.1	Preface .....	64
2.3.2	Introduction .....	65
2.3.3	Specific Reagents and Equipment.....	68
2.3.4	Detailed protocol.....	69
2.3.4.1	CVD synthesis of nitrogen-doped carbon nanotube cups (NCNCs).....	69
2.3.4.2	Oxidation of as-synthesized NCNCs by a mixture of acids.....	70
2.3.4.3	Physical separation of NCNCs by probe-tip sonication .....	71
2.3.4.4	Quantitative analysis of amine functional groups on NCNCs by Kaiser test .....	71
2.3.4.5	Functionalization of NCNCs with GNPs.....	72
2.3.5	Representative Results .....	72
2.3.6	Discussion .....	77
2.3.7	Conclusions.....	81
2.3.8	Acknowledgement.....	81

<b>3.0</b>	<b>ENZYMATIC DEGRADATION OF MULTIWALLED CARBON NANOTUBES.....</b>	<b>82</b>
<b>3.1</b>	<b>CHAPTER PREFACE.....</b>	<b>82</b>
<b>3.2</b>	<b>INTRODUCTION .....</b>	<b>83</b>
<b>3.3</b>	<b>EXPERIMENTAL SECTION.....</b>	<b>85</b>
<b>3.3.1</b>	<b>Materials.....</b>	<b>85</b>
<b>3.3.2</b>	<b>Carboxylation of MWCNTs .....</b>	<b>85</b>
<b>3.3.3</b>	<b>Synthesis and purification of n-MWCNTs.....</b>	<b>86</b>
<b>3.3.4</b>	<b>Incubation with HRP and H<sub>2</sub>O<sub>2</sub> .....</b>	<b>87</b>
<b>3.3.5</b>	<b>Transmission Electron Microscopy (TEM).....</b>	<b>87</b>
<b>3.3.6</b>	<b>Raman Spectroscopy .....</b>	<b>87</b>
<b>3.3.7</b>	<b>Gas Chromatography–Mass Spectrometry (GC-MS).....</b>	<b>88</b>
<b>3.3.8</b>	<b>Dynamic Light Scattering (DLS).....</b>	<b>88</b>
<b>3.4</b>	<b>RESULTS AND DISCUSSION .....</b>	<b>89</b>
<b>3.4.1</b>	<b>Carboxylation of MWCNTs through acid treatment.....</b>	<b>89</b>
<b>3.4.2</b>	<b>Enzymatic degradation of carboxylated MWCNTs .....</b>	<b>92</b>
<b>3.4.3</b>	<b>Enzymatic degradation of nitrogen-doped MWCNTs.....</b>	<b>101</b>
<b>3.5</b>	<b>CONCLUSIONS.....</b>	<b>104</b>
<b>3.6</b>	<b>ACKNOWLEDGEMENT .....</b>	<b>105</b>
<b>4.0</b>	<b>NANO-GOLD CORKING AND ENZYMATIC UNCORKING OF CARBON NANOTUBE CUPS .....</b>	<b>106</b>
<b>4.1</b>	<b>CHAPTER PREFACE.....</b>	<b>106</b>
<b>4.2</b>	<b>INTRODUCTION .....</b>	<b>107</b>

<b>4.3</b>	<b>EXPERIMENTAL SECTION.....</b>	<b>109</b>
4.3.1	Synthesis of separated NCNCs .....	109
4.3.2	Corking of NCNCs with GNPs.....	110
4.3.3	Enzyme-triggered opening and degradation of GNP-corked NCNCs....	110
4.3.4	Neutrophils isolation and incubation with nanocups .....	111
4.3.5	hMPO contents in cells and its release.....	112
4.3.6	Characterization .....	112
<b>4.4</b>	<b>RESULTS AND DISCUSSION.....</b>	<b>113</b>
4.4.1	Growth mechanism of GNP corks on NCNCs .....	117
4.4.2	Enzyme-triggered uncorking and degradation of GNP/NCNCs.....	120
<b>4.5</b>	<b>CONCLUSIONS.....</b>	<b>126</b>
<b>4.6</b>	<b>ACKNOWLEDGEMENT .....</b>	<b>127</b>
<b>5.0</b>	<b>RECENT STUDIES AND FUTURE DIRECTIONS .....</b>	<b>128</b>
<b>5.1</b>	<b>CHAPTER PREFACE.....</b>	<b>128</b>
<b>5.2</b>	<b>THE EFFECT OF METAL CATALYST ON THE ELECTROCATALYTIC ACTIVITY OF NITROGEN-DOPED CARBON NANOTUBES .....</b>	<b>129</b>
5.2.1	Preface .....	129
5.2.2	Introduction and brief results .....	129
5.2.3	Future directions.....	131
<b>5.3</b>	<b>OXIDATIVE UNZIPPING OF STACKED-CUP NITROGEN-DOPED CARBON NANOTUBES.....</b>	<b>132</b>
5.3.1	Preface .....	132

5.3.2	Introduction and brief results .....	133
5.3.3	Future directions.....	134
5.4	CORKING OF NANOTUBE CUPS AND MOLECULAR ENCAPSULATION .....	135
5.4.1	Introduction and brief results .....	135
5.4.2	Future directions.....	136
5.5	GRAPHENE NANOSHEETS AND QUANTUM DOTS BY UNZIPPING NITROGEN-DOPED CARBON NANOTUBE CUPS.....	137
5.5.1	Introduction and brief results .....	137
5.5.2	Future directions.....	138
6.0	CONCLUDING REMARKS .....	139
	BIBLIOGRAPHY .....	186

## LIST OF TABLES

Table 1-1. Standard reduction potentials (at pH 7) along the peroxidase cycle for peroxidase involved in CNT degradation/biodegradation. <sup>169</sup> .....	34
Table 2-1. Primary amine and total amine loadings from Kaiser test results on as-synthesized NCNCs and separated NCNCs. <sup>a</sup> .....	55
Table 2-2. Reagents involved in the experiment .....	68
Table 2-3. Equipment used in the experiment .....	69
Table 2-4. Elemental analysis of as-synthesized NCNCs and final separated NCNCs based on energy-dispersive X-ray (EDX) spectroscopy. ....	81
Table 5-1. Nanomaterials catalytic activity toward oxygen reduction reaction (ORR). ....	131
Table A3-1. Length distribution of as-synthesized nitrogen-doped CNT fibers, oxidized NCNCs, and separated NCNCs obtained from TEM images and DLS analysis. ....	167
Table A3-2. Elemental composition of as-synthesized nitrogen-doped CNTs, separated NCNCs and NCNCs functionalized with GNPs based on energy-dispersive X-ray (EDX) spectroscopy. ....	167

## LIST OF FIGURES

Figure 1-1. (a) Morphological illustration of single-walled carbon nanotube (SWCNT) and multiwalled carbon nanotube (MWCNT); (b) Schematic of a graphene sheet with two lattice vectors $a_1$ and $a_2$ , and one roll-up vector $C_h = na_1 + ma_2$ ; (c) Schematic representations of zigzag, armchair, and chiral SWCNTs. (a) is adapted from Ref. 20, Copyright 2007 John Wiley & Sons; (b) is adapted from Ref. 13, with permission from <i>Nature</i> 1998, 391, 62-64, Copyright 1998 Nature Publishing Group; and (c) is reproduced from Ref. 12, with permission from <i>Nanoscale</i> 2009, 1, 96-105, Copyright 2009 Royal Society of Chemistry. ....	3
Figure 1-2. Energy structure of (a) metallic SWCNTs and (b) semiconducting SWCNTs, where X-axis is the density of states (DOS) and Y-axis is energy (E). The valence bands (VB) are colored and the conduction bands (CB) are white. The spikes in the band structure represent the Van Hove singularities.....	4
Figure 1-3. Illustration of the instrumental setup for (a) arc-discharge synthesis, (b) laser ablation synthesis, and (c) CVD synthesis of carbon nanotubes. (a) and (b) are adapted from Ref. 28, with permission from <i>Appl. Phys. A</i> 1998, 67, 1-9, Copyright 1998 Springer. ....	6
Figure 1-4. TEM images of different nitrogen-doped CNTs with (a) “bamboo-like” morphology; (b) “stacked-cup” morphology; and (c) Corrugated random interlinkages between the sidewalls. (a) is adapted from Ref. 141, with permission from <i>Appl. Phys. Lett.</i> 2007, 90, 113116, Copyright 2007 AIP Publishing LLC; (b) is adapted from Ref. 108, with permission from ACS	

*Nano* 2008, 2, 1914-1920, Copyright 2008 American Chemical Society; and (c) is adapted from Ref. 127, with permission from *Carbon* 2010, 48, 1498-1507, Copyright 2010 Elsevier. .... 23

Figure 1-5. (a) Schematic illustration showing the CVD growth of a N-doped CNT on a metal catalytic nanoparticle via either “base-growth mode” (left) or “tip-growth mode” (right); (b) The detailed growth mechanism of the “base-growth mode”: (i) formation of a liquid catalyst particle and dissolution of C and N atoms, (ii) precipitation of C, N atoms on the droplet surface, (iii) the curvature effect stretching the catalyst particle, (iv) precipitating the first graphite layer of a nanocup, (v) stopping growth when the cup edge is saturated with N, and (vi) beginning to precipitate the graphite sheets of the next nanocup. (a) is reproduced from Ref. 145, with permission from *Nano Lett.* 2007, 7, 2234-2238, Copyright 2007 American Chemical Society; and (b) is reproduced from Ref. 107, with permission from *J. Appl. Phys.* 2002, 91, 9324-9332, Copyright 2002 AIP Publishing LLC. .... 25

Figure 1-6. Molecular modeling of a carboxylated SWCNTs binding to the active site of (a) HRP; and (b) hMPO. (c) Scheme of the peroxidase cycle for HRP and hMPO (black circle), the red lines show the halogenation cycle for hMPO. Reproduced from Ref. 169, with permission from *Adv. Drug Delivery Rev.* 2013, 65, 1921-1932, Copyright 2013 Elsevier..... 32

Figure 2-1. (a) Chemical vapor deposition (CVD) synthesis of nitrogen-doped carbon nanotube cups (NCNCs) and their mechanical separation via probe-tip sonication. (b) Transmission electron microscopy (TEM) image of as-synthesized NCNC fibers. (c) High-resolution TEM image showing one segment from a stacked NCNC fiber, the white dashed lines in the figure depict the directions of the graphitic walls and the tube axis, the white arrow shows the existence of amorphous carbon. (d) TEM image of an individual NCNC after mechanical separation. (e) High-resolution TEM image of an individual NCNC..... 49

Figure 2-2. (a) Raman spectra of NCNCs after different duration of probe-tip sonication: (1) as-synthesized, (2) 2 hr, (3) 4 hr, (4) 10 hr, and (5) 15 hr. (b) Plot and linear fit of the D to G band ratio versus sonication time. .... 50

Figure 2-3. High-resolution TEM images (insets) and their corresponding electron energy loss spectroscopy (EELS) of (a) an uncompartmented section and (b) a compartmented section of NCNCs. X-ray photoelectron spectroscopy (XPS) of (c) as-synthesized NCNCs and (d) separated NCNCs after 15 hr of sonication. (e) Structural scheme of one graphitic layer from separated NCNCs showing the varieties of possible nitrogen functionalities. This scheme is not drawn to scale. .... 52

Figure 2-4. (a) Schematic illustration of functionalization of NCNCs with 10 nm gold nanoparticles (GNPs). (b, c) TEM images of separated NCNCs functionalized with 3-mercaptopropionic acid before (b) and after (c) attachment of GNPs. The insets in each panel show the corresponding images of individual NCNCs. (d) TEM image showing the distribution of GNPs among separated NCNCs without thiolation treatment. (e) UV-Vis spectra showing the surface plasmon resonance (SPR) band of GNPs with NCNC samples with or without thiolation treatment. .... 57

Figure 2-5. (a) TEM image of a NCNC retaining amorphous carbon inside the open cavity and (b) a thiolated NCNC corked with a 40 nm GNP and two other GNPs attached to its sidewall. (c) AFM contact-mode image of an individual NCNC functionalized with 40 nm GNPs. .... 59

Figure 2-6. (a) TEM image of one GNP with 40 nm of diameter corking the opening of separated NCNCs. Inset: the energy filtered TEM (EFTEM) image of gold elemental mapping. (b,c) EFTEM images for nitrogen (colored blue) and sulfur (colored red) and (d) overlap of b and c. All scale bars represent 40 nm. .... 61

Figure 2-7. (a) Schematic setup of a tube furnace used for chemical vapor deposition (CVD) synthesis of NCNCs. (b) Photograph of the as-synthesized NCNC film peeled from the quartz substrate. (c) An overview transmission electron microscopy (TEM) image of as-synthesized NCNCs. (d) High-resolution TEM image showing the tip of an individual as-synthesized NCNC. .... 74

Figure 2-8. TEM images of (a) oxidized NCNCs and (b) NCNCs after subsequent 12 hr probe-tip sonication and filtration. Inset shows an individual separated NCNC. .... 75

Figure 2-9. (a) Length distribution histograms for NCNC samples of (1) after 12 hr probe-tip sonication only, (2) after oxidation, (3) after oxidation and 12 hr probe-tip sonication, and (4) the final product after filtration through a 220 nm pore-size membrane. (b) Zeta potentials of as-synthesized, oxidized, and the final NCNC samples. (c) Amine loadings on NCNCs after 12 hr sonication only and after both oxidation and 12 hr sonication. .... 75

Figure 2-10. (a) TEM image of NCNCs functionalized with GNPs by citrate reduction of HAuCl<sub>4</sub> and collected by centrifugation. (b) TEM image showing an individual nanocup corked with GNP. (c) UV-Vis spectra of the reaction mixture, the supernatant solution and the precipitate of the GNP functionalization reaction. The inset photograph shows the color difference between the supernatant (left) and the precipitate (right) solutions. .... 76

Figure 3-1. Normalized Raman spectra of MWCNTs with 0 hr (black), 5 hr (red) and 8 hr (blue) carboxylation before degradation. Inset: D to G band ratio vs. carboxylation time. .... 90

Figure 3-2. Photograph showing enzymatic degradation process of MWCNTs after carboxylation for different durations on (a) Day 0 and (b) Day 60. (c) DLS showing decrease in size distribution of different MWCNTs before (dash lines) and after (solid lines) incubation with HRP and H<sub>2</sub>O<sub>2</sub> for 60 days. .... 91

Figure 3-3. TEM images of carboxylated MWCNTs incubated with HRP and H<sub>2</sub>O<sub>2</sub>. Each row corresponds to different carboxylation times (0, 5 and 8 hours) and each column corresponds to different enzymatic incubation times (0, 4, 30 and 60 days). All scale bars are 200 nm. .... 93

Figure 3-4. Evolution of CO<sub>2</sub> in the sample headspace as a final product of MWCNT enzymatic degradation measured by GC-MS on Day 0, 9 and 35 of incubating MWCNTs with HRP and H<sub>2</sub>O<sub>2</sub>. The control sample was made by mixing HRP and H<sub>2</sub>O<sub>2</sub> only..... 95

Figure 3-5. Raman spectra of (a) p-MWCNT, (b) o-MWCNT (5hr), and (c) o-MWCNT (8hr) showing decay of the D and G band intensity during the enzymatic degradation process (asterisk indicates contribution from quartz substrate). Insets: The changes of D to G band ratio of each sample versus degradation time..... 96

Figure 3-6. Comparison of the diameter distributions of MWCNTs before and after 60 days of incubation with HRP and H<sub>2</sub>O<sub>2</sub>. For each sample 100 measurements of nanotube diameters were obtained via TEM imaging. The numbers above each histogram are the corresponding average values. .... 99

Figure 3-7. High-resolution TEM images taken on o-MWCNT (8hr) samples. All scale bars correspond to 5 nm. (a) o-MWCNTs (8hr) before enzymatic degradation. (b) o-MWCNTs (8hr) after 60 days of enzymatic degradation. .... 100

Figure 3-8. TEM images of nitrogen-doped MWCNT (n-MWCNT) samples during enzymatic degradation: (a) As synthesized and purified n-MWCNT at Day 0. The inset shows the schematic illustration of its stacked-cup structure. (b) Day 15, (c) Day 50, and (d) Day 80. (e) Photographs comparing n-MWCNT samples before (left) and after (right) enzymatic degradation. (f) Raman spectra for n-MWCNT samples before (black) and after (red) enzymatic degradation. .... 102

Figure 4-1. (a) Separation and corking of NCNCs with gold nanoparticles (GNPs) by (i) acid oxidation with  $\text{H}_2\text{SO}_4/\text{HNO}_3$ , (ii) probe-tip sonication, (iii) incubation with  $\text{HAuCl}_4$  and (iv) sodium citrate reduction. (b) Transmission electron microscopy (TEM) images of separated NCNCs. The upper right inset shows a magnified TEM image of an individual nanocup, the lower left inset shows the length distribution of the separated cups. (c) TEM images of separated NCNCs functionalized with GNP corks. The inset shows the TEM image of an individual nanocup corked by a GNP on the opening. (d) High-resolution TEM image of the corked GNP/NCNC structure. .... 115

Figure 4-2. (a) UV-Vis absorption spectra and photograph of aqueous suspensions of separated NCNCs (1), supernatant (2) and precipitate (3) of NCNC/GNP conjugates after centrifugation. (b) Raman spectra of separated NCNCs (black), NCNCs mixed with commercial GNPs (blue), and NCNCs corked with GNPs by in situ reduction process (red). The dotted line indicates the baseline. .... 116

Figure 4-3. (a) – (d), TEM images of the growth process of GNPs on individual NCNCs sampled at (a) 5 min, (b) 20 min, (c) 50 min, and (d) 80 min after the addition of  $\text{HAuCl}_4$ . Sodium citrate was added at 20 min right after sampling. The arrows in (a) show the nucleation of gold seeds. (e), (f), Minimum energy reaction pathways for diffusion of  $\text{Au}_{20}$  cluster from the central region of the  $(7 \times 11)$  graphene flake surface toward the zigzag edge (e) decorated with a  $\text{CH}_2\text{NH}_2$  group and (f) when a second  $\text{Au}_{20}$  cluster is anchored to the  $-\text{CH}_2\text{NH}_2$  group at the graphene edge. For both sets of pathways the initial and final configurations are represented in the inset panels. Legend of atoms: C, green; N, blue; H, white; O, red; and Au, orange. .... 119

Figure 4-4. (a) – (c), TEM images of the degradation process of NCNCs corked with GNPs under  $\text{hMPO}/\text{H}_2\text{O}_2/\text{NaCl}$  at (a) Day 5, (b) Day 10, and (c) Day 20 after incubation. (d) UV-Vis

absorption spectra and (e) Raman spectra of the sample during the degradation process. The inset in (d) shows the red-shift of the GNP surface plasmon resonance (SPR) band. (f), Intensity plots of the Raman G bands from the sample (black), the NaCl control (red), and the H<sub>2</sub>O<sub>2</sub> control (blue). The intensity was averaged and normalized to the initial value and the error bars correspond to the standard errors of the mean. .... 124

Figure 4-5. (a) TEM image of the GNP/NCNC sample treated with human neutrophils after 18 h of incubation. (b) Percentages of the NCNCs decorated with GNPs in ~100 NCNCs treated with neutrophils, before and after 18 h of incubation. The error bars correspond to the standard errors of the mean. (c), (d) Optical images of the cell fragments from the GNP/NCNC sample treated with neutrophils: (c) before and (d) after 18 h of incubation, under Raman microscope. The insets in panels c and d show the Raman intensity mapping of the G-band corresponding to the areas inside the dashed boxes. .... 125

Figure A1-1. (a) TEM image at an intermediate magnification showing an overview of separated NCNCs after 15 hr of probe-tip sonication. Individual and short-stacked nanotube cups less than 400 nm in length exist with large abundance of over 70%. Stacked cups longer than 400 nm are also observed, but few of them exceed 1 μm. The amorphous materials surrounding the NCNCs may be due to unevaporated solvent residues. (b – g) More TEM images of isolated individual and short-stacked cups. They all have common cup-like shapes with one end sealed and the other open..... 145

Figure A1-2. (a) Average lengths of NCNCs as-synthesized and after 2, 4, 10 and 15 hr of probe-tip sonication. Over 300 NCNCs in each sample were measured from TEM images. The error bars represent the standard deviations of the length distribution. (b) Upper panel: histograms of length distribution of as-synthesized NCNCs (red bars) and separated NCNCs (blue lines) and

lower panel: magnified histograms of length distribution of separated NCNCs (blue bars), obtained from TEM images. .... 146

Figure A1-3. High-resolution TEM images showing damaged graphitic lattices on the sidewall (a) and the tip (b) of NCNCs after probe-tip sonication. .... 147

Figure A1-4. (a) Raman spectra of undoped MWCNTs (1) and as-synthesized NCNCs with acetonitrile fractions of 7 wt% (2), 10 wt% (3), and 15 wt% (4) in the precursor, respectively. The spectra were normalized to the G band. (b) D/G band ratios in the Raman of the corresponding four samples. .... 147

Figure A1-5. (a) TEM image of a short stack of four individual NCNCs. (b) Energy filtered TEM image at N K edge of 401 eV showing the distribution of nitrogen (colored blue) on the NCNCs. Both scale bars represent 50 nm. .... 148

Figure A1-6. FTIR spectra of undoped MWCNTs (blue), as-synthesized NCNCs (black), and separated NCNCs (red). .... 148

Figure A1-7. Visible spectra of the control Kaiser tests performed on glycine (red, 10 times diluted) and 8-aminoquinoline (black). The glycine shows a strong absorption peak at 570 nm indicating the existence of primary amines, while no peak at 570 nm is detectable for 8-aminoquinoline, indicating that the aromatic amine and pyridinic nitrogen do not give positive results in the Kaiser test. .... 149

Figure A1-8. (a, b) High-resolution TEM images showing that amorphous carbon residues were frequently observed inside the open cavity of NCNCs after the separation process. (c) High-resolution TEM image showing that one smaller cup was trapped inside the opening of a larger NCNC. All scale bars represent 5 nm. .... 150

Figure A1-9. (a – d) Other examples of TEM images of individual thiolated NCNCs corked by 40 nm GNPs. (e) TEM image at a lower magnification showing that several NCNCs were corked by GNPs at their open rims, indicating a preferential interaction between GNPs and the open sides of NCNCs..... 151

Figure A1-10. TEM images of GNPs attached on the sidewalls of NCNCs and on the open rims of NCNCs but not exactly corking the cups. .... 152

Figure A1-11. (a) TEM image of a thiolated individual NCNC capped by a silver nanoparticle with diameter of ~40 nm. (b) TEM image of an unfunctionalized individual NCNC capped by aldehyde-functionalized polystyrene latex nanoparticles with diameters of ~40 nm. The polymer nanoparticle fitting on the opening of the NCNC was shown to be stretched toward the inner cavity, presumably due to the capillary effect. .... 152

Scheme A1-1. Boc<sub>2</sub>O protection of amine groups on NCNCs to yield NH-Boc groups which prevented the amines from being detected by Kaiser test. Upon removal of the Boc groups, the amines gave a positive Kaiser test result again..... 153

Figure A2-1. (a) TGA curve of p-MWNTs in air. There was almost no material left after burning in air above 600 °C. (b) Energy-dispersive X-ray spectroscopy (EDS) elemental analysis of p-MWNTs. No iron peaks (6 – 8 keV) were observed. .... 156

Figure A2-2. Histogram showing increasing acidic group loadings on the surface of MWNTs along with 0, 5 and 8 hr carboxylation determined by Boehm’s Titration. .... 157

Figure A2-3. TGA curves for p-MWNTs, o-MWNTs (5hr) and o-MWNTs (8hr) in N<sub>2</sub> atmosphere. The TGA curves showed a progressively increasing weight loss along with the increasing carboxylation time, indicating more functional groups grafted on the nanotubes. ... 158

Figure A2-4. FTIR spectra for p-MWNTs, o-MWNTs (5hr) and o-MWNTs (8hr) before enzymatic degradation. The spectra show different vibrational modes in each sample including C=O stretching ( $1640\text{ cm}^{-1}$ ), C–O stretching ( $1100\text{ cm}^{-1}$ ), C–H stretching ( $2980\text{ cm}^{-1}$ ), O–H stretching ( $3440\text{ cm}^{-1}$ ) and so on, which indicate the existence of oxygen-containing defects such as carboxylic groups on MWNTs. .... 159

Figure A2-5. TEM images for (a) p-MWNT, (b) o-MWNT (5hr), and (c) o-MWNT (8hr) samples incubated with HRP under daily  $\text{H}_2\text{O}_2$  additions for 80 days. The morphology of nanotubes remained similar to samples observed at Day 60, however, the carbonaceous “flakes” were seen to be continuously degraded into even smaller pieces. All scale bars are 200 nm. ... 160

Figure A2-6. (a) TEM image of magnified carbonaceous flakes for o-MWNT (8hr) enzymatically degraded with constant  $\text{H}_2\text{O}_2$  addition at Day 2. The black dots with diameters around 5 nm adsorbed on the flakes are presumably HRP particles. (b) AFM image for the sample at Day 4. Large amounts of carbonaceous flakes were seen with thickness of about 0.65 nm. .... 161

Figure A2-7. Visible absorption spectra of HRP activity tested by Amplex Red and  $\text{H}_2\text{O}_2$  for p-MWNT, o-MWNT (5hr), o-MWNT (8hr) and n-MWNT samples before (dash lines) and after (solid lines) 80 days of degradation process. .... 162

Figure A2-8. Images from the optical microscope on the Raman sample stage. (a) Image of o-MWNTs (8hr) before enzymatic degradation, and (b) after enzymatic degradation. The sample before enzymatic degradation tended to aggregate into discrete spots after dried on a sample glass slide, while the sample after degradation formed an even, continuous film. Both samples appeared to be homogeneous as visually observed. 5 spectra were collected and averaged from different spots for both samples. .... 163

Figure A2-9. High-resolution TEM images for o-MWNTs (8hr) (a), and p-MWNTs (b) before enzymatic degradation. All scale bars are 5 nm. The defective sites are shown on the surface of o-MWNT samples as arrowed, in which about 5 – 8 graphitic walls were broken, while the p-MWNTs remain high graphitic integrity with well-defined walls..... 164

Figure A2-10. (a) TGA curves for n-MWNTs before (black) and after (red) purification process in air. (b) TEM image of purified n-MWNT samples after 80 days of incubation in Fenton oxidation environment. The extent of degradation was limited. .... 165

Figure A3-1. Raman spectra of as-synthesized stacked NCNCs (blue), oxidized NCNCs (red) and separated NCNCs (black). The corresponding D to G band ratios are shown in the parentheses..... 168

Figure A3-2. Magnified high-resolution TEM images of the corked NCNC in Figure 1d, focused on (a) the GNP, and (b) the nanocup. A citrate coating layer was typically observed on the outer surface of GNPs, but not on the inner surface in the cups, suggesting a direct interaction between GNPs and NCNCs. Small gold nanocrystals were also found sparsely bound on the graphitic sidewalls of the nanocup, however, they failed to grow into large nanoparticles, possibly due to the scarcity of functional groups on the sidewalls..... 169

Figure A3-3. TEM image of the supernatant solution of the GNP reduction reaction. Free GNPs are somewhat smaller than the GNPs bound to the NCNCs, because of the strong binding of GNPs toward NCNCs, GNPs tend to aggregate on the surface of NCNCs..... 170

Figure A3-4. (a) TEM images of NCNC mixed with commercial 30 nm GNPs. (b) UV-Vis spectra of NCNC mixed with commercial 30 nm GNPs (black) and free commercial GNPs (red). The TEM image shows that the commercial citrate-coated GNPs are not directly attached on the NCNCs, but leaving a gap in between, possibly due to the citrate coating layer. The SPR band of

the GNPs did not shift after mixing with NCNCs, indicating the absence of electronic interaction between GNPs and NCNCs. .... 170

Figure A3-5. TEM images of the supernatant (a) and the precipitate (b) of treated MWCNTs decorated with GNPs by reduction. (c) UV-Vis spectra of the supernatant and precipitate of MWCNT+GNP. (d) Raman spectra of MWCNTs decorated with GNPs (red) compared to MWCNTs only..... 171

Figure A3-6. X-ray photoelectron spectra (XPS) of N1s peak of NCNCs before (a) and after (b) corking with GNPs, and C1s peak of NCNCs before (c) and after (d) functionalization of GNPs. The carbon 1s profile is shown in (c,d). The peaks at 284.9 eV and 285.5 eV were assigned to graphitic  $sp^2$  carbon and C – N structures, respectively. After the GNP functionalization, the peaks corresponding to C – O and C = O structures at 286.7 eV and ~289 eV significantly increased, indicating the oxidation of carbon atoms by chloroauric acid..... 172

Figure A3-7. UV-Vis spectra of NCNCs with GNPs sampled at different reaction times. The sodium citrate was added 20 min after the incubation of NCNCs with  $HAuCl_4$ ..... 173

Figure A3-8. Pictorial views of the atomic configurations corresponding to adsorption of a  $Au_{20}$  cluster: (a) on a  $(7 \times 11)$  graphene flake in the central region of the flake; (b) on the graphene flake near the hydrogen terminated zigzag graphene edge; (c) above a graphene defect functionalized with three pyridinic N atoms; (d) above a substitutional N (graphitic N) on the graphene surface; (e) above a pyridinic N on the graphene edge, (f) above an aromatic amine group on the graphene edge; (g) above a graphitic N on the graphene edge; (h) above a  $CH_2NH_2$  group on the graphene edge; (i) near the edge of a graphene sheet functionalized with a carboxylic group; (j) attached to the edge of a bare graphene sheet; (k) attached to the amine group on the edge of a graphene sheet; (l) attached to the pyridinic N on the edge of graphene

sheet. Insets: top view of the bare graphene sheet with the corresponding bare or functionalized graphene flake. For each configuration the corresponding adsorption energy (in kcal/mol) of the Au<sub>20</sub> cluster is also provided. Legend of atoms: green; N, blue; H, white; O, red; and Au, orange.

..... 174

Figure A3-9. Degradation of separated NCNCs with hMPO in the presence of H<sub>2</sub>O<sub>2</sub> and NaCl.

(a – c) TEM images at (a) Day 5, (b) Day 10 and (c) Day 20. (d) Photograph of (1) the active sample of NCNCs treated with hMPO in the presence of H<sub>2</sub>O<sub>2</sub> and NaCl for 20 days, and (2) the control sample of NCNCs treated only with H<sub>2</sub>O<sub>2</sub> after 20 days; (2) the control sample of NCNCs treated with H<sub>2</sub>O<sub>2</sub> only for 20 days. (e) UV-Vis spectra and (f) Raman spectra of the activated sample during degradation. .... 177

Figure A3-10. Degradation of separated NCNCs in the NaClO control, with only NaClO as oxidant.

(a – c) TEM images at (a) Day 5, (b) Day 10 and (c) Day 15. (d) UV-Vis spectra and (f) Raman spectra of the sample during degradation. Incomplete degradation was observed on the sample treated with NaClO, the peak at 290 nm indicates the presence of NaClO..... 178

Figure A3-11. Separated NCNCs treated only with H<sub>2</sub>O<sub>2</sub>. (a) TEM image at Day 20; (b) UV-Vis

spectra and (c) Raman spectra of the sample during treatment. No significant degradation was observed on the NCNC sample treated only with H<sub>2</sub>O<sub>2</sub>. .... 179

Figure A3-12. Degradation of GNP-corked NCNCs with NaClO as oxidant. (a – c) TEM images

at (a) Day 5, (b) Day 10 and (c) Day 15. (d) UV-Vis spectra and (f) Raman spectra of the sample during degradation. NaClO only partially degrades the NCNCs by oxidizing the graphitic shells but does not release the GNPs from the nanocups, which is reflected by unchanged SPR bands and a monotonic decrease of D and G Raman bands..... 180

Figure A3-13. GNP-corked NCNCs treated with H<sub>2</sub>O<sub>2</sub> as a control. (a) TEM image at Day 20. The GNPs are still bound to NCNCs showing no apparent degradation. (b) UV-Vis spectra and (c) Raman spectra of the sample during the period of 20 days..... 181

Figure A3-14. GNP-corked NCNCs treated with hMPO and H<sub>2</sub>O<sub>2</sub>. (a,b) TEM image at (a) Day 5 and (b) Day 20. The GNPs were detached from NCNCs forming large agglomerates, but NCNCs were not significantly degraded. (c) UV-Vis spectra and (d) Raman spectra of the sample during the degradation process. The detachment and agglomeration of GNPs are reflected by the red-shift and disappearance of GNPs' surface plasmon resonance (SPR) bands and the loss of the surface-enhanced Raman scattering (SERS) effect..... 182

Figure A3-15. (a) TEM images showing that most of the GNPs were still attached to NCNCs in the sample treated with neutrophils without incubation. (b) Raman spectra of the NCNC sample treated with neutrophils before incubation (red) and after 18 h incubation (black). ..... 183

## PREFACE

I would first like to express my sincerest thanks to my research advisor, Professor Alexander Star, for the six years' academic guidance and financial support, without whom I would not have made all the achievement for my PhD degree. As a great mentor, his professional attitude and kind personality have always encouraged me in overcoming the challenges and pursuing more academic achievement. Not only have I developed as a scientist under his guidance, but I also have received precious career development opportunity and support from him over these years that lead me to a job position with Bayer MaterialScience. It has been a true honor to work with and learn from him.

I would like to express my appreciation to the members of my committee, Professor Valerian Kagan, Professor Paul Floreancig, and Professor Haitao Liu. I would like to thank their patience and valuable advice, as well as their inspirational discussions and excellence in their respective fields.

Furthermore, I wanted to give my full gratitude to all of my colleagues in the Star group. I am sincerely grateful to all the past and present Star group members, Dr. Douglas Kauffman, Dr. Brett Allen, Dr. Pingping Gou, Dr. Yanan Chen, Dr. Mengning Ding, Dr. Yifan Tang, Dr. Gregg Kotchey, Dr. HarindraVedala, Dr. Nadine Kraut, Dr. Haifeng Dong, Professor Yan Xing, Ian Feigel, Brian Barth, Gordon Chiu, Zachary Michael, Hao Bai, Wanji Seo, Seth Burkert, James Ellis, and others, for our wonderful collaborative experience and joyful time. My special

thanks to Dr. Yifan Tang, Dr. Gregg Kotchey, Dr. Yanan Chen, Dr. Mengning Ding. I extremely treasure the time we have worked together, the constructive discussion, and the enjoyable lunch time. It has been my great pleasure to work with all of you for the past 6 years. I also extend my thanks to Professor Dan Sorescu, and Professor Valerian Kagan, with whom I have collaborated outside the department.

Next, I would like to thank the faculty and staff of the Department of Chemistry for the guidance and assistance that I received from you throughout the years. In particular, I would like to thank Fran Nagy for her patient and warm-hearted help. On the first day when I came to the US, her kindness made me feel like home when I was ten thousand miles away. Also, to Joel Gillespie, his professional knowledge and training equipped me with essential instrumental skills. To Professor Haitao Liu, thank you for being my proposal mentor with all the fruitful discussions and precious advice. I appreciate all the work from Darlene Lanz, Toni Weber, and the chemistry stockroom. I hope to give my thanks to Tom Harper from the Department of Biological Sciences for the help on electron microscopy, and especially to Dr. Susheng Tan from NCF, who kindly trained me on many instruments and offered assistance with great patience.

I would not be where I am today without the constant support from my family and friends. Here, I would like to express my heartfelt gratitude to my parents, who unconditionally gave me all the love, cultivated my personality, and offered complete support all the time. To my friends in college and high school, I will never forget the happy memory of our time together. To my fiancée, Naiying Peng, thank you for your unconditional love, support, and encouragement, which are the most valuable fortune in my life.

Finally, I would like to extend my gratitude to the University of Pittsburgh, National Science Foundation, and especially, Bayer MaterialScience for the precious career opportunity.

## 1.0 INTRODUCTION

### 1.1 OVERVIEW

Carbon is the most fundamental element in materials and life sciences. The four valence electrons endow carbon with versatile bonding ability, leading to formation of diverse organic and inorganic compounds. Carbon also forms different elemental allotropes, such as  $sp^3$  hybridized diamond and  $sp^2$  hybridized graphite. During the rapid development of nanotechnology over the past three decades, carbon nanomaterials which are based on the  $sp^2$  graphitic structure have spawned enormous research interest. Graphene, a one-atom thick layer of graphite, is considered to be the basic building block of all graphitic materials.<sup>1-3</sup> When graphene sheets are conceptually rolled-up along certain axis, one-dimensional carbon nanotubes (CNTs) are formed. Ever since their discovery in the early 1990's,<sup>4-5</sup> CNTs have been at the forefront of nanoscience research because of their outstanding physical, chemical, and electronic properties as well as their high aspect ratios and surface areas.<sup>6-9</sup>

Depending on the number of graphitic walls, CNTs are classified as single-walled carbon nanotubes (SWCNTs) and multiwalled carbon nanotubes (MWCNTs) (**Figure 1-1a**). Essentially, SWCNTs can be viewed as a graphene sheet rolled up along the vector  $C_h = na_1 + ma_2$  (**Figure 1-1b**), where  $a_1$  and  $a_2$  are the graphene lattice vectors. The roll-up vector  $(n, m)$  determines the electric properties and chirality of nanotubes.<sup>7, 10</sup> For example, when  $|n-m| = 3q$  ( $q$  is an integer),

the nanotubes are metallic; and otherwise they are semiconducting. When  $n = m$ , the SWCNTs are referred to have an armchair configuration; when  $m = 0$ , the SWCNTs are zig-zag; otherwise the SWCNTs are chiral.<sup>11-13</sup> **Figure 1-2** shows typical electronic band structure of metallic and semiconducting SWCNTs. Semiconducting SWCNTs have a band gap of 0.5 – 2 eV, depending on their diameter and chirality as defined by roll-up vectors. Particular to their one-dimensional structure, the density of states (DOS) is found as discontinuous sharp spikes across the Fermi levels, known as the Van Hove singularities.<sup>14-15</sup> The electronic transitions exist in both semiconducting and metallic SWCNTs, corresponding to transitions between the first (namely,  $S_{11}$  for semiconducting and  $M_{11}$  for metallic SWCNTs) or between the second ( $S_{22}$ ) Van Hove singularities. The electronic transitions form spectroscopic bands that can be revealed by vis-NIR absorption spectroscopy.<sup>16</sup>

The MWCNTs consist of multiple concentric SWCNTs cylinders with typical diameters from several to tens of nanometers. The interlayer spacing between each graphitic wall is 0.34 nm,<sup>17</sup> which is slightly larger than the interlayer spacing of graphite sheets (0.335 nm) due to the constrain in the curved  $sp^2$  carbon sheets. While SWCNTs have typical diameters of around 0.4 to 3 nm, the outer diameters of MWCNTs span from 2 – 100 nm, with inner diameters from several to tens of nanometers.<sup>18</sup> Because the concentric SWCNTs that constitute MWCNTs are of different diameters and chirality, the MWCNTs overall are metallic with zero band gaps.<sup>19</sup>

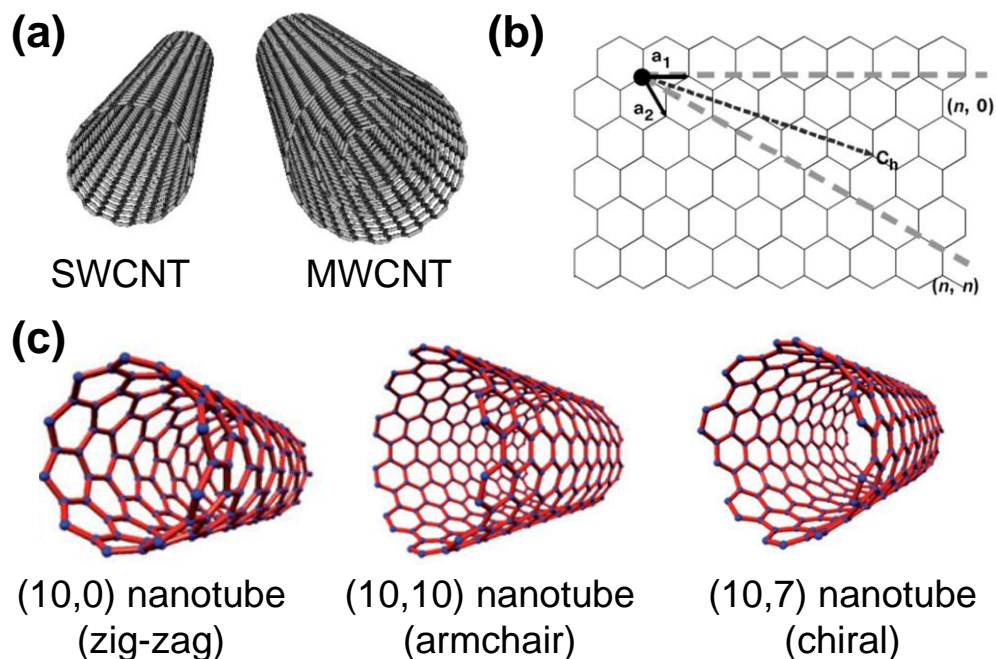


**Figure 1-1.** (a) Morphological illustration of single-walled carbon nanotube (SWCNT) and multiwalled carbon nanotube (MWCNT); (b) Schematic of a graphene sheet with two lattice vectors  $a_1$  and  $a_2$ , and one roll-up vector  $C_h = na_1 + ma_2$ ; (c) Schematic representations of zig-zag, armchair, and chiral SWCNTs. (a) is adapted from Ref. 20, Copyright 2007 John Wiley & Sons; (b) is adapted from Ref. 13, with permission from *Nature* **1998**, 391, 62-64, Copyright 1998 Nature Publishing Group; and (c) is reproduced from Ref. 12, with permission from *Nanoscale* **2009**, 1, 96-105, Copyright 2009 Royal Society of Chemistry.

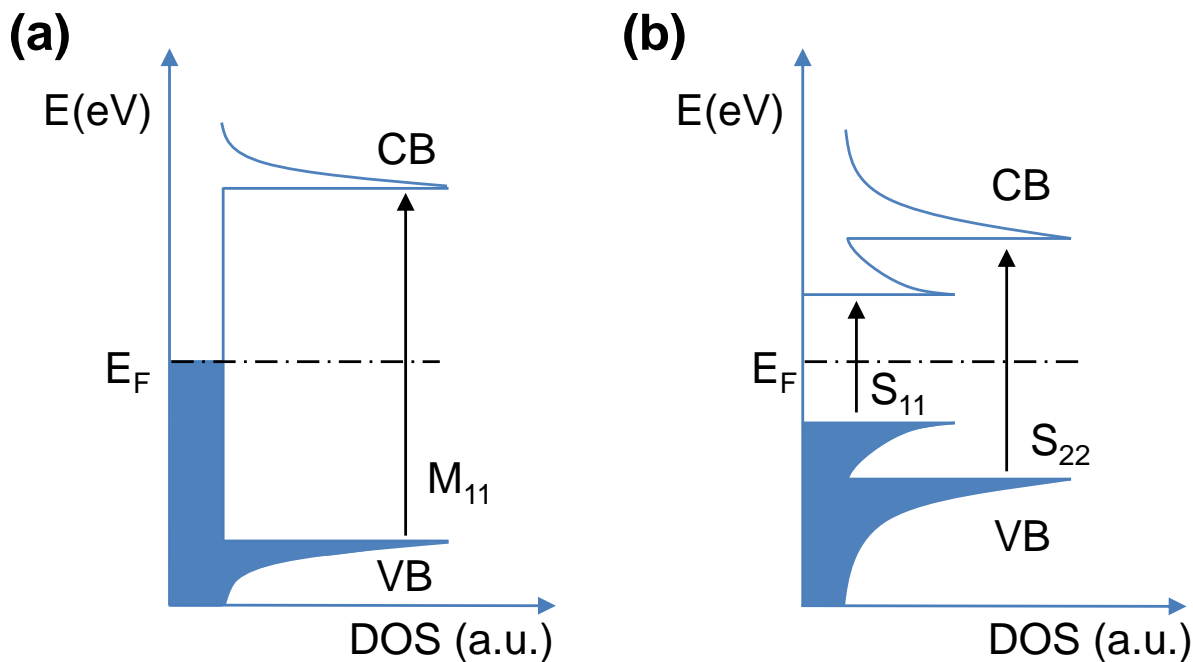


**Figure 1-2.** Energy structure of (a) metallic SWCNTs and (b) semiconducting SWCNTs, where X-axis is the density of states (DOS) and Y-axis is energy (E). The valence bands (VB) are colored and the conduction bands (CB) are white. The spikes in the band structure represent the Van Hove singularities.

### 1.1.1 Synthesis of Carbon Nanotubes

CNTs are mainly synthesized by three methods: arc-discharge, laser ablation, and chemical vapor deposition (CVD).<sup>10</sup> The typical reactor set-up is shown in **Figure 1-3**. Arc-discharge was the first method reported to synthesize CNTs,<sup>4,5</sup> in which a direct-current voltage is applied between two graphite-rod electrodes. Arc-discharge generates MWCNTs deposited on the cathode when pure graphite is used; however when the graphite-rod anode is infused with metal catalysts, such as Ni and Co, SWCNTs are produced in the form of soot.<sup>21</sup> In 1995, Smalley and

co-workers produced carbon nanotubes using the laser ablation technique.<sup>22</sup> In this method, a graphite target is irradiated by high-intensity laser and the carbon is evaporated under high temperature and then deposited on the collector to form either MWCNTs or SWCNTs. Similar to the arc-discharge method, formation of SWCNTs can be controlled by introducing metal catalyst in the graphite target.<sup>23</sup> Despite large amount of byproducts, both methods can yield SWCNTs with narrow diameter distribution. The CVD method uses evaporated hydrocarbon as precursors to deposit carbon nanomaterials on a substrate under pyrolysis.<sup>10</sup> Compared to the former two methods, the CVD synthesis requires less energy input and lower temperature, yields less byproducts, and can be scaled up. However, the CVD method is more suitable for synthesis of MWCNTs<sup>10, 24</sup> or graphenes,<sup>25</sup> because CVD synthesis of SWCNTs requires careful experimental control<sup>26-27</sup> to produce highly uniform SWCNTs compared with those produced by arc-discharge or laser ablation. More detailed discussion of CVD synthesis is provided in the following chapters.

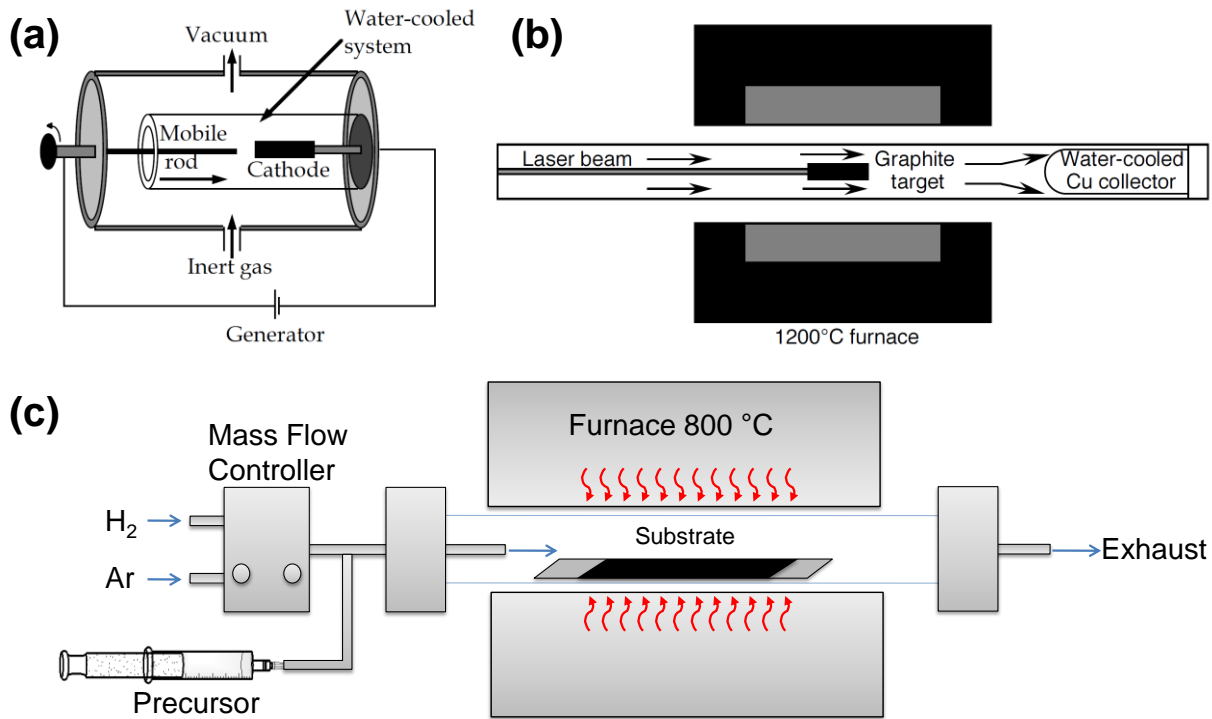


**Figure 1-3.** Illustration of the instrumental setup for (a) arc-discharge synthesis, (b) laser ablation synthesis, and (c) CVD synthesis of carbon nanotubes. (a) and (b) are adapted from Ref. 28, with permission from *Appl. Phys. A* **1998**, 67, 1-9, Copyright 1998 Springer.

### 1.1.2 Applications of Carbon Nanotubes

The unique morphology and outstanding properties of CNTs enable a wide range of applications. For example, the semiconducting properties of SWCNTs lead to applications in electronic devices such as field effect transistor (FET) sensors,<sup>29-33</sup> field emitters,<sup>34-36</sup> and transparent displays.<sup>37-39</sup> The strong mechanical properties and good conductivity make MWCNTs a good candidate for reinforcement in composite materials<sup>40-43</sup> and as a support for electrochemical catalysts.<sup>44-46</sup>

With their large surface area and diverse chemical properties for chemical functionalization, both SWCNTs and MWCNTs been explored as nanocarriers for drug delivery.<sup>47-51</sup> Compared to the traditional chemotherapy with nonspecific injection of drugs, the highly efficient delivery of drug molecules to targeted cells is desired because it improves the local concentration of drugs in targeted tissues while reduces side effects on healthy tissues.<sup>49, 52</sup> The major advantages of CNTs for drug delivery are that they accommodate high payload of drugs on their surfaces<sup>51</sup> or inside their tubular cavities,<sup>53</sup> while through a double functionalization strategy<sup>54</sup> other moieties can also be attached on CNTs to increase their solubility or cellular specificity, thus making CNTs excellent candidates for drug delivery carriers.

### **1.1.3 Functionalization of Carbon Nanotubes**

Chemical functionalization of CNTs is often necessary to modify their properties for different applications. Typical chemical modification involves covalent and noncovalent functionalization approaches. Pristine CNTs are not soluble in water, and thus oxidation is a common approach to introduce oxygen functionalities on the surface of CNTs to improve their solubility<sup>55-56</sup> and biocompatibility.<sup>57-60</sup> The most common oxidation method uses 3:1 v/v H<sub>2</sub>SO<sub>4</sub>/HNO<sub>3</sub> mineral acid mixture to react with CNTs under sonication. Such harsh condition opens the end caps of SWCNTs, creates structural defects on both the ends and the sidewalls of CNTs, and introduces oxygen-containing functional groups such as carboxylic, hydroxyl, and epoxy groups.<sup>61-62</sup> The oxidation of CNTs opens a wide range of chemical functionalization based on the reactivity of carboxylic groups,<sup>63</sup> especially the coupling reaction with amine groups.<sup>64</sup> Through a typical carbodiimide-based coupling reagent such as 1-ethyl-3-(3-dimethylaminopropyl) carbodiimide

(EDC),<sup>65</sup> different functional moieties, from small molecules to proteins, DNA, and polymers, can be grafted on the surface of CNTs.<sup>66</sup>

The graphitic nature endows CNTs with rich chemical reactivity associated with  $sp^2$  carbon.<sup>8, 67</sup> A number of organic reactions can be applied to functionalize the graphitic surface, including halogenation reaction followed by Grignard reaction,<sup>66, 68</sup> cycloaddition,<sup>67, 69-70</sup> radical addition,<sup>71-72</sup> and other reactions.<sup>8, 67</sup> The 1,3 dipolar cycloaddition of azomethine ylides on graphitic structures are one of the most common sidewall functionalization methods previously applied to fullerenes.<sup>73</sup> This zwitterion-mediated reaction was adopted by the Swager group for both SWCNTs and MWCNTs with good reactivity and scalability under mild conditions.<sup>74</sup> The 1,3 dipolar addition has been used in combination with the carboxyl/amine coupling reactions to achieve double or multiple functionalization on the same CNTs, which is highly preferred for drug delivery applications as the potential nanocarriers can be simultaneously functionalized with targeting groups, labeling groups, and drug payloads.<sup>50-51, 54</sup>

Covalent functionalization unavoidably alters the structure and the electronic properties of CNTs. The noncovalent functionalization, which is based on van der Waal's interactions achieved via either polymer-wrapping or  $\pi$ - $\pi$  stacking with aromatic molecules, is more advantageous in terms of preserving the intrinsic properties of CNTs.<sup>8, 75</sup> The graphitic structures show strong interaction toward compounds with  $\pi$  conjugated electrons. Aromatic molecules, such as doxorubicin (DOX), fluorescein isocyanate (FTIC), or pyrene derivatives can be efficiently attached on to the graphitic surfaces as "sticky labels".<sup>33, 76-77</sup> Moreover, the strength of  $\pi$ - $\pi$  stacking interaction is dependent on pH, thus reversible attachment of the aromatic molecules can be controlled by adjusting the pH levels of the mixture.<sup>76</sup>

Polymer wrapping method was earlier reported by O'Connell and co-workers for the noncovalent functionalization of SWCNTs with polyvinyl pyrrolidone (PVP) and polystyrene sulfonate (PSS) polymers.<sup>78</sup> Polymer-wrapping around the surface of SWCNTs can disrupt the bundles formed by individual CNTs and allow better dispersion of CNTs. Star and co-workers reported that starch amylose complexed with iodine can effectively form inclusion complexes with SWCNTs displacing the included iodine molecules.<sup>79</sup> The formation of starch-SWCNT complexes was indicated by the color fading of the starch-iodine complex and the much improved dispersion of SWCNTs in water. Liu and co-workers used phospholipid-polyethylene glycol (PL-PEG) to functionalize SWCNTs.<sup>77</sup> The PL chains wrap around the CNTs via hydrophobic interactions, and the hydrophilic PEG residues improve the water solubility and biocompatibility of SWCNTs leading to enhanced blood circulation.<sup>80</sup> The other terminal of the PEG molecules can be further functionalized with targeting groups or fluorescent tags to create multifunctional SWCNTs biological transporters.<sup>81</sup> Some aromatic group-containing polymers, such as poly(meta-phenylenevinylene) (PmPV)<sup>82-83</sup> or single-stranded DNAs (ss-DNAs),<sup>84</sup> have significantly high affinity toward CNTs, due to the existence of both  $\pi$ - $\pi$  stacking and hydrophobic interactions.

## 1.2 CHARACTERIZATION OF CARBON NANOMATERIALS

Both microscopic and spectroscopic techniques are utilized for characterization of carbon nanomaterials. The imaging of the carbon nanomaterial morphology is usually performed by electron or probe microscopes. Spectroscopic methods are often applied to characterize the

structural and chemical properties of the nanomaterials. This section introduces six of the most frequently used characterization techniques in the carbon nanomaterial research.

### **1.2.1 Transmission Electron Microscopy**

Transmission electron microscopy (TEM) is the most applied technique for imaging of nanomaterials. TEM operates an accelerated electron beam (80 – 400 kV) to pass through a thin specimen. During the transmission the electrons are scattered by the electron-rich atoms of the specimen, producing a pattern characteristic of the morphology of the sample in the transmitted beam.<sup>85</sup> The transmitted electron signals are collected by fluorescent screen or a CCD camera. Due to the small de Broglie wavelength of an electron (12.2 pm for 10 kV electrons and 2.5 pm for 200 kV electrons), the resolution limit of an electron beam is much lower than that of an optical microscopy. A high acceleration voltage can result in point-to-point resolution as low as 0.2 nm. TEM is particularly useful in characterization of carbon nanomaterials, as the transmitted electron beams not only probe the surface morphology, but also provide insight into the morphology of their hollow cavities. One drawback of imaging carbon-based nanomaterials is that the carbon may be burned by electrons with high energy, thus electron beams under low acceleration voltages such as 80 keV are frequently used. Because the TEM images are formed from the projection of the transmitted electrons through the sample, TEM can only provide imaging at x-y dimensions but is unable to probe the depth profile of the sample, unless special techniques are used, such as TEM tomography.<sup>86</sup> TEM is not only limited to the transmitted electrons, but the scattered electrons can also provide rich information on the structure and chemical composition of the sample. Different spectroscopic techniques have been developed as the accessory of TEM where the scattered electrons are collected for the chemical composition

analysis. For example, energy-dispersive X-ray spectroscopy (EDX) measures emitted X-rays corresponding to the unique energy difference between electron shells of a certain element; and electron energy loss spectroscopy (EELS) measures the energy loss of an incident electron beam due to the inelastic collision between the incident electrons and the shell electrons from the atoms of samples.

### **1.2.2 Scanning Electron Microscopy**

Scanning electron microscopy (SEM) produces the image of a sample by scanning a focused electron beam on its surface with typical energy from 0.2 keV to 40 keV.<sup>87</sup> A number of signals can be produced when the electron beam interacts with the atoms of the sample, including secondary electrons, back-scattered electron, and X-rays; each of them bears different information on either morphological topography or elemental composition.<sup>85</sup> The secondary electron imaging (SEI) is the standard equipment in SEM. The signals are derived from the ionized electrons of the specimen surface atoms generated by the inelastic scattering interaction with the incident electron beam. The secondary electrons having energy less than 50 eV are collected by a photomultiplier. The number of secondary electrons is related to the angle between the surface and the beam, based on which the surface topographic information can be obtained. The SEI can provide high resolution images of the surface to the detail of as low as 1 nm. SEI imaging requires that the specimen is electrically conducting to transfer the generated electrons, so non-conducting samples need to be first sputter-coated with metals. This step is, however, not required for imaging graphitic materials because of their inherent conductance. In addition to the surface imaging, SEM can also be equipped with EDX accessory to measure the

X-ray emitted during the ionization process, which can also provide elemental composition of the specimen.

### **1.2.3 Atomic Force Microscopy**

Atomic force microscopy (AFM) is a type of scanning probe microscopy (SPM) with high resolution,<sup>88</sup> which consists of micrometer-long probe with a sharp tip of several nanometers, connected to a cantilever. Different from a SPM that measures the tunneling current between the tip and the conductive specimen, AFM measures different types of atomic forces between the tip and the sample surface at enough proximity, including but not limited to van der Waals force, electrostatic force, and chemical bonding.<sup>85</sup> The atomic forces lead to a deflection in the cantilever according to Hooke's law.<sup>89</sup> The deflection is recognized by the shift of a laser spot reflected on the cantilever, which is then converted to the surface topography. The advantage of AFM is in its vertical resolution, which typically can reach about 1 Å; but the lateral resolution is much lower – of about 100 nm.<sup>88</sup> According to the nature of the tip motion, the AFM measurements are usually categorized to three modes: contact mode, tapping mode, and non-contact mode. In the contact mode, the tip is adjusted by a feedback signal from the force in order to hold at a fixed distance toward the surface of specimen. In the tapping mode, the cantilever is driven to oscillate vertically with amplitude of 100 – 200 nm. The amplitude of the oscillation is adjusted according to the force from the surface so as to prevent the tip from contacting the surface, thus the tapping mode lessens the damages to the surface and to the tips, compared to the contact mode. The non-contact mode is similar to the tapping mode, but the amplitude of the tip is much smaller to < 10 nm, which is suitable to measure the van der Waals

forces toward a soft surface. AFM is a very useful technique to characterize the thickness of a sample, especially the number of layers of graphene sheets.<sup>90-92</sup>

#### 1.2.4 Absorption Spectroscopy

Depending on the energy range corresponding to either electronic transitions or vibrational transitions, absorption spectroscopies are commonly referred to as ultraviolet-visible-near infrared (UV-Vis-NIR) spectroscopy or Fourier transform infrared (FTIR) spectroscopy. UV-Vis-NIR spectroscopy probes the electronic transitions of a material from the wavelength of ~200 nm to ~3000 nm, where SWCNTs have rich characteristic bands due to the electronic transition between the Van Hove singularities.<sup>14, 35</sup> A typical mixture of metallic and semiconducting SWCNTs have strong  $M_{11}$ ,  $S_{22}$ , and  $S_{11}$  transitions at about 725 nm, 1050 nm, and 1900 nm, respectively.<sup>16</sup> Noteworthy, the change of intensity of the  $S_{11}$  band characterizes the process of the electron donation/withdrawal by the adsorbed molecular species to/from SWCNTs.<sup>16</sup> For MWCNTs, however, no characteristic UV-Vis-NIR bands are discernable except only the  $\pi$ -conjugate electron broad peak at ~ 265 nm.<sup>93</sup> The concentration of CNTs can be calibrated using one of their characteristic bands according to the Beer-Lambert law.

FTIR spectroscopy uses IR light to probe the vibrational states of chemical bonds in organic materials, which usually have absorption peaks from 500  $\text{cm}^{-1}$  to 4000  $\text{cm}^{-1}$ . Only those vibrational modes causing a polarity change are IR active, so pristine carbon nanotubes do not have characteristic absorption bands.<sup>94</sup> However, after oxidation, due to the introduction of oxygen-containing groups such as carbonyls and hydroxyl groups, these functionalities can be distinctively characterized from FTIR spectra.<sup>95-96</sup> Similarly, hetero-atomic doping with N or B induces dipole-moments in the vibration modes, which can also be characterized by FTIR. For

example, the FTIR spectra of N-doped CNT samples show different vibrational bands from nitrogen bonding structures including N-H ( $3430\text{ cm}^{-1}$ ), C-N ( $1110\text{ cm}^{-1}$ ), C=N ( $1630\text{ cm}^{-1}$ ) and so on, confirming the existence of nitrogen functionalities.

### 1.2.5 Raman Spectroscopy

When a monochromatic light (e.g., a laser beam) irradiates on the sample substrate, the light may be scattered by the material, which excites an electron to a virtual energy state. When the excited electrons relax to their original energy state, they emit a photon with the same energy as the incident light, which is called Rayleigh scattering or elastic scattering; but when the excited electrons return to a different vibrational state, the emitted photon will have different energy relative to the incident light and the scattering is considered as inelastic, or Raman scattering.<sup>97</sup> The energy difference between the incident light and the scattered light gives the information of the vibrational modes in the material. Different from IR spectroscopy, Raman spectroscopy measures the change in the polarizability of a vibrational mode instead of the change in dipole moments. Therefore Raman is sensitive to nonpolar materials with symmetric vibrational modes, especially for the graphitic materials in which C-C bond vibrations do not typically induce IR activity.

Raman spectroscopy is commonly used to characterize the graphitic structures such as carbon nanotubes and graphenes. There are two Raman bands characteristic for graphitic materials known as the G band and the D band.<sup>98</sup> In which, the G band, appearing at  $\sim 1580\text{ cm}^{-1}$ , represents the tangential in-plane vibrational mode of graphitic carbon; and the D band at  $\sim 1345\text{ cm}^{-1}$  is due to the disorder-induced symmetry breaking in  $sp^2$  carbon. Typically, Raman spectra of CNTs are taken by drop-casting and drying nanotube suspensions on a quartz slide and then

focusing a 633 nm laser on the spot. The intriguing change of D and G bands makes Raman the most sensitive way to characterize the defects in carbon nanotubes. With increasing levels of the D to G band ratios, the graphitic structures are considered to be more defective.<sup>98</sup> In addition, the 2D band at about  $2600\text{ cm}^{-1}$ , which is an overtone of the D band, also indicates the number of layers in graphene sheets.<sup>98</sup>

One important application of Raman spectroscopy is the remarkable enhancement of Raman signals on substrate coated with small gold or silver nanoparticles, an effect known as surface-enhanced Raman scattering (SERS). The Raman enhancement is believed to arise from the interaction of the surface plasmon of Au/Ag NPs with the local electromagnetic field. Although the detailed mechanism of SERS by GNPs is still unclear, it is generally accepted that the SERS effect may arise from electromagnetic (EM) or charge-transfer (CT) mechanisms. The EM theory emphasizes on the local enhanced electromagnetic field “hot spot” induced by the surface plasmon resonance of GNPs,<sup>99</sup> which is typically more prominent on structures with sharp terminus or close interparticle proximity,<sup>100-101</sup> and can usually incur more than  $10^4$  enhancement.<sup>102</sup> The CT mechanism attributes the SERS to the chemical charge transfer between metal nanoparticles and the substrate, and typically accounts for 10 – 100 folds of enhancement.<sup>103</sup> It was mentioned by Osawa and co-workers that the SERS effect could be caused by a photon-induced charge-transfer process from Ag to the LUMO of the adsorbed molecules.<sup>104</sup>

### **1.2.6 X-ray Photoelectron Spectroscopy**

X-ray photoelectron spectroscopy (XPS) is an elemental analysis technique which provides the elemental composition and bonding information of the material. When a material is irradiated by

high-intensity X-ray, the X-ray ionizes the core electrons from the materials. XPS measures the kinetic energy of the escaped electrons, equal to the energy difference between the incident light and the binding energy of the core electrons, which is determined by the type and structure of the specific atoms. The binding energy of a core electron is weakened by the shielding effect from other electrons, thus the slight shift in the binding energy of an element indicates its chemical environment. When an atom is donating electrons, the shielding effect is reduced and the binding energy is increased, and vice versa. Because XPS detects those excited electrons that can actually escape out of the material, it only provides elemental information within 10 nm from the surface of the material. The quantitative ratio of element A and B can be determined from the XPS data using the following expression (Equ. 1):

$$\frac{n_A}{n_B} = \frac{I_A S_B}{I_B S_A} \quad (1)$$

In which  $n$  is the atomic concentration,  $I$  is the spectral intensity obtained by integrating the signal and  $S$  is the corresponding atomic sensitivity factor. Pristine  $sp^2$  carbon nanomaterials have a carbon XPS signal at about 285 eV, oxidation of the carbon structure leads to the shift of the carbon signal toward higher binding energy.<sup>56</sup> XPS is also useful to characterize the chemical structure of the doped heteroatoms in the graphitic lattice, such as characterizing N-doped CNTs.<sup>105</sup> The nitrogen atoms show a peak profile at around 400 eV, which can be deconvoluted into different subpeaks corresponding to different binding configuration of nitrogen.

### 1.3 NITROGEN-DOPED CARBON NANOTUBES

In addition to the aforementioned post-synthesis surface functionalization methods, doping of heteroatoms such as boron,<sup>106</sup> nitrogen<sup>107-108</sup> or phosphorus<sup>109</sup> into the graphitic structures of CNTs is another important route of chemical functionalization. These dopant atoms, either behaving as electron acceptors (B) or donors (N, P), disturb the graphitic integrity of CNTs, and can efficiently tailor their intrinsic chemical and electronic properties. Both theoretical<sup>110</sup> and experimental<sup>111</sup> research showed that the mechanical strength such as Young's modulus is weakened by doping B or N atoms into SWCNTs. And substitutional doping of B and N introduces strongly localized electronic features in the valence or conduction bands of CNTs, respectively,<sup>112</sup> causing the materials to be either p-type or n-type semiconductors. Remarkably, nitrogen-doping into the graphitic structure of MWCNTs greatly alters the tubular morphology<sup>108</sup> of the CNTs and endows the MWCNTs with significantly enhanced electrochemical catalytic activity toward oxygen reduction reaction (ORR) comparable to the performance of the noble metal platinum catalysts.<sup>113</sup> As a result, nitrogen-doped CNTs are intensively investigated materials nowadays compared to other doped CNTs.

#### 1.3.1 Synthesis of Nitrogen-doped Carbon Nanotubes

Nitrogen doping can be performed by either in situ doping during the CNT synthesis or post-synthesis doping. The common synthetic methods for in situ doping involve CVD and solvent-thermal reactions.<sup>108, 114-119</sup> Nitrogen species are introduced into the CVD furnace or an autoclave reaction chamber together with the precursors of carbon sources and metal catalysts. The principle of synthesis is based on the pyrolysis/atomization of the carbon and nitrogen

compounds and re-deposition on the metal catalytic nanoparticles (NPs). For the post-synthesis doping, nitrogen atoms are implanted into the pre-formed graphitic nanostructures by exposure of carbon nanomaterials to nitrogen-containing gas (e.g.,  $\text{NH}_3$ ) at high temperature,<sup>120-121</sup> or alternatively, by electrochemical functionalization in a nitrogen-containing electrolyte.<sup>122-123</sup> Other methods such as arc-discharge<sup>124</sup> and dc magnetron sputtering<sup>125</sup> were also reported for synthesis of nitrogen-doped CNTs. Comparatively, CVD is the most prevalently applied method for synthesis of nitrogen-doped CNTs because of its advantages of the simple procedures and ease of control.

For the CVD synthesis, the nitrogen sources are typically small molecules such as acetonitrile,<sup>108</sup> ammonia,<sup>114</sup> melamine,<sup>126</sup> pyridine,<sup>127</sup> and other nitrogen-containing organic molecules. Iron NPs are the mostly used as CVD catalysts. Depending on the way Fe NPs are introduced to the CVD system, there are two different methods of CVD growth, namely “floating catalyst” and “fixed-bed catalyst” schemes.

In the floating catalyst method, ferrocene is used as the catalyst-precursor and mixed with the liquid feed stock, which is then continuously injected to the tube furnace during the growth process. This method provides a much higher yield than the fixed-bed method because of the abundance of catalytic particles.<sup>128</sup> In our synthetic method, the liquid precursor is comprised of xylenes (89.25 w%), acetonitrile (10 w%) and ferrocene (0.75 w%). In a double zone furnace, the liquid precursor is first injected into the lower-temperature zone at  $\sim 300$  °C, where the thermal decomposition of ferrocene provides in situ generation of iron catalytic NPs brought on to the quartz slide placed in the higher-temperature zone (800 °C). The carbon and nitrogen sources are atomized and deposited on the Fe NPs to form tubular structures. The as-synthesized N-doped CNTs appear as a thick carpet on the quartz substrate and can be collected by peeling

off with a razor blade. The resulted CNTs are typically 1 – 4  $\mu\text{m}$  long with diameters ranging from 12 – 40 nm.<sup>108</sup>

The potential issue with the floating catalyst scheme is the random deposition of Fe NPs during the growth process. Due to lack of control over the diameter of the Fe NPs, the resulted nanotubes tend to exhibit a random distribution of diameters and higher levels of iron catalyst residues. Alternatively, in the “fixed-bed” catalyst scheme, the Fe NPs are pre-synthesized and spin-coated on quartz substrate. Cheung and co-workers developed the method to control the diameter of undoped CNTs during CVD synthesis by controlling the sizes of iron particles deposited on the substrate.<sup>129</sup> Fe NPs were first synthesized by thermal decomposition of iron pentacarbonyl ( $\text{Fe}(\text{CO})_5$ ) and their sizes were controlled by using different fatty acid as capping ligands (oleic ( $\text{C}_{18}$ ), lauric ( $\text{C}_{12}$ ), or octanoic acid ( $\text{C}_8$ )). It was found that the capping ligands with longer carbon chains result in smaller iron nanoparticles and that the diameter of as-synthesized CNTs depends on the size of iron nanoparticles. This fixed-bed catalytic scheme was adopted in the synthesis of N-doped CNTs.<sup>114</sup> The Fe NPs capped with either  $\text{C}_{18}$ ,  $\text{C}_{12}$ , or  $\text{C}_8$  fatty acid were synthesized. The Fe NP suspension was spin-coated on a quartz slide and placed in the quartz tube, and the synthesis was carried out at 950  $^\circ\text{C}$  with a precursor absent of iron (5%  $\text{NH}_3$  in EtOH). The resultant N-doped CNTs showed fairly uniform diameters, ranging from  $16 \pm 4$  nm for  $\text{C}_{18}$ -capped Fe NPs, to  $33 \pm 5$  nm for  $\text{C}_8$ -capped Fe NPs.<sup>114</sup> The iron impurities were greatly reduced. This method provides good control over the size of N-doped CNTs and high purity, but the only drawback is the low yield per batch synthesis, due to the scarce density of iron catalyst on the quartz slides. With increasing amount of Fe NPs coated, however, the NPs tend to melt together under high temperature and lose the uniform size.<sup>114</sup>

### 1.3.2 Purification of As-synthesized N-doped Carbon Nanotubes

The introduction of impurities such as Fe NPs and amorphous carbon in the as-synthesized CNTs is a major issue for CVD synthesis. The presence of the impurities hinders the accurate characterization of the N-doped CNTs' chemical and electrical properties,<sup>130</sup> and may also trigger additional toxicity and carcinogenicity in biomedical applications, due to fine-metal-particle induced health risks.<sup>131</sup> The purification procedures are usually needed before further applications of N-doped CNTs. The purification methods can typically fall into three categories: physical separation, gas-phase oxidation, and liquid-phase oxidation.<sup>131</sup> The physical separation typically involves filtration, centrifugation or chromatographic methods which separate impurities based on their different morphology or physical properties. One example is the magnetic filtration performed by Luzzi et al.,<sup>132-133</sup> which uses a strong magnetic field to pull out the ferromagnetic metal particles during a filtration process. This method often has a low efficiency because most nanotubes containing metal particles enclosed are also pulled out. The purification method targeting to remove amorphous carbon is the gas-phase oxidation which is performed in the furnace after CVD growth in air, O<sub>2</sub>, or H<sub>2</sub>O vapor atmosphere at a temperature range of 300 – 600 °C. This method is fairly effective for purifying MWCNTs<sup>134</sup> because of their resistance to high temperature at which the amorphous carbon impurities are burned off, and it is frequently combined with liquid-phase oxidation for the removal of metal NPs.<sup>135</sup> For liquid-phase oxidation, acid solutions including mixtures of HNO<sub>3</sub>/H<sub>2</sub>SO<sub>4</sub> are often used to oxidize catalytic metal particles. However, this mixture is also known to damage graphitic walls.<sup>136</sup> Alternatively, HCl as a non-oxidative acid, is a good candidate to remove metal particles from nanotubes without damaging the graphitic structure, but during the CVD synthesis, the catalytic metal particles are often coated with amorphous carbon or entrapped inside nanotubes and thus

become inaccessible to HCl. Wang and co-workers developed a one-pot, solution-phase reaction to remove carbon-coated iron nanoparticles from SWNTs with good selectivity and efficiency.<sup>137</sup> By heating raw SWCNTs at 40 – 70 °C in an aqueous mixture of H<sub>2</sub>O<sub>2</sub> and HCl, both amorphous carbon and iron particles can be effectively removed leaving SWCNTs intact. During this process, the iron impurities can catalyze H<sub>2</sub>O<sub>2</sub> to form hydroxyl radicals (OH), known as Fenton chemistry.<sup>138</sup> The latter is a stronger oxidant that oxidizes the carbon coating shell, and opens the access of HCl to the iron particles.

Although many research studies have addressed purification of undoped CNTs, a little is known about N-doped CNTs.<sup>139</sup> Because the nitrogen doping disturbs the graphitic integrity of the nanotubes, N-doped CNTs are thought to be more susceptible to oxidation. Therefore, aggressive purification methods were avoided and the H<sub>2</sub>O<sub>2</sub>/HCl purification routine mentioned above was adopted.<sup>137</sup> The as-prepared N-doped CNT samples contain large amounts of iron nanoparticle impurities with sizes 5 – 15 nm, most of which are either coated with amorphous carbon, or confined inside the nanotube shells. After the purification process, the iron nanoparticles outside the nanotubes were mostly removed, leaving mainly those inside the nanotubes unaffected, presumably due to higher resistance of the multi-walled structure toward H<sub>2</sub>O<sub>2</sub> than amorphous carbon. This result suggests that the removal of iron contents from N-doped CNTs is not as easy as from SWCNTs without damaging the graphitic structure. However, sonication with oxidative acids H<sub>2</sub>SO<sub>4</sub>/HNO<sub>3</sub> can effectively remove the most majority of the iron impurities, but also introduce oxygen-functionalized structural defects.<sup>140</sup>

### 1.3.3 Morphology, Structure, and Growth Mechanism of Nitrogen-doped Carbon

#### Nanotubes

Unlike undoped MWCNTs with continuous tubular morphology, the N-doped CNTs consist of many compartmented structures resembling the shapes of bamboo joints or stacked cups.<sup>105, 107-108, 141-143</sup> The difference between the “bamboo-like” and the “stacked-cup” nanotubes are distinct in the case that the latter do not have covalent contact between adjacent segments.<sup>142</sup> The morphology of the N-doped CNTs depends on the experimental condition such as the type and concentration of nitrogen source and catalyst.<sup>127, 143-144</sup> For example, when melamine is pyrolyzed on Ni catalysts,<sup>126</sup> or when cyanuric chloride ( $C_3N_3Cl_3$ ), ferrocene, and sodium azide ( $NaN_3$ ) are heated in a sealed system,<sup>141</sup> the more “bamboo-like” morphology is obtained, where each compartment is cylindrical with parallel side walls more like bamboo joints (**Figure 1-4a**); Under some other conditions, such as using gaseous nitrogen sources ( $N_2$  or  $NH_3$ ),<sup>114, 142, 144</sup> or using acetonitrile as in our laboratory,<sup>105, 108</sup> the “stacked-cup” morphology is obtained, where the compartments are more of conical shape with sidewalls unparallel to the tubular axis (**Figure 1-4b**). In this case, each of the cup-shaped compartments is inserted into the cavity of adjacent ones and connected via interlayer van der Waal’s interaction.<sup>105</sup> The concentration of nitrogen is highly responsible to the formation of compartmented structures: with increasing amount of nitrogen source in the precursor, the well-defined uniform compartments eventually turn into corrugation of random interlinkages between the sidewalls (**Figure 1-4c**).<sup>127, 143</sup>

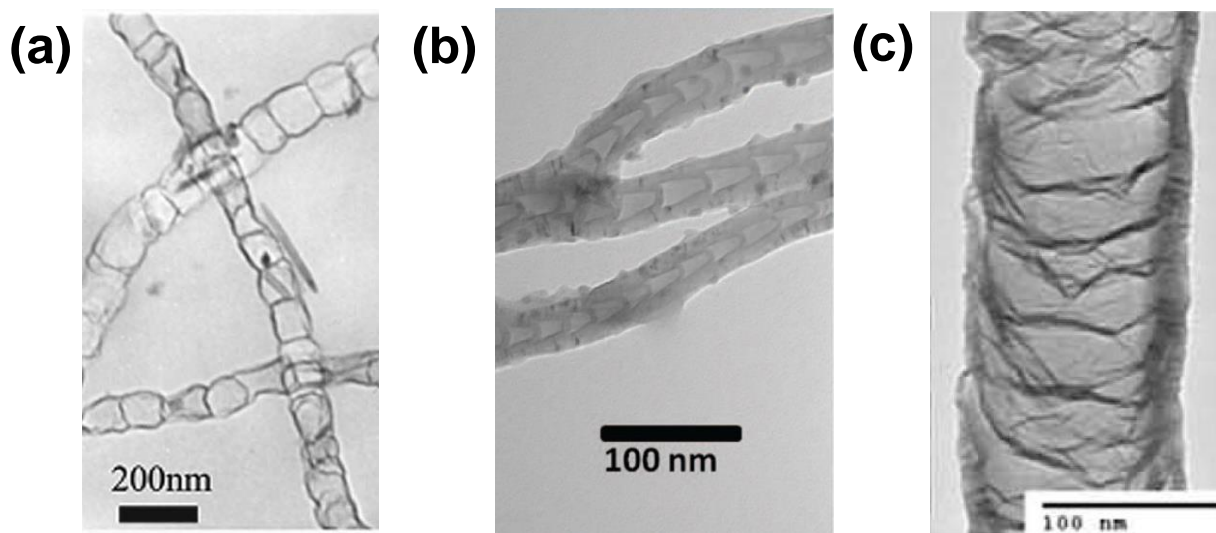


**Figure 1-4.** TEM images of different nitrogen-doped CNTs with (a) “bamboo-like” morphology; (b) “stacked-cup” morphology; and (c) Corrugated random interlinkages between the sidewalls. (a) is adapted from Ref. 141, with permission from *Appl. Phys. Lett.* **2007**, *90*, 113116, Copyright 2007 AIP Publishing LLC; (b) is adapted from Ref. 108, with permission from *ACS Nano* **2008**, *2*, 1914-1920, Copyright 2008 American Chemical Society; and (c) is adapted from Ref. 127, with permission from *Carbon* **2010**, *48*, 1498-1507, Copyright 2010 Elsevier.

The growth of N-doped CNTs follows a vapor-liquid-solid (VLS) mechanism via either “base-growth mode” or “tip-growth mode” as proposed by previous studies (**Figure 1-5a**).<sup>107, 145</sup> The Fe NPs form liquid nanosized droplets under high temperature, in which atomized carbon and nitrogen are dissolved and precipitated on the liquid surface. The precipitation of the graphitic layers on the catalytic iron particles forms compression strain stretching the particles. Due to the size similarity between C and N atoms, nitrogen is easily incorporated into the graphitic lattices. Because N has one more electron in the valence shell than C, the dopant N atoms tend to introduce disorder in the graphitic structure, and cause a negative curvature change in the graphitic walls,<sup>146</sup> which possibly generates a stretching force to the liquefied catalytic

metal particles during CVD growth and pulls them into cup-like shapes. The N atoms on the surface of graphitic walls mainly exist in two types (**Figure 1-5b**):<sup>112</sup> substitutional (graphitic) N coordinated to three C atoms in a  $sp^2$ -like fashion, which are possibly located at the tip of the cups inducing curvature; and the pyridine-type N with two N-C bonds and one electron pair, which tend to reside at the edges of either structural holes or the opening basal planes. However, both theoretical calculation<sup>147</sup> and experimental characterization<sup>142</sup> showed that the N atoms are energetically unfavorable to incorporate into the graphitic network, but tend to form dangling bonds such as pyridines, pyrroles, and amines at the graphitic edge, discontinuing the subsequent nanotube growth. When the growth of graphitic basal plane is stopped by nitrogen doping, an individual cup is formed and the iron nanoparticle is ejected to form a new cup. The N atoms preferentially stay at the open edge of the nanotube cups, and the length of each compartment can be controlled by N/C ratio during the growth process.<sup>114, 127</sup>

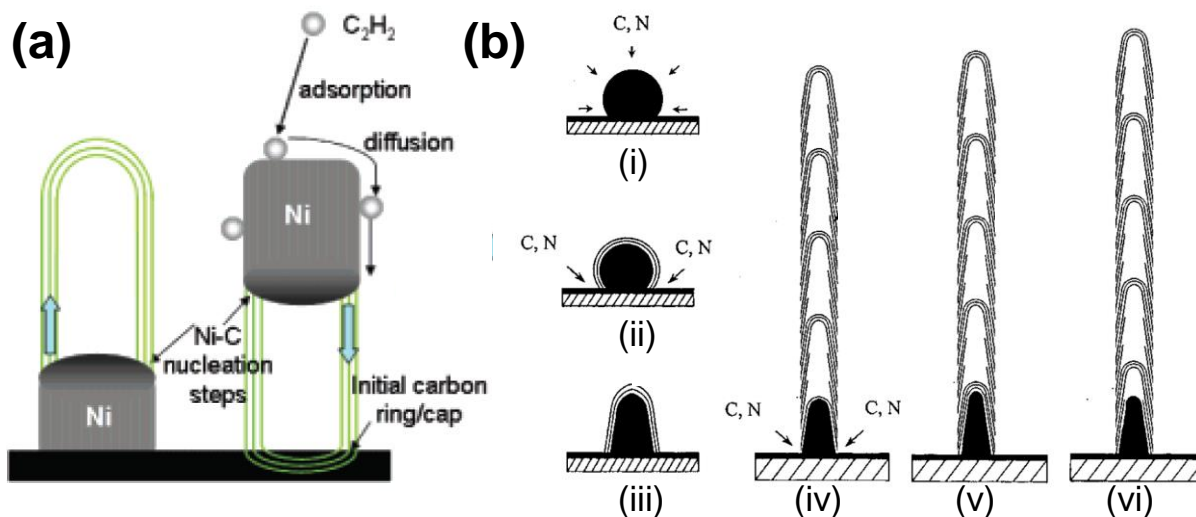


**Figure 1-5.** (a) Schematic illustration showing the CVD growth of a N-doped CNT on a metal catalytic nanoparticle via either “base-growth mode” (left) or “tip-growth mode” (right); (b) The detailed growth mechanism of the “base-growth mode”: (i) formation of a liquid catalyst particle and dissolution of C and N atoms, (ii) precipitation of C, N atoms on the droplet surface, (iii) the curvature effect stretching the catalyst particle, (iv) precipitating the first graphite layer of a nanocup, (v) stopping growth when the cup edge is saturated with N, and (vi) beginning to precipitate the graphite sheets of the next nanocup. (a) is reproduced from Ref. 145, with permission from *Nano Lett.* **2007**, *7*, 2234-2238, Copyright 2007 American Chemical Society; and (b) is reproduced from Ref. 107, with permission from *J. Appl. Phys.* **2002**, *91*, 9324-9332, Copyright 2002 AIP Publishing LLC.

### 1.3.4 Potential Applications of N-doped Carbon Nanotubes

Nitrogen doping in MWCNTs leads to many potential applications including energy storage and conversion as well as electrochemical catalysis. Wang’s group showed that the N-doped CNTs have good performance in hydrogen<sup>148</sup> and lithium storage<sup>149</sup> and attributed it to the unique short

cup-shaped structure with discontinuous graphitic layers between each cup that opens access to H<sub>2</sub> and Li binding. The Li nanocrystals were found on the inside surface of nanotube walls upon intercalation and brought disorder to the graphitic structures. Due to this interaction, the capacity of the Li ion in N-doped CNTs as the anode is much higher than that of graphite, which makes the material a potential candidate for the anodic material of Li ion battery. Recently, the N-doped CNT electrodes were found to catalyze a four-electron oxygen reduction reaction (ORR) with high electrocatalytic activity.<sup>113</sup> Compared to commercial platinum-based electrodes, the N-doped CNT electrodes have many advantages such as lower overpotential, smaller crossover effect, and better stability. The effective catalysis is thought to be due to a side-on adsorption of O<sub>2</sub> (with both O atoms adsorbed) on the carbon atoms adjacent to nitrogen dopants where a charge delocalization happens. This diatomic adsorption configuration can weaken the O–O bond so as to facilitate the ORR. It is suggested that both nitrogen and iron residues in the N-doped CNTs contribute to the ORR catalytic activity.<sup>150</sup> Besides the ORR catalysis, the N-doped CNTs were also found to have similar electrocatalytic activity toward oxidation of H<sub>2</sub>O<sub>2</sub>,<sup>151-152</sup> which can be potentially used in electrochemical sensors for H<sub>2</sub>O<sub>2</sub> and biosensors.

So far, most of the reports focused on undoped SWCNTs or MWCNTs for drug delivery applications, with rare examples of N-doped CNTs.<sup>153</sup> However, their cup-shaped segments may act as excellent candidate as drug delivery carriers if they can be individually separated out of the stack. The intrinsic nitrogen functionalities may presumably provide more binding sites for different purposes, and the cup interior can be loaded with drug cargo. More importantly, N-doped CNTs were found to have better biocompatibility with reduced pulmonary toxicity in mice even at high doses compared to SWCNTs and MWCNTs.<sup>154</sup> These findings indicate that N-doped CNTs may have better performance in drug delivery applications.

### 1.3.5 Separation and Manipulation of Individual Nanocups from N-doped Carbon

#### Nanotubes

Attracted by their potential applications as nanoscale containers, great efforts have been devoted to preparation of short CNTs since their discovery.<sup>155-158</sup> Typical shortening of SWCNTs and MWCNTs involves cutting with strong oxidative acids (e.g., H<sub>2</sub>SO<sub>4</sub>/HNO<sub>3</sub>),<sup>62, 155</sup> or physical separation by probe-tip sonication.<sup>159</sup> However, the interior space of short SWCNTs is very limited for material storage, and cutting MWCNTs is hard due to their structural integrity. Comparatively, the cup-shaped segments in the N-doped CNTs are very promising for nanocontainer applications, and the noncovalent interaction between adjacent stacked cups ensures the easy isolation of individual nanocups, which are termed as nitrogen-doped carbon nanotube cups or NCNCs for short.

Both physical and chemical methods have been used for separation of NCNCs. Physical techniques involve simple grinding with a mortar and pestle,<sup>107-108, 160</sup> ball milling,<sup>161</sup> or ultrasonication,<sup>105, 162</sup> each with varying effectiveness. Chemically, the N-doped CNTs can be cut short following similar acid-oxidation treatment such as in H<sub>2</sub>SO<sub>4</sub>/HNO<sub>3</sub> mixture,<sup>140, 163</sup> or under microwave-assisted plasma etching.<sup>164</sup> In our group, N-doped CNTs were earlier separated by mortar-pestle grinding.<sup>108</sup> The as-synthesized N-doped CNTs were transferred into a glass mortar and pestle, to which several drops of ethanol were added, and constant grinding was performed for 30 min. The procedure is labor-intensive, time-consuming, and with low yield as individual nanocups are only sporadically obtained. The separation effect was greatly improved after the adoption of the probe-tip sonication technique, which provides ultrasonic energy with high power density into the solution. Long duration (10 – 15 hr) sonication of N-doped CNTs in DMF solution effectively separated the cup segments into short stacks and individual cups.<sup>105</sup>

Furthermore, we combined both chemical oxidation and physical sonication for NCNC separation.<sup>140</sup> The N-doped CNTs were first treated with the H<sub>2</sub>SO<sub>4</sub>/HNO<sub>3</sub> mixture, and then processed with probe-tip sonication. The oxidative acid mixture creates oxygen defects on the graphitic structure, which weakens the interaction between adjacent cups and greatly facilitates the subsequent ultrasonic separation. The individual nanocups can thus be obtained with much improved yield.

The separated NCNCs have active chemical properties due to the exposure of the nitrogen functionalities and can be further manipulated as nanocontainers.<sup>105</sup> We have previously shown that by reacting with glutaraldehyde, they can be crosslinked to form nano-sized “capsules” and confine gold nanoparticle “cargo” in their interior cavities.<sup>114, 165</sup> This phenomenon indicates the existence of the amine groups at the open rims of the cups that react with the aldehyde groups by imine condensation reaction. In this research, the intrinsic amine groups were confirmed by Kaiser test and were thiolated with 3-mercapto-propionic acid.<sup>105</sup> The thiolated NCNCs showed high affinity towards commercial gold nanoparticles (GNPs), which effectively form corks on the opening of the cups, sealing the interior space. Most recently, we have demonstrated that the GNP corks can be more effectively formed on the open rims by in situ reduction of chloroauric acid (HAuCl<sub>4</sub>) in the presence of sodium citrate. These results will be discussed in detail in the following chapters.

#### **1.4 ENZYMATIC DEGRADATION OF CARBON NANOMATERIALS**

The intrinsic chemical inertness of graphitic structure makes CNTs rather stable unless that harsh oxidation conditions, such as high temperature or strong acid treatment, have been applied.<sup>136, 166</sup>

Our group has shown that oxidized SWCNTs can be further enzymatically degraded in horseradish peroxidase (HRP) environment with assistance of H<sub>2</sub>O<sub>2</sub>,<sup>167-168</sup> which opens a promising pathway to degrade carbon nanomaterials under mild and environmentally friendly conditions.

Some of the material contained in this section was published as a review article in the journal *Advanced Drug Delivery Reviews* and reproduced with permission from *Adv. Drug Delivery Rev.* **2013**, 65, 1921-1932, Copyright 2013 Elsevier. The full citation is listed as Ref. 169.

**List of Authors:** Gregg P. Kotchey, Yong Zhao, Valerian E. Kagan, and Alexander Star

**Author Contributions:** All authors contributed to the writing of this review article.

#### **1.4.1 Toxicity and Environmental Impact of Carbon Nanotubes**

Although many promising applications have been proposed for carbon nanotube materials, their potential health risks and environmental impact are still not fully understood, which inevitably hindered their potential biological or industrial applications. CNTs injected in vivo are likely captured by antibody opsonization inducing immune responses.<sup>80</sup> It was observed that CNTs can cause pulmonary toxicity upon inhalation,<sup>170-171</sup> including inflammatory response<sup>169, 172</sup> and asbestos-like pathogenicity.<sup>173</sup> In vitro cellular studies also showed oxidative stress, cytotoxic responses and apoptosis induced by CNTs.<sup>174-176</sup>

The toxicity of CNTs varies a lot with different nanotubes, depending on their geometric structures such as length and specific surface area, and also the surface functional groups and

defects. For example, it was reported that MWCNTs have less cellular toxicity than SWCNTs; the latter showed less tendency toward phagocytosis by macrophages.<sup>177</sup> Depending on their length, CNTs may exhibit different pathogenic behaviors.<sup>169</sup> Long fibrous CNTs are difficult for macrophages to phagocytose, inducing asbestos-like pathogenicity and formation of granulomas and fibrosis in the lungs,<sup>57, 173, 178</sup> while short and functionalized CNTs are more easily phagocytosed and cleared eventually.<sup>179-181</sup> The surface modification of CNTs also directly affects their inflammatory response and toxicity. Some study showed that the oxidized CNTs with more defects have higher cytotoxicity than pristine CNTs,<sup>175</sup> though the better hydrophilicity of oxidized CNTs allows for better cellular uptake and blood circulation. But this does not necessarily mean that pristine CNTs are more biocompatible, they are more easily captured by the reticuloendothelial system (RES) in vivo.<sup>182</sup> A number of strategies are available to tune the surface properties of CNTs and mitigate their cytotoxicity, such as functionalization with DNA, protein, or polymers.<sup>183-185</sup> Especially, Dai's group showed that short SWCNTs functionalized with branched PEGylated phospholipids exhibited long circulation time and resistance to opsonization/nonspecific binding of proteins.<sup>80</sup>

As the applications of carbon nanotube materials continue to rise, industrial products containing CNTs are likely to be more and more prevalent in our daily life and have better chances to pervade into the eco-systems.<sup>186-187</sup> So far, there are reports showing that the CNT materials can be stabilized in aqueous systems by natural organic matter (NOM)<sup>188-189</sup> and have toxic effects on aquatic organisms,<sup>179</sup> but the detailed route of CNT materials in ecological circulations is not known yet, and they are likely to accumulate along the food chain due to their resistance to physiological or environmental degradation. Therefore, there is a necessity to investigate the subsequent disposal of these materials.

## 1.4.2 Peroxidases and Mechanism of Enzymatic Oxidation

Peroxidases are a family of hemoprotein enzymes that catalyze the oxidation reaction by hydrogen peroxide ( $\text{H}_2\text{O}_2$ ) in the organisms.<sup>190</sup> Most peroxidases have a heme cofactor as the active site, which consists of a ferric ( $\text{Fe}^{3+}$ ) ion contained in a porphyrin structure (i.e., ferriprotoporphyrin IX) in the resting state of the enzyme. There are two superfamilies of peroxidases derived from either plants (and fungi),<sup>191</sup> or mammals,<sup>192</sup> which are significantly different from each other in terms of sizes and the bonding mechanism of hemes. Mammal peroxidases often have much large sizes with about 576–738 amino acids compared to plant peroxidases (~ 300 amino acids).<sup>190</sup> The major role of peroxidases in both plants and mammals is the defense against pathogens and stress, although they also participate in biosynthesis, metabolism, and degradation of toxic redundant. The ideal substrate for most peroxidases is  $\text{H}_2\text{O}_2$ , by which the heme active sites gets oxidized, resulting highly oxidative transient intermediates known as Compound I, able to oxidize a number of physiological donors or xenobiotics.<sup>190, 193</sup> Here, two types of peroxidases derived from either horseradish roots (horseradish peroxidase, HRP) or human blood (human myeloperoxidase, hMPO) are introduced.

### 1.4.2.1 Horseradish Peroxidase

Horseradish peroxidase (HRP) is a secretory plant peroxidase excreted from the root of horseradish (*Armoracia rusticana*), participating a series of bioprocesses such as metabolism, biosynthesis, and extracellular defense.<sup>190</sup> This enzyme has a wide biochemistry applications due to its sensitivity to catalyze  $\text{H}_2\text{O}_2$  oxidation that allows the amplification a weak signal from a target molecules involved in a biological process.<sup>194</sup> As shown in **Figure 1-6a**, HRP is a

monomeric enzyme containing a noncovalently bound ferriprotoporphyrin IX heme active center (molecular weight ~44 kDa).<sup>195</sup> The iron in the heme center is ferric state ( $\text{Fe}^{3+}$ ) in the resting enzyme with a coordination bond to the imidazole side chain from a histidine residue at the proximal site to the enzyme. When  $\text{H}_2\text{O}_2$  binds to the heme group, it oxidizes the iron core forming a peroxide intermediate, which then undergoes proton-migration and dehydration forming an active enzyme with a oxy-ferryl ( $\text{Fe}^{4+}=\text{O}$ ) state and a porphyrin  $\pi$  cation radical known as Compound I.<sup>173, 193</sup> Compound I is highly oxidative and gets reduced back to the Fe(III) state while oxidizing the enzyme substrate  $\text{AH}_2$ , through a transient intermediate Compound II as described in the peroxidase cycle in **Figure 1-6c**. During this process a  $\text{H}_2\text{O}_2$  is reduced and the enzyme substrate, such as CNTs, gets oxidized.

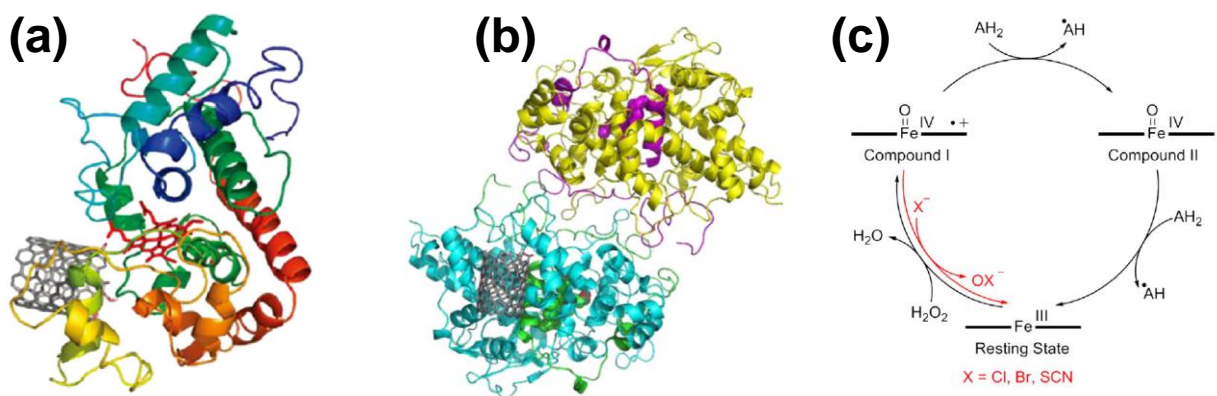


**Figure 1-6.** Molecular modeling of a carboxylated SWCNTs binding to the active site of (a) HRP; and (b) hMPO. (c) Scheme of the peroxidase cycle for HRP and hMPO (black circle), the red lines show the halogenation cycle for hMPO. Reproduced from Ref. 169, with permission from *Adv. Drug Delivery Rev.* **2013**, 65, 1921-1932, Copyright 2013 Elsevier.

### 1.4.2.2 Myeloperoxidase

Different from plant-excreted HRP, myeloperoxidase (MPO) is a dimeric hemoprotein that is predominantly expressed in granules of neutrophils (i.e., a type of professional phagocytes) from animals.<sup>169</sup> Human MPO (hMPO) is extracted from human blood with a molecular weight about 144 kDa, large than that of HRP (**Figure 1-6b**). In response to environmental stress (e.g., exposure to nanoparticles or bacteria), the cellular homeostasis is disrupted, which triggers the activation of NADPH oxidases in the phagocytic immune cells such as neutrophils leading to massive increasing levels of intracellular reactive oxygen species (ROS), known as the “oxygen burst”.<sup>196</sup> The ROS including hydroxyl radicals are highly reactive and quickly converted to H<sub>2</sub>O<sub>2</sub>. Upon activation, the neutrophils also release MPO primarily into phagolysosomal compartment where the peroxidases are activated by the generated H<sub>2</sub>O<sub>2</sub> and function as bactericide through the generation of oxidative species. There are two catalytic cycles for MPO (**Figure 1-6c**):<sup>195, 197-199</sup> the peroxidase cycle generates the reactive enzyme intermediates such as Compound I and Compound II following the similar route as HRP; in addition, activated MPO is also able to oxidize halides Cl<sup>-</sup>, Br<sup>-</sup>, and pseudohalides SCN<sup>-</sup>, forming strong oxidative (pseudo)hypohalous acids, known as the halogen cycle. Both catalytic path ways function synergistically thus creating a much stronger peroxidase of MPO compared to HRP.<sup>200-201</sup> The standard redox potential between each state of both enzyme is shown in **Table 1-1**, in comparison to the standard potential of SWCNTs (0.5 eV)<sup>202-203</sup> and HClO (1.48 V).<sup>204</sup>

**Table 1-1.** Standard reduction potentials (at pH 7) along the peroxidase cycle for peroxidase involved in CNT degradation/biodegradation.<sup>169</sup>

Redox couple	HRP	hMPO
Compound I/resting state	—	1.16 eV
Compound I/compound II	0.898 eV	1.35 eV
Compound II/resting state	0.869 eV	0.970 eV

### 1.4.3 In vitro Degradation of Carbon Nanomaterials

#### 1.4.3.1 Degradation by HRP outside Living Systems

It was previously discovered that oxidized SWCNTs undergo morphological changes such as shortening and deformation when statically incubated at 4 °C in the presence of HRP and H<sub>2</sub>O<sub>2</sub> (~40 μM) within a time frame of about 8 weeks.<sup>167</sup> The SWCNTs eventually lost their tubular structures leaving only a few globular residues after 12 weeks of degradation. It was found that pristine SWCNTs without oxidation experienced minimal degradation over the periods, based on which the degradation is considered to be defect-associated. In the following mechanistic study,<sup>168</sup> the degradation period was shortened to 10 days by performing the experiment at room temperature with daily supplement of H<sub>2</sub>O<sub>2</sub> and confirmed the importance of oxygen moieties and defects on the enzymatic degradation of SWCNTs. The oxygen functionalities such as carboxyl, carbonyl, and hydroxyl groups introduced by acid oxidation not only facilitates the dispersion of SWCNTs in aqueous solution, but also help the SWCNTs to orient themselves to the positively charged domains in HRP with close proximity toward the heme active center, as

studied by molecular modeling. In contrast, due to their hydrophobicity, pristine SWCNTs do not orient the same way as carboxylated SWCNTs, but stay in a conformation with remote distance to the heme active site of HRP, therefore are not degraded. Bianco and coworkers observed the similar degradation behavior in a study of HRP/H<sub>2</sub>O<sub>2</sub> treatment of carboxylated SWCNTs and MWCNTs over 30 days.<sup>205</sup> In our subsequent studies, we found the same defect-induced enzymatic degradation behavior on different other carbon nanomaterials such as MWCNTs,<sup>206</sup> N-doped CNTs, and graphene.<sup>91</sup> During the enzymatic degradation by HRP on graphene oxide (GO) nanosheets, an intermediate holey structure is formed, termed as holey graphene (hGO). After reduction, the holey reduced GOs (hRGOs) showed semiconducting electronic properties with good sensitivity as FET sensing materials.<sup>207</sup>

HRP represents a model system for the enzymatic degradation of carbon nanomaterials which provides fundamental knowledge on the degradation process. The HRP/H<sub>2</sub>O<sub>2</sub> system has potential environmental applications related to the bioremediation of carbon nanomaterials as possible pollutant. To understand the toxicological effect and biological behavior of carbon nanomaterials in the living system, hMPO is used for degradation of CNTs both *in vitro* and *in vivo*.

#### **1.4.3.2 Degradation of Carbon Nanotubes by hMPO *in vitro***

In a representative study,<sup>208</sup> Kagan and collaborators demonstrated the effective degradation of SWCNTs by hMPO in presence of H<sub>2</sub>O<sub>2</sub> and NaCl. The hMPO appeared to be a potent oxidative enzyme with almost complete degradation of SWCNTs observed after 24 hr of incubation in the test tube. The dispersion of SWCNTs in the solution became almost clear in color as evidenced by the diminishing of the UV-Vis absorption bands of SWCNTs and their characteristic Raman bands. The nanomaterials were observed to be completely amorphous under TEM images. In the

control experiments with absence of chloride ions or  $H_2O_2$ , the SWCNTs underwent minimal degradation, which confirmed the importance of the synergetic function of both peroxidase cycle and halogen cycle in the degradation of SWCNTs. Presumably, the generated HClO as a strong oxidative agent is more efficient to degrade SWCNTs due to its ability to diffuse among the bulky nanostructures.<sup>209</sup>

The hMPO catalyzed degradation of SWCNTs was further carried out in vitro by incubating SWCNTs with neutrophils.<sup>208</sup> The neutrophils were first treated with fMLP and cytochalasin B to increase the activity of the cells and trigger the release of hMPO. Short, oxidized SWCNTs were opsonized with IgG for efficient internalization in the cells, and incubated with active neutrophils. The activated neutrophils were shown to undergo “oxygen burst” with increasing levels of superoxide and  $H_2O_2$ . The complete degradation of SWCNTs was confirmed by the Raman spectra over the period of 12 hr. Without the IgG opsonization, the SWCNTs were not internalized into the cells and only 30% of them were degraded, which indicated that the majority of hMPO are generated inside the cells despite small amount of extracellular hMPO.<sup>210</sup> It was noted that the NADPH oxidase is also essential for the degradation to proceed, because NADPH oxidase is responsible to generate ROS which leads to  $H_2O_2$  formation. The extent of degradation in neutrophils is much higher than that in macrophages, which contain much lower level of MPO. The biodegradation process renders the SWCNTs much less toxic; after pharyngeal aspiration of the residual CNT materials after MPO degradation, the degraded CNTs induced minimal pulmonary inflammation.

#### **1.4.3.3 Degradation of Carbon Nanotubes in vivo**

The biodistribution, clearance, and fate of CNTs in vivo are intensively investigated,<sup>80, 170, 173, 211-212</sup> which are influenced by many factors such as the administration method, length, and

functionalization of the nanomaterials. By far, the internal clearance of CNTs are mostly referring to the excretion of CNTs through lymphatic, biliary, or renal pathways, but the alternative clearance mechanism via *in vivo* enzyme-catalyzed biodegradation is rarely discussed in the literature. Different groups recently addressed the *in vivo* degradation of CNTs in mouse lungs and brains, respectively.<sup>213-215</sup>

In an earlier study by Elgrabli et al.,<sup>214</sup> oxidized MWCNTs were intratracheally instilled into rat lungs. The injected MWCNTs were found to be predominantly distributed in the lungs and gradually diminished from the lungs during 180 days, with a significant increase of alveolar macrophages (AMs) responsible for engulfing MWCNTs. The AM cells underwent apoptosis after engulfing MWCNTs and were then phagocytosed by other AMs. During this process, MWCNTs were found undergoing structural deformation with decrease in length and loss of tubular structure 15 days after instillation, which might indicate their potential degradation in AMs. In a later collaborative study, we investigated the *in vivo* degradation of oxidized SWCNTs instilled via pharyngeal aspiration into the lungs of either wild-type (w/t) or myeloperoxidase knockout (MPO k/o) mice (mice with MPO deficiency).<sup>213</sup> It was found that SWCNTs underwent significant diminution in the lungs of w/t mice, and the phagocytized SWCNTs remained persistent in the neutrophils of MPO k/o mice through quantitative imaging of the lung tissue sections. Further TEM and Raman characterization showed the significant degradation of SWCNTs in the w/t mice after 28 days, which indicate the crucial role of MPO in the *in vivo* degradation of CNTs.

Nunes et al. recently investigated the fate of MWCNTs in mouse neuronal tissues using amine-functionalized MWCNTs.<sup>215</sup> MWCNTs were stereotactically injected into the motor cortex of a mouse brain, where the microglia cells function as the primary professional

phagocytes for the brain's immune system. From TEM imaging, any MWCNTs internalized into microglia underwent severe structural deformation forming amorphous debris, indicating the initiation of degradation by microglia 2 days after injection. The degradation of MWCNTs was confirmed by Raman spectra which showed a decrease of D and G band intensities after 14 days of incubation. The authors attributed the *in vivo* degradation of MWCNTs to the high phagocytotic ability of microglia that possess both oxidative and low-pH lysosomal environment and rich hydrolytic enzymes. However, the detailed degradation mechanism still remains elusive.

## 2.0 SYNTHESIS, CHARACTERIZATION, AND GNP-CORKING OF NITROGEN-DOPED CARBON NANOTUBE CUPS

### 2.1 CHAPTER PREFACE

Inspired by the unique cup-shaped morphology of the nitrogen-doped carbon nanotube cups (NCNCs), this project aim to effectively obtain the individual NCNCs from their stacked structure and use them for applications as drug delivery carriers. The first section of this chapter is focused on the synthesis and characterization of these individual nanocups. The amine functionalities on the NCNCs were determined and functionalized with commercial gold nanoparticles (GNPs). Due to the preferential distribution of amines on the open rims of the nanocups, the bound GNPs acted as stoppers corking on the opening of nanocups. In the subsequent study described in the second section, we greatly improved the efficiency of NCNC separation by introducing both chemical and physical methods. And the resulted separated nanocups were more effectively corked with GNPs through sodium citrate reduction of chloroauric acid (HAuCl<sub>4</sub>). The material contained in this chapter was reproduced with permission from *ACS Nano* **2012**, 6, 6912-6921, Copyright 2012 American Chemical Society, and from *J. Vis. Exp.* **2013**, e50383, Copyright 2013 JoVE.

## 2.2 CORKING CARBON NANOTUBE CUPS WITH GOLD NANOPARTICLES

### 2.2.1 Preface

Nitrogen doping of carbon nanotubes during chemical vapor deposition (CVD) synthesis can create unique stacked cup-shaped structures termed as nitrogen-doped carbon nanotube cups (NCNCs). These cups have semi-elliptical hollow cavities and elevated reactivity which could lead to various applications. In this work, by applying intense ultrasonication to the as-synthesized NCNCs, we demonstrated an effective mechanical method to isolate the individual cups with opened cavities from their stacks. The graphitic structures of the isolated cups and their inherent nitrogen functionalities were characterized by comprehensive microscopic and spectroscopic methods. In particular, we quantitatively determined the existence of amine functionalities on NCNCs and found that they were preferentially distributed at the open edges of the cups, providing localized reactive sites. Further, by thiolating the amine groups with 3-mercaptopropionic acid, we were able to effectively cork the isolated cups by gold nanoparticles with commensurate diameters. These cup-shaped carbon nanomaterials with controlled inner volumes and gold nanoparticle corks could find potential applications as nanoscale reaction containers or drug delivery vehicles.

The material contained in this section was published as a full article in the journal *ACS Nano* and reproduced with permission from *ACS Nano* **2012**, *6*, 6912-6921, Copyright 2012 American Chemical Society. The full citation is listed as Ref. 105.

**List of Authors:** Yong Zhao, Yifan Tang, Yanan Chen, and Alexander Star

**Author contributions:** YZ and AS conceived the project, designed the experiments and wrote the manuscript. YZ and YT performed the synthesis and purification the NCNC material. YZ carried out the characterization and functionalization of the material. YT contributed to the XPS analysis, and YC conducted the AFM analysis.

### 2.2.2 Introduction

Robust development of carbon nanotube (CNT) materials in various research fields over the past decade has been motivated by their outstanding mechanical, electrical, and chemical properties.<sup>6-8, 216</sup> The  $sp^2$  graphitic structure of CNTs allows either post-synthesis functionalization<sup>50,217</sup> or in situ chemical doping during the synthesis,<sup>109, 218</sup> which can tailor the intrinsic properties of CNTs for different applications such as in composite materials,<sup>40</sup> chemical sensing,<sup>29-30</sup> and drug delivery.<sup>49, 51</sup> Among different functionalization methods, nitrogen-doped CNTs are of particular interest. The incorporation of nitrogen atoms into the  $sp^2$  graphitic structure results in the formation of cup-shaped compartments in CNTs,<sup>142</sup> as well as the changes in their electronic and chemical properties.<sup>143, 219</sup> These unique properties may lead to many potential applications. For example, nitrogen-doped CNTs have been explored for hydrogen<sup>148</sup> and lithium<sup>149</sup> storage. Recently, researchers showed that nitrogen-doped CNTs have excellent electrochemical catalytic activity toward the oxygen reduction reaction.<sup>113,151</sup> Moreover,

nitrogen-doped CNTs were found to have better biocompatibility and mitigated cytotoxicity as compared to undoped pristine CNTs,<sup>154, 220</sup> and they were degraded by enzymatically catalyzed oxidation at ambient conditions.<sup>206</sup> These findings are important when considering nitrogen-doped CNTs as potential carriers in drug delivery applications.

Previous studies have addressed different strategies to fill CNTs with different materials such as ferromagnetic nanoparticles,<sup>221</sup> fluorescent polymers,<sup>53</sup> and organic molecules.<sup>222</sup> However, to achieve better performance, especially in biomedical applications, carriers with small sizes and facile surface modification are preferred.<sup>223</sup> In this sense, cup-shaped segments in nitrogen-doped CNTs can serve as desirable candidates for nanoscale containers. As-synthesized nitrogen-doped CNTs are composed of separate cup-shaped segments, which can be isolated as individual “cups” by grinding with a mortar and pestle.<sup>108</sup> These graphitic cups, termed later in the text as nitrogen-doped carbon nanotube cups (NCNCs), have a hollow structure with one end sealed and the other open. The open rims of these cups possess reactive nitrogen groups that can be functionalized<sup>108</sup> and cross-linked with glutaraldehyde.<sup>165</sup>

Nitrogen doping has been shown to be essential to determine the unique morphology and properties of NCNCs.<sup>219</sup> Although the exact assignment of nitrogen functional groups remains elusive, pyridinic nitrogen and graphitic nitrogen were considered as two main types of nitrogen functionalities in NCNCs.<sup>112</sup> Moreover, the existence of dangling bonds such as amine groups was also suggested based on NCNC reactivity<sup>108,165</sup> and acid-base titration experiments.<sup>224</sup> In this work, we synthesized NCNCs by chemical vapor deposition (CVD) method and separated them into individual cups by treating them with a probe-tip sonicator. A number of microscopic and spectroscopic techniques were implemented to scrutinize the morphological and chemical characteristics of NCNCs. We have found that individual separated NCNCs largely maintained

their cup-shape and graphitic structure as in their stacked forms, whereas their nitrogen functionalities became more distinct after the sonication process. By employing the Kaiser test and selectively decorating NCNCs with gold nanoparticles (GNPs), we were able to quantitatively determine both the concentration and distribution of amine functionalities on NCNCs. By utilizing localized amine groups on the basal plane of the cups, we further managed to cover the opening of the cups with GNPs as “stopper corks”, which demonstrated a new pathway to implement these cup-shaped carbon nanomaterials as nanoscale containers and drug delivery carriers.

### **2.2.3 Materials and Methods**

Citrate-coated gold nanoparticles with 10 nm diameters and silver nanoparticles with 40 nm diameters were purchased from Sigma Aldrich, and citrate-coated gold nanoparticles with 40 nm diameters were purchased from nanoComposix. Aldehyde-functionalized latex nanoparticles were purchased from Invitrogen. MWCNTs were purchased from Baytubes. All other analytical grade reagents and solvents were purchased from Sigma Aldrich and used as received.

#### **2.2.3.1 Growth of NCNCs via chemical vapor deposition (CVD)**

NCNCs were synthesized using CVD technique in a Lindberg/Blue tube furnace. NCNCs were grown on a quartz substrate placed in a quartz tube (1” dia.) inside the furnace. A liquid precursor containing 7.0 wt% of acetonitrile, 0.75 wt% of ferrocene, and 92.25 wt% of xylenes was injected at a rate of 1 mL/min under a H<sub>2</sub> (37.5 sccm) and Ar (126.8 sccm) atmosphere. The system was maintained at 800 °C for 90 min and then allowed to cool down under an Ar

atmosphere for 1 hr. NCNC product formed as a black coating on the quartz substrate was then scraped off and collected using a razor blade.

### **2.2.3.2 Mechanical separation of as-synthesized NCNCs**

Approximately 5 mg of as-synthesized NCNC fibers were first transferred to an agate mortar and pestle, to which several drops of EtOH were added. After 30 min of grinding, the sample was collected and redispersed in 25 mL of DMF. The suspension was then processed under Qsonica XL-2000 ultrasonic disassembler equipped with a ¼” titanium microprobe at 60 % of its maximal amplitude for 10 – 15 hr in ice bath. The resultant NCNC suspensions were briefly centrifuged to remove any large particles.

### **2.2.3.3 Decoration of NCNCs with gold nanoparticles**

The separated NCNCs were first thiolated by reaction with 3-mercapto-propionic acid (MPA) through EDC/DMAP coupling reaction. Approximately 0.1 mg of separated NCNCs were suspended in 4 mL of DMF. To the suspension, 20 µL of MPA, 22 mg 1-Ethyl-3-(3-dimethylaminopropyl)carbodiimide (EDC) and 1.4 mg 4-Dimethylaminopyridine (DMAP) were added and the mixture was stirred under N<sub>2</sub> at room temperature overnight. After repeated wash with EtOH, the thiolated NCNC suspension in EtOH was incubated overnight with citrate-coated GNPs with diameters either 10 nm or 40 nm.

## **2.2.4 Results and Discussion**

NCNCs were synthesized using CVD method from a mixture of 92.25 wt% xylenes, 7.0 wt% acetonitrile and 0.75 wt% ferrocene as precursors (**Figure 2-1a**). At 800 °C under H<sub>2</sub> and Ar

atmosphere, the precursor was injected into the CVD reactor at a rate of 1 mL/hr. After 90 min of the reaction, NCNC product was formed as a thick carpet of a black material weighing 4 – 5 mg and was then peeled off by a razor blade and dispersed in ethanol. Transmission electron microscopy (TEM) images of the as-synthesized material (**Figure 2-1b**) showed that NCNCs have diameters ranging from 20 – 50 nm and lengths up to 15  $\mu\text{m}$ . Unlike undoped multi-walled carbon nanotubes (MWCNTs) with continuous hollow interior, tubular NCNCs consist of many conical compartments resembling the shape of stacked cups. The nanotube cups were stacked in a head-to-tail fashion along the common direction of the tube axis. Compared to our previous CVD synthesis method which used ethanol/acetonitrile/ferrocene as the precursors,<sup>108</sup> we noticed that by changing ethanol to xylenes as the carbon source and decreasing the content of ferrocene catalyst, the shape and the diameters of resultant NCNCs became more uniform. We assume that ethanol may introduce additional oxygen-containing defects in the graphitic structure<sup>225</sup> that may influence the formation of the cup shape. The reduced ferrocene catalyst concentration is assumed to result in a more uniform size distribution of iron nanoparticle seeds. From TEM images (**Figure 2-1b**) it was occasionally observed that iron nanoparticles were confined between the graphitic segments, defining the inner diameters of nanotube cups.

High resolution TEM images (**Figure 2-1c**) showed that the graphitic walls of stacked nanotube cups were not parallel to the longitudinal axis, but extended diagonally outward and terminated at the lateral surface. A layer of amorphous carbon was often observed at the surface with about 2 nm thickness. Due to the size similarity, the cups were compactly nesting into each other's cavity taking up most the inner volume of the cup, with no interconnection of graphitic walls between each other. This observation indicated that the adjacent cups were not covalently connected but rather held together by the interlayer  $\pi$ - $\pi$  interaction. As a result, potential

separation of individual nanotube cups can be achieved via mechanical or chemical processes. Previous attempts of NCNCs separation involving grinding with a mortar and pestle have obtained individual nanotube cups out of their stacked structure only with a limited yield.<sup>108</sup> To improve the efficiency of separation, we applied probe-tip sonication to the sample after grinding. The sample was dispersed in DMF forming a stable suspension and then was treated with a 1/4"-probe sonicator for 15 hr in ice bath. The probe-tip sonication effectively broke the stacked compartments in the long fiber into short stacked cups and individual cups. The individual cups have common but moderately different shapes and sizes, mostly ranging 50 – 200 nm in length and 30 – 50 nm in diameter (**Appendix A1, Figure A1-1**). **Figure 2-1d** shows TEM image of a typical individual nanotube cup isolated from the stacking structure, having a semi-elliptical shape with the top sealed and the basal plane open. High resolution TEM image (**Figure 2-1e**) revealed that the isolated individual nanotube cups maintained the graphitic structure on the sidewall where the parallel graphitic layers extended with a certain angle from the tube axis. The graphitic edge at the basal plane of the cup was distinctly depicted which proved the three-dimensional cup-shaped morphology with open access to the hollow interior.

Although incompletely separated nanotube cups in short stacks of several units were frequently observed (**Appendix A1, Figure A1-1**), the probe-tip sonication process significantly broke long NCNCs into smaller sections. Based on over 300 measurements obtained from TEM images, the average lengths of NCNCs showed a significant decrease with the sonication time (**Appendix A1, Figure A1-2a**). The length distribution histograms reflected a ten-fold decrease in the average length of NCNCs from *ca.* 4.3  $\mu\text{m}$  to *ca.* 380 nm after 15 hr of mechanical separation (**Appendix A1, Figure A1-2b**). A majority of over 70% NCNCs in the final sample ranged from 50 – 400 nm in length, corresponding to individual cups and short stacks of less

than 10 units. Dynamic light scattering (DLS) measurements also showed that the length of NCNCs decreased from  $2.24 \pm 0.25 \mu\text{m}$  to  $229 \pm 15 \text{ nm}$  after separation. While the DLS results may not reflect the actual length of nanotubes because the DLS measurement calculates the sizes based on hydrodynamic volume of the nanoparticles in solution, the data still reveals the significant trend of decreasing in the length of NCNCs as the result of probe-tip sonication.

Raman spectra further revealed that the probe-tip sonication process not only physically dissociated the nanotube cups from their stacks, but also cut more open edges on the graphitic surface of nanotube cups. The relative intensity of D band ( $\sim 1325 \text{ cm}^{-1}$ ) and G band ( $\sim 1575 \text{ cm}^{-1}$ ) in Raman spectra reflects the extent of structural disorders of graphitic materials.<sup>98</sup> The Raman spectra were taken on samples after different duration of probe-tip sonication. **Figure 2-2a** shows the Raman spectra of NCNCs as-synthesized and after 2 – 15 hr of sonication, normalized to the G band. The D to G band ratios were calculated and shown to increase linearly with the sonication time (**Figure 2-2b**). The increase in D/G band ratio was accompanied with significant decrease in the length of NCNCs (**Appendix A1, Figure A1-2a**) and revealed the effect of high-intensity ultrasonication on physical dissociation of stacked NCNCs, which might have resulted in more cut edges on the graphitic structures.<sup>226</sup> These extrinsic edges were further visualized by high-resolution TEM images (**Appendix A1, Figure A1-3**), as graphitic layers were observed to be damaged at the sidewalls and the tips of the cups. Raman spectra were also acquired on as-synthesized NCNCs at different N doping levels with 7%, 10% and 15% acetonitrile fractions in the precursor (**Appendix A1, Figure A1-4a**). Compared to Raman spectra of undoped MWCNTs, as-synthesized NCNCs have much higher D/G band ratio, which increases along with increasing fractions of nitrogen source in the

precursor (**Appendix A1, Figure A1-4b**), showing that nitrogen-doping also resulted in more structural disorder in the graphitic lattice.

It was previously proposed that the cup-shaped compartments arise from the incorporation of nitrogen atoms into the graphitic lattice during the growth process.<sup>107</sup> Due to the extra electron in the valence shell, the nitrogen atoms tend to introduce disorder to the carbon graphitic structure, causing a negative curvature change in the graphitic walls,<sup>146</sup> which then generates a stretching force to the liquefied catalytic particles and pull them into cup-like shapes, defining the shape of subsequent cups.<sup>145</sup> The concentration and location of nitrogen functionalities in NCNCs can be approximately measured by electron energy-loss spectroscopy (EELS) combined with high-resolution TEM. Figure 3a,b show high-resolution TEM images on two different sections of NCNCs and their corresponding EELS signals. On the section with continuous hollow interiors (**Figure 2-3a**), EELS showed only signals from K shell ionization of carbon atoms at around 300 eV. This continuous tubular structure resembling undoped MWCNTs may be due to insufficient local nitrogen supply during the CVD process. On the other section with tightly-packed compartments (**Figure 2-3b**), the additional signal arising from nitrogen K shell at 401 eV appeared on the EELS spectrum,<sup>164</sup> corresponding to a nitrogen content of about 1 – 2 at.%. The enrichment of nitrogen content at the joint between the adjacent cups was also visualized by EELS elemental mapping shown in **Appendix A1, Figure A1-5**, as the nitrogen signal showed higher intensity at the intersections of a short stack of NCNCs. These results supported the growth mechanism of NCNCs in which nitrogen-doping leads to the formation of cup-shaped compartments by creating curvatures on the graphitic networks of the cups.

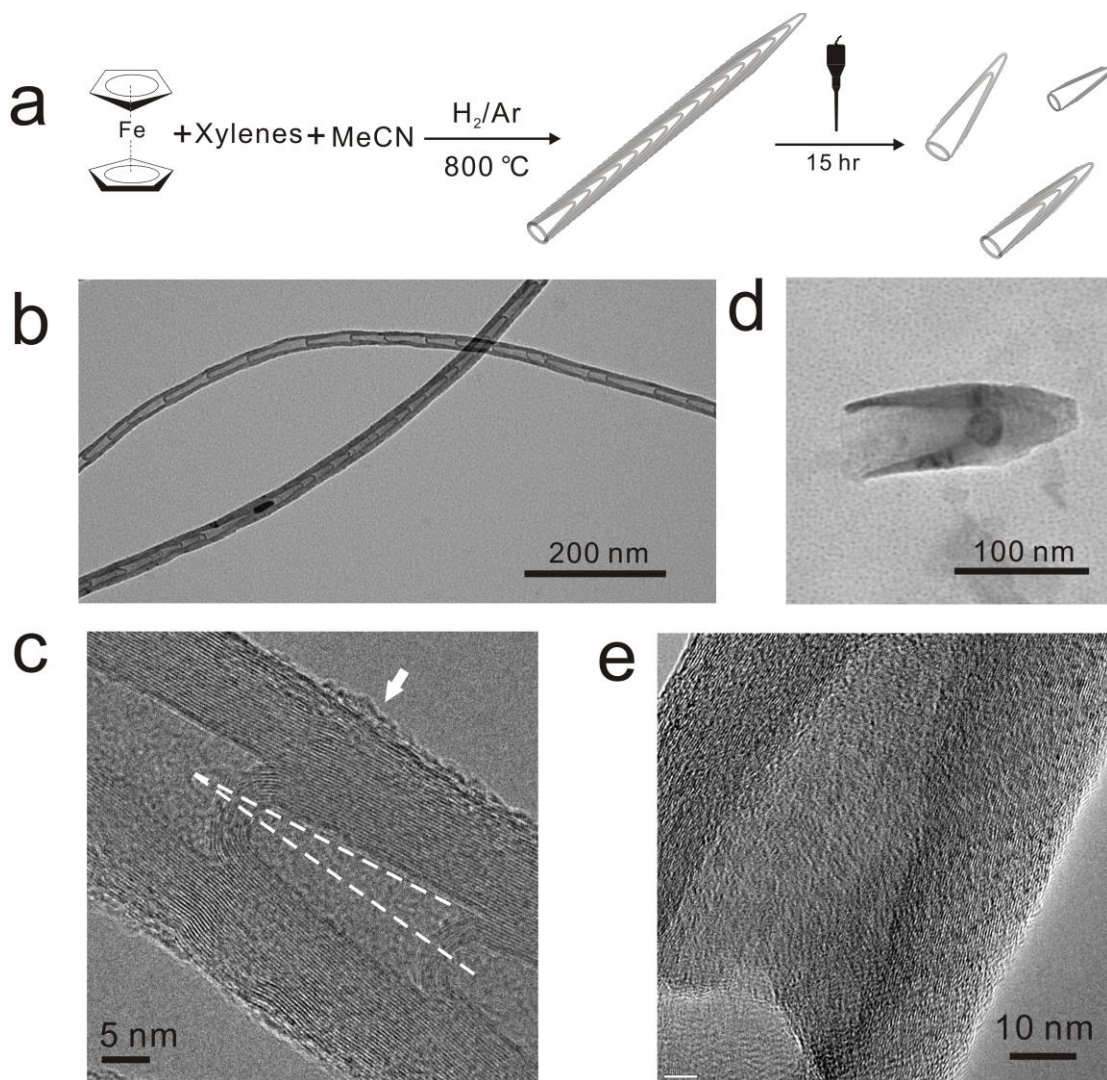


**Figure 2-1.** (a) Chemical vapor deposition (CVD) synthesis of nitrogen-doped carbon nanotube cups (NCNCs) and their mechanical separation via probe-tip sonication. (b) Transmission electron microscopy (TEM) image of as-synthesized NCNC fibers. (c) High-resolution TEM image showing one segment from a stacked NCNC fiber, the white dashed lines in the figure depict the directions of the graphitic walls and the tube axis, the white arrow shows the existence of amorphous carbon. (d) TEM image of an individual NCNC after mechanical separation. (e) High-resolution TEM image of an individual NCNC.

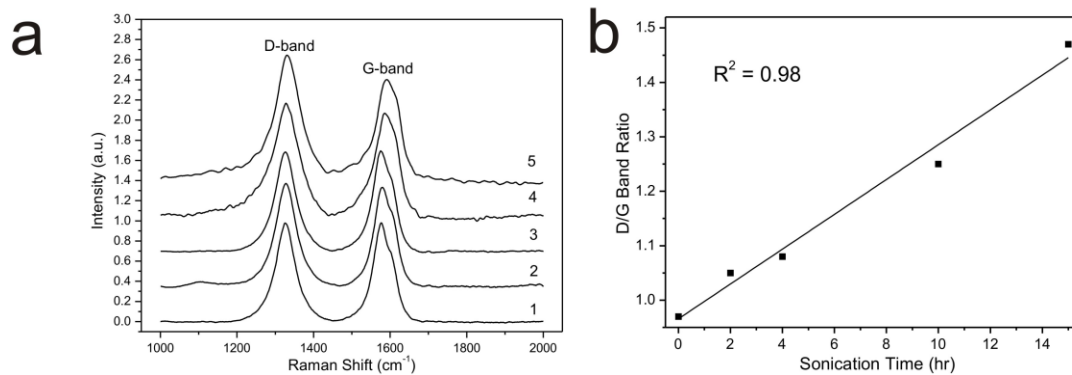


**Figure 2-2.** (a) Raman spectra of NCNCs after different duration of probe-tip sonication: (1) as-synthesized, (2) 2 hr, (3) 4 hr, (4) 10 hr, and (5) 15 hr. (b) Plot and linear fit of the D to G band ratio versus sonication time.

Elemental analysis revealed that the NCNCs have an overall 1.01 at.% of nitrogen and 1.72 at.% of hydrogen. X-ray photoelectron spectroscopy (XPS) further analyzed the nitrogen functionalities in both as-synthesized and separated NCNC samples. **Figure 2-3c** shows nitrogen 1s peaks for both samples at about 400 eV. Since XPS only probes the elemental composition within several nm from the surface of the sample, it does not probe nitrogen functionalities in bulk materials. However, an increase in nitrogen concentration was found from 0.6 at.% in the as-synthesized NCNC samples to 1.6 at.% in the separated samples, which may suggest that more nitrogen functionalities were exposed after the probe-tip sonication process, possibly due to the removal of surface amorphous carbon and the increasing surface area.

The overall N1s profiles can be fitted into different nitrogen components. It is necessary to mention that the sub-peaks for N1s high-resolution spectra in nitrogen-containing carbonaceous materials all have a relative broad full width at half maximum (FWHM) around 2 – 3 eV due to the complicated chemical environment of nitrogen functionalities presented at a heterogeneous carbon structure.<sup>227</sup> Therefore, the peaks were fitted by optimizing the peak shape

and position at a fixed Gaussian/Lorentzian ratio of 80:20 (S.I., Table S1).<sup>228</sup> Four peaks were deconvoluted from the N1s profiles of the as-synthesized NCNC samples (**Figure 2-3c**). The peak N1 at ~398.3 eV in the as-synthesized NCNCs may correspond to pyridinic nitrogen bonded with two carbon atoms in a six-membered ring structure.<sup>229</sup> The assignment of the peak N2 at 399.9 – 400.0 eV can be different. While pyrrolic nitrogen is typically assigned at 400.1 – 400.6 eV,<sup>229,230</sup> this peak can be more likely ascribed to amine functionalities.<sup>227,231,232</sup> The peak N3 at 401.6 – 401.7 eV may be assigned to graphitic (quaternary) nitrogen atoms which are triple-coordinated nitrogen incorporated in the graphitic networks by direct substitution of carbon atoms.<sup>227,233</sup> The peak N4 at 404.3 – 404.6 eV may represent the molecular nitrogen which arises from the gaseous N<sub>2</sub> molecules intercalated between the graphitic walls or trapped inside the sealed cups during the synthesis process.<sup>127,234</sup> After the probe-tip sonication, the separated NCNCs showed a different N1s profile (**Figure 2-3d**). The peak N2 greatly increased with dominant intensity. We speculate that the increase of this peak results from the dissociation of nitrogen-containing compartments under the effect of intense sonication. Presumably, the abrasion to the outer graphitic layers not only caused removal of surface amorphous carbon and exposure of the existing amine functionalities, but also altered the local C-N frameworks and created more dangling bonds such as amines. On the other hand, the peak N1 became indistinguishable in the separated NCNCs, which may partially be due to the overshadowing by the outshoot of the peak N2, but may also indicate the transformation of pyridinic nitrogen to amines under sonication. After the separation process, there was a notable decrease in the peak N4, which may possibly be due to the release of molecular N<sub>2</sub> once the cups were opened.

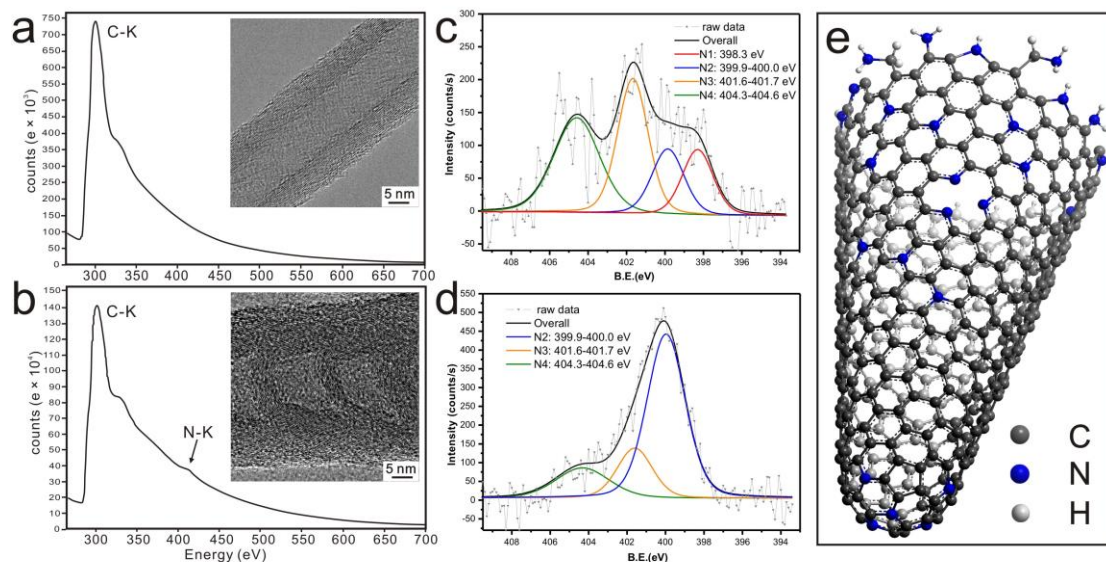


**Figure 2-3.** High-resolution TEM images (insets) and their corresponding electron energy loss spectroscopy (EELS) of (a) an uncomparted section and (b) a compartmented section of NCNCs. X-ray photoelectron spectroscopy (XPS) of (c) as-synthesized NCNCs and (d) separated NCNCs after 15 hr of sonication. (e) Structural scheme of one graphitic layer from separated NCNCs showing the varieties of possible nitrogen functionalities. This scheme is not drawn to scale.

Fourier transform infrared spectroscopy (FTIR) provided qualitative bonding information on the overall chemical functionalities of NCNCs (**Appendix A1, Figure A1-6**). The spectra were taken on both as-synthesized and separated NCNCs dried in a vacuum oven. Because of their graphitic nature and limited functionalities, neither sample showed strong IR intensities. However, in comparison to pristine MWCNTs, the major absorption bands at  $\sim 3435\text{ cm}^{-1}$  may correspond to the N-H stretching vibration that arises from the potential pyrrolic or amine functionalities. Small increases were observed on the bands at 2850 and 2920  $\text{cm}^{-1}$  after sonication, corresponding to the C-H vibrational modes in methylene groups,<sup>231</sup> which supported

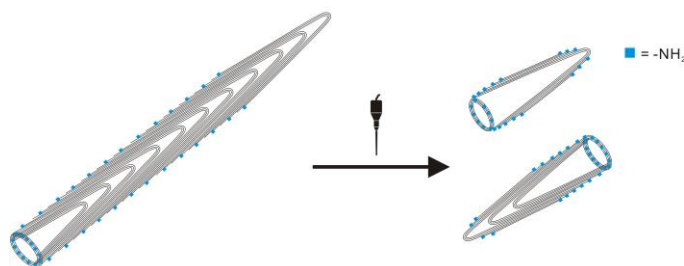
the assumption that the probe-tip sonication may damage the carbon  $sp^2$  networks and create more saturated bonds. Two broad bands appearing at  $\sim 1200\text{ cm}^{-1}$  and  $\sim 1550\text{ cm}^{-1}$  may be assigned to C–N and C=N stretching modes, respectively,<sup>235</sup> which may arise from pyridinic or graphitic C/N functionalities. A schematic illustration in **Figure 2-3e** depicts the proposed morphology and structure of one graphitic layer of the separated NCNCs. Possible nitrogen functionalities such as pyridinic, graphitic nitrogen and amine groups are shown based on the results of characterization.

Although the exact assignment of all nitrogen functionalities cannot be explicitly determined, the potential existence of amine functionalities is of particular interest because they can provide diverse reactivity for surface functionalization of NCNCs. Previously, the existence of amine groups on NCNCs was inferred based on the reactivity of NCNCs with (+)-Biotin *N*-hydroxy-succinimide ester<sup>108</sup> and glutaraldehyde.<sup>165,114</sup> In this work, type and amount of amine functionalities on NCNCs were further quantitatively measured using a chemical colorimetric method known as Kaiser test, which was widely applied for amine detection in peptide synthesis.<sup>236</sup> Both as-synthesized and separated samples were first analyzed without additional treatment. The test results showed the existence of primary amines on the separated NCNCs, but no primary amines were detected in the as-synthesized samples. The appearance of primary amines in separated NCNCs is consistent with the XPS results and supports our hypothesis that the probe-tip sonication can remove the surface amorphous carbon and create saturated structures such as primary amines. The primary amine loading in separated NCNCs was calculated as  $1.06 \pm 0.35\ \mu\text{mol/g}$  (**Table 2-1**), which was comparable to the literature value of amine loadings in NCNCs determined by an acid-base titration method.<sup>224</sup> It should be noted that the Kaiser test only detects the surface primary amines with hydrogen on the alpha carbon, so presumably

aromatic amines and other  $sp^2$  nitrogen in NCNCs do not give a positive result (**Appendix A1, Figure A1-7**). In order to quantify the total amine functionalities, NCNCs were functionalized with glycine molecules to yield primary amine terminals on the inherent amine groups. Both as-synthesized and separated NCNCs were reacted with Boc-protected glycine (N-(*tert*-Butoxycarbonyl)glycine, Boc-Gly-OH) through EDC/DMAP coupling reaction, and then the materials were repeatedly washed and deprotected off the Boc groups to afford NCNC-glycine conjugates, on which the Kaiser test was performed. After glycine functionalization, Kaiser test gave positive results on both as-synthesized and separated NCNC samples, indicating the inherent existence of aromatic amines on their surfaces. The total amine loading in separated NCNCs further increased almost twice after glycine functionalization (**Table 2-1**), showing that aromatic amines account for a large part of the total amine functionalities.

To confirm that the positive results were indeed attributed to amine functionalities, the amine reactive sites on separated NCNCs were reacted with di-*tert*-butyl dicarbonate ( $Boc_2O$ ) as illustrated in Scheme S1 to yield *N-tert*-butoxycarbonyl (NH-Boc) groups which protected the amine groups from Kaiser test reactions. It turned out that Boc-protected NCNCs gave a negative Kaiser test result. Upon removal of Boc groups, amine groups were detected again (**Appendix A1, Scheme A1-1**). The amine loading was  $0.97 \pm 0.07 \mu\text{mol/g}$ , which was close to that of separated NCNCs before any treatment, showing that the protected amine groups could be almost completely recovered.

**Table 2-1.** Primary amine and total amine loadings from Kaiser test results on as-synthesized NCNCs and separated NCNCs.<sup>a</sup>



	As-synthesized	Separated
Primary	—	$1.06 \pm 0.35 \mu\text{mol/g}$
Total	$0.85 \pm 0.12 \mu\text{mol/g}$	$2.76 \pm 0.09 \mu\text{mol/g}$

<sup>a</sup> To obtain the total amine loadings, both samples were functionalized by Boc-Gly-OH and then deprotected off the Boc groups before Kaiser test.

The existence of amine groups enables facile surface functionalization of separated NCNCs. By EDC/DMAP coupling reaction, we were able to add thiol functionalities, which have strong affinity to gold nanoparticles (GNPs) through Au-S interaction,<sup>237</sup> to the amine terminals using 3-mercaptopropionic acid (MPA) (**Figure 2-4a**). The resulting thiolated nanocups showed no morphological differences from the untreated ones (**Figure 2-4b**). After repeated washing and centrifugation, NCNCs were combined with citrate-coated GNPs with 10 nm diameters. From TEM images it was observed that GNPs were densely anchored on the surface of NCNCs (**Figure 2-4c**). On short stacked NCNCs, GNPs prefer to decorate the lower part of each section, especially at the bottom open rim. Because GNPs are bound to the thiolated amine sites, the distribution of GNPs can effectively provide a “mapping” of amine

functionalities on the surface of separated NCNCs. Theoretical calculations showed that the nitrogen-doping sites are more energetic and tend to hinder the subsequent growth of the graphitic network.<sup>147</sup> As amine groups are incompatible to the  $sp^2$  networks, they are likely to stay at the edge of graphitic walls which eventually terminate at the surface of NCNCs. The inset in **Figure 2-4c** shows an individual NCNC functionalized with GNPs. The GNPs were preferentially attached on the open rim of the cup marking the enrichment of amine functionalities at the opening. The interaction between GNPs and thiolated NCNCs is strong and specific. By simply mixing the GNPs with nonthiolated NCNCs in ethanol, free GNPs were randomly distributed throughout the sample with no specific interaction with NCNCs (**Figure 2-4d**). The GNPs can be easily washed off from nonthiolated NCNCs by centrifugation, but were bound strongly to thiolated NCNCs even after repeated washing. UV-Vis spectroscopy shows that the surface plasmon resonance (SPR) band for GNPs bound to thiolated NCNCs had a substantial red shift compared to free GNPs (**Figure 2-4e**), which may be caused by the specific interaction between GNPs and the thiol chain ligands,<sup>238</sup> as well as the close proximity between adjacent GNPs.<sup>239</sup>

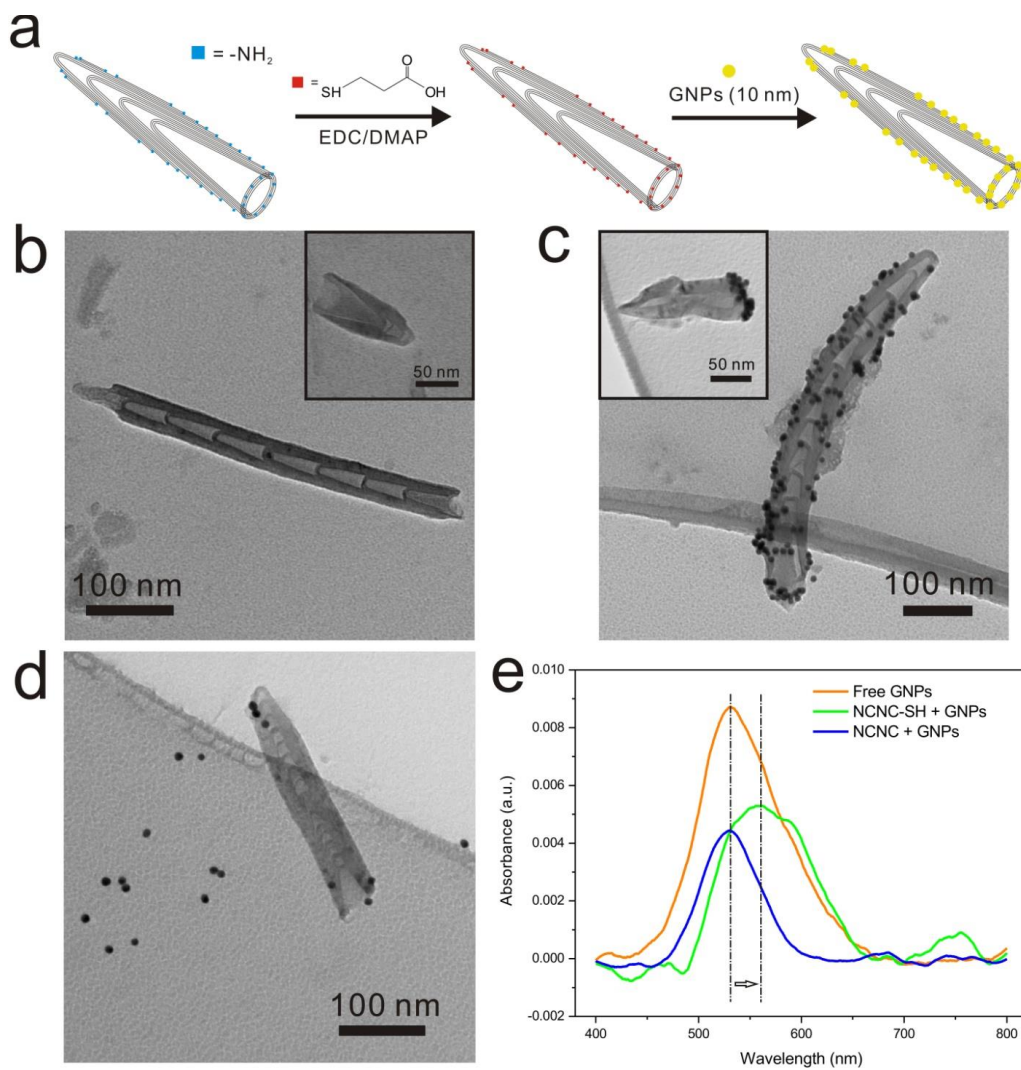


**Figure 2-4.** (a) Schematic illustration of functionalization of NCNCs with 10 nm gold nanoparticles (GNPs). (b, c) TEM images of separated NCNCs functionalized with 3-mercaptopropionic acid before (b) and after (c) attachment of GNPs. The insets in each panel show the corresponding images of individual NCNCs. (d) TEM image showing the distribution of GNPs among separated NCNCs without thiolation treatment. (e) UV-Vis spectra showing the surface plasmon resonance (SPR) band of GNPs with NCNC samples with or without thiolation treatment.

With their cup-shaped structure and localized amine reactive sites, separated NCNCs can be considered as nanoscale containers to accommodate various cargo molecules inside their cavities. From TEM images of separated NCNCs, we frequently noticed some residual amorphous material retained in the open cavities of separated NCNCs. As shown in Figure 5a, in the short stack of three cups, the open cup on top showed a darker color than the sealed cups at the bottom. This material was assumed to be the amorphous carbon residues formed during the sonication process that were adsorbed on the inner graphitic walls of the cups due to their hydrophobic interaction (**Appendix A1, Figure A1-8**). In addition, the preferential distribution of thiolated amine groups on the open edge allowed us to effectively “cork” the opening of the cups using GNPs with appropriate sizes that fit the diameters of the cups. **Figure 2-5b** shows that when incubating thiolated NCNCs with 40 nm GNPs, one GNP can fit on the open rim of the cup and confine the residual material inside. Individual thiolated NCNCs corked by GNP “stoppers” were frequently observed in the samples (**Appendix A1, Figure A1-9a-d**). This corking interaction between GNPs and NCNCs was fairly effective as depicted at a lower magnification (**Appendix A1, Figure A1-9e**), where the GNPs had preferentially corked several individual or short-stacked NCNCs at their open sides. It was noted that the interactions were not exclusive on the open rims because GNPs may also bind to the thiol groups on the sidewalls of the cups due to their high aspect ratio (**Figure 2-5b**), and GNPs attached to the open sides might not necessarily be perfectly “corking” (**Appendix A1, Figure A1-10**). However, the “corking” position is supposed to be thermodynamically more stable for 40 nm GNPs due to the enrichment of thiol groups at the open rims and their fitting shapes. Statistically, there were *ca.* 54% of short NCNCs functionalized with 40 nm GNPs, in which about 42% were corked, accounted for a percentage of *ca.* 23% corked NCNCs in total (**Appendix A1**). On average,

each functionalized NCNC had about 2.6 GNPs, with over 1/3 of them staying at the open sides. Considering the high aspect ratio of NCNCs, the surface area of the sidewalls is roughly 19 times as that of the openings (**Appendix A1**), so the binding of GNPs to the open rims of NCNCs must be energetically favored. The atomic force microscopy (AFM) image in a contact mode (**Figure 2-5c**) also confirmed the observation that GNPs with diameters about 40 nm tended to bind to the end of the individual NCNCs as well as on the sidewalls.

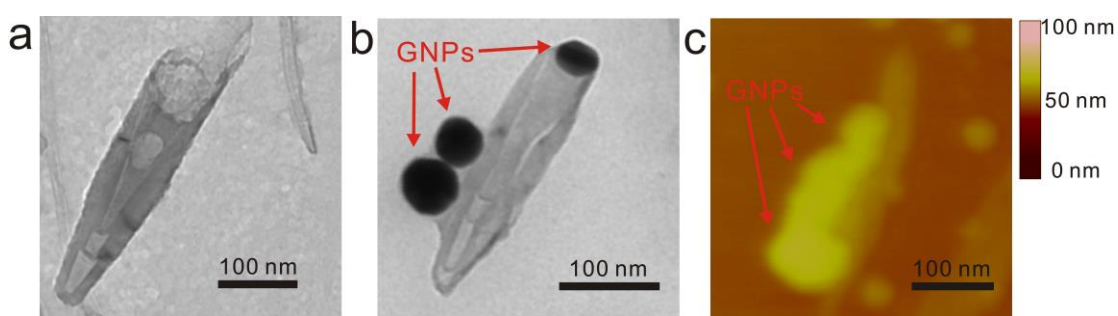


**Figure 2-5.** (a) TEM image of a NCNC retaining amorphous carbon inside the open cavity and (b) a thiolated NCNC corked with a 40 nm GNP and two other GNPs attached to its sidewall. (c) AFM contact-mode image of an individual NCNC functionalized with 40 nm GNPs.

The preferential interactions between GNPs and thiolated amine groups on the open rims of the separated NCNCs were further confirmed using EELS elemental mapping in an energy filtered TEM (EFTEM) mode. **Figure 2-6a** shows a typical TEM image of a GNP bound to the opening of the thiolated NCNCs. The GNP with 40 nm in diameter was slightly wider than the inner diameter of NCNCs and effectively corked the cup. We recorded the corresponding elemental maps for Au, N, and S. The energy filtered image of Au O edge at 54 eV showed a bright sphere at the end of NCNCs confirming the chemical composition of GNPs (**Figure 2-6a, inset**). Nitrogen map taken at the N K edge of 401 eV revealed that nitrogen was mainly

distributed at the lower part of NCNCs (**Figure 2-6b**). Notably, the elemental mapping for sulfur at S L edge of 165 eV showed the enriched existence of thiol groups at the open edge of the NCNCs which essentially reflected the localized distribution of amine functionalities (**Figure 2-6c,d**). The thiol groups shared the same position as GNPs, which factually proved the mechanism of the “corking” behavior between GNPs and thiolated NCNCs.

Because of the diverse chemical nature of the localized amine functionalities, the corking materials were not exclusive to GNPs. Silver nanoparticles also had strong affinity to thiols and were able to stopper NCNCs as well (**Appendix A1, Figure A1-11a**). Furthermore, by introducing 40-nm polystyrene latex nanoparticles containing aldehyde groups to separated NCNCs in ethanol, NCNCs can also be capped by these polymer nanoparticles with no need of further functionalization, presumably due to the formation of imine bonds (**Appendix A1, Figure A1-11b**). The similar corking behavior was also observed in another study using amine functionalized silica nano test tubes.<sup>240</sup> Our experimental results point to the application of NCNCs as graphitic nanoscale containers which can be corked with different nanoparticles. These hybrid carbon nanocup/metal or polymer nanoparticle nanoassemblies can be explored as multifunctional vehicles for applications such as drug delivery and biological targeting. Future *in vivo* studies on these nanomaterials are necessary to test their effectiveness for the biological applications.

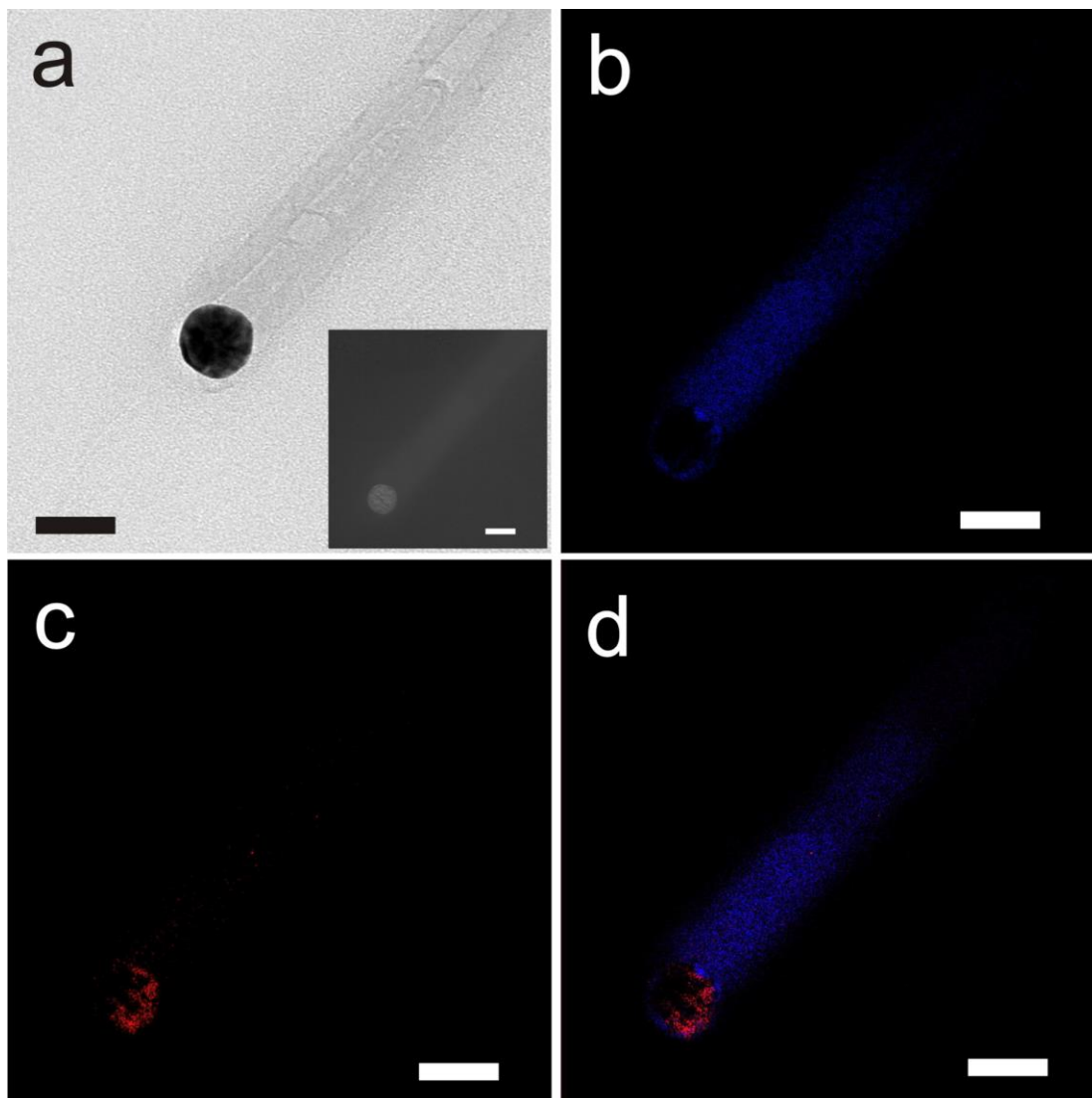


**Figure 2-6.** (a) TEM image of one GNP with 40 nm of diameter corking the opening of separated NCNCs. Inset: the energy filtered TEM (EFTEM) image of gold elemental mapping. (b,c) EFTEM images for nitrogen (colored blue) and sulfur (colored red) and (d) overlap of b and c. All scale bars represent 40 nm.

## 2.2.5 Conclusions

In this study, we introduced a new methodology to obtain individual NCNCs using probe-tip sonication. We showed that this method can effectively separate NCNCs from their stacked structures. TEM images revealed that separated NCNCs largely existed as individuals or short stacks with less than 400 nm in length, and maintained their cup-shaped structures with more graphitic edges. Spectroscopic characterization showed the existence of different nitrogen functionalities in separated NCNCs that are responsible for their cup-shaped morphology. By adopting Kaiser test, we quantified the type and concentration of amine functionalities on the surface of NCNCs, which are particularly interesting due to their diverse reactivity. By thiolation of the amine groups and functionalization with GNPs, we were able to visualize the distribution of amine groups on NCNCs and found that they were preferentially located at the open basal plane of the cups. Taking advantage of these groups, we managed to effectively close NCNCs with larger GNPs as “corks” or “stoppers” due to the localized amine distribution, which was proved by EELS elemental mapping. These novel cup-shaped nanomaterials showed versatile property toward modification and manipulation, and may lead to potential applications such as nanoscale containers and drug delivery systems.

## **2.2.6 Acknowledgement**

Dedicated to Professor Sir J. Fraser Stoddart on the occasion of his 70th birthday. This work was supported by an NSF CAREER Award No. 0954345. The authors thank NCFE at the University of Pittsburgh and especially Dr. Susheng Tan for the provision of access to the instruments and assistance. We gratefully acknowledge RJ Lee group for access to the XPS instrumentation and Professor R. A. Butera for his comments on the XPS data analysis.

## **2.3 SYNTHESIS AND FUNCTIONALIZATION OF NITROGEN-DOPED CARBON NANOTUBE CUPS WITH GOLD NANOPARTICLES AS CORK STOPPERS**

### **2.3.1 Preface**

This work is follow-up study of separation and GNP corking of NCNCs. We discuss in this section the synthesis of individual graphitic nanocups, and improved the separation procedures including acid oxidation, probe-tip sonication, and filtration. By citrate reduction of  $\text{HAuCl}_4$ , the graphitic nanocups were corked with gold nanoparticles on the chemically reactive nanocup edges with much better effectiveness.

Nitrogen-doped carbon nanotubes consist of many cup-shaped graphitic compartments termed as nitrogen-doped carbon nanotube cups (NCNCs). These as-synthesized graphitic nanocups from chemical vapor deposition (CVD) method were stacked in a head-to-tail fashion held only through noncovalent interactions. Individual NCNCs can be isolated out of their stacking structure through a series of chemical and physical separation processes. First, as-synthesized NCNCs were oxidized in a mixture of strong acids to introduce oxygen-containing defects on the graphitic walls. The oxidized NCNCs were then processed using high-intensity probe-tip sonication which effectively separated the stacked NCNCs into individual graphitic nanocups. Owing to their abundant oxygen and nitrogen surface functionalities, the resulted individual NCNCs are highly hydrophilic and can be effectively functionalized with gold nanoparticles (GNPs), which preferentially fit in the opening of the cups as cork stoppers. These graphitic nanocups corked with GNPs may find promising applications as nanoscale containers and drug carriers.

The material contained in this section is the manuscript published as a video clip in *Journal of Visualized Experiment* and reproduced with permission from *J. Vis. Exp.* **2013**, e50383, Copyright 2013 JoVE. The full citation is listed as Ref. 140. The actual publication is a video format in which a film described the detailed experiments in order to help better disseminate and reproduce our results.

**List of Authors:** Yong Zhao, Yifan Tang, and Alexander Star

**Author Contributions:** YZ and AS conceived and designed the project and wrote the manuscript. YZ and YT performed the synthesis and functionalization of the nanocup materials. YZ conducted the characterization. All authors participated in the video-filming.

### **2.3.2 Introduction**

With their inherent inner cavities and versatile surface chemistry, hollow carbon-based nanomaterials, such as carbon nanotubes (CNTs), are considered to be good nanocarriers in drug delivery applications.<sup>8,241</sup> However, the fibril structure of pristine CNTs has rather inaccessible hollow interiors and may cause severe inflammatory response and cytotoxic effects in biological systems.<sup>172, 177</sup> Nitrogen-doped CNTs, on the other hand, have been found to possess higher biocompatibility than undoped multiwalled carbon nanotubes (MWCNTs)<sup>154, 220</sup> and may have better drug delivery performance. Doping of nitrogen atoms into the nanotube graphitic lattices results in a compartmented hollow structure resembling stacked cups which can be separated out to obtain individual nitrogen-doped carbon nanotube cups (NCNCs) with typical length under 200 nm.<sup>108,105</sup> Due to their graphitic structure and additional nitrogen functionalities, the NCNCs

are open to further surface functionalization to develop diverse chemical properties. With their chemical activity and accessible interiors, these individual graphitic cups, are highly advantageous for drug delivery applications.

Among different synthetic methods for nitrogen-doped CNTs including arc-discharge<sup>124</sup> and dc magnetron sputtering,<sup>125</sup> chemical vapor deposition (CVD) has been the most prevalent method due to several advantages such as higher yield and easier control over nanotube growth conditions. The vapor-liquid-solid (VLS) growth mechanism is commonly employed to understand the CVD growth process of nitrogen-doped CNTs.<sup>242</sup> Generally there are two different schemes to use metal catalyst seeds in the growth. In the “fixed-bed” scheme, iron nanoparticles with defined sizes were first synthesized by thermal decomposition of iron pentacarbonyl and then plated on quartz slides by spin coating for subsequent CVD growth.<sup>114</sup> In the “floating catalyst” scheme, iron catalyst (typically ferrocene) was mixed and injected with carbon and nitrogen precursors, and the thermal decomposition of ferrocene provided in situ generation of iron catalytic nanoparticles on which the carbon and nitrogen precursors were deposited. While fixed-bed catalyst provides better size control over the resultant NCNCs, the yield of product is typically lower compared to the floating catalyst scheme. Based on our experience, the yield of NCNCs per batch of fixed-bed synthesis is less than 1 mg per mL precursor, compared to ~5 mg per mL precursor in the floating catalyst scheme. As the floating catalyst scheme also provides fairly uniform size distribution of NCNCs, it was adopted in this paper for CVD synthesis.

CVD method affords as-synthesized NCNCs which exhibit fibril morphology comprised of many stacked cups. Although there is no chemical bonding between adjacent cups,<sup>105</sup> challenges remain in effective isolation of the individual cups because they are firmly inserted

into each other's cavities and held by multiple noncovalent interactions and an outer layer of amorphous carbon.<sup>105</sup> Attempts to separate the stacked cups include both chemical and physical approaches. While oxidation treatment in a mixture of strong acids is a typical procedure to cut CNTs and introduce oxygen functionalities,<sup>62,206</sup> it can also be applied to cut NCNCs into shorter sections. Microwave plasma etching procedures have been also shown to separate the NCNCs.<sup>164</sup> Compared to the chemical approaches, physical separation is more straightforward. Our previous study showed that by simply grinding with a mortar and pestle individual NCNCs can be partially isolated from their stacked structure.<sup>108</sup> In addition, high-intensity probe-tip sonication, which was reported to effectively cut single-walled carbon nanotubes (SWCNTs),<sup>159</sup> was also shown to have a significant effect on separation of NCNCs.<sup>105</sup> The probe-tip sonication delivers high-intensity ultrasonic power to the NCNC solution that essentially "shakes" the stacked cups and disrupts the weak interactions that hold the cups together. While other potential separation methods are either inefficient or destructive to the cup structure, probe-tip sonication provides a highly effective, cost-efficient and less-destructive physical separation method to obtain individual graphitic cups.

The as-synthesized fibril NCNCs were first treated in concentrated H<sub>2</sub>SO<sub>4</sub>/HNO<sub>3</sub> acid mixture prior to their separation with probe-tip sonication. The resultant separated NCNCs were highly hydrophilic and effectively dispersed in water. We have previously identified nitrogen functionalities such as amine groups on NCNCs and utilized their chemical reactivity for NCNCs functionalization.<sup>108,105,165</sup> Compared to our previously reported method of capping NCNCs with commercial nanoparticles,<sup>105</sup> in this work, gold nanoparticles (GNPs) were effectively anchored to the surface of the cups by citrate reduction from chloroauric acid. Due to the preferential distribution of nitrogen functionalities on the open rims of NCNCs, the GNPs synthesized *in situ*

from the gold precursors tended to have better interaction with the open rims and form GNP “cork stoppers” on the cups. Such synthesis and functionalization methods have resulted in a novel GNP-NCNC hybrid nanomaterial for potential applications as drug delivery carriers.

### 2.3.3 Specific Reagents and Equipment

**Table 2-2.** Reagents involved in the experiment

Reagent Name	Company	Catalogue Number
H <sub>2</sub>	Valley National Gases	Grade 5.0
Ar	Valley National Gases	Grade 5.0
Ferrocene	Sigma-Aldrich	F408-500G
Xylenes	Fisher Scientific	X5-500
Acetonitrile	EMD	AXO149-6
H <sub>2</sub> SO <sub>4</sub>	Fisher Scientific	A300-500
HNO <sub>3</sub>	EMD	NX0409-2
DMF	Fisher Scientific	D119-500
Ethanol	Decon	2716
Phenol	Sigma-Aldrich	P1037-100G
Pyridine	EMD	PX2020-6
Hydridantin	Sigma-Aldrich	H2003-10G
Ninhydrin	Alfa Aesar	43846
HAuCl <sub>4</sub>	Sigma-Aldrich	52918-1G
Sodium Citrate	SAFC	W302600

**Table 2-3.** Equipment used in the experiment

<b>Equipment Name</b>	<b>Company</b>	<b>Catalogue Number</b>
CVD Furnace	Lindberg/Blue	—
TEM (low-resolution)	FEI Morgagni	—
TEM (high-resolution)	JOEL	2100F
Probe-tip Sonicator	Qsonica	XL-2000
UV-Vis Spectrometer	Perkin-Elmer	Lambda 900
Zeta Potential Analyzer	Brookhaven	ZetaPlus
EDX spectroscopy	Phillips	XL30 FEG

### **2.3.4 Detailed protocol**

#### **2.3.4.1 CVD synthesis of nitrogen-doped carbon nanotube cups (NCNCs)**

NCNCs were synthesized employing chemical vapor deposition (CVD) technique on quartz substrate using liquid precursors (Figure 1A).

1.1) Place a three-foot long quartz tube (2.5 cm i.d.) in a Lindberg/Blue tube furnace as the reaction chamber. Place a quartz plate (1" × 12") inside the tube as the substrate for product collection. Seal the quartz tube using homemade stainless steel caps with built-in gas and liquid injection connections/tubes.

1.2) Make a solution of liquid precursor containing 0.75 wt% ferrocene, 10 wt% acetonitrile and 89.25 wt% xylenes. Before the growth, draw about 5 mL of liquid precursor into a gas tight syringe connected to the inlet to the quartz tube. Place the syringe on a syringe pump.

1.3) Assemble the CVD system. Connect all gas inlet and outlet. Flow Ar (845 sccm) to purge the CVD system and check leakage using Snoop® liquid leak detector. After purging for 20 min, turn on H<sub>2</sub>. Set the flow rate of H<sub>2</sub> to 37.5 sccm and Ar to 127 sccm. Turn on the furnace. Set the temperature of the furnace to 800 °C and wait till it is stable at 800 °C.

1.4) Use the syringe pump to inject the liquid precursor into the quartz tube. Set the injection rate at 9 mL/h for 6 min to fill the dead volume of the injector tube. Then turn down the injection rate to 1 mL/h for the growth of NCNCs. After 90 min of growth, turn off the syringe pump and H<sub>2</sub> gas flow, and shut down the furnace. Keep Ar flowing to maintain an inert atmosphere until the furnace was cooled down to room temperature.

1.5) Disconnect all gas inlets and outlets, and the injection system. Disassemble the CVD system and take the quartz plate out. Use a one-sided razor blade to peel off the NCNCs film from the quartz plate. Disperse the collected product in ethanol. Respiratory protection is needed to prevent inhaling possible carbon materials if the work is conducted outside of fume hood.

#### **2.3.4.2 Oxidation of as-synthesized NCNCs by a mixture of acids**

2.1) Transfer about 10 mg of as-synthesized NCNCs to a 200 mL round-bottom flask. Add 7.5 mL of concentrated HNO<sub>3</sub> to the flask. Briefly sonicate the mixture in water bath for better dispersion. Then add 22.5 mL of concentrated H<sub>2</sub>SO<sub>4</sub> slowly. (CAUTION: the strong acid mixture is highly corrosive; carefully handle these acids with safety protection.) Sonicate the reaction mixture in water bath at room temperature for 4 hr.

2.2) Dilute the reaction mixture with 100 mL of water while cooling down in ice bath. Filter the mixture through a polytetrafluoroethylene (PTFE) membrane with pore size of 220 nm using a water aspirator.

2.3) Wash the material on the filter membrane with 200 mL of 0.01 M NaOH solution to remove any acidic residual byproduct.<sup>243</sup> Then wash with 200 mL of 0.01 M HCl solution, followed by copious amount of water until a neutral pH of the filtrate was achieved. Disperse the resultant material (oxidized NCNCs) in water (20 mL) by sonication. The resulted suspension can be stored at room temperature for further experiments.

#### **2.3.4.3 Physical separation of NCNCs by probe-tip sonication**

3.1) Transfer the suspension of oxidized NCNCs in water to a 50 mL centrifuge tube placed in ice bath. Fill the centrifuge tube to the 25 mL mark with water. Set the probe-tip sonicator equipped with a 1/4" diameter titanium microtip at 60% maximum magnitude (12 W). Submerge the microtip to the center of the solution and then process for 12 hr with 30 sec on/off interval. Change the ice every 30 min to prevent overheating.

3.2) Stop the sonication. Filter the NCNC suspension through a 220 nm pore-size PTFE filter membrane to remove any large particles. The resultant NCNC samples can be store at room temperature for further applications.

3.3) (Optional) As a comparison experiment, disperse another sample of as-synthesized NCNCs in DMF and directly sonicate the suspension with probe-tip sonication for 12 hr at the same settings as above.

#### **2.3.4.4 Quantitative analysis of amine functional groups on NCNCs by Kaiser test**

4.1) Prepare the reagent A: mix 1 g of phenol and 250  $\mu$ L of EtOH in 2.5 mL of pyridine, add 50  $\mu$ L of 0.01 M hydrindantin in H<sub>2</sub>O to the mixture. Prepare the reagent B: dissolve ninhydrin (50 mg) in 1 mL of EtOH.

4.2) Weigh the NCNCs samples (~0.5 mg) on a microbalance and disperse them in 1 mL of 3:2 EtOH/water in small test tubes. Add 100  $\mu$ L of Reagent A and 25  $\mu$ L of Reagent B to the sample suspension. Seal the test tubes with parafilms and heat the mixture at 100  $^{\circ}$ C oil bath for 10 min. Filter the sample through a syringe filter to remove solid particles and collect the filtrate solution.

4.3) Take the visible spectra on the filtrate for colorimetric analysis with the blank sample made in the same process without adding NCNCs. Record the absorbance of the peak centered at 570 nm and calculate the amine loadings according to the Beer-Lambert law.

#### **2.3.4.5 Functionalization of NCNCs with GNPs**

5.1) Sonicate 4 mL of aqueous suspension containing separated NCNCs (0.01 mg/mL) using a water-bath sonicator for 5 min to achieve a uniform dispersion.

5.2) Add 1 mL of HAuCl<sub>4</sub> aqueous solution (1 mg/mL) to the NCNC suspension during sonication. Then add 250  $\mu$ L of 1 wt % trisodium citrate aqueous solution dropwise. Vigorously stir the reaction mixture at 70  $^{\circ}$ C on a hot plate for 2 hr.

5.3) Centrifuge the reaction mixture at 3400 rpm for 15 min. Collect the NCNCs functionalized with GNPs in the precipitate and wash with water by centrifugation. Disperse the precipitate in water (4 mL).

#### **2.3.5 Representative Results**

The as-synthesized NCNCs from CVD growth appeared as a carpet of black material on quartz substrate. Thick films of NCNCs weighing about several mg were obtained by peeling with a razor blade (**Figure 2-7b**). TEM images show the morphology of as-synthesized NCNCs

at different magnifications (**Figure 2-7**). At the lower magnification (**Figure 2-7c**), the as-synthesized NCNCs all showed a fibril structure with lengths of typically several micrometers and diameters of 20 – 30 nm. Unlike the continuous tubular structure of undoped CNTs, the NCNC fibers were compartmented with many cup-shaped segments. High-resolution TEM imaging of the tip of a NCNC fiber reveals the curved graphitic structure of nanotube cups that are stacked on top of each other (**Figure 2-7d**).

**Figure 2-8a** shows the TEM images of NCNCs after acid oxidation. The oxidation process cut the long fibers into shorter sections of about 1  $\mu\text{m}$  in length in which the graphitic cups remained stacked. The oxidized NCNCs formed stable suspension in water which was then processed with probe-tip sonication. After 12 hr of sonication and filtration, TEM image shows the significant decrease in the length of NCNCs (**Figure 2-8b**). Most NCNCs appeared as individual cups with length less than 200 nm. The individual cups isolated from the stacks typically have a semi-elliptical shape with one end sealed and the other open.

The size distribution of NCNCs was based upon ~300 measurements from TEM images. The length distribution histograms (**Figure 2-9a**) of oxidized NCNCs, NCNCs after 12 hr sonication, and the final product show the effect of probe-tip sonication on separation of stacked NCNCs and obtaining individual cups. The oxidation process resulted in a change in zeta potential of NCNCs from positive to negative (**Figure 2-9b**), while the inherent amine groups on NCNCs were not affected according to Kaiser test (**Figure 2-9c**).

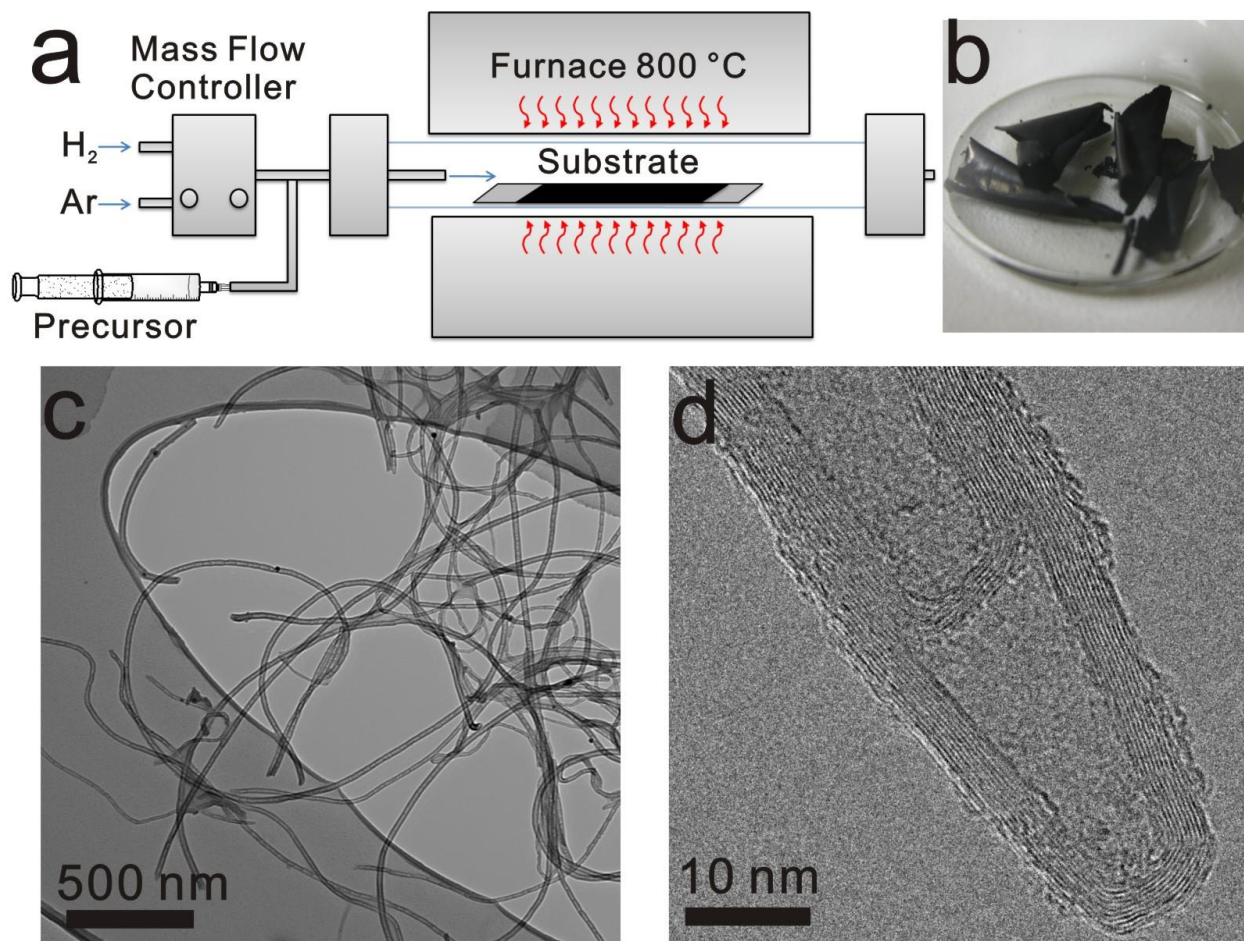


**Figure 2-7.** (a) Schematic setup of a tube furnace used for chemical vapor deposition (CVD) synthesis of NCNCs. (b) Photograph of the as-synthesized NCNC film peeled from the quartz substrate. (c) An overview transmission electron microscopy (TEM) image of as-synthesized NCNCs. (d) High-resolution TEM image showing the tip of an individual as-synthesized NCNC.

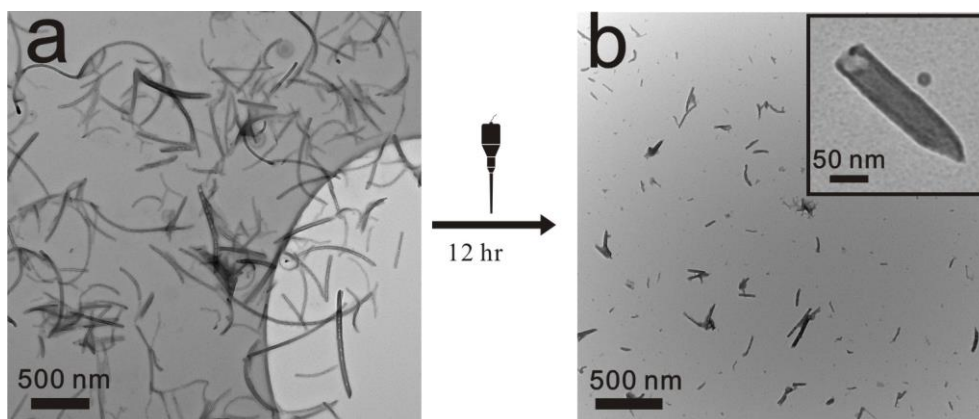


**Figure 2-8.** TEM images of (a) oxidized NCNCs and (b) NCNCs after subsequent 12 hr probe-tip sonication and filtration. Inset shows an individual separated NCNC.

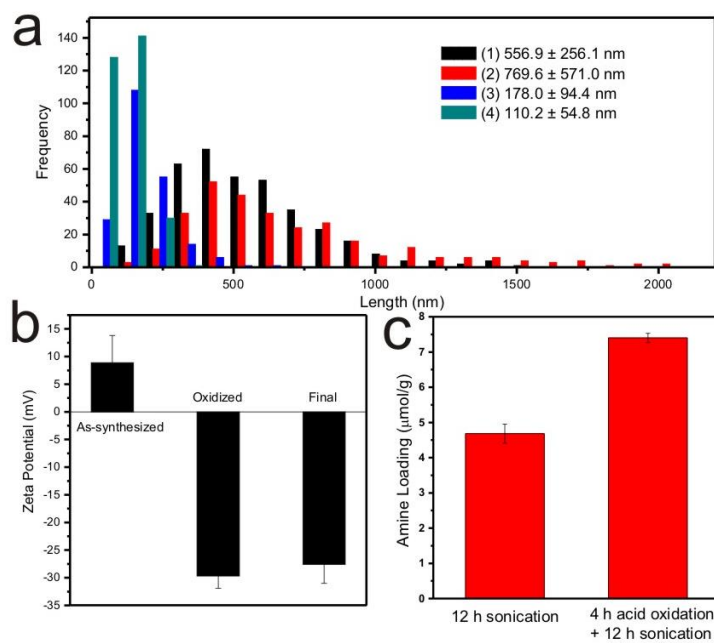


**Figure 2-9.** (a) Length distribution histograms for NCNC samples of (1) after 12 hr probe-tip sonication only, (2) after oxidation, (3) after oxidation and 12 hr probe-tip sonication, and (4) the final product after filtration through a 220 nm pore-size membrane. (b) Zeta potentials of as-synthesized, oxidized, and the final NCNC samples. (c) Amine loadings on NCNCs after 12 h sonication only and after both oxidation and 12 h sonication.

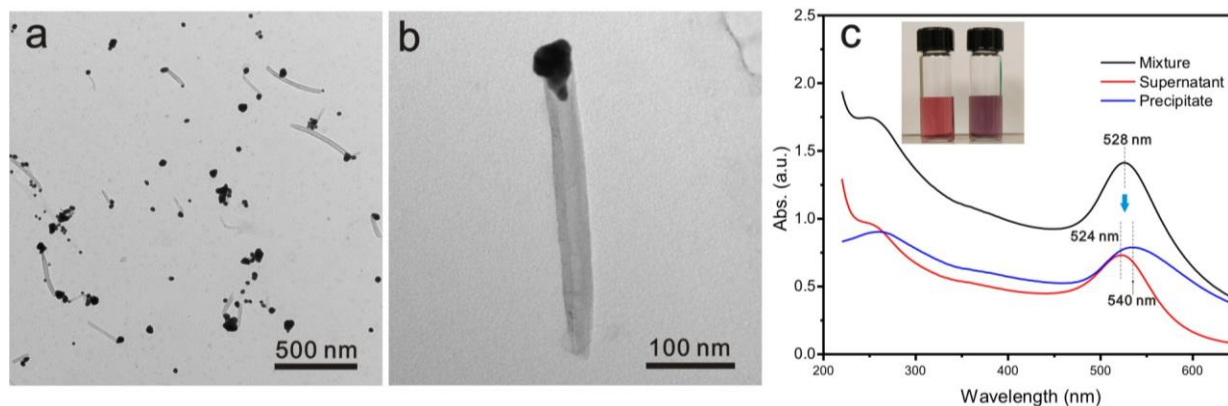


**Figure 2-10.** (a) TEM image of NCNCs functionalized with GNPs by citrate reduction of  $\text{HAuCl}_4$  and collected by centrifugation. (b) TEM image showing an individual nanocup corked with GNP. (c) UV-Vis spectra of the reaction mixture, the supernatant solution and the precipitate of the GNP functionalization reaction. The inset photograph shows the color difference between the supernatant (left) and the precipitate (right) solutions.

The separated NCNCs were then functionalized with GNPs by citrate reduction of  $\text{HAuCl}_4$ . The reduction reaction occurred at  $70\text{ }^\circ\text{C}$  under vigorous agitation. The initially colorless solution started to turn blue after 30 min and gradually changed to wine-red within 2 hr. TEM image of the centrifuge precipitate in **Figure 2-10a** shows the high coverage of GNPs on NCNCs. Almost all nanotube cups were functionalized with GNPs, and the GNPs were frequently found to be preferentially located at the open rim serving as cork stoppers for the cups. A magnified TEM image (**Figure 2-10b**) reveals that some GNPs were actually grown into the cup interior forming a “tight” cork. There was a difference in color between the precipitate and the supernatant solution. UV-Vis absorption spectra show that the surface plasmon resonance (SPR) band of GNPs in the precipitate has a red-shift compared to that of the supernatant (**Figure 2-10c**).

### 2.3.6 Discussion

The primary goal of our experiments was to effectively produce graphitic nanocups from nitrogen-doped CNTs. However, nitrogen-doping in the CVD synthesis does not guarantee the formation of the stacked cup-shaped structure. Depending on the chemical composition of the precursor and other growth conditions, the morphology of the resulted product may vary a lot.<sup>127</sup> The concentration of nitrogen source is the primary factor influencing the structure because the compartmented structure results from the incompatibility of nitrogen atoms in the graphitic lattices.<sup>146</sup> Generally, the length of the compartments decreases with increasing nitrogen concentration in the precursor. At higher concentrations, the lateral segmentation layers become irregular and corrugated and the uniform cup-shaped compartmented structure is lost.<sup>127</sup> In our procedure, we used 10% MeCN as the precursor which resulted in uniform cup-shaped structure with similar diameters. Carbon source is another pivotal factor for NCNC synthesis. Previous attempts using ethanol as carbon source sometimes formed irregular tear-drop-shaped segments in the resulted NCNCs,<sup>114</sup> presumably due to oxygen defects originated from ethanol. Replacing ethanol with xylenes eliminated formation of any irregular shapes. Moreover, reduced ferrocene concentration (0.75 wt%) helped to form small uniform iron catalyst nanoparticles and relatively low carrier gas flow rate facilitated vertical growth. All these factors resulted in formation of NCNCs with more uniform diameters and higher yield.

The as-synthesized NCNCs are long fibers of stacked cups. High-resolution TEM image (**Figure 2-7d**) clearly shows the graphitic structure of adjacent stacked cups. The graphitic walls of each cup extend along the direction with a certain angle from the cup axis, having no connections between adjacent cups. The adjacent cups were assumed to be held together by noncovalent interactions between graphitic layers, and also by an outer layer of amorphous

carbon as observed in **Figure 2-7d**. The weak interactions that keep the cups together can be disrupted and individual nanocups can be isolated *via* chemical or physical methods.

In our previous study,<sup>105</sup> the separation procedure was carried out by physical separation only. The as-synthesized NCNCs were directly sonicated in N,N-dimethylformamide (DMF) under probe-tip sonication. 12 hr of sonication significantly reduced the average length of NCNCs from several micrometers to  $556.9 \pm 256.1$  nm and effectively derived individual nanocups, though unseparated NCNCs were still frequently observed. A major drawback for direct ultrasonication was that the as-synthesized NCNC fibers were highly hydrophobic and even poorly suspended in DMF. The efficiency of separation was compromised in this case because the NCNCs were not well dispersed initially. To improve the dispersion of NCNCs in solvent and facilitate the ultrasonic separation, as-synthesized NCNCs were first treated with strong acids. This treatment was widely applied for oxidation of pristine CNTs.<sup>62</sup> Energy-dispersed X-ray (EDX) spectroscopy shows a significant increase of oxygen concentration in NCNCs after acid treatment (**Table 2-4**), indicating that oxygen functionalities were introduced to the graphitic structure. The oxidation step not only increased the hydrophilicity of NCNCs, but might have also weakened the interactions between the graphitic layers of the adjacent cups by introducing oxygen lattice defects and removing the outer amorphous carbon. The oxidized NCNCs formed even dispersion in water and thus were more susceptible to the subsequent ultrasonic separation. The average length of oxidized NCNCs measured from TEM images was  $770 \pm 571$  nm. Upon 12 hr of probe-tip sonication, most individual cups were isolated out, and the average length was reduced to  $178 \pm 94$  nm, which was below the 220 nm pore size of the PTFE membranes. A filtration process thus further removed any longer NCNCs and reduced the average length to  $110 \pm 55$  nm, leaving only individual and short stacked nanocups in the filtrate.

The final separated NCNCs were well dispersed in water forming stable suspension which showed little precipitation over period of several weeks.

The acid oxidation process greatly altered the surface properties of NCNCs. Due to the existence of nitrogen functionalities that tend to be protonated in solution, the as-synthesized NCNCs were slightly positively charged with a zeta potential of +9 mV. Acid oxidation made NCNCs more suspendable with a negative zeta potential of about  $-30$  mV. It should be noted that the oxidation process did not alter the inherent amine functionalities on the surface of NCNCs as was quantified by Kaiser test. On the contrary, more amine groups were found on separated NCNCs after 4 hr acid oxidation than on the samples separated by sonication only, which indicated that better separation exposed more amine functionalities. The acid oxidation process also effectively removed iron catalyst residues from NCNCs as revealed by the EDX elemental analysis (**Table 2-4**).

A main problem of the prolonged probe-tip sonication was the wear-out of titanium tips. Long and intensive ultrasonic vibration generates a lot of heat and is abrasive to the microtip. With the tip being worn out, the separation effect was weakened and the titanium particles tended to come off the tip as contamination. To better protect the tip from damage, the sample was processed on 30 sec on/off intervals and the ice bath was replaced every 30 min to prevent overheating. Due to its chemical inertia, the titanium contaminant was hard to be completely removed. The filtration procedure through a 220-nm-pore membrane was effective in removal of any large titanium particles, and small particles could also be mostly removed by brief centrifugation at 3400 rpm for 4 min, though in the final separated NCNC samples about 0.2 at.% of titanium was still present (**Table 2-4**).

The separated NCNCs have both oxygen and nitrogen functionalities on their graphitic framework, which provide diverse chemical properties essential for drug delivery applications. By thiolation of the amine groups, we were previously able to attach commercial GNPs on to the graphitic nanocups.<sup>105</sup> Those GNPs, with an average diameter fitting the opening of the cups, tended to seal the cup as cork stoppers. Using the hydrophilic oxidized NCNCs, GNPs can be more effectively anchored on the cups in aqueous phase by direct reduction of chloroauric acid with trisodium citrate as the reduction reagent. GNPs are likely to nucleate on the nitrogen functionalities and continue to grow under the reaction conditions. This bottom-up functionalization approach resulted in strong and specific interaction between GNPs and NCNCs. Due to the preferential distribution of nitrogen functionalities on the open rim of the cups, GNPs had better chance to nucleate at the opening, and the subsequent growth often formed cork-shaped nanoparticles that extended to the interior of the cups. This corking interaction was more frequently observed using the reduction approach compared to our previous method. Free GNPs in solution were also present during the reduction reaction; they can be removed by centrifugation at 3400 rpm for 15 min. There was distinct difference between the solution colors of the supernatant and the precipitate. The former appeared as wine red with a SPR absorption band at 524 nm and the latter was purple with a SPR band at 540 nm. The red-shift in the SPR band may be attributed to the strong electronic interaction of GNPs on the surface of NCNCs.

**Table 2-4.** Elemental analysis of as-synthesized NCNCs and final separated NCNCs based on energy-dispersive X-ray (EDX) spectroscopy.

Element (K Shell)	As-synthesized at. %	Final separated at. %
C (including N)	98.0	95.9
O	0.6	3.8
Fe	1.4	0.1
Ti	—	0.2

### 2.3.7 Conclusions

In conclusion, we adopted a series of synthetic techniques to obtain individual graphitic nanocups (i.e., NCNCs) from their stacking structures. Introduction of the acid oxidation and probe-tip sonication procedures is essential to ensure the high efficiency of separation and the hydrophilicity of the final nanocups. Through citrate reduction of  $\text{HAuCl}_4$ , the NCNCs were then functionalized with GNPs which effectively closed the cups as cork stoppers. This novel GNP-NCNC hybrid nanomaterial may have promising applications as nanoscale containers and drug-delivery carriers.

### 2.3.8 Acknowledgement

This work was supported by an NSF CAREER Award No. 0954345.

### **3.0 ENZYMATIC DEGRADATION OF MULTIWALLED CARBON NANOTUBES**

#### **3.1 CHAPTER PREFACE**

Because of their unique properties, carbon nanotubes and in particular multi-walled carbon nanotubes (MWCNTs) have been used for the development of advanced composite and catalyst materials. Despite their growing commercial applications and increased production, the potential environmental and toxicological impacts of MWCNTs are not fully understood; however, many reports suggest that they may be toxic. Therefore, a need exists to develop protocols for effective and safe degradation of MWCNTs.

In our previous investigation, we showed that a naturally existing enzyme – horseradish peroxidase (HRP) catalyzed the degradation of single-walled carbon nanotubes (SWCNTs) under a mild aqueous condition containing dilute hydrogen peroxide ( $\text{H}_2\text{O}_2$ ).<sup>167</sup> The degradation is considered to be oxygen-defect-mediated such that the oxygen functionalities on carboxylated SWCNTs help the enzymatic interaction with the CNTs.<sup>168</sup> In this article, we investigated the effect of chemical functionalization of MWCNTs on their enzymatic degradation with HRP and  $\text{H}_2\text{O}_2$ . We investigated HRP/ $\text{H}_2\text{O}_2$  degradation of purified, oxidized, and nitrogen-doped MWCNTs and proposed a layer-by-layer degradation mechanism of nanotubes facilitated by side wall defects. These results provide a better understanding of the interaction between HRP and

carbon nanotubes and suggest an eco-friendly way of mitigating the environmental impact of nanotubes.

The material presented in this section was published as a full article in *The Journal of Physical Chemistry A* in a special issue: David W. Pratt Festschrift, and reproduced with permission from *J. Phys. Chem. A* **2011**, *115*, 9536-9544, Copyright 2011 American Chemical Society. The full citation is listed as Ref. 206.

**List of Authors:** Yong Zhao, Brett L. Allen, and Alexander Star

**Author Contributions:** All authors contributed to the design of project and participated in the results discussion. YZ performed the experiments and conducted the characterization. YZ and BA prepared the figures. YZ and AS wrote the manuscript.

### 3.2 INTRODUCTION

After almost 20 years since their discovery,<sup>4</sup> carbon nanotubes (CNTs) still spawn broad research interest in numerous disciplines and are a primary focus of nanoscience research. Their unique tubular graphitic structure and outstanding mechanical, electronic and chemical properties<sup>6-8</sup> lead to a wide range of applications such as in composite materials,<sup>415,40</sup> chemical sensing,<sup>29-31</sup> and drug delivery.<sup>50-51</sup> There are two main types of CNTs: single-walled carbon nanotubes (SWCNTs) and multi-walled carbon nanotubes (MWCNTs). MWCNTs consist of several to dozens of concentric graphitic walls. Due to their low cost and large availability,<sup>136</sup> MWCNTs are advantageous over SWCNTs for high volume applications such as composite

materials. Their metallic nature also put forward the potential applications in fuel cells as electrode catalyst support.<sup>46</sup> In addition, their multi-walled structure enhances their resistance to chemical treatment, which allows grafting of chemical functionalities at the surface of nanotubes while retaining their intrinsic mechanical and electrical properties.<sup>244</sup> Acid oxidation is a common scheme of functionalizing MWCNTs, which can introduce oxygen-containing defective sites within their outer graphitic walls,<sup>136, 166</sup> forming carboxylated MWCNTs (o-MWCNTs). Additionally, MWCNTs can also be doped with heteroatoms such as nitrogen into the graphitic structures during the synthesis process,<sup>108</sup> forming nitrogen-doped MWCNTs (n-MWCNTs) which were reported to have excellent catalytic activity in oxygen-reduction reaction (ORR).<sup>113, 151</sup> The promising applications of MWCNTs and their low cost of synthesis have spurred a global production about 40 times higher than SWCNTs,<sup>245</sup> which highly stressed the importance of investigating the enzymatic degradation of MWCNTs as their potential disposal in the environment increases.

In addition to the potential environmental impact, there are reports that carbon nanomaterials may possess cytotoxicity, and pathogenicity.<sup>173, 177, 179, 188</sup> By functionalizing CNTs with various bioconjugates such as DNA,<sup>183</sup> peptides<sup>184</sup> or phospholipid components,<sup>213</sup> the biocompatibility of carbon nanotubes is largely increased; still, CNTs remain resistant to physiological or environmental degradation under mild conditions in the long term, even after such functionalization.<sup>80, 188</sup> We have recently demonstrated that carboxylated SWCNTs can be enzymatically degraded in the presence of low concentrations of H<sub>2</sub>O<sub>2</sub> and peroxidases, such as horseradish peroxidase (HRP)<sup>167-168</sup> and human myeloperoxidase (hMPO).<sup>208</sup> As a result of their multi-walled morphology, MWCNTs are considered more difficult to be degraded than SWCNTs by enzymatic catalysis, which was shown in a recently published work.<sup>205</sup> However,

the detailed mechanism of MWCNTs' enzymatic degradation is still ambiguous. In this study, we explored the enzymatic degradation of o-MWCNTs with different degrees of carboxylation and n-MWCNTs. A variety of characterization methods were implemented to monitor possible degradation including dynamic light scattering (DLS), transmission electron microscopy (TEM), Raman spectroscopy, and gas chromatography–mass spectrometry (GC-MS). For up to 80 days of degradation with daily additions of H<sub>2</sub>O<sub>2</sub>, o-MWCNTs appeared to decrease in both diameter and length, although a complete disappearance of o-MWCNTs was not observed. In contrast, when incubated under the same HRP/H<sub>2</sub>O<sub>2</sub> conditions, n-MWCNTs showed a complete degradation behavior within 80 days. In essence, these findings suggest that the presence of defects in MWCNT sidewalls play a critical role in the enzymatic degradation process.

### **3.3 EXPERIMENTAL SECTION**

#### **3.3.1 Materials**

MWCNTs were received from Columbian Chemical Company (Marietta, GA). Lyophilized HRP type VI and 3% H<sub>2</sub>O<sub>2</sub> were purchased from Sigma Aldrich. Amplex Red (10-acetyl-3,7-dihydroxyphenoxazine) was procured from Molecular Probes, Invitrogen.

#### **3.3.2 Carboxylation of MWCNTs**

As-received MWCNTs were pretreated by sonication in concentrated HNO<sub>3</sub> at room temperature for 4 hr in order to eliminate impurities such as amorphous carbon and metal catalysts.

MWCNTs were then filtered through a 0.22  $\mu\text{m}$  Teflon membrane and washed with  $\text{H}_2\text{O}$  until a neutral pH was measured. Carboxylation of MWCNTs was performed by sonicating approximately 10 mg of pretreated MWCNTs in 5 mL of 3:1  $\text{H}_2\text{SO}_4/\text{HNO}_3$  mixture at 40  $^\circ\text{C}$ . (This solution is highly oxidizing. Caution must be taken when handling this system.) After 5 and 8 hours respectively, 2.5 mL of the suspension was taken out, diluted with 10 mL of double-distilled water, filtered through a 0.22  $\mu\text{m}$  Teflon membrane, and washed with copious amounts of water until the pH was approximately 6 to 7. The pretreated MWCNT samples are noted as “p-MWCNT” and the 5 hr and 8 hr carboxylated samples are respectively noted as “o-MWCNT (5hr)” and “o-MWCNT (8hr)” herein and after.

### 3.3.3 Synthesis and purification of n-MWCNTs

Nitrogen-doped MWCNTs were synthesized using chemical vapor deposition (CVD) technique in a Lindberg/Blue tube furnace.<sup>16</sup> The quartz substrate was placed in a three-foot long sealed quartz tube under 950  $^\circ\text{C}$  in the furnace. A liquid precursor containing 5.0 w% of MeCN, 1.25 w% of ferrocene, and 93.75 w% of EtOH was injected at a rate of 5 mL/min in  $\text{H}_2$  and Ar atmosphere. After 1 hr growth, the sample on the substrate was taken out and collected using a razor blade.

Purification of as-synthesized n-MWCNTs was performed using the method adopted from Smalley et al.<sup>137</sup> A sample of 4.4 mg as-synthesized n-MWCNTs was suspended in a mixture of 2 mL HCl (1 M) and 2 mL  $\text{H}_2\text{O}_2$  (30%) and stirred at 60  $^\circ\text{C}$  for 4.5 hr with the same amount of HCl and  $\text{H}_2\text{O}_2$  supplemented every 1 hr. After filtration of the slurry and washing with copious amount of water, purified n-MWCNT samples were collected and re-suspended in water.

### **3.3.4 Incubation with HRP and H<sub>2</sub>O<sub>2</sub>**

Around 1 mg of p-MWCNTs, o-MWCNTs (5hr and 8hr), and n-MWCNTs were transferred into four vials and sonicated in 4 mL of water for 1 hr to afford a stable suspension. HRP type VI aqueous solution (4 mL of 0.385 mg/mL) was then added into each vial followed by incubation for 24 hr. To start the degradation process, 8 mL of 800  $\mu$ M H<sub>2</sub>O<sub>2</sub> was added, and all vials were sealed with septum stoppers and wrapped with parafilm to keep them gastight. Additions of 250  $\mu$ L of 800  $\mu$ M H<sub>2</sub>O<sub>2</sub> were performed on a daily basis to compensate for H<sub>2</sub>O<sub>2</sub> consumption. All vials were placed on a rotary shaker with constant shaking (220 rpm) at room temperature in the dark to prevent photolysis of H<sub>2</sub>O<sub>2</sub>.<sup>246</sup>

### **3.3.5 Transmission Electron Microscopy (TEM)**

TEM samples were prepared by centrifuging 250  $\mu$ L the MWCNT suspension at 3400 rpm for 2 hr. After removal of the supernatant, the precipitate was resuspended in 1 mL of EtOH through sonication, and around 10  $\mu$ L of this suspension was dropped on a lacey carbon grid and dried in ambient conditions overnight for TEM imaging (FEI Morgagni, 80 keV, or JEOL 2100F, 200 keV). Alternatively, TEM sampling was done by directly drop-casting sample solution on to grids.

### **3.3.6 Raman Spectroscopy**

Approximately 50  $\mu$ L of sample suspension before and during degradation was drop-casted onto a quartz slide and dried under ambient conditions. Raman spectra were taken on a Renishaw

inVia Raman microscope with an excitation wavelength of 633 nm. Spectra were scanned from 1000-1800  $\text{cm}^{-1}$  for 5 times at 15 s exposure time. For each sample 5 Raman spectra from different sample spots were collected and averaged.

### **3.3.7 Gas Chromatography–Mass Spectrometry (GC-MS)**

The  $\text{CO}_2$  content in the headspace of the sample vials was measured with GC-MS. During the degradation process around 25  $\mu\text{L}$  of headspace gases were injected using a gastight syringe into a Shimadzu QP5050A GC-MS unit through an XTI-F capillary column (150  $^\circ\text{C}$ ).

### **3.3.8 Dynamic Light Scattering (DLS)**

DLS was performed using a quasi-elastic light scattering spectrometer (Brookhaven 90 Plus Particle Size Analyzer) under 678 nm wavelength laser irradiation. MWCNT samples before and after 60 days of the enzymatic degradation were dispersed in 3 mL double-distilled water by sonication for 2 hr forming a translucent suspension, and DLS data were taken by averaging results from 5 runs with each run lasting for 1 min.

## 3.4 RESULTS AND DISCUSSION

### 3.4.1 Carboxylation of MWCNTs through acid treatment

It was previously shown that the exposure of either SWCNTs or MWCNTs to oxidative conditions (such as concentrated oxidative acids) could cause shortening in the length and introduction of defects on both the ends and side walls of carbon nanotubes.<sup>51, 62, 247</sup> The defects are functionalized by oxygen-containing groups including mainly carboxylic groups, but also lactonic and phenolic groups.<sup>61</sup> In this experiment, MWCNTs were first purified with nitric acid pretreatment, after that, there was almost no catalytic iron content left in the sample as shown by thermogravimetric analysis (TGA) and elemental analysis (**Appendix A2, Figure A2-1**). Then MWCNTs were carboxylated by sonication in H<sub>2</sub>SO<sub>4</sub>/HNO<sub>3</sub> mixture for 5 hr and 8 hr respectively.

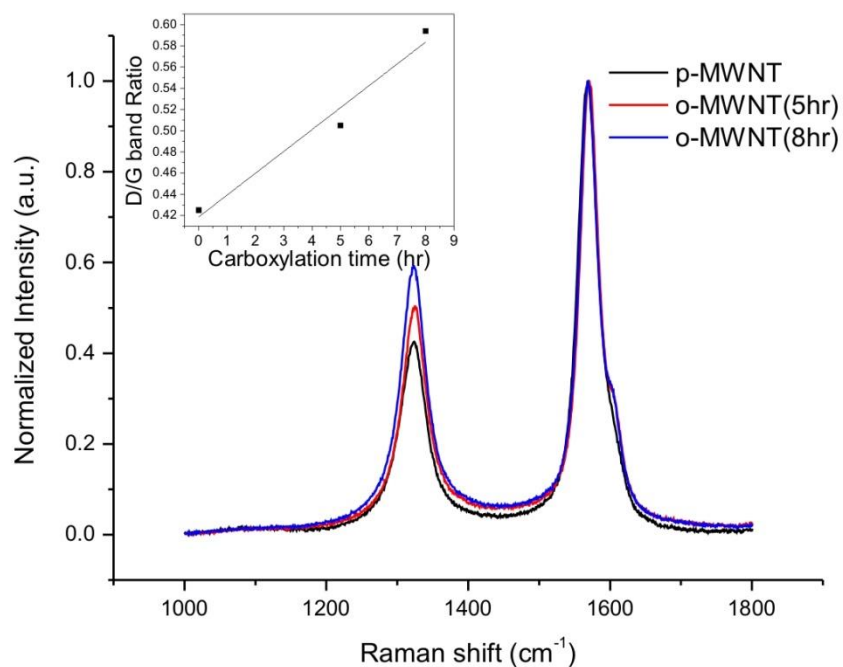


**Figure 3-1.** Normalized Raman spectra of MWCNTs with 0 hr (black), 5 hr (red) and 8 hr (blue) carboxylation before degradation. Inset: D to G band ratio vs. carboxylation time.

**Figure 3-1** shows the Raman spectra of pretreated, 5 hr, and 8 hr carboxylated MWCNTs before the enzymatic degradation process. The spectra were normalized to the G band at around  $1570\text{ cm}^{-1}$  in order to compare the change in the D band at around  $1323\text{ cm}^{-1}$ . The D to G band intensity ratio was observed to be increasing proportionally to carboxylation time. Since the D band characterizes the disorder-induced mode due to symmetry-lowering effects such as defects in  $sp^2$  hybridized carbon systems,<sup>98, 248</sup> increase in D to G band intensity suggests an increase of defect sites introduced on MWCNTs. In order to quantify the functional group loadings on CNTs' surfaces, we performed an acid–base titration<sup>249</sup> following a modified procedure.<sup>61, 250</sup> As expected, the titration results showed an increasing acidic group loading along with increasing carboxylation time (**Appendix A2, Figure A2-2**), indicating that the surface functional group

loadings are positively correlated with the amount of defect sites on MWCNTs as quantified by TGA (**Appendix A2, Figure A2-3**). It should be mentioned that it is possible that small amounts of defects were also introduced on p-MWCNTs' surface during the pretreatment process. Fourier transform infrared spectroscopy (FTIR) further revealed the existence of oxygen-containing functionalities on MWCNT samples (**Appendix A2, Figure A2-4**).

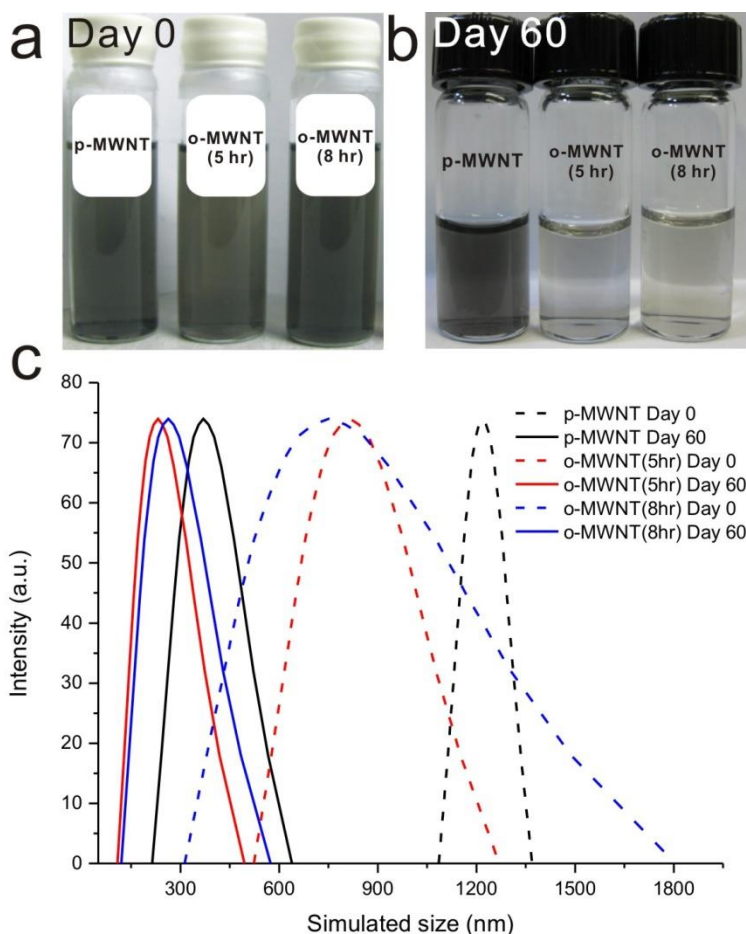


**Figure 3-2.** Photograph showing enzymatic degradation process of MWCNTs after carboxylation for different durations on (a) Day 0 and (b) Day 60. (c) DLS showing decrease in size distribution of different MWCNTs before (dash lines) and after (solid lines) incubation with HRP and  $H_2O_2$  for 60 days.

### 3.4.2 Enzymatic degradation of carboxylated MWCNTs

Our previous study suggested that oxygen-functionalized defects play an important role in facilitating the enzymatic degradation process of SWCNTs by providing hydrophilic binding sites for HRP molecules.<sup>168</sup> Since MWCNTs are essentially multiple layers of concentric SWCNTs, similar degradation behaviors on carboxylated MWCNTs were expected. To compare the degradation kinetics of differently carboxylated MWCNTs, samples of p-MWCNT, o-MWCNT (5hr) and o-MWCNT (8hr) were investigated. MWCNTs were first incubated with HRP for 24 hr to allow sufficient interaction between the enzyme and the substrate, and the reaction was initiated by adding 8 mL of 800  $\mu\text{M}$   $\text{H}_2\text{O}_2$  into the suspension. In comparison to our previous work,<sup>167-168</sup> 800  $\mu\text{M}$   $\text{H}_2\text{O}_2$  (as opposed to 80  $\mu\text{M}$ ) was used in the presence of HRP. We speculated that by raising  $\text{H}_2\text{O}_2$  concentration an order of magnitude, the degradation kinetics would be greatly accelerated, without denaturing HRP.<sup>168</sup> Upon daily additions of 250  $\mu\text{L}$   $\text{H}_2\text{O}_2$  for over 60 days, visual evidence of degradation was observed as shown in Figure 2. The photographs of sample vials taken on Day 0 (**Figure 3-2a**) and Day 60 (**Figure 3-2b**) show an apparent decrease in light scattering and absorbance from the solutions of o-MWCNT (5hr) and o-MWCNT (8hr). This observation might indicate a decrease in MWCNT concentration after the degradation process, and it appeared that the p-MWCNT samples were less degraded compared to the others.

To confirm this observation, Dynamic Light Scattering (DLS) measurements were implemented for all three samples before and after degradation (**Figure 3-2c**). It should be noted that DLS calculates the effective hydrodynamic radii of the particles which are presumably considered as spherical and monodisperse, thus the DLS data do not reflect the actual sizes of MWCNTs. The data showed a significant decrease in size distribution after 60 days of

degradation process. This decrease could be attributed to two effects: a decrease in the actual sizes (i.e., diameters and lengths) and (or) a decrease in the bundling effect of carbon nanotubes. While the bundling effect is primarily due to the  $\pi$ - $\pi$  interaction between the sidewalls of nanotubes,<sup>251</sup> a decreased bundling effect could point to disturbance in the surface  $sp^2$  carbon system. Thus for both reasons, the DLS data suggested the fact that MWCNTs were being degraded. It is seen that the pretreated MWCNTs were also degraded, albeit to a lesser degree; this was possibly because of the small amount of defects introduced on to the nanotubes during the pretreatment process.

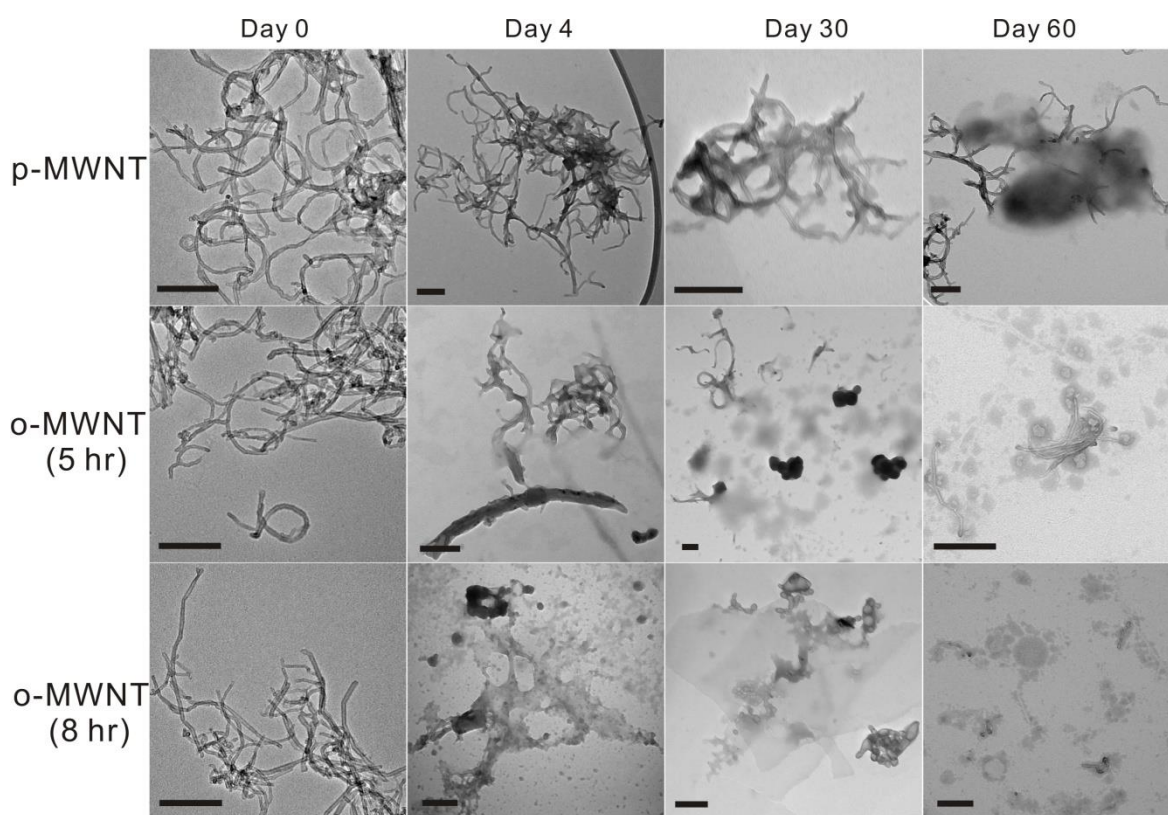


**Figure 3-3.** TEM images of carboxylated MWCNTs incubated with HRP and H<sub>2</sub>O<sub>2</sub>. Each row corresponds to different carboxylation times (0, 5 and 8 hours) and each column corresponds to different enzymatic incubation times (0, 4, 30 and 60 days). All scale bars are 200 nm.

Transmission electron microscopy (TEM) was used to track the morphological changes of MWCNTs as a result of enzymatic degradation (**Figure 3-3**). Before incubation with HRP and H<sub>2</sub>O<sub>2</sub> (Day 0), all the carbon nanotube samples appeared to be intact with lengths of approximately 1 μm. After 4 days of incubation, it was seen that the boundary of nanotubes began to be distorted, forming carbonaceous sheets that spread among nanotubes. This phenomenon became more significant as the carboxylation time increased. For o-MWCNT (8hr) samples, the carbonaceous sheets became prevalent in the visual field surrounding most of the tubular structures. After 30 days, the continuous sheet structures were broken down into nebulous “flakes”. For the 8 hr carboxylated samples, most of the tubular structures became more undefined, and there appeared to be holes forming on these carbonaceous materials. The nanotubes and the residual flakes continued to undergo degradation in following days. At Day 60, it was shown that the sizes of both nanotubes and flakes significantly decreased for o-MWCNT (5hr) and o-MWCNT (8hr) samples. The length of 8 hr carboxylated MWCNTs was shortened from an initial 1 μm to around 100 – 400 nm, and significant bundling effects were not seen over 60 days as each nanotube was surrounded by a layer of carbonaceous sheets. The TEM images showed that MWCNT samples with a higher degree of carboxylation have a faster degradation rate. It was observed that the pretreated MWCNTs were also undergoing a degradation process, but at a much slower rate. The degradation experiment was continued for another 20 days (Day 80). From TEM images (**Appendix A2, Figure A2-5**) it was seen that there were no apparent changes to remaining nanotubes, while the carbonaceous flakes (**Appendix A2, Figure A2-6**) oxidized into progressively smaller pieces. This observation suggested that the degradation of nanotubes was inhibited in the later stage of degradation. It should be mentioned that the decrease in degradation rate is not because of denaturing of the

HRP enzyme, because after the degradation process, an Amplex Red assay<sup>168</sup> was carried out for each sample and showed no decrease in the enzymatic activity (**Appendix A2, Figure A2-7**).

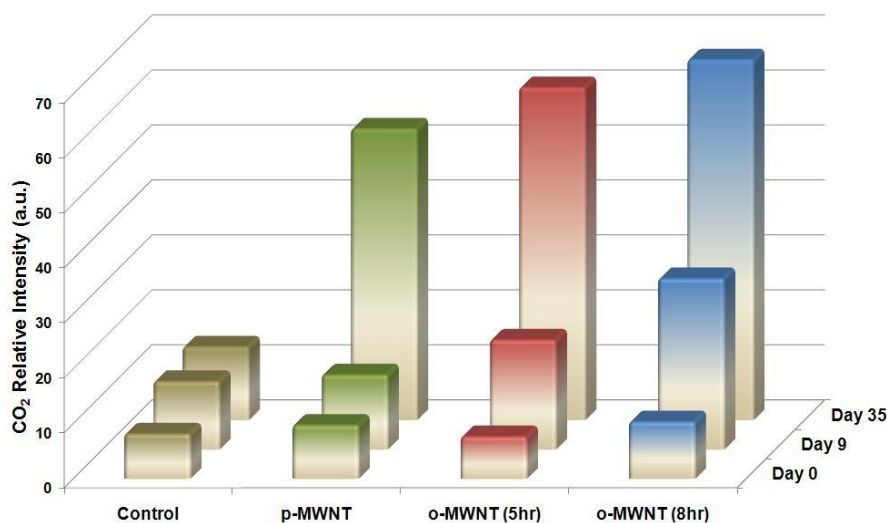


**Figure 3-4.** Evolution of CO<sub>2</sub> in the sample headspace as a final product of MWCNT enzymatic degradation measured by GC-MS on Day 0, 9 and 35 of incubating MWCNTs with HRP and H<sub>2</sub>O<sub>2</sub>. The control sample was made by mixing HRP and H<sub>2</sub>O<sub>2</sub> only.

Since the degradation process is a further oxidation of carboxylated nanotubes, a final degradation product of carbon dioxide (CO<sub>2</sub>) is expected. The CO<sub>2</sub> content in the headspace was monitored by GC-MS. Figure 4 shows the CO<sub>2</sub> (m/z: 44) content relative to N<sub>2</sub> (m/z: 28) in the headspace measured at Days 0, 9 and 35 of incubation. Compared to the control sample (HRP and H<sub>2</sub>O<sub>2</sub>, no CNTs), CO<sub>2</sub> was evolved progressively for all three MWCNT samples. The CO<sub>2</sub> concentration increased 4 – 5 times the initial level at Day 35 for MWCNT samples while remaining relatively stable for the control. Furthermore, the trend that more carboxylated MWCNTs had a faster CO<sub>2</sub> evolution was observed as expected.

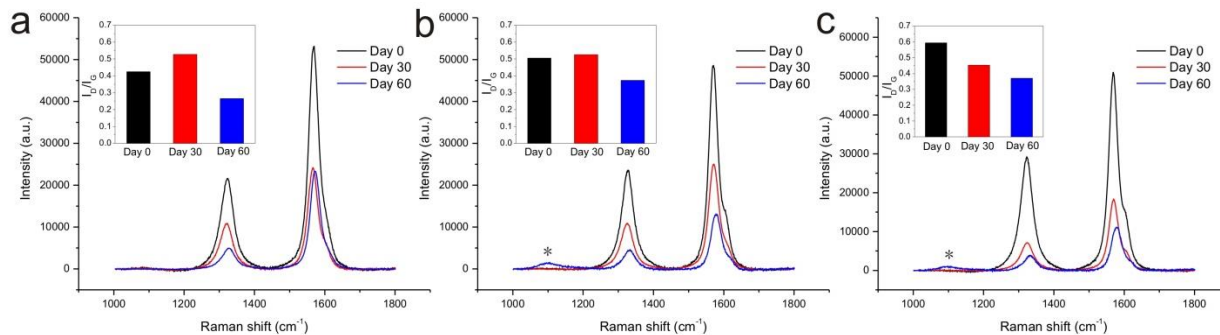
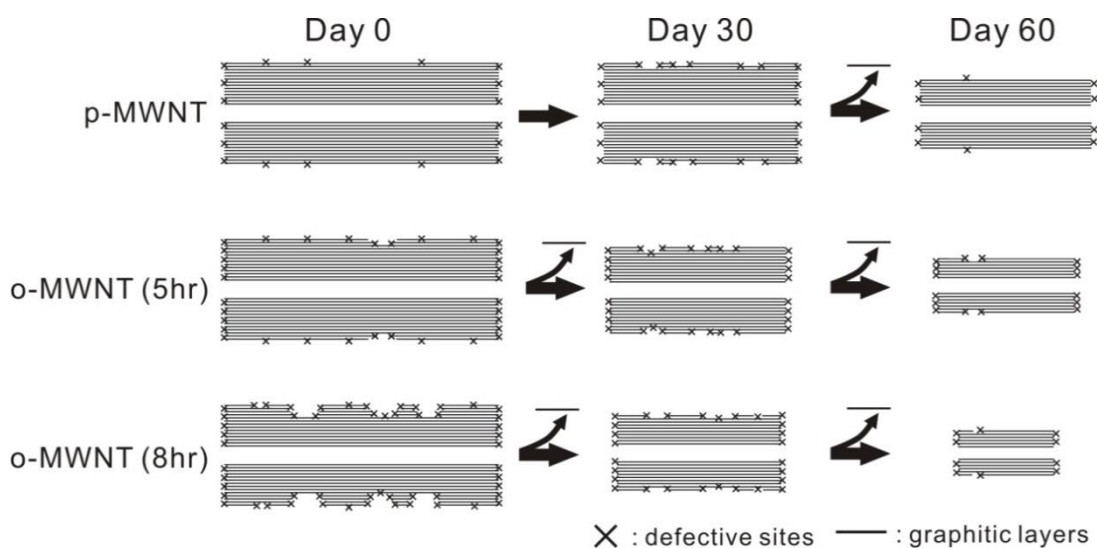


**Figure 3-5.** Raman spectra of (a) p-MWCNT, (b) o-MWCNT (5hr), and (c) o-MWCNT (8hr) showing decay of the D and G band intensity during the enzymatic degradation process (asterisk indicates contribution from quartz substrate). Insets: The changes of D to G band ratio of each sample versus degradation time.

In addition, Raman spectroscopy (**Figure 3-5**) was performed to characterize the degradation process. It is known that the tangential G band and disorder-induced D band are characteristic for graphitic carbon materials,<sup>252</sup> thus their intensities can reflect the abundance of graphitic material present in degraded samples. The Raman samples were prepared by drop-casting and drying the residual suspension on quartz slide in ambient (**Appendix A2, Figure A2-8**). All Raman spectra were baseline-corrected in order to compare the D and G band changes. For o-MWCNT (5hr) and o-MWCNT (8hr) samples, the intensities of both D and G bands were seen to decrease progressively, suggesting a gradual diminishing of graphitic material so that only a small portion was left in the sample after 60 days of degradation. For p-MWCNT samples, however, the G band intensity remained the same at Day 30 to Day 60, while D band intensity continued to decrease as the enzymatic degradation progressed. The decrease in D to G band intensity ratio ( $I_D/I_G$ ) was also observed in o-MWCNT (5hr) and o-MWCNT (8hr) samples (**Figure 3-5**). It should be reminded here that in the case of SWCNT enzymatic degradation,<sup>208</sup>

the D to G band ratio increased monotonically until both bands were completely suppressed, indicating an increasing defective site abundance created during degradation. However, for p-MWCNT and o-MWCNT (5hr) samples, it was seen that the D to G band ratio increases during the first 30 days of incubation, but decreases in the next 30 days. Such an observation alludes to a more complex degradation mechanism for MWCNTs (**Scheme 3-1**).



**Scheme 3-1.** Proposed mechanism of MWCNT enzymatic degradation. Different carboxylation times result in different amounts of surface defects, which proportionally influence the rate of enzymatic degradation. The degradation on the outer layers brings more defects on to the nanotubes; while as the outer layers are exfoliated, the more pristine inner cores are gradually exposed and resistant to HRP degradation.

Unlike SWCNTs, MWCNTs have multiple graphitic layers. During the carboxylation process, the oxidative acid can create defects within the first several layers of sidewalls<sup>136</sup> and also to both ends.<sup>50</sup> These defects (oxygen functionalities) presumably provide preferable binding sites for the enzyme,<sup>168</sup> thus the degradation will start from both ends as well as the defective sites on the outer layers of sidewalls. When the outer layers undergo enzymatic

degradation, the graphitic structures are further oxidized and thus the D to G band ratio increases. However, following this further oxidation, the graphitic lattice becomes more distorted and is exfoliated from the nanotubes, forming carbonaceous residues which presumably do not have characteristic Raman bands. Thus, as the outer layers are peeled off, further Raman spectra were essentially collected on exposed inner layers. It may be that oxidative acids cannot effectively oxidize the inner layers, which would result in their more pristine structure compared to outer layers. Therefore, the D to G band ratio would decrease when the outer graphitic layers were degraded and the inner layers were exposed. In this sense, the degradation rate of all three samples would greatly slow as pristine inner layers are more resistant to enzymatic degradation. Comparing the D to G band ratios for all three samples at Day 60, we found that p-MWCNTs were the most pristine (with little influence from inner wall oxidation). This may be why the pretreated sample had the slowest degradation kinetics. Conversely, the degradation rate of o-MWCNT (8hr) was comparatively accelerated, showing an effect that degradation may have penetrated through additional walls, as the D to G band ratios progressively decreased during 60 days.

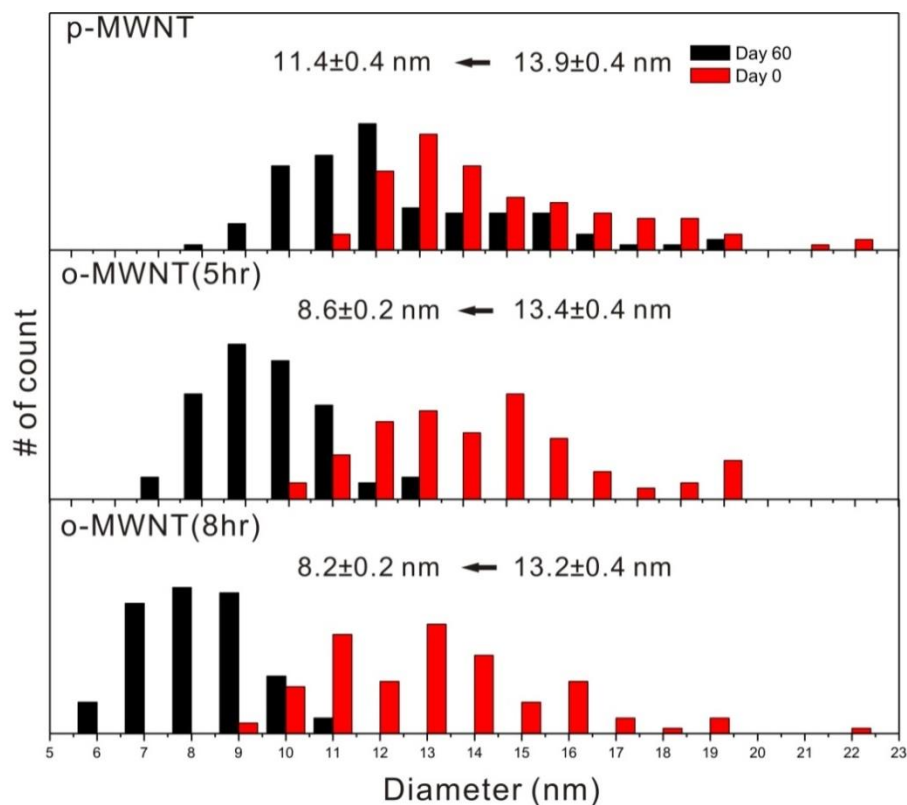


**Figure 3-6.** Comparison of the diameter distributions of MWCNTs before and after 60 days of incubation with HRP and H<sub>2</sub>O<sub>2</sub>. For each sample 100 measurements of nanotube diameters were obtained via TEM imaging. The numbers above each histogram are the corresponding average values.

While the enzymatic degradation from both ends of MWCNTs would shorten the nanotube length, as clearly shown in TEM images, the degradation from the sidewalls would cause decrease in the nanotube diameters. To verify the degradation mechanism, the diameter distributions of MWCNT samples were measured from low-resolution TEM images. For each sample before and after 60 days of degradation, 100 measurements of nanotube diameters were obtained and shown in **Figure 3-6**, with the corresponding average values listed above. Nanotube diameters from all three samples significantly decreased after 60 days of incubation from approximately 14 nm to 8 – 11 nm. This diameter decline can only be attributed to the fact

that the outer layers of MWCNTs were etched away by the enzyme. Since the interlayer spacing of MWCNTs was reported to approach 0.344 nm when the diameters are over 7 nm,<sup>17</sup> the statistical data can roughly tell the number of layers that have been oxidized. Based on the assumption of 0.688 nm in diameter reduction per layer oxidized, on average, there were approximately 3 layers degraded for the p-MWCNT samples, and 7 to 8 layers for o-MWCNT (5hr) and o-MWCNT (8hr) samples.

To better reveal structural morphology, high-resolution TEM imaging was performed on o-MWCNT (8hr) samples before and after 60 days of degradation (**Figure 3-7a, b**). The initial MWCNTs were observed with diameters around 16 nm and 13 – 14 graphitic walls; while the diameters of degraded MWCNTs reduced to around 8 nm with 5 – 6 graphitic walls. The high-resolution TEM (**Appendix A2, Figure A2-9**) also shows that there are defective sites on o-MWCNT (8hr) samples where the lattice structures within 5 – 8 outer graphitic layers were broken by the effect of oxidative acids.

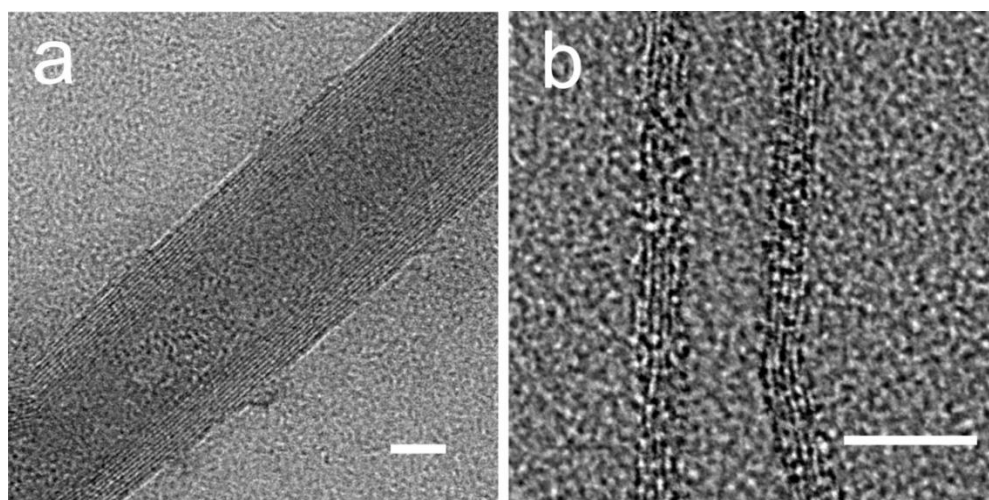


**Figure 3-7.** High-resolution TEM images taken on o-MWCNT (8hr) samples. All scale bars correspond to 5 nm. (a) o-MWCNTs (8hr) before enzymatic degradation. (b) o-MWCNTs (8hr) after 60 days of enzymatic degradation.

### 3.4.3 Enzymatic degradation of nitrogen-doped MWCNTs

The post-synthesis functionalization methods such as carboxylation with strong oxidizing agents can introduce defective sites only in outer walls, which retain the pristine inner layers that are resistant to enzymatic degradation. However, MWCNTs can also be intrinsically functionalized by doping with nitrogen atoms during the synthesis process. By introduction of nitrogen source (MeCN) into the liquid precursor, the CVD synthesis produces a tubular structure compartmented by stacked cup-shaped sections as a result of nitrogen doping. Previous research<sup>108, 142</sup> showed that the graphitic walls between two adjacent cups are not connected but extend outward unparallel to the tubular axis. As nitrogen has one more electron than carbon, the doped nitrogen atoms are not compatible to the graphitic structure and energetically prefer to stay at the open edge of the discontinuous graphitic walls forming dangling bonds.<sup>147</sup> In this case, there are nitrogen-functionalized defective sites throughout all graphitic walls in n-MWCNTs.

**Figure 3-8a** shows an n-MWCNT after purification process. Unlike MWCNTs with continuous and hollow tubular structures, the nitrogen doping causes compartmentalization in the nanotube forming small stacked cups about 40 nm in length. For enzymatic degradation, the n-MWCNT samples were incubated under the same HRP conditions as o-MWCNTs with daily addition of 800  $\mu\text{M}$   $\text{H}_2\text{O}_2$ . TEM images tracked the morphological changes of n-MWCNTs. On Day 15 (**Figure 3-8b**), the distinctive edge of the nanotubes became unidentified; the tubular structure started to be distorted, and there appeared to be carbonaceous sheets surrounding each nanotube. These results were consistent to the observations of o-MWCNTs at the initial stage of degradation. After 50 days (**Figure 3-8c**), these carbonaceous sheets were observed to spread all over the sample, with holes appearing on top of them, which indicated further degradation of the

carbonaceous sheets. However, the tubular structure was hardly observed at this stage, and they appeared to be merging into the sheets. Eventually, at Day 80, there were no tubular structures observed, and the only materials left over were some amorphous flakes. The absence of tubular structures showed a complete degradation behavior of n-MWCNTs by HRP/H<sub>2</sub>O<sub>2</sub>. Photograph images (**Figure 3-8e**) taken before and after 90 days of degradation process showed a significant disappearance of the grey color in the solution. This complete degradation of n-MWCNTs was confirmed by Raman spectroscopy (**Figure 3-8f**), which shows almost complete absence of D and G bands after enzymatic degradation.

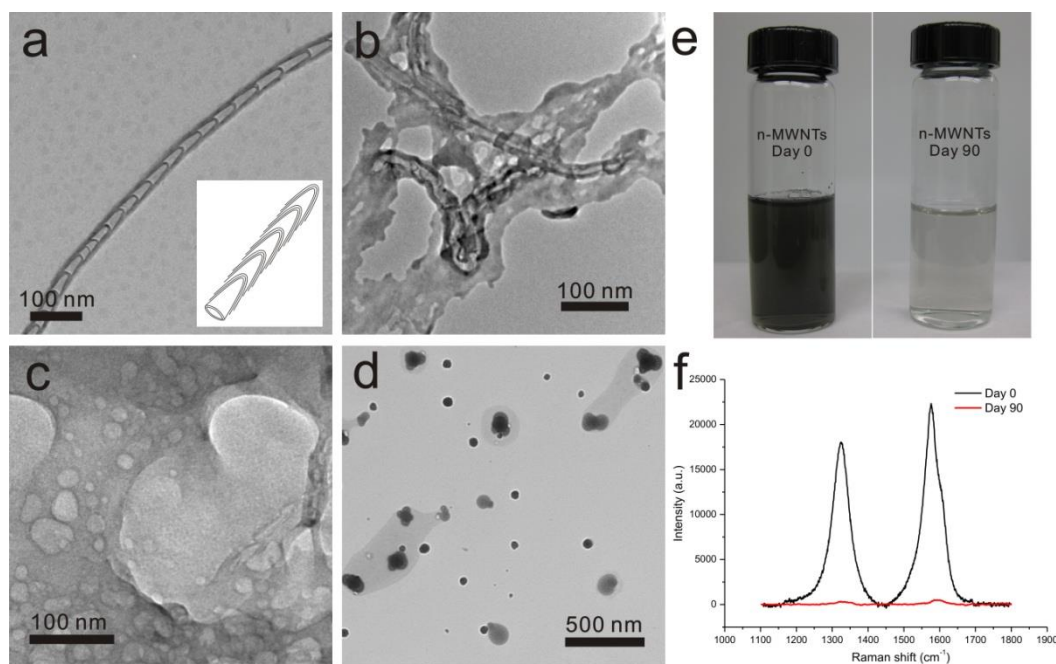


**Figure 3-8.** TEM images of nitrogen-doped MWCNT (n-MWCNT) samples during enzymatic degradation: (a) As synthesized and purified n-MWCNT at Day 0. The inset shows the schematic illustration of its stacked-cup structure. (b) Day 15, (c) Day 50, and (d) Day 80. (e) Photographs comparing n-MWCNT samples before (left) and after (right) enzymatic degradation. (f) Raman spectra for n-MWCNT samples before (black) and after (red) enzymatic degradation.

This observation showed a significant contrast to the incomplete enzymatic degradation of o-MWCNTs, further supporting the “layer-by-layer” degradation mechanism proposed above. In essence, the nitrogen doping introduces much more defects into the graphitic structure, which can be reflected from the Raman spectra (**Figure 3-8f**) because the D/G band ratio of n-MWCNTs are much higher than that of o-MWCNTs. Since nitrogen was doped in situ during the synthesis process, these defective sites not only exist in the outer graphitic layers, but are present in all graphitic walls. These nitrogen functionalized defects are then assumed to provide binding sites for HRP enzyme throughout the whole process leading to complete degradation.

It should be noted here that the as-synthesized n-MWCNTs were subject to a purification process with HCl and H<sub>2</sub>O<sub>2</sub> in order to reduce the content of iron impurities. Thermogravimetric analysis (TGA) taken on the samples before and after purification showed that there was a considerable decrease in the iron content after purification, although the left-over iron content was still significant (**Appendix A2, Figure A2-10**). It is possible that the residual iron impurities may cause a Fenton catalytic oxidation<sup>168</sup> of n-MWCNTs and influence the result of enzymatic degradation. In a control experiment, we replaced the HRP by 1×10<sup>-4</sup> M FeCl<sub>3</sub> aqueous solution with daily addition of the same amount of H<sub>2</sub>O<sub>2</sub>, in order to observe the Fenton oxidation effect on n-MWCNTs. However, after 80 days of incubation, there were still a considerable amount of nanotubes present from TEM images (**Appendix A2, Figure A2-10b**), which showed that the Fenton oxidation may have much slower degradation kinetics on n-MWCNTs than HRP. Thus, the effect of iron impurities on HRP/H<sub>2</sub>O<sub>2</sub> enzymatic degradation was minor.

### 3.5 CONCLUSIONS

In this study, the enzymatic degradation of carboxylated MWCNTs and nitrogen-doped MWCNTs was investigated in the presence of HRP and H<sub>2</sub>O<sub>2</sub>. Different degrees of carboxylation were achieved by controlling the time of oxidative acid treatment, and the resultant degradation rate was associated with the degree of carboxylation on MWCNTs, which further supported the fact that it is the hydrophilic interaction between HRP's heme active site and the oxygen-containing defective sites on nanotubes that causes the nanotubes to be oxidized and degraded, as we investigated in our previous work.<sup>168</sup> The degradation is confirmed by monitoring the evolution of CO<sub>2</sub> gas as a final oxidation product by GC-MS. Furthermore, because of their multi-layer graphitic structures, the MWCNTs are more resistant to HRP degradation and it takes a significantly longer time to degrade MWCNTs than SWCNTs in the same experimental conditions. The fact that MWCNTs with reduced diameters and lengths remained over 80 days of degradation leads to a layer-by-layer mechanism of degradation revealed by TEM and Raman spectroscopy. The degradation of MWCNTs is taking place on the defective sites of outer graphitic walls which are exfoliated layer-by-layer leaving the pristine inner walls more resistant to HRP oxidation. In contrast to carboxylated MWCNTs, nitrogen-doped MWCNTs, having intrinsic nitrogen-functionalized defective sites in all graphitic walls, showed complete enzymatic degradation within 80 days, which well supported the proposed mechanism.

### **3.6 ACKNOWLEDGEMENT**

The project described was supported by Award Number R01ES019304 from the National Institute of Environmental Health Sciences. The content is solely the responsibility of the authors and does not necessarily represent the official views of the National Institute of Environmental Health Sciences or the National Institutes of Health. The authors thank Tom Harper and NCF for the provision of access to the instruments.

## 4.0 NANO-GOLD CORKING AND ENZYMATIC UNCORKING OF CARBON NANOTUBE CUPS

### 4.1 CHAPTER PREFACE

The previous chapter provided fundamental understanding of the degradative behavior of MWCNTs in the presence of HRP and H<sub>2</sub>O<sub>2</sub>. In this chapter, we extended our degradation study to a more practical and physiological-relevant situation by monitoring the degradation of GNP-corked NCNCs under a more potent mammal peroxidase – human myeloperoxidase (hMPO).

Derived from nitrogen-doped carbon nanotubes, the unique stacked cup-shaped hollow compartments, termed as nitrogen-doped carbon nanotube cups (NCNCs), have promising potential as nanoscale containers. In this work, individual NCNCs are effectively isolated out from their as-synthesized stacked structure by a combination of acid oxidation and probe-tip sonication. Based on the intrinsic localized nitrogen functionalities, we managed to effectively cork the NCNCs with gold nanoparticles (GNPs) grown in situ by sodium citrate reduction of chloroauric acid, which formed a graphitic nanocapsule confined with GNP “stoppers”. Mechanistically, the growth of the GNP corks starts from the nucleation and welding of gold seeds on the open rims of NCNCs enriched with nitrogen functional groups. Quantitatively, this mechanism is in good agreement with density functional theory (DFT) calculations. A potent oxidizing enzyme of neutrophils, myeloperoxidase, effectively opened the corked NCNCs through GNP detachment, with subsequent complete enzymatic degradation of the graphitic

shells. This controlled opening and degradation was further carried out in vitro with human neutrophils, which alludes to new strategies in drug delivery applications based on GNPs-corked NCNCs.

The material in this section contains a manuscript submitted for publication.

**List of Authors:** Yong Zhao, Yifan Tang, Dan C. Sorescu, Alexander A. Kapralov, Valerian E. Kagan, and Alexander Star

**Author Contributions:** YZ and AS conceived and designed the experiments; YZ carried out the experiments; YZ and YT performed the characterization; DS led the theoretical study; AK and VK performed the cellular study; YZ and AS analyzed the data and wrote the manuscript.

## 4.2 INTRODUCTION

Because of their enhanced permeability and retention effect in tumor cells,<sup>253-254</sup> the emerging use of nanocarriers such as liposomes, nanoparticles and macromolecules has exhibited compelling promises in drug delivery applications,<sup>255-257</sup> providing fundamental advantages such as longer circulation time, lower immunogenicity, better biocompatibility, and selective targeting.<sup>258-260</sup> In particular, given their nanoscale dimensions and versatile reactivities, carbon nanomaterials such as carbon nanotubes (CNTs) and graphenes have received increasing research attention for drug delivery.<sup>48, 50-51</sup> Drugs loaded on the outer surface of CNTs via covalent<sup>9</sup> or noncovalent<sup>77</sup> functionalization risks unnecessary exposure causing side-effects or

early drug degradation.<sup>261</sup> Comparatively, filling the drugs in the hollow interior of nanotubes is more desirable in terms of protecting drugs before reaching the target.<sup>53, 262-263</sup> Accordingly, nitrogen-doped carbon nanotube cups (NCNCs), a cup-shaped carbon nanostructure derived from nitrogen-doped CNTs, may serve as ideal drug delivery carriers: Their small sizes ranging from 50 – 200 nm may exhibit a delayed rate of bloodstream clearance by the mononuclear phagocytic system (MPS),<sup>182, 223</sup> and their unique morphology allows easy access to both inner and outer surfaces for diverse functionalization.<sup>105, 165, 167</sup>

Being well recognized for their oxygen-reduction catalytic activity,<sup>113, 150-151</sup> as-synthesized NCNCs consist of cup-shaped compartments stacked up via van der Waals interactions,<sup>160</sup> which can be readily separated into individual nanocups via various methods.<sup>105, 161-162, 167</sup> Recently, we found that a combination of pre-oxidation and high-intensity probe-tip sonication greatly improved the efficiency of separation which yielded mostly individual hydrophilic nanocups.<sup>140</sup> Due to the intrinsic nitrogen functionalities localized at the cup opening, the separated NCNCs show strong affinity to gold nanoparticles (GNPs) in aqueous solution, which preferentially “cork” the opening of nanocups, forming self-confined nanocapsules. The hydrophilic surfaces of NCNCs after oxidation impede adsorption of opsonin proteins, which may inhibit early phagocytotic removal and ensure prolonged blood circulation for NCNCs,<sup>264</sup> leading to promising drug delivery applications.

Despite the preferred confined morphology for drug delivery, strategies need to be sought to trigger the opening of the nanocapsules for potential release of their cargo, typically under stimuli involving chemicals, pH, or light.<sup>76, 217, 265</sup> On the other hand, the nanocarriers should be subject to clearance after delivery to mitigate their potential in vivo toxicity, especially for carbon nanomaterials,<sup>169, 173</sup> although the nitrogen-doped CNTs were found to be more

biocompatible than undoped single- or multi-walled CNTs.<sup>154, 220</sup> Naturally existing peroxidases, such as horseradish peroxidase (HRP) and myeloperoxidase (MPO) in combination with hydrogen peroxide ( $H_2O_2$ ), can act as strong oxidation agents to enzymatically degrade carbon nanomaterials such as single- and multi-walled CNTs and graphenes in vitro or in vivo.<sup>167-168, 205-206, 208</sup> In this work, human MPO (hMPO) was applied to degrade the GNP-corked NCNCs in the presence of  $H_2O_2$  and NaCl, which built a stronger enzymatic oxidation system via both peroxidase cycle.<sup>169, 208</sup> Interestingly, we found that at the initial stage of degradation, the enzyme triggered the release of GNP corks from the nanocups, which actively opened the cups, followed by a complete degradation of NCNC shells within a course of 20 days. Such triggered opening of corked nanocups was also observed in presence of human neutrophils, a type of leukocytes capable to release MPO upon activation during the inflammatory response.<sup>210</sup> These findings may lead to an innovative drug release scheme carried out by the innate immune system, which may find potential applications for treating acute/chronic inflammation, where antibiotics and/or protection agents can be delivered upon the enzymatic release triggered by activated immune cells.<sup>266</sup>

## **4.3 EXPERIMENTAL SECTION**

### **4.3.1 Synthesis of separated NCNCs**

The stacked NCNCs were synthesized using chemical vapor deposition (CVD) methods from a liquid precursor consisting of 10.0 wt % of acetonitrile, 0.75 wt % of ferrocene and 89.25 wt % of xylenes.<sup>105</sup> To perform NCNC separation, 10 mg of the as-synthesized material was dispersed

into 40 mL of 3:1 (v/v) H<sub>2</sub>SO<sub>4</sub>/HNO<sub>3</sub> in a round bottle flask. The mixture was sonicated in a water bath sonicator for 4 h at room temperature, then diluted with water and washed repeatedly with 0.01 M NaOH, 0.01 M HCl, and water. The oxidized NCNCs in water were then sonicated for 8 h at a probe-tip ultrasonicator (Qsonica Q500) equipped with a ½” probe. The solution was centrifuged at 4000 – 8000 rpm for 15 min, and the supernatant was collected and filtered through 200-nm-pore PTFE membrane. The filtrate containing short separated NCNCs were obtained.

#### **4.3.2 Corking of NCNCs with GNPs**

250 µL of HAuCl<sub>4</sub> aqueous solution (1 mg/mL) was added into 5 mL of ~0.01 mg/mL separated NCNC aqueous solution when stirring on a hot plate at 70 °C. After 20 min of incubation, 150 µL of 1 wt % trisodium citrate solution was added dropwise and the reaction was stirred for another 2 h. GNP/NCNC conjugates were precipitated from free GNPs by centrifugation at 3400 rpm for 15 min.

#### **4.3.3 Enzyme-triggered opening and degradation of GNP-corked NCNCs**

The separated NCNCs with or without GNPs were dispersed at a concentration of 0.015 mg/mL into 0.01 M phosphate buffer solution in a total volume of 1000 µL. The enzymatic degradation was conducted following published procedure.<sup>208</sup> To the NCNC sample, NaCl at a concentration of 1 µM is added on the initial day; Lyophilized purified native human MPO (Athens Research and Technology, Inc.) is added daily at a concentration of 8.35 µg/mL; 1 µL of 100 mM H<sub>2</sub>O<sub>2</sub> is added every 2 h, four times per day. For the NaClO control experiment, 1 µL of 100 mM NaClO

was added every 2h, four times per day in absence of hMPO and H<sub>2</sub>O<sub>2</sub>. For the H<sub>2</sub>O<sub>2</sub> control experiment, 1  $\mu$ L of 100 mM H<sub>2</sub>O<sub>2</sub> was added every 2 h, four times per day in absence of hMPO, NaCl, and NaClO. The hMPO/H<sub>2</sub>O<sub>2</sub> control was the same as the active sample but without NaCl. All samples were incubated at 37 °C for 20 days, with daily agitation by vortex shaker for better dispersion.

#### **4.3.4 Neutrophils isolation and incubation with nanocups**

Human neutrophils were isolated by a procedure utilizing Histopaque (Sigma, St. Louis, MO, USA). Briefly, human buffy coat (Central blood bank, Greentree, PA, USA) was mixed with 6% Dextran T-500 in phosphate-buffered saline (PBS) in ratio 5:1 and allowed to sediment for 30 min at room temperature. The leukocyte-rich plasma (top layer) was aspirated, diluted two times with PBS, layered over Histopaque solution with density 1.077 g/ml (Sigma, St. Louis, MO, USA) and subjected to centrifugation (700 g for 45 min at room temperature without brake). The pellet containing neutrophils was collected and contaminated erythrocytes were removed by hypotonic lysis with ice-cold water. Neutrophils were washed twice with calcium and magnesium free PBS; and suspended in RPMI-1640 without phenol red, containing 10% fetal bovine serum in concentration  $10 \times 10^6$  cells/ml. 50  $\mu$ g of nanocups incubated with purified human IgG (Invitrogen, Carlsbad, USA) in 1:1 ratio (w/w) for 18 hrs at 37 °C were incubated with neutrophils ( $25 \times 10^6$ ) for 16 hrs and the extent of biodegradation was assessed.

#### **4.3.5 hMPO contents in cells and its release**

Levels of hMPO in cells were determined by ELISA kit (Alpco Diagnostics, NH, USA) after 30 min incubation with samples. Neutrophils were centrifuged at 1000 g for 10 min. The supernatant and pellet were obtained and used separately for hMPO measurements according to the manufacturer's manual. The amounts of hMPO were expressed as mg/mL.

#### **4.3.6 Characterization**

TEM at lower resolution was performed with FEI Morgagni microscope at an accelerating voltage of 80 kV. High-resolution TEM was on JEOL 2100F microscope with 200 kV accelerating voltage. Samples were dropcasted on a lacey carbon TEM grid. The cell samples were first subjected to a protease k digest. Raman spectra were taken on Renishaw inVia Raman microscope with an excitation wavelength of 633 nm and 10 second exposure time. XPS was performed on a Thermo Scientific K-Alpha using monochromated Al Ka x-rays as the source. UV-Vis spectroscopy was carried out on a Perkin-Elmer Lambda 900 spectrometer. EDX spectroscopy was performed on a Phillips XL30 FEG microscope equipped with an EDAX assembly. DLS was performed using a quasi-elastic light scattering spectrometer (Brookhaven 90 Plus Particle Size Analyzer).

#### 4.4 RESULTS AND DISCUSSION

The stacked NCNCs were synthesized following a modified chemical vapor deposition (CVD) method from a mixture of acetonitrile, ferrocene, and xylenes,<sup>105</sup> which were then effectively separated through acid oxidation and subsequent probe-tip sonication (**Figure 4-1a**).<sup>140</sup> The separated NCNCs consist of mostly individual and short stacks of nanocups between 80 – 200 nm in length as revealed by transmission electron microscopy (TEM) imaging (**Figure 4-1b**) and dynamic light scattering (DLS) measurements (**Appendix A3, Table A3-1**). A typical individual NCNC has a cup-shaped morphology with an open interior of ~30 nm in diameter. The oxidation and sonication left the separated NCNCs with higher levels of graphitic defects as reflected by Raman spectroscopy (**Appendix A3, Figure A3-1**), which lead to their hydrophilic nature.

The intrinsic nitrogen functionalities are preferentially located at the open rim of the separated nanocups, preventing them from further growth during CVD synthesis<sup>145</sup> and providing reactive sites for further functionalization.<sup>105</sup> The separated NCNCs form stable water dispersion for months, allowing the growth of GNPs directly on the nanocups by sodium citrate reduction. Briefly, chlorauric acid was first mixed with NCNCs aqueous suspension for 20 min, and sodium citrate was then added to the reaction mixture at 70 °C. Upon removal of free GNPs by centrifugation, elemental analysis from energy-dispersive X-ray (EDX) spectroscopy confirmed the existence of Au on NCNCs (**Appendix A3, Table A3-2**). TEM images show that almost every nanocup was evenly decorated with 1–2 GNPs of about 30 nm in diameter. A large proportion of the GNPs was found bound to the open end of the nanocups, which effectively form stoppers corking the cups (**Figure 4-1c**). Once bound to the rim of the cups, the GNPs appear to adapt the shape of the opening seamlessly and completely seal their interior space, as shown by high-resolution TEM image (**Figure 4-1d**). High-resolution TEM images reveal the

polycrystalline nature of the GNP cork with lattice distance of 0.23 nm corresponding to gold (111) surfaces, which suggest that the GNP corks are resulted from the welding of many fcc gold nanocrystals (**Appendix A3, Figure A3-2a**).<sup>267-268</sup>

The UV-Vis absorption spectra of separated NCNCs show a characteristic peak located at 260 nm (**Figure 4-2a**), corresponding to the  $\pi$  electron plasmon band in conjugated systems.<sup>93</sup> After GNP growth, the reaction mixture turned from brown to red and the NCNC/GNP conjugates were collected by centrifugation. There is a distinct color difference between the red supernatant and the purple precipitate suspensions, which is confirmed by the red-shift of the gold surface plasmon resonance (SPR) band from 526 nm to 537 nm (**Figure 4-2a**). This red-shift may be due to both the size difference (**Appendix A3, Figure A3-3**) and the direct electronic interaction between the GNPs and the NCNC substrate.<sup>105</sup> The presence of GNPs on NCNCs causes strong surface-enhanced Raman scattering (SERS) effect, allowing sensitive detection of this hybrid material by Raman spectroscopy in biological samples. **Figure 4-2b** shows the Raman spectra of NCNCs decorated with GNPs compared with unfunctionalized NCNCs. Enhancements of about 15 and 18 fold were noticed for the intensities of D ( $\sim 1350\text{ cm}^{-1}$ ) and G ( $\sim 1582\text{ cm}^{-1}$ ) bands, respectively. We speculate that the SERS effect is mainly originated from the charge transfer between GNPs and NCNCs,<sup>103</sup> due to the electronic interaction between GNPs and NCNCs. By mixing NCNCs with commercial citrate-coated GNPs, in which GNPs are physically adsorbed on NCNCs without direct contact (**Appendix A3, Figure A3-4**), the SERS effect was not observed (**Figure 4-2b**). On the other hand, the functionalization of GNPs is more favorable on nitrogen-doped graphitic structure. Undoped multiwalled CNTs treated by the same procedure did not bind effectively to GNPs (**Appendix A3, Figure A3-5**).

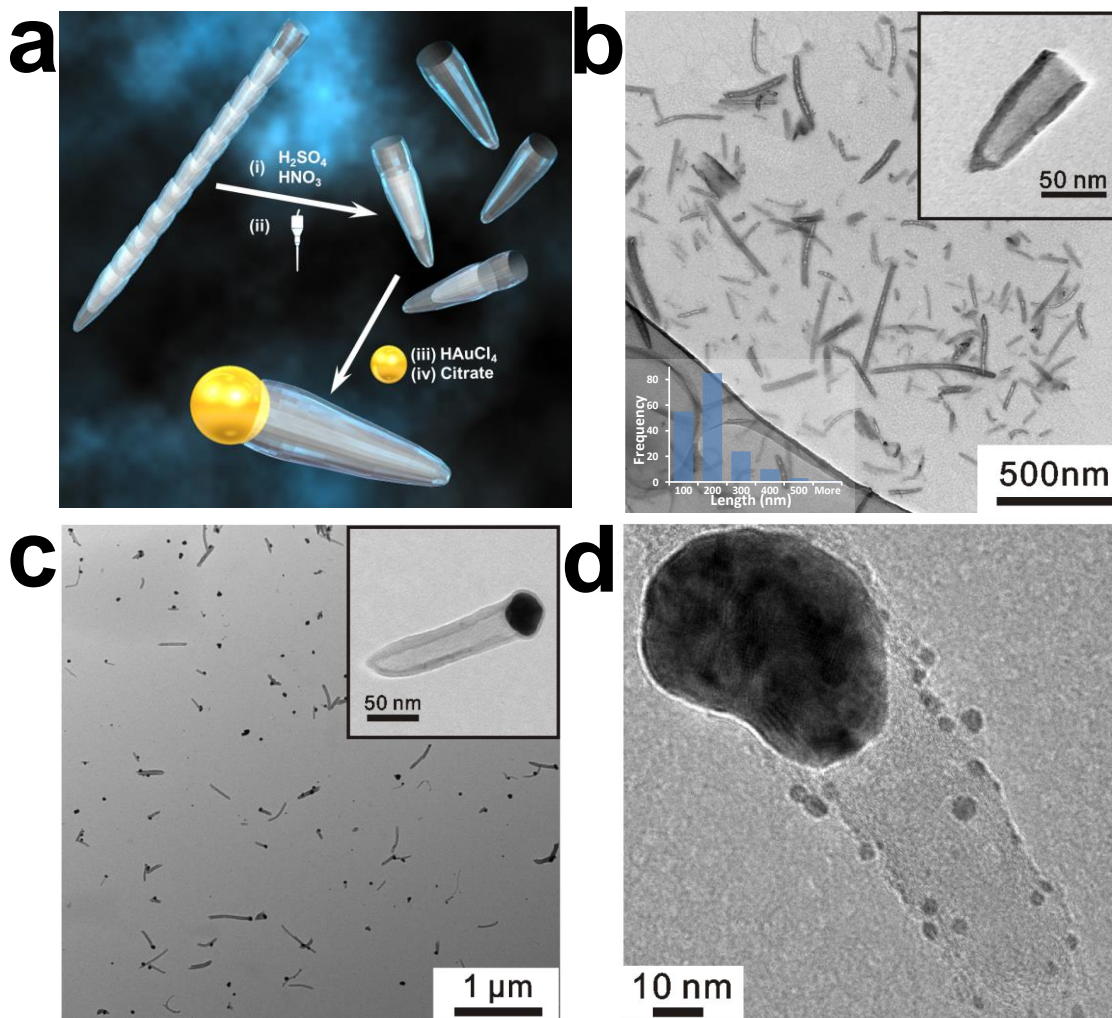


**Figure 4-1.** (a) Separation and corking of NCNCs with gold nanoparticles (GNPs) by (i) acid oxidation with  $\text{H}_2\text{SO}_4/\text{HNO}_3$ , (ii) probe-tip sonication, (iii) incubation with  $\text{HAuCl}_4$  and (iv) sodium citrate reduction. (b) Transmission electron microscopy (TEM) images of separated NCNCs. The upper right inset shows a magnified TEM image of an individual nanocup, the lower left inset shows the length distribution of the separated cups. (c) TEM images of separated NCNCs functionalized with GNP corks. The inset shows the TEM image of an individual nanocup corked by a GNP on the opening. (d) High-resolution TEM image of the corked GNP/NCNC structure.

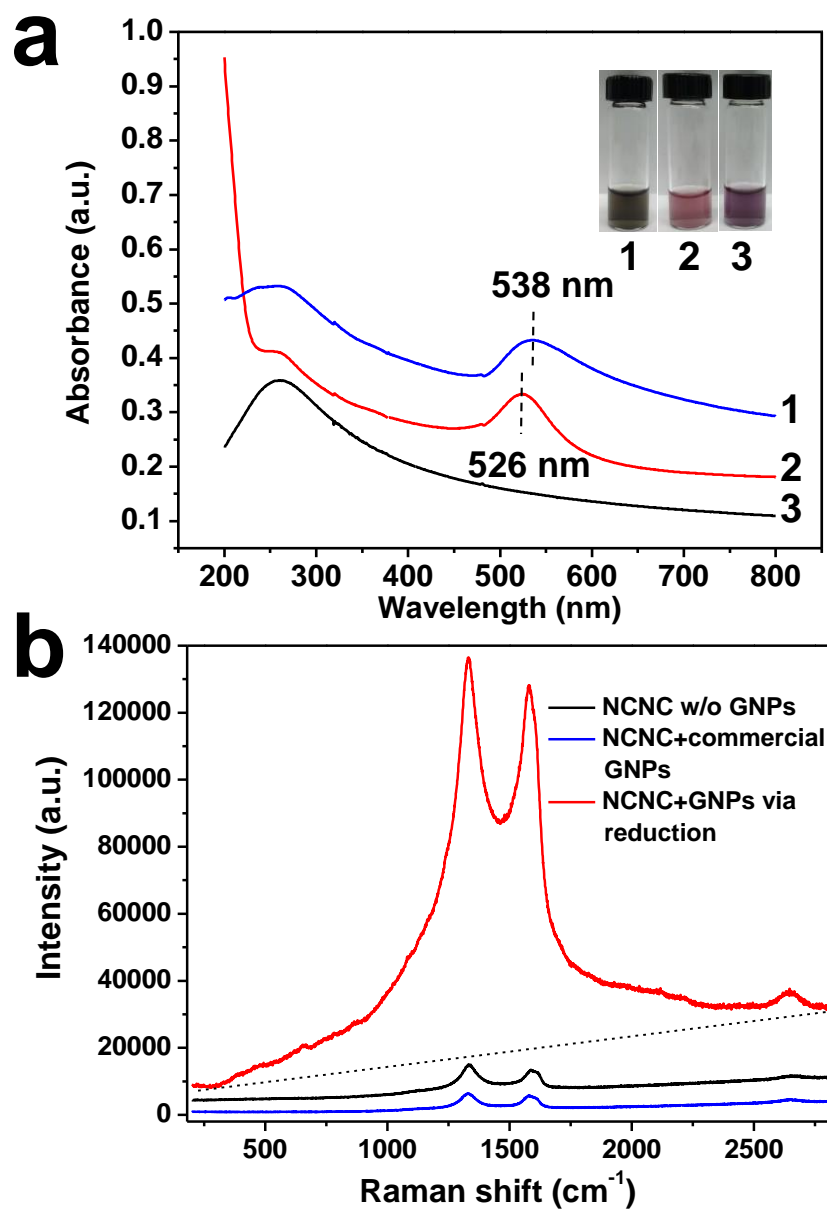


**Figure 4-2.** (a) UV-Vis absorption spectra and photograph of aqueous suspensions of separated NCNCs (1), supernatant (2) and precipitate (3) of NCNC/GNP conjugates after centrifugation. (b) Raman spectra of separated NCNCs (black), NCNCs mixed with commercial GNPs (blue), and NCNCs corked with GNPs by in situ reduction process (red). The dotted line indicates the baseline.

#### 4.4.1 Growth mechanism of GNP corks on NCNCs

In order to understand the mechanism of the GNP cork formation, the chemical structure of nitrogen present in separated NCNCs was characterized by X-ray photoelectron spectroscopy (XPS) (**Appendix A3, Figure A3-6**). Nitrogen was detected at about 1 – 2 at.% on the surface of NCNCs. The high-resolution profiles of nitrogen peak were fitted into different components with a Gaussian/Lorentzian ratio of 80:20. The N1s profile indicates the existence of functionalities such as pyridinic, pyrrolic, amine, and oxidized nitrogen. Before GNP functionalization, the nitrogen 1s profile can be deconvoluted to 5 peaks, 4 of which can be assigned as pyridinic (398.6 eV), pyrrolic (399.8 eV), amine (400.8 eV), and oxidized nitrogen (405.8 eV), according to existing literature.<sup>105, 229, 269-270</sup> The origin of peak N4 at 402.1 eV is debated. We assign this peak to protonated amine groups ( $-\text{NH}_3^+$ ),<sup>269</sup> because amine groups may be partially protonated after the acid treatment process. After GNP functionalization, the peak at 402.1 eV disappeared, along with the appearance of the graphitic nitrogen peak at 401.2 eV,<sup>233, 271</sup> and the outshooting of the amine peak. We suspect that the amine groups were deprotonated during the GNP reduction, likely due to the interaction with gold salt and citrate. There is a slight decrease in the binding energy of nitrogen species after GNP function, indicating potential electronic interaction between gold and nitrogen functionalities. The change of amine groups alludes to the initial binding sites of GNPs on NCNCs. We speculate that the growth of the GNP corks begins with a nucleation step on the open rims enriched with amine groups, followed by subsequent growth under citrate reduction. Presumably, during the initial incubation, the gold precursor  $\text{AuCl}_4^-$  was first electrostatically bound to the  $-\text{NH}_3^+$  groups, and then reduced by the graphitic network, leading to further oxidation of carbon (**Appendix A3, Figure A3-6**) and deprotonation of amines.

The growing process of the GNP corks was examined by TEM of the reaction mixture sampled at different reaction times (**Figure 4-3a-d**). The initial gold nucleation on the open rim and the subsequent welding of adjacent GNP seeds are observed during the first 20 min of reaction. After addition of sodium citrate to the reaction mixture, the formation of GNPs was further accelerated. After 50 min, the agglomeration of GNP seeds on the opening of nanocups has occupied the entire rim, which eventually leads to the formation of molded GNP corks after 80 min of reaction. The corresponding UV spectra during the reaction show the appearance of the gold SPR band after 50 min, with a gradual red-shift indicating the increasing size of GNPs (**Appendix A3, Figure A3-7**).

The observed nucleation of GNP seeds on the NCNC openings and subsequent growth into GNP corks was further supported by first principles calculations (**Appendix A3, Computational Methods**). We simulated the initial stage of the nucleation process for the case of a Au<sub>20</sub> cluster adsorbed initially either at the center or at the edge of a 7×11 graphene flake functionalized with different nitrogen functional groups (**Appendix A3, Figure A3-8**). By comparing the adsorption energy at the most stable binding configurations, we found that the graphene edge functionalized with an aliphatic primary amine (–CH<sub>2</sub>NH<sub>2</sub>) incurred the strongest binding with Au<sub>20</sub>. In this case, the –CH<sub>2</sub>NH<sub>2</sub> group is extruding out of the graphene plane such that the lone electron pair from N is unconjugated and forms a covalent bond with the Au<sub>20</sub> cluster (**Figure 4-3e**). Since the existence of aliphatic amine groups on separated NCNCs is confirmed by both XPS and Kaiser test,<sup>105, 140</sup> the anchoring effect of amine groups explains the nucleation mechanism during GNP growth. The energy plot in **Figure 4-3e** shows the minimum energy reaction pathways of the Au<sub>20</sub> cluster migrating from the central region of the graphene flake toward the edge where it gets bonded with a –CH<sub>2</sub>NH<sub>2</sub> group. The reaction profile

demonstrates that anchoring of Au<sub>20</sub> cluster mediated by this group is highly favorable and the barriers involved are very small (< 0.5 kcal/mol). In addition, when a given Au<sub>20</sub> cluster is already bonded with the -CH<sub>2</sub>NH<sub>2</sub> group, another Au cluster can easily diffuse toward it and becomes bonded with formation of a larger cluster through a nanowelding process (**Figure 4-3f**).<sup>267</sup> This cumulative effect eventually leads to formation of large GNPs preferentially on the opening of the NCNCs, where the graphitic edges are enriched with amine groups.

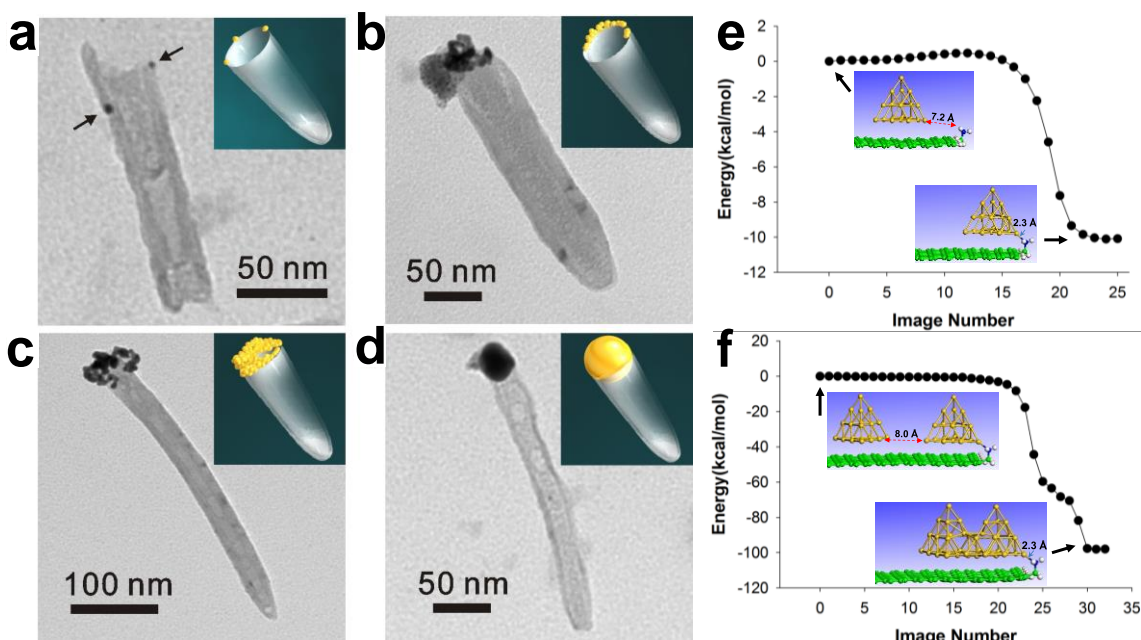


**Figure 4-3.** (a) – (d), TEM images of the growth process of GNPs on individual NCNCs sampled at (a) 5 min, (b) 20 min, (c) 50 min, and (d) 80 min after the addition of HAuCl<sub>4</sub>. Sodium citrate was added at 20 min right after sampling. The arrows in (a) show the nucleation of gold seeds. (e), (f), Minimum energy reaction pathways for diffusion of Au<sub>20</sub> cluster from the central region of the (7×11) graphene flake surface toward the zigzag edge (e) decorated with a CH<sub>2</sub>NH<sub>2</sub> group and (f) when a second Au<sub>20</sub> cluster is anchored to the -CH<sub>2</sub>NH<sub>2</sub> group at the graphene edge. For both sets of pathways the initial and final configurations are represented in the inset panels. Legend of atoms: C, green; N, blue; H, white; O, red; and Au, orange.

#### 4.4.2 Enzyme-triggered uncorking and degradation of GNP/NCNCs

While the confinement of interior with GNP corks endows the nanocups with potential as drug delivery carriers, the enzymatic degradation ensures the subsequent optimized release of the payloads and clearance of the nanocup shells for improved biocompatibility. The stacked nitrogen-doped CNTs were previously shown to undergo a slow degradation by plant HRP/H<sub>2</sub>O<sub>2</sub> initiated at the defect sites on graphitic surface over the period of 90 days.<sup>206</sup> Using a biomedically more relevant oxidative enzyme hMPO, we hereby examined the degradation of separated NCNCs. The separated NCNCs were dispersed in phosphate buffer solution containing 1 mM NaCl, which is necessary for producing NaClO in the halogenation cycle. With daily supplement of MPO and H<sub>2</sub>O<sub>2</sub>, the separated NCNCs were seen gradually degraded within 20 days, as evidenced by the morphological deformation from TEM images, and the suppression of their UV-Vis and Raman characteristic peaks (**Appendix A3, Figure A3-9**). On the other hand, with only NaClO as oxidant, incomplete degradation was observed during the 20-day timeframe (**Appendix A3, Figure A3-10**), which indicates that the synergetic effect of peroxidase cycle and halogenation cycle is important to expedite the degradation of NCNCs.<sup>208</sup> As the control, without hMPO or NaClO as oxidants, only H<sub>2</sub>O<sub>2</sub> did not incur any significant degradation of NCNCs (**Appendix A3, Figure A3-11**).

Interestingly, when the NCNCs were corked with GNPs, we found that the hMPO not only degraded the graphitic shell, but also triggered the opening of nanocups by releasing the GNP corks at the early stage of incubation. The initial GNP/NCNC sample was centrifuged several times to ensure the removal of free GNPs. With daily additions of hMPO and H<sub>2</sub>O<sub>2</sub> to the sample in the presence of NaCl, TEM images show that most of the GNPs were detached from NCNCs within the first 5 days of degradation (**Figure 4-4a**). Subsequently, the NCNCs

underwent significant degradation after releasing the GNP corks and eventually vanished after 20 days (**Figure 4-4b,c**), leaving only agglomerations of GNPs. UV-Vis spectra in Figure 4b show the similar trend of disappearing  $\pi$  electron band within 15 days of degradation (**Figure 4-4d**). Notably, the SPR band from GNPs was observed to gradually red-shift from initial 538 nm to 561 nm. We infer that this red-shift is due to the agglomeration of free GNPs detached from NCNCs, because the GNP corks are not entirely coated with citrate leaving bare active surfaces that can easily weld with each other.<sup>267</sup> Once detached, the GNPs failed to induce surface-enhanced Raman effect on NCNCs. The Raman spectra of the degradation sample show a drastic decrease of D and G band intensities within the first 2 days of degradation, followed by a slower decrease afterward until a complete suppression (**Figure 4-4e**). However, when the degradation was carried out in the NaClO-only sample, the GNP corks largely remained attached on the nanocups without apparent agglomeration, till most nanocups were degraded (**Appendix A3, Figure A3-12**). The attachment of GNPs on the NCNCs was evidenced by the absence of red-shift in their SPR bands, as well as a strong lasting SERS effect within the first 5 days of degradation. When the GNP/NCNCs were incubated with only H<sub>2</sub>O<sub>2</sub>, no significant detachment of GNPs or degradation of NCNCs was observed (**Appendix A3, Figure A3-13**).

The different behaviors of the GNP/NCNC conjugates under different degradation conditions were monitored by the intensity plot of the G band from Raman spectra (**Figure 4-4f**). Each data point was averaged from five Raman spectra at different spots and normalized to the initial intensity. Two decreasing stages are distinguished in the hMPO/H<sub>2</sub>O<sub>2</sub>/NaCl sample: The first fast-decaying stage corresponds to the detachment of GNPs from NCNCs when they mostly aggregated and lost the direct interaction with NCNCs. The second stage reflects the actual degradation of nanocups, which shows a slower but complete decay within 20 days. In contrast,

the intensity plot in the NaClO sample shows a slower and more constant decreasing slope throughout the 20 days, largely due to the loss of graphitic structure instead of GNP detachment. The plot in the H<sub>2</sub>O<sub>2</sub> control remains stable during the experiment, indicating that the GNP/NCNC conjugate is stable under physiological conditions. The Raman plots confirm that the interaction with hMPO uniquely triggers the dissociation of GNPs from NCNCs, which is not due to simple oxidation of the graphitic shell. We speculate that the detachment of GNPs is caused by the strong binding of hMPO toward the defective sites of NCNCs during the peroxidase cycle and the interaction with negatively-charged GNPs,<sup>208</sup> with corresponding weakening of the interaction between GNPs and nanocups. On the other hand, the ClO<sup>-</sup> produced in the halogenation cycle is a strong oxidant that oxidizes the whole graphitic framework with no preferential binding sites<sup>272</sup> and has limited effect on GNPs. To prove the uncorking effect from the peroxidase cycle, we incubated the GNP/NCNCs in the presence of hMPO and H<sub>2</sub>O<sub>2</sub> and in the absence of NaCl. It turned out that the GNPs were readily detached from NCNCs during the first 5 days, inducing a red-shift of the SPR band and a sudden drop of Raman intensity, while the NCNCs were not significantly degraded throughout the 20 days (**Appendix A3, Figure A3-14**).

The hMPO-triggered uncorking and degradation of GNP/NCNCs was further studied in vitro with human neutrophils, a type of immune cells primarily involved in inflammatory responses and MPO generation.<sup>169</sup> Using ELISA kit, we found that neutrophils contained 1.8 mg hMPO per 10<sup>6</sup> neutrophils. Upon neutrophil activation, 75% of the total hMPO remained inside the cells and only 25% of the amount of enzyme was released into extracellular environment. The neutrophils were administered with 50 µg GNP-corked NCNCs opsonized with IgG. The cells were then dissolved with sodium dodecyl sulfate (SDS) for analysis. After 18 h of

incubation at 37 °C, TEM image shows that most GNPs were detached from NCNCs and aggregated with each other (**Figure 4-5a**). Hints of degradation were observed on NCNCs as the graphitic surfaces started to be deformed. Comparatively, when the GNP-NCNCs were mixed with neutrophils which were directly collected without incubation, no signs of either GNP detachment or NCNC degradation were shown (**Appendix A3, Figure A3-15a**). Among ~100 NCNCs observed from different TEM images, the percentage of NCNCs decorated with GNPs is significantly reduced after the 18 h incubation (**Figure 4-5b**), suggesting that human neutrophils can effectively uncork the cups in vitro. Raman spectra (**Appendix A3, Figure A3-15b**) and the Raman intensity mapping (**Figure 4-5c,d**) on the G-bands further confirmed the detachment of GNPs. The cell residues without incubation show strong signals of the nanocups due to the enhancement from the GNPs, appearing as bright yellow spots in the optical image (**Figure 4-5c**); while in the sample after 18 h incubation, the signals from nanocups are greatly suppressed. These data indicate that the reactive MPO intermediates generated by neutrophils during the cellular inflammatory response may trigger the release of drug cargo in the potential nanocup drug delivery system.

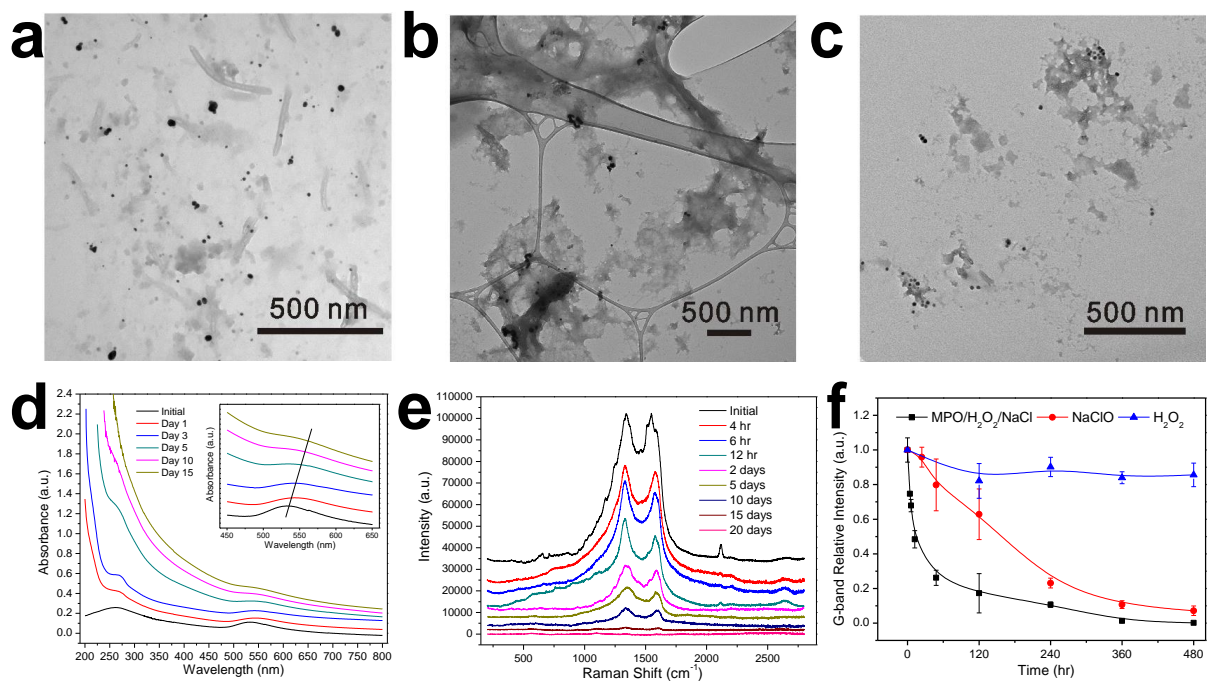


**Figure 4-4.** (a) – (c), TEM images of the degradation process of NCNCs corked with GNPs under hMPO/H<sub>2</sub>O<sub>2</sub>/NaCl at (a) Day 5, (b) Day 10, and (c) Day 20 after incubation. (d) UV-Vis absorption spectra and (e) Raman spectra of the sample during the degradation process. The inset in (d) shows the red-shift of the GNP surface plasmon resonance (SPR) band. (f), Intensity plots of the Raman G bands from the sample (black), the NaCl control (red), and the H<sub>2</sub>O<sub>2</sub> control (blue). The intensity was averaged and normalized to the initial value and the error bars correspond to the standard errors of the mean.

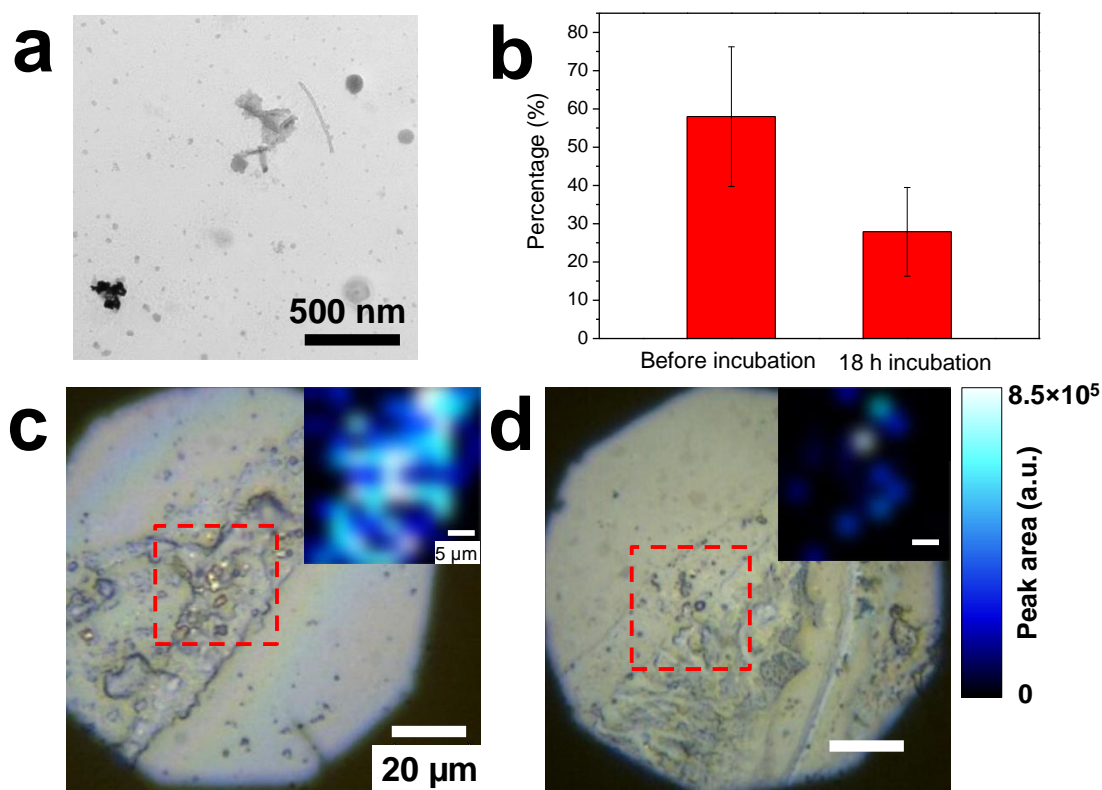


**Figure 4-5.** (a) TEM image of the GNP/NCNC sample treated with human neutrophils after 18 h of incubation. (b) Percentages of the NCNCs decorated with GNPs in ~100 NCNCs treated with neutrophils, before and after 18 h of incubation. The error bars correspond to the standard errors of the mean. (c), (d) Optical images of the cell fragments from the GNP/NCNC sample treated with neutrophils: (c) before and (d) after 18 h of incubation, under Raman microscope. The insets in panels c and d show the Raman intensity mapping of the G-band corresponding to the areas inside the dashed boxes.

## 4.5 CONCLUSIONS

We developed a novel cup-shaped graphitic structure using nitrogen-doped carbon nanotube cups (NCNCs), which can be efficiently isolated out from the stacked nitrogen-doped CNTs fibers through a combination of acid oxidation and high-intensity ultrasonication. Through a sodium citrate reduction, the separated nanocups can be effectively corked with GNPs on their open rims due to the preferential distribution of nitrogen functionalities on the edge. A pronounced SERS effect on these GNP-corked NCNCs was observed, indicating direct electronic interaction between GNPs and NCNCs. Based on both experimental and theoretical analysis, we identified the growth mechanism of the GNP corks, initiated by the nucleation of small GNP seeds toward the nitrogen functionalities, especially aliphatic amines on the opening of the cups. In addition, we demonstrated that the GNP-corked NCNCs can be effectively “opened” by hMPOs, followed by a complete degradation of the graphitic cup shells. The uncorking effect was further observed in the presence of MPO-containing human neutrophils, indicating the potential of the GNP-corked NCNCs in drug delivery applications, particularly in the treatment of acute/chronic inflammations.

## 4.6 ACKNOWLEDGEMENT

This work at the University of Pittsburgh was supported by an NSF CAREER Award No. 0954345 and NIH R01ES019304. The authors thank the Nanoscale Fabrication and Characterization Facility and the Department of Biological Sciences at the University of Pittsburgh for provision of access to the TEM and Raman instruments and acknowledge RJ Lee group for access to the XPS instrumentation. Y.Z. thanks the support from Bayer MaterialScience Fellowship.

## 5.0 RECENT STUDIES AND FUTURE DIRECTIONS

### 5.1 CHAPTER PREFACE

Currently, there are several completed or ongoing projects related to nitrogen-doped CNTs in the Star's research group, including but not limited to: (1) the effect of metal residues on the electrocatalytic activity of N-doped CNTs; (2) unzipping of N-doped CNTs to form graphene nanostructures; (3) encapsulation of molecular cargo in GNP-corked NCNCs; (4) surface-enhanced Raman spectroscopy study using GNP-functionalized graphene flakes as a substrate. This chapter provides a brief introduction to these recent studies that I have participated in, and discusses the future directions of research concerning the electrochemical and biomedical applications of N-doped CNTs and derivative nanomaterials.

The material in Section 5.2 was recently published in *The Journal of Physical Chemistry C*, and reproduced with permission from *J. Phys. Chem. C* **2013**, *117*, 25213-25221, Copyright 2013 American Chemical Society, with full citation listed in Ref. 150. The material in Section 5.3 is summarized from a manuscript submitted for publication.

## 5.2 THE EFFECT OF METAL CATALYST ON THE ELECTROCATALYTIC ACTIVITY OF NITROGEN-DOPED CARBON NANOTUBES

### 5.2.1 Preface

This material was recently published in *The Journal of Physical Chemistry C*, and reproduced with permission from *J. Phys. Chem. C* **2013**, *117*, 25213-25221, Copyright 2013 American Chemical Society, with full citation listed in Ref. 150.

**List of Authors:** Yifan Tang, Seth C. Burkert, Yong Zhao, Wissam A. Saidi, and Alexander Star

**Author Contributions:** All authors contributed to the design of experiments and writing of paper. YT, SCB, YZ synthesized the materials using CVD. YT and SCB performed the TEM characterization and electrochemical analysis, YT and YZ conducted the SEM and EDX characterization. YZ characterized the materials using Raman spectroscopy.

### 5.2.2 Introduction and brief results

Nitrogen-doped carbon nanomaterials have been shown to be great candidates for substituting expensive Pt-based catalysts in fuel cells for oxygen reduction reaction (ORR).<sup>113, 151, 229</sup> Some metal catalyst-based synthetic techniques, such as chemical vapor deposition (CVD) and thermal-solution pyrolysis<sup>108, 114-119</sup> of N-doped carbon nanomaterials unavoidably introduce transition metal nanoparticles into the as-synthesized carbon nanomaterials, which which have well-known catalytic activity on their own<sup>273</sup> and may affect the electrochemical catalytic

activity at above middle parts per million (ppm) range.<sup>274</sup> The debated effects of residual metal on the electrocatalytic activity of carbon nanomaterials have prompted the development of new metal-free electrocatalysts, which confirmed the necessity of nitrogen doping for improved ORR catalytic activity in the absence of transition metals.<sup>275</sup> However, the effects of different metals on the ORR mechanism that occurs at the active site have not previously been determined.

In this work, nitrogen-doped CNTs were synthesized using ferrocene, nickelocene or cobaltocene as catalysts via CVD method. All three resulted N-doped CNTs showed similar stacked-cup morphology (termed as nitrogen-doped carbon nanotube cups, or NCNCs) as in our previous study,<sup>105</sup> denoted as NCNC[Fe], NCNC[Ni], and NCNC[Co], respectively. Accordingly, their non-doped counter parts were also synthesized in the absence of nitrogen sources, denoted as MWCNT[Fe], MWCNT[Ni], and MWCNT[Co] respectively. The Electrochemical testing results demonstrated that NCNCs synthesized from ferrocene had improved ORR activity over un-doped MWCNTs synthesized from ferrocene, and NCNCs synthesized from nickelocene or cobaltocene, in terms of the reduction half-wave potential and the current. On the other hand, NCNC[Ni] and NCNC[Co] only showed some improved catalytic activity compared to MWCNT[Ni] and MWCNT[Co]. The detailed ORR mechanisms for the abovementioned materials were also different: NCNC[Ni] and MWCNT[Ni] demonstrated almost a four-electron reduction ORR pathway, while NCNC[Fe], MWCNT[Fe], NCNC[Co], and MWCNT[Co] showed a combination of two-electron and four-electron mechanisms. The detailed results from electrochemical test are summarized in **Table 5-1**. The observed difference in their performance supports the hypothesis that the ORR mechanism can be controlled through changing the metal catalyst utilized during material synthesis. Such understanding is of great

importance to the future design of non-precious-metal catalysts for low-cost fuel cells and other electrocatalytic applications.

**Table 5-1.** Nanomaterials catalytic activity toward oxygen reduction reaction (ORR).

Material	n <sup>a</sup>	Half-wave potential/V <sup>b</sup>
NCNC[Fe]	2.6 ± 0.1	-0.297 ± 0.006
NCNC[Ni]	3.9 ± 0.1	-0.334 ± 0.003
NCNC[Co]	3.1 ± 0.2	-0.316 ± 0.008
MWCNT[Fe]	2.6 ± 0.1	-0.358 ± 0.026
MWCNT[Ni]	3.8 ± 0.1	-0.351 ± 0.002
MWCNT[Co]	2.7 ± 0.1	-0.343 ± 0.004
Pt	4.0 ± 0.1	-0.174 ± 0.006

a) Transferred electron number (n) per oxygen molecule was calculated, from RRDE at -0.5 V; b) half-wave potential was calculated based on the ORR current at -0.5V during RRDE versus a 1.0 M Ag/AgCl reference electrode (+0.235 versus the Standard Hydrogen Electrode). All trials were done in triplicate with the mean and standard deviation reported in the table.

### 5.2.3 Future directions

The current study provides critical information toward the next step in the ORR catalyst development. The lower onset potential of NCNC[Fe] and the higher electron transfer number of NCNC[Ni] provide potential strategies to actively control the electrochemical performance of NCNCs during their synthesis process. However, the underlying mechanism, especially the reason of such a high electron transfer number for Ni catalyzed NCNCs, is still to be

investigated. The future direction of this project is to develop NCNC[Ni] with higher nitrogen content in order to provide enough active sites to increase the ORR peak potential closer to that of commercial Pt catalysts. On the other hand, potential improvement may be achieved by using a mixture of Fe and Ni catalyst during the CVD process. With a certain catalytic metal ratio, we may optimize both the yield and the electrochemical performance of the resulted NCNC materials.

### **5.3 OXIDATIVE UNZIPPING OF STACKED-CUP NITROGEN-DOPED CARBON NANOTUBES**

#### **5.3.1 Preface**

The material below is summarized from a manuscript submitted for publication.

**List of Authors:** Haifeng Dong, Yong Zhao, Yifan Tang, Seth C. Burkert, and Alexander Star

**Author Contributions:** AS conceived the project and designed the experiment; HD and YZ synthesized the material; HD, YZ and YT performed the microscopic and spectroscopic study; HD, YT, and SB performed the electrochemistry experiments, HD, YZ, and SB analyzed the data and wrote the manuscript. HD and YZ have contributed equally to the work being described.

### 5.3.2 Introduction and brief results

Since the first successful isolation of graphene sheets in 2004 by Geim and coworkers,<sup>276</sup> this novel two-dimensional one-atomic-thick nanomaterial has gathered enormous research attention for its outstanding electronic and mechanical properties.<sup>277-280</sup> In addition to other common preparation methods for graphenes such as mechanical peeling,<sup>276, 281</sup> CVD synthesis,<sup>282-283</sup> and oxidative exfoliation,<sup>284-285</sup> the Tour's group developed a facile permanganate oxidation method that longitudinally unzipped MWCNTs to yield graphene nanoribbons with defined morphology and semiconducting properties.<sup>286</sup> Nitrogen-doped carbon nanomaterials have attracted significant research interest because of their excellent electrocatalytic properties. Although varieties of nitrogen-doped carbon nanostructures with different dimensions have been developed for eletrocatalysis, their optimized morphology has not been well established. In this project, we prepared nitrogen-doped graphene structures from unzipping nitrogen-doped CNTs and investigated their electrocatalytic activity toward oxygen reduction reaction (ORR). We found that nitrogen-doping greatly altered the unzipping behavior of MWCNTs resulting structures with improved ORR activity. The ORR electrocatalytic activity is considered to be enhanced by increasing exposure of chemically active graphitic edges.<sup>287</sup> However, systematic investigations of the morphological influence on the electrochemical properties of the nitrogen-doped nanomaterials remain unexplored. Recently, Li et al. developed a GNR-nanotube complex by exfoliating the outer graphene layer from double-walled CNTs,<sup>121</sup> which showed good ORR activity due to the combination of the ORR-active GNRs with conductive CNT cores. This finding indicates hybrid nitrogen-doped structure as the optimized morphology for ORR electrocatalysis.

In this project, we demonstrated a facile and robust technique to produce nitrogen-doped nanostructures by unzipping of nitrogen-doped CNTs, comprised of many stacked cup-shaped segments termed as NCNCs. The oxidative unzipping method was employing a mixture of sulfuric acid ( $\text{H}_2\text{SO}_4$ ) and potassium permanganate ( $\text{KMnO}_4$ ), as described previously.<sup>286</sup> Different from the tubular un-doped CNTs, long-stacked NCNCs are more resistant to the unzipping process, resulting in a unique partially unzipped hybrid carbon nanostructure with nitrogen-doped GNRs connected through center tubular “cores”. We found that the extent of unzipping highly depends on the number of stacked cups in NCNCs: Upon ultrasonic separation of the stacked structure,<sup>105, 140</sup> the obtained short-stacked and individual nanocups can be completely unzipped into graphene nanosheets (GNSs) and graphene quantum dots (GQDs) exhibiting a strong fluorescence. Our approach provides an facile synthetic route to N-doped GQDs by direct unzipping of nitrogen-doped nanotubes. Moreover, the partially unzipped NCNCs exhibit excellent ORR electrocatalytic activity superior to as-synthesized NCNCs and their other derivatives, which provides a strong support for the GNR-carbon nanotube hybrid structure as the optimal morphology for electrocatalysis. Such enhancement results from the alternation of both nitrogen functionality and morphology of NCNCs by  $\text{H}_2\text{SO}_4/\text{KMnO}_4$  oxidation. The nitrogen-doped GNRs formed on the unzipped part of the outer wall of the nanotubes make an excellent and efficient ORR electrocatalyst, whereas the intact inner walls facilitate charge transport during electrocatalysis due to their retained electrical conductivity.

### **5.3.3 Future directions**

Although the partially unzipped N-doped CNT/GNR hybrid structures shows improved ORR catalytic performance compared our other N-doped CNT materials, they are still outperformed

by some existing studies based on the similar system. In addition, the mechanism is still needed that explicitly explains the structure – performance correlation of the unzipped materials with different morphologies. As for the future directions, multiple characterization techniques such as XPS, TEM and electrochemical analysis will be involved and re-examined to better support the current results, and different unzipping conditions will be tested to create GNRs with more exposed active edges.

## **5.4 CORKING OF NANOTUBE CUPS AND MOLECULAR ENCAPSULATION**

### **5.4.1 Introduction and brief results**

We have found that a pre-oxidation process can greatly improve the efficiency of the subsequent sonication separation of N-doped CNT cups (NCNCs), which yielded mostly to formation of individual nanocups. And by functionalization of the NCNCs with GNPs, we were able to specifically cork the opening of the nanocups by GNP corks.<sup>105, 140</sup> To this end, however, we are still unable to directly show the encapsulation molecular cargo in the hollow cavity of the corked nanocups. As the acid oxidation procedure is carried out on the stacked NCNC structure, we assumed that the inner sidewalls of NCNCs are not affected by oxidation, so that after the physical ultrasonic separation, the graphitic sidewalls in the opened cavities should be more pristine than the outside walls, leading better  $\pi$ - $\pi$  interaction with aromatic species

In this work, we tried to load Rhodamine 123 (Rh123) into the nanocups and seal them with GNP corks. Rhodamine derivatives have been frequently used as fluorescent tags and Raman probes for demonstrating high-sensitivity analysis such as SERS.<sup>288</sup> The Rh123 was first

mixed with NCNCs in aqueous solution, followed by GNP corking following the method described in Ref. 140. As a control the NCNCs were first corked with GNPs, then mixed with Rh123. Both samples are then repeatedly washed to remove any unencapsulated Rh123. The small molecules are not observable under TEM, however the close proximity of encapsulated Rh123 toward the GNP corks may incur the surface-enhanced Raman signal of Rh123 molecules. In order to indirectly verify the existence of Rh123, we took Raman spectra on both the repeatedly-washed samples. Before centrifugation, SERS signals of Rh123 can be detected on both the sample and the control. After repeated centrifugal wash, the active sample still shows a fairly high surface-enhanced spectrum of Rh123 peaks between  $300\text{ cm}^{-1}$  and  $1700\text{ cm}^{-1}$ , but the control did not show any Rh123 signals other than the D and G bands from NCNCs. It is inferred that the repeated wash is able to remove any free Rh123 molecules outside the cups, while the remaining of Raman signals in the active sample after wash may be incurred from the trapped Rh123 adsorbed on the inner surface of the GNP corks, but the Rh123 was completely washed off in the control. Such observation provided indirect evidence that the corked NCNCs have the capability of encapsulating small molecule cargo.

#### **5.4.2 Future directions**

Current cargo loading experiment lack direct evidence as it is only based on the SERS signals from Rh123, which are not reliable enough because SERS signals are not stable and greatly differ from samples to samples. The future directions of this project are to load larger cargo such as fullerenes, macromolecules, or nanoparticles into the nanocups, which can be directly observed by TEM. As a simple molecule,  $C_{60}$  is large enough to be imaged under TEM and has been frequently utilized to form “peapod” structure inside SWCNTs.<sup>289</sup> While typical

encapsulation of C<sub>60</sub> into SWCNTs require high-temperature evaporation,<sup>290</sup> the loading of C<sub>60</sub> was also reported to be achieved via “nano-extraction” or “nano-condensation” in liquid phase under room temperature.<sup>291</sup> Therefore, the attempts of loading C<sub>60</sub> in to NCNCs and corking with GNPs will be tried. The direct observation of C<sub>60</sub> under TEM images will provide the proof-of-concept evidence of the drug loading capacity of NCNCs.

## **5.5 GRAPHENE NANOSHEETS AND QUANTUM DOTS BY UNZIPPING NITROGEN-DOPED CARBON NANOTUBE CUPS**

### **5.5.1 Introduction and brief results**

In Section 5.3 we described a novel route to synthesis graphene nanostructures with different morphology by permanganate oxidative unzipping of NCNCs with different initial lengths. The partially unzipped NCNC/GNR structure showed good electrochemical catalytic performance toward ORR. Whereas the graphene nanosheets (GNSs) and graphene quantum dots (GQDs) from unzipping of separated short NCNCs also exhibited appealing properties such bright blue fluorescence from GQDs. The nitrogen-doping in the GQDs is believed to play an essential role in tuning the fluorescence properties of the QDs.<sup>123</sup>

Furthermore, the localized nitrogen reactive sites in the N-doped GNS were employed to be functionalized with gold nanoparticles (GNP) to form GNS/GNP hybrid composite, which exhibits efficient surface enhanced Raman spectrum and potential promising application in biosensing. The functionalization follows the same route of the sodium citrate reduction of H<sub>2</sub>AuCl<sub>4</sub> as describe previously.<sup>140</sup> TEM images showed that the GNPs were densely decorating

on the GNSs especially on the edge. The GNP-decorated GNSs were then used as a SERS substrate for detection of Rhodamine 6G (R6G) and Rhodamine 123 (Rh123) molecules. It was found that SERS signals were detected over 100 times of the regular Raman for R6G and Rh123 at the concentrations even as low as  $10^{-5}$  M. At the same time, the signals from the graphene were also significantly enhanced. The GNP-decorated GNSs can thus be potentially used as either Raman substrates for molecular sensing, or in vivo probes for SERS bioimaging.

### **5.5.2 Future directions**

For the subsequent investigation, two directions are of importance. First, the SERS mechanism is always a debated issue between electromagnetic or chemical charge-transfer mechanisms. The GNP-decorated GNSs may serve as a promising system for mechanistic study. With different electron donating or withdrawing substances on the Raman substrate, it is interesting to observe the potential influence of charge-transfer on the change of Raman behaviors. On the other hand, cellular experiments will be performed for the GNP-decorated GNSs as potential Raman bioimaging probes. With initial information on SERS performance and cytotoxicity, in vivo experiments can be further carried out.

## 6.0 CONCLUDING REMARKS

This dissertation covers the two major projects (i.e., nitrogen-doped carbon nanomaterials and enzymatic degradation of CNTs) that I have carried out during past the six years of my PhD studies at the University of Pittsburgh, under supervision of Professor Alexander Star. The research projects that I have completed and published are described in Chapter 2, Chapter 3, and Chapter 4 of this dissertation, with my humble hope to contribute to the development of nanoscience research.

As stated in the title of the dissertation, my research interests are focused on nitrogen-doped carbon nanomaterials, especially individual nitrogen-doped carbon nanotube cups (NCNCs), which possess intriguing cup-shaped morphology and rich chemical properties with promising potential for drug delivery applications. Based on the previous work from our research group,<sup>108</sup> I improved the synthetic method of the CVD growth of NCNCs, by changing experimental conditions. I introduced the probe-tip ultrasonic method to separate the stacked NCNCs, which greatly improved the separation efficiency compared to hand-grinding. The resulted separated NCNCs were carefully examined for their graphitic structures and nitrogen functionalities. I demonstrated that the nitrogen preferentially exist on the open rims of the nanocups in the form of amine groups, to which GNPs can be functionalized, forming nano-corks on the opening of the cups. This work is published in *ACS Nano*, as Ref. 105. In the following study, I improved the efficiency of both cup separation and GNP-cork

functionalization, by introducing a pre-oxidation step before probe-tip sonication, and by sodium citrate reduction of  $\text{HAuCl}_4$ , respectively. The work is published in the form of a video in *Journal of Visualized Experiments*, as Ref. 140.

Another aspect of my research was on the enzymatic degradation of carbon nanomaterials. I first extended the HRP degradation phenomenon to MWCNTs, and demonstrated the different degradation behavior of MWCNTs compared to SWCNTs. The MWCNTs are not completely degraded by HRP/ $\text{H}_2\text{O}_2$ , with a diminishing degradation rate during the course of 80 days; depending on the extent of surface oxidation; oxidized MWCNTs showed different degradation rate. The incomplete degradation of MWCNTs, together with a decrease of defective level on the surface, suggested a layer-by-layer degradation fashion, which ceased the degradation as the pristine inner tubes are exposed to HRP. This work was published in *The Journal of Physical Chemistry*, as Ref. 206.

The following project of enzymatic opening/degradation of GNP-corked NCNCs by hMPO combined the previous two projects together and applied the knowledge to create a practical drug releasing scheme for the potential GNP/NCNC delivery vehicle. Through both experimental and theoretical analysis, we clarified the growth mechanism of GNP corks on NCNCs stemming from the gold nucleation on the basal amine groups. Upon exposure to the oxidative environment with hMPO/ $\text{H}_2\text{O}_2$ / $\text{NaCl}$ , the interactions between GNPs and amine groups were disrupted within several hours, which released the GNPs corks and opened the nanocarriers. Following the ensuing degradation, the opened NCNC shells were readily deformed and disappeared within 20 days of treatment. The degradative opening of the GNP-corked NCNCs provides a promising route for potential drug releasing models.

## APPENDIX A

### SUPPORTING INFORMATION FOR CHAPTER 2, 3 AND 4

#### A1. CORKING CARBON NANOTUBE CUPS WITH GOLD NANOPARTICLES

##### Supplemental Experimental Procedures and Calculations:

##### 1. Functionalization on NCNCs and quantification of amine groups via Kaiser Test.

Functionalization with glycine was performed on 1 mg of either as-synthesized or separated NCNCs suspended in 4 mL of DMF. To each of the suspensions, 20 mg *N*-(*tert*-Butoxycarbonyl)glycine (Boc-Gly-OH), were added through EDC/DMAP coupling reaction. The mixture was stirred under nitrogen at room temperature overnight. The product was then washed and stirred at room temperature in 4 mL of 2:1 v/v dioxane/HCl for 2 hr to remove the Boc protecting groups. The resulting material was washed repeatedly with EtOH to remove any residual glycine. Di-*tert*-butyl dicarbonate (Boc<sub>2</sub>O) was used to protect the inherent amine groups on NCNCs. 22 mg of Boc<sub>2</sub>O and 20 mg of NaHCO<sub>3</sub> were added to 1 mg separated NCNCs in 4 mL tetrahydrofuran (THF). The reaction mixture was stirred overnight at room temperature under N<sub>2</sub>.

The Kaiser test was conducted on both as-synthesized and separated NCNCs with or without chemical treatment. Briefly, the Reagent A for the Kaiser test was prepared by mixing 1 g of phenol and 250  $\mu\text{L}$  of EtOH in 2.5 mL of pyridine, to which 50  $\mu\text{L}$  of 0.01 M hydrindantin in  $\text{H}_2\text{O}$  were added. For the Reagent B, 50 mg ninhydrin was dissolved in 1 mL of EtOH. For each test, the sample was first weighed on a microbalance and then dispersed in 1 mL of 60% EtOH, to which 100  $\mu\text{L}$  of Reagent A and 25  $\mu\text{L}$  of Reagent B were added. The mixture was heated at 100  $^\circ\text{C}$  oil bath for 10 min and filtered to remove solid particles. A blank sample was made in the same process without adding nanotubes. Visible spectroscopy (Lambda 900 spectrometer, Perkin-Elmer) was taken on the filtrate for colorimetric analysis. A positive result of Kaiser test shows an absorption peak centered at 570 nm.

## **2. Characterization of NCNCs.**

Transmission electron microscopy (TEM) images with lower resolution were obtained with FEI Morgagni microscope at an accelerating voltage of 80 kV. High-resolution TEM images were taken at JEOL 2100F microscope with 200 kV accelerating voltage. Samples were first dispersed in EtOH or DMF then dropcasted on a lacey carbon TEM grid (Pacific Grid-Tech) for low-resolution TEM imaging or on C-FLAT holey TEM grid (Electron Microscopy Sciences) for high-resolution TEM imaging, respectively. Electron energy loss spectroscopy (EELS) and energy-filtered TEM (EFTEM) were performed on the JEOL 2100F TEM microscope.

Raman spectra were taken on Renishaw inVia Raman microscope with an excitation wavelength of 633 nm. NCNC samples after different duration of probe-tip sonication were dropcasted on a quartz slide and dried. Spectra were scanned from 1000 to 2000  $\text{cm}^{-1}$  at 10% laser intensity with 15 s exposure time.

Fourier transform infrared spectroscopy (FTIR) was performed on a Shimadzu IRprestige-21 spectrometer in a transmission mode. Both as-synthesized and separated samples were ground with dry KBr powder and pressed into pellets. The pellets were baked in vacuum oven at 120 °C for 2 h prior to characterization.

AFM imaging was performed in a contact mode configuration on a Multimode scanning probe microscope (Veeco). 10 µL of sample solution (aq) was spin-coated on freshly cleaved mica and dried in ambient.

Dynamic light scattering (DLS) was performed using a quasi-elastic light scattering spectrometer (Brookhaven 90 Plus Particle Size Analyzer) under laser irradiation with 678 nm wavelength. The elemental analysis was performed on a CE 440 CHN Analyzer (Exeter Analytical).

X-ray photoelectron spectroscopy (XPS) was performed on a Thermo Scientific K-Alpha using monochromated Al K $\alpha$  x-rays (1486.6 eV) as the source, with a spot size of 400 µm and pass energy of 50eV. XPS samples were prepared by briefly sonicating the NCNCs in ethanol and dropcasting them onto an aluminum substrate heated to 100 °C. XPS binding energies were corrected using the C1s peak at 285 eV as an internal standard. The spectra were fitted after background subtraction of a Shirley type baseline. Peak shapes were optimized by using a Gaussian:Lorentzian ratio of 80:20.

### **3. Statistics on the quantities of functionalized NCNCs and GNPs and calculations.**

The percentages of NCNCs with open sides corked by GNPs were calculated by statistically analyzing 100 TEM images from the samples of thiolated NCNCs incubated with 40 nm GNPs. Only short NCNCs with length less than 400 nm were counted. In total of 656 short NCNCs,

356 of them were observed to be functionalized with GNPs, in which 150 NCNCs were corked by GNPs at their open rims, giving a percentage of ~23% corked NCNCs overall. There were totally 928 GNPs found attached on the NCNCs, 339 of which were attached to the open sides of NCNCs (150 of them exactly corking), taking up about 37%.

The area ratio between the sidewalls and the basal planes was calculated by considering a cylindrical model of NCNC with the average length of 380 nm and the diameter in the basal plane of 40 nm. In this case, the areas of the side and the bottom of the cylinder are  $23876 \text{ nm}^2$  and  $1257 \text{ nm}^2$ , respectively, with a ratio of 19:1. Therefore, it would be much less possible for the GNPs to bind to the open sides if the binding was not energetically favored.

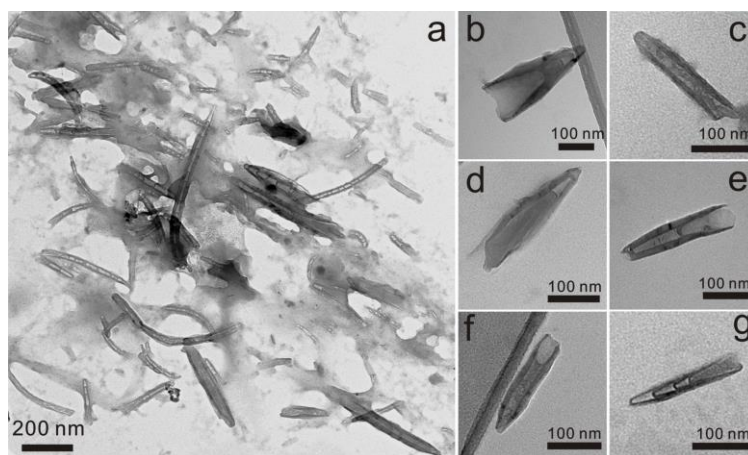


**Figure A1-1.** (a) TEM image at an intermediate magnification showing an overview of separated NCNCs after 15 hr of probe-tip sonication. Individual and short-stacked nanotube cups less than 400 nm in length exist with large abundance of over 70%. Stacked cups longer than 400 nm are also observed, but few of them exceed 1  $\mu\text{m}$ . The amorphous materials surrounding the NCNCs may be due to unevaporated solvent residues. (b – g) More TEM images of isolated individual and short-stacked cups. They all have common cup-like shapes with one end sealed and the other open.

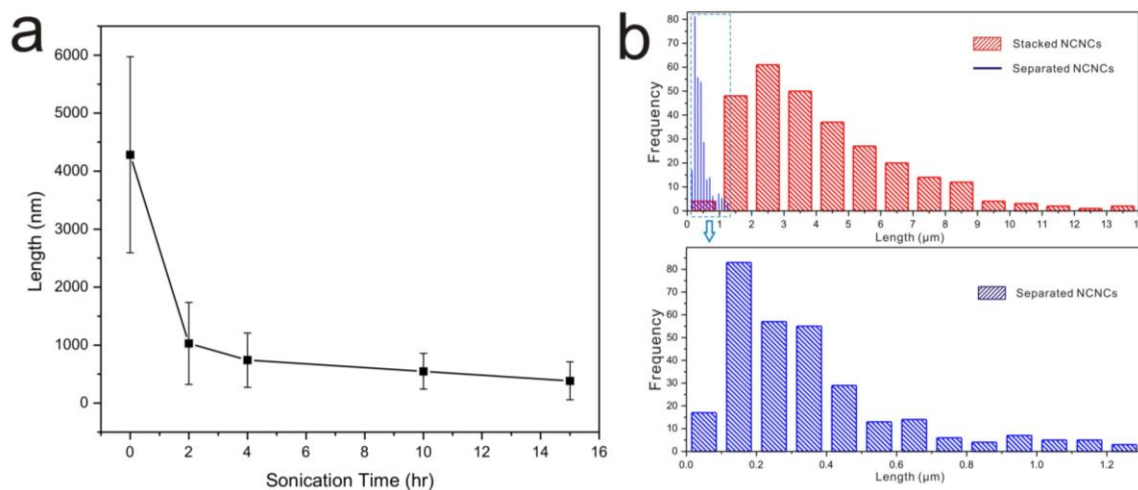


**Figure A1-2.** (a) Average lengths of NCNCs as-synthesized and after 2, 4, 10 and 15 hr of probe-tip sonication. Over 300 NCNCs in each sample were measured from TEM images. The error bars represent the standard deviations of the length distribution. (b) Upper panel: histograms of length distribution of as-synthesized NCNCs (red bars) and separated NCNCs (blue lines) and lower panel: magnified histograms of length distribution of separated NCNCs (blue bars), obtained from TEM images.

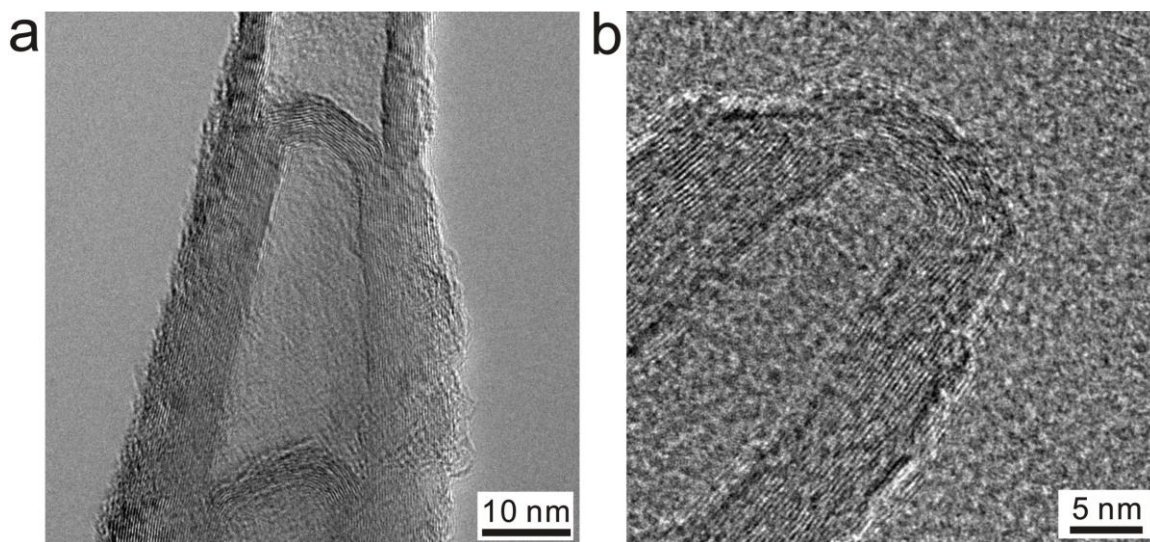


**Figure A1-3.** High-resolution TEM images showing damaged graphitic lattices on the sidewall (a) and the tip (b) of NCNCs after probe-tip sonication.

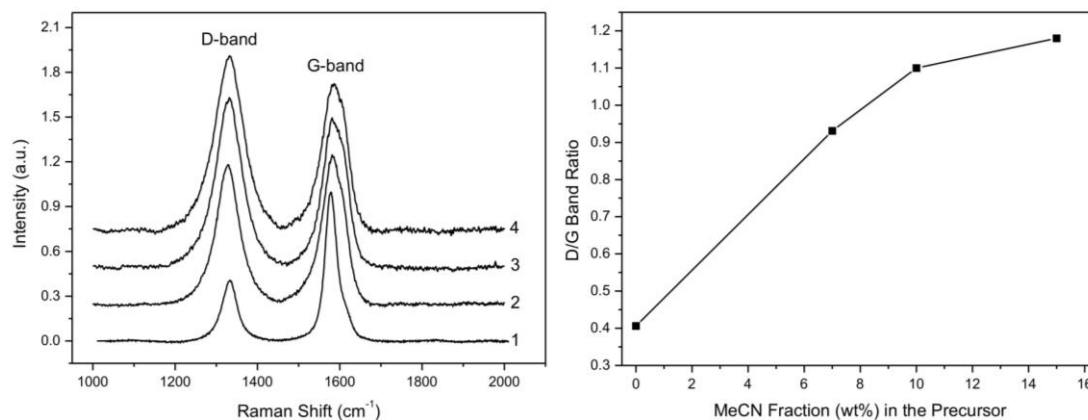


**Figure A1-4.** (a) Raman spectra of undoped MWCNTs (1) and as-synthesized NCNCs with acetonitrile fractions of 7 wt% (2), 10 wt% (3), and 15 wt% (4) in the precursor, respectively. The spectra were normalized to the G band. (b) D/G band ratios in the Raman of the corresponding four samples.

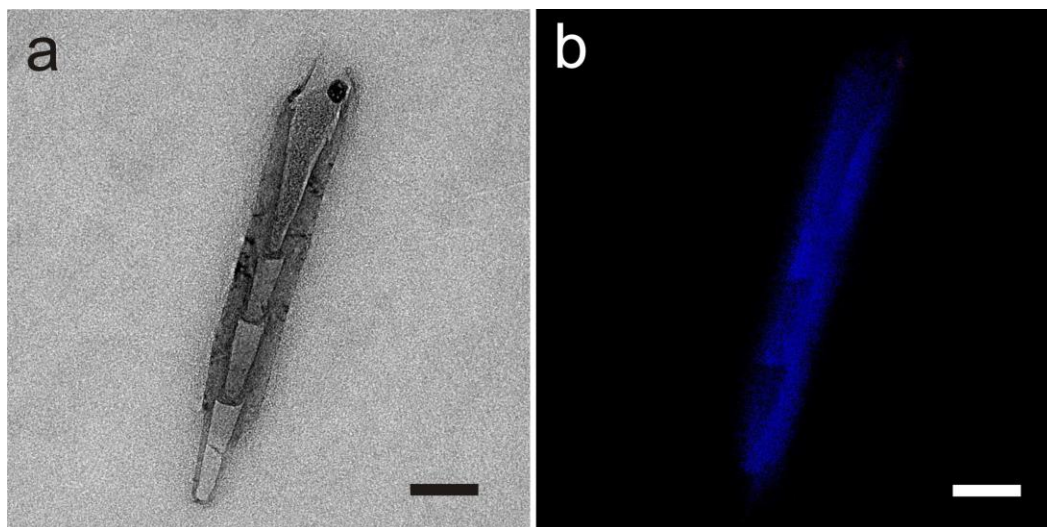


**Figure A1-5.** (a) TEM image of a short stack of four individual NCNCs. (b) Energy filtered TEM image at N K edge of 401 eV showing the distribution of nitrogen (colored blue) on the NCNCs. Both scale bars represent 50 nm.

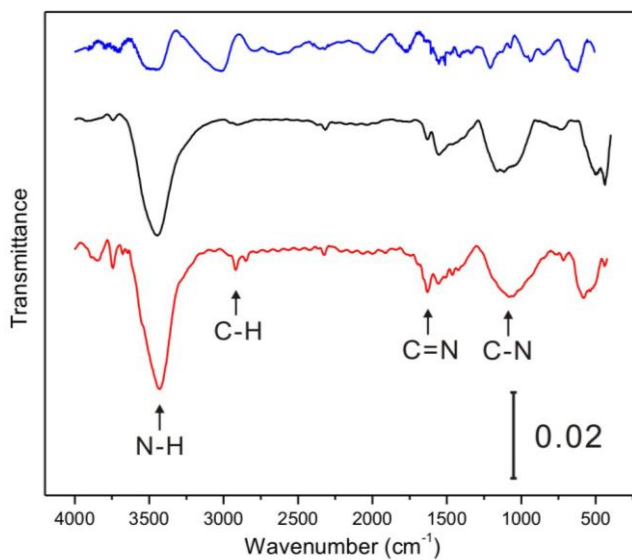


**Figure A1-6.** FTIR spectra of undoped MWCNTs (blue), as-synthesized NCNCs (black), and separated NCNCs (red).

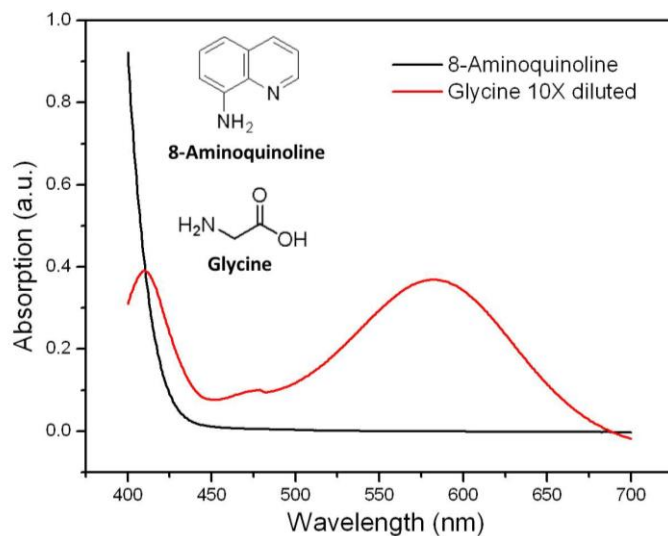


**Figure A1-7.** Visible spectra of the control Kaiser tests performed on glycine (red, 10 times diluted) and 8-aminoquinoline (black). The glycine shows a strong absorption peak at 570 nm indicating the existence of primary amines, while no peak at 570 nm is detectable for 8-aminoquinoline, indicating that the aromatic amine and pyridinic nitrogen do not give positive results in the Kaiser test.

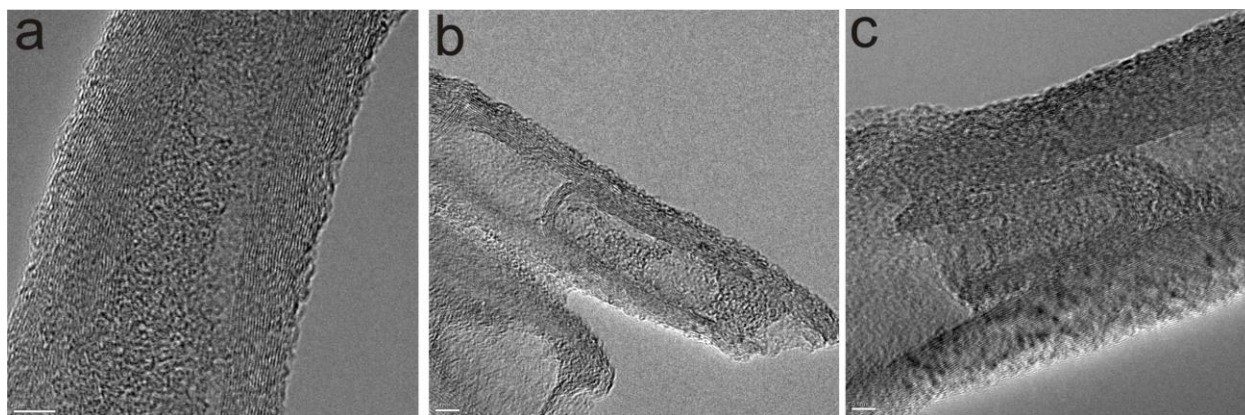


**Figure A1-8.** (a, b) High-resolution TEM images showing that amorphous carbon residues were frequently observed inside the open cavity of NCNCs after the separation process. (c) High-resolution TEM image showing that one smaller cup was trapped inside the opening of a larger NCNC. All scale bars represent 5 nm.

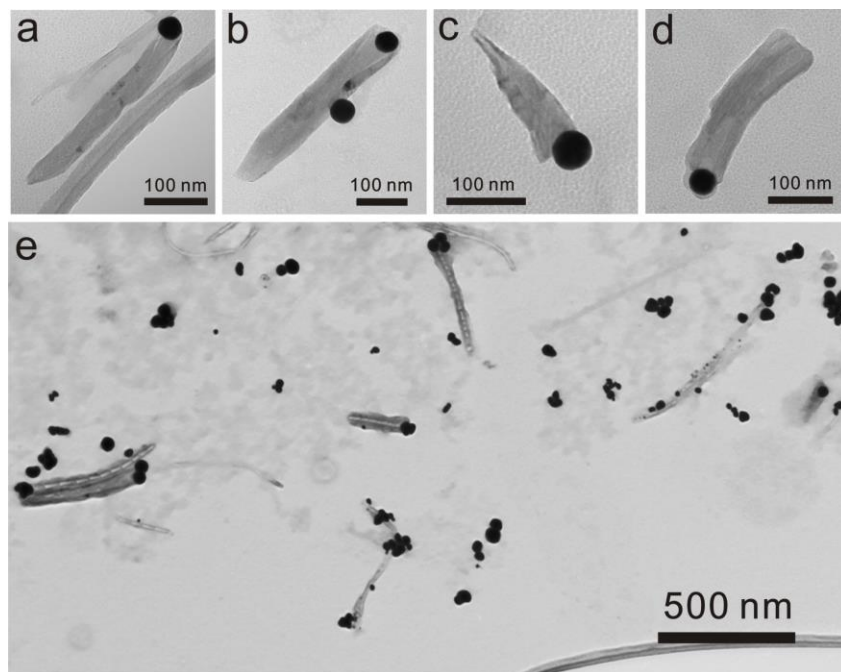


**Figure A1-9.** (a – d) Other examples of TEM images of individual thiolated NCNCs corked by 40 nm GNPs. (e) TEM image at a lower magnification showing that several NCNCs were corked by GNPs at their open rims, indicating a preferential interaction between GNPs and the open sides of NCNCs.

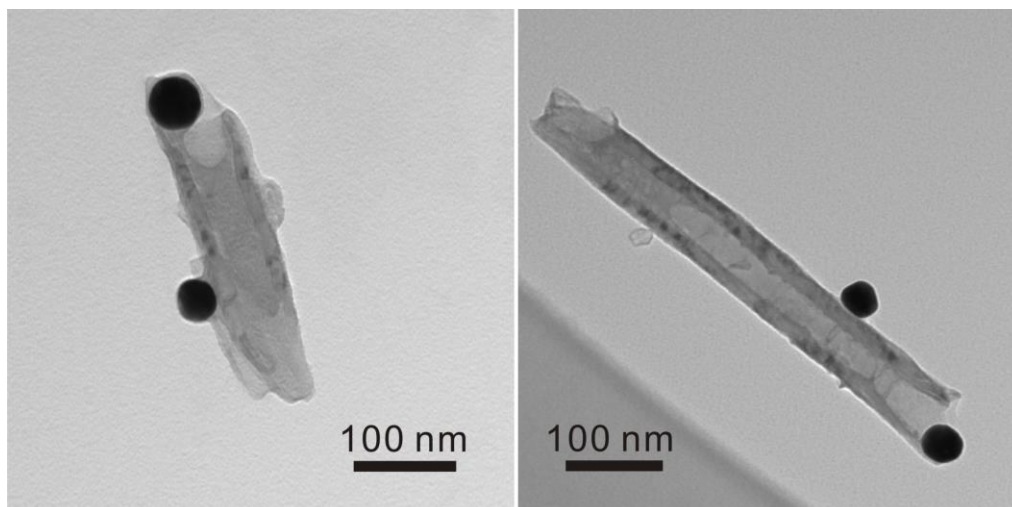


**Figure A1-10.** TEM images of GNPs attached on the sidewalls of NCNCs and on the open rims of NCNCs but not exactly corking the cups.

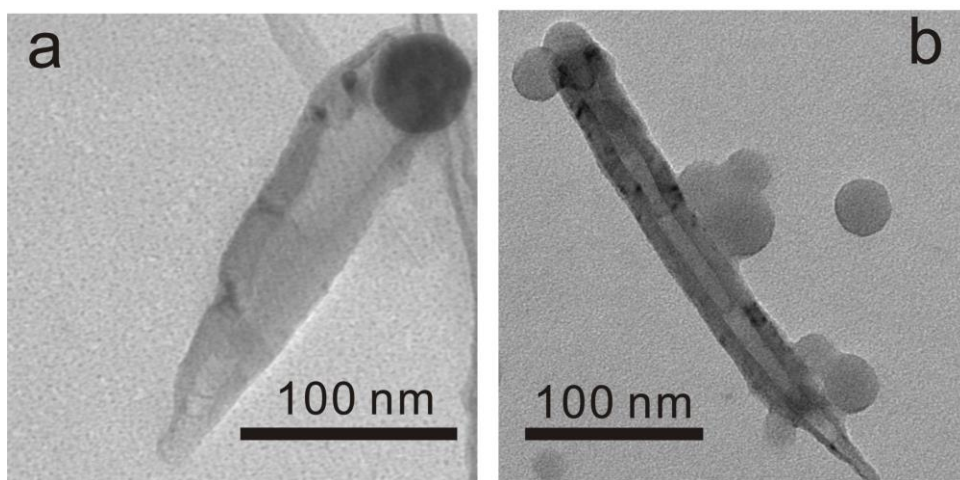
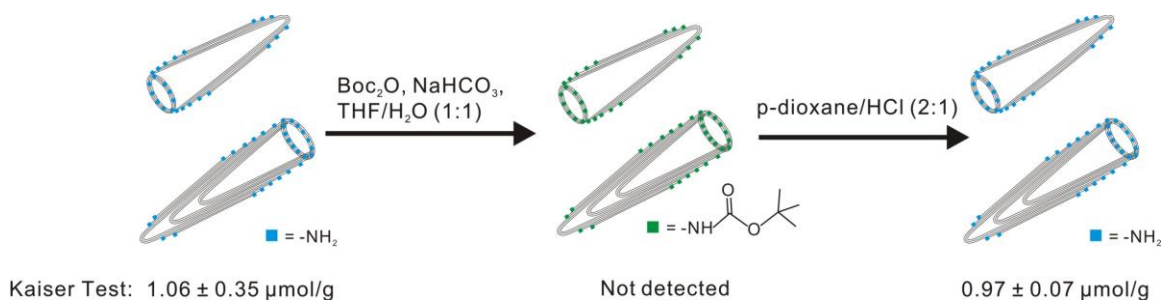


**Figure A1-11.** (a) TEM image of a thiolated individual NCNC capped by a silver nanoparticle with diameter of ~40 nm. (b) TEM image of an unfunctionalized individual NCNC capped by aldehyde-functionalized polystyrene latex nanoparticles with diameters of ~40 nm. The polymer nanoparticle fitting on the opening of the NCNC was shown to be stretched toward the inner cavity, presumably due to the capillary effect.



**Scheme A1-1.**  $\text{Boc}_2\text{O}$  protection of amine groups on NCNCs to yield NH-Boc groups which prevented the amines from being detected by Kaiser test. Upon removal of the Boc groups, the amines gave a positive Kaiser test result again.

## A2. ENZYMATIC DEGRADATION OF MULTI-WALLED CARBON NANOTUBES

### Supplemental experimental procedures:

**Methods for Boehm's Titration:** Boehm's Titration is an acid–base titration method for determination of functional groups on the surface of carbon materials. Approximately, 5 mg of p-MWNT, o-MWNT (5hr), and o-MWNT (8hr) samples were respectively immersed in sample vials with 5 mL of 10 mM NaOH aqueous solution. Then each vial was sonicated under vacuum for 2.5 min in order to disperse the sample and degas  $\text{CO}_2$  from the solution. All three vials were then sealed with septum stoppers and parafilm and placed on a rotary shaker with continuous shaking (220 rpm) at room temperature for 72 hr. After the incubation process, the sample solution was filtered through a 0.22  $\mu\text{m}$  Teflon membrane, and 1 mL of filtrate was taken and added with 2 drops of 0.1% Bromocresol Green and Methyl Red mixture (indicator, v/v = 3:2).

The filtrate was titrated with approximately 1 mM HCl aqueous solution using a 10 mL buret. Three parallel titrations were performed on each sample to obtain reproducible results, and a reference sample with 5 mL of 10 mM NaOH was analysed the same way to give the accurate concentration of NaOH. The surface acidic group loading (mM / gram of MWNTs) was estimated by the following equation:

$$\text{Loading} = \frac{(c_{\text{ref}} - c) \times 5 \times 10^{-3} L}{m_{\text{MWNT}}}$$

where:

$c_{\text{ref}}$ : Concentration of NaOH solution (mM);

$c$ : Concentration of the NaOH filtrate after incubation with MWNTs (mM);

$m_{\text{MWNT}}$ : Weight of each MWNT sample.

**Atomic Force Microscopy (AFM):** AFM imaging and height analysis was performed on a Multimode scanning probe microscope (Veeco). Sample was prepared on freshly cleaved mica substrate spin-coated with 20  $\mu\text{L}$  of 0.1% (w/w) poly-L-lysine (aq) at 1400 rpm. 10  $\mu\text{L}$  of sample solution (aq) was then spin-coated on the substrate and dried in ambient. AFM imaging was performed using a ‘‘Supershar’’ Si tip (AppNano) in tapping mode, with a drive frequency of 193.023 Hz, an amplitude set point of 0.6066 V, and a drive amplitude of 261 mV. The cross-sectional height of samples was quantified using sectional analysis.

**Thermogravimetric Analysis (TGA):** Three samples of p-MWNTs, o-MWNTs (5hr) and o-MWNTs (8hr) before enzymatic degradation were dried in oven overnight. From each sample about 4 mg of materials were transferred into a platinum boat on which TGA were performed (TA instrument, Q50). The temperature ramping was set from room temperature to 850  $^{\circ}\text{C}$  at 5  $^{\circ}\text{C}$  per min at  $\text{N}_2$  atmosphere. Other samples were analyzed in air atmosphere with the temperature ramping to 800  $^{\circ}\text{C}$  at 5  $^{\circ}\text{C}$  per min.

**Amplex Red assay for monitoring HRP activity:** HRP activity throughout the degradation process was monitored by Amplex Red reagent. A 10 mM stock solution was prepared by dissolving 5 mg of lyophilized Amplex Red in 1.94 mL dimethyl sulfoxide (DMSO) and kept in the dark at  $-20\text{ }^{\circ}\text{C}$ . To test the enzymatic activity, 250  $\mu\text{L}$  of sample suspensions before and during degradation were taken out and diluted with 235  $\mu\text{L}$  double-distilled water, followed by adding 1  $\mu\text{L}$  Amplex Red stock solution and 15  $\mu\text{L}$  of 800  $\mu\text{M}$   $\text{H}_2\text{O}_2$ . The mixture was then analyzed using visible spectroscopy on a Lambda 900 spectrometer (Perkin-Elmer) with double-distilled water as the background.

The Amplex Red is often associated with HRP which is activated by  $\text{H}_2\text{O}_2$ . The Amplex Red is assumed to experience a one-electron transfer to active HRP and form phenoxy radicals which undergo a dismutation reaction forming resorufin, a colored compound with distinct absorption band at 570 nm. The reaction is quantitative with 1:1 ratio of Amplex Red to  $\text{H}_2\text{O}_2$  and the presence of active HRP enzyme. Therefore a colorimetric assay can be performed for either testing the HRP activity or measuring the  $\text{H}_2\text{O}_2$  concentration.

**Fourier transform infrared spectroscopy (FTIR):** Samples of p-MWNTs, o-MWNTs (5hr) and o-MWNTs (8hr) were synthesized and dried in oven overnight. FTIR spectra were taken using a Diffuse Reflectance Infrared Fourier Transform Spectroscopy (DRIFTS) accessory with dry SiC powder as matrix.

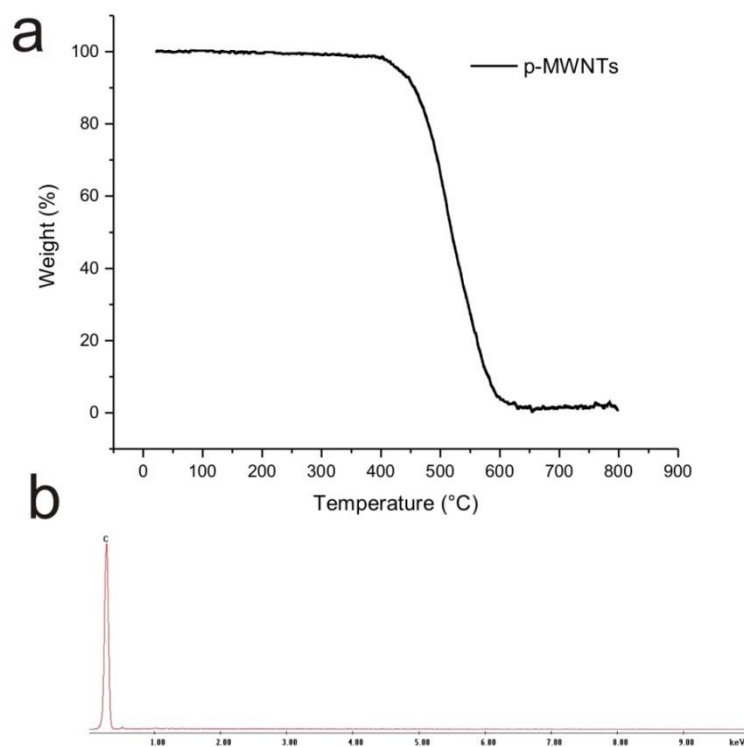


**Figure A2-1.** (a) TGA curve of p-MWNTs in air. There was almost no material left after burning in air above 600 °C. (b) Energy-dispersive X-ray spectroscopy (EDS) elemental analysis of p-MWNTs. No iron peaks (6 – 8 keV) were observed.

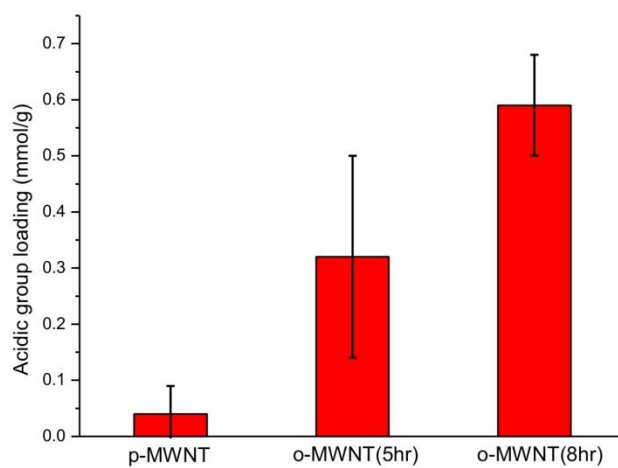


**Figure A2-2.** Histogram showing increasing acidic group loadings on the surface of MWNTs along with 0, 5 and 8 hr carboxylation determined by Boehm's Titration.

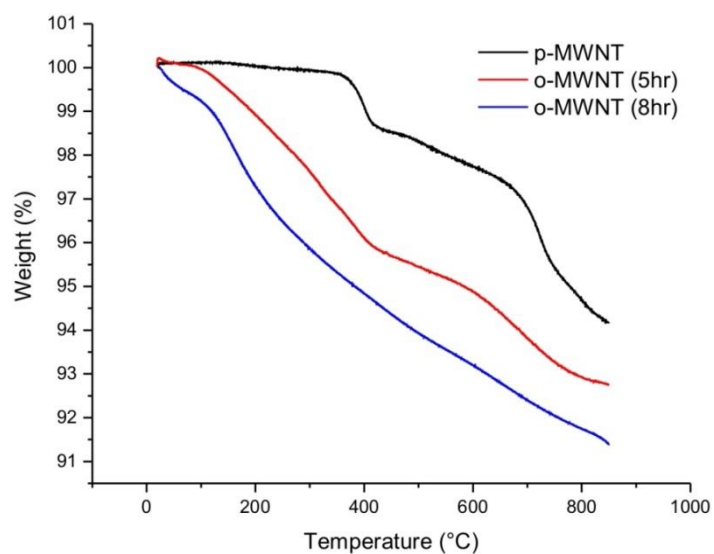


**Figure A2-3.** TGA curves for p-MWNTs, o-MWNTs (5hr) and o-MWNTs (8hr) in N<sub>2</sub> atmosphere. The TGA curves showed a progressively increasing weight loss along with the increasing carboxylation time, indicating more functional groups grafted on the nanotubes.

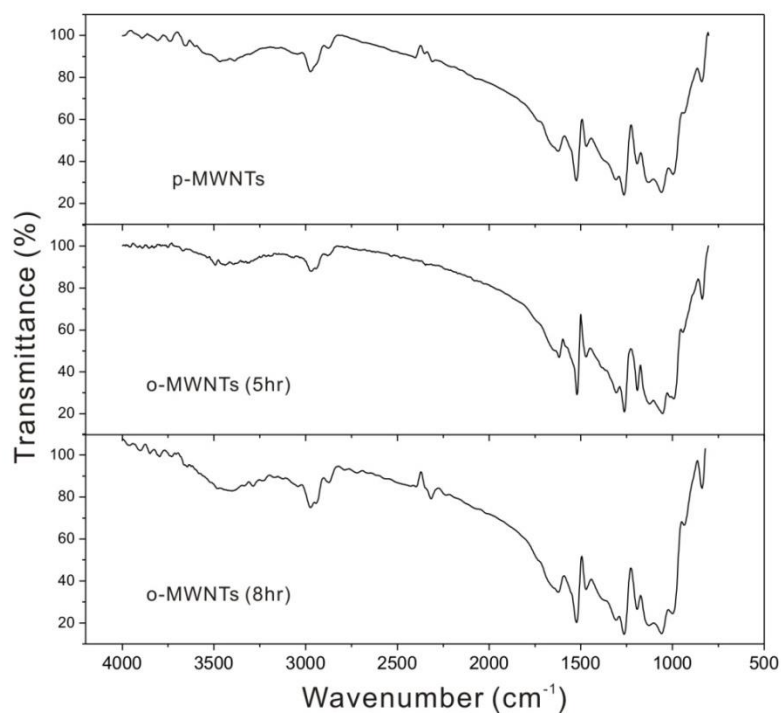


**Figure A2-4.** FTIR spectra for p-MWNTs, o-MWNTs (5hr) and o-MWNTs (8hr) before enzymatic degradation. The spectra show different vibrational modes in each sample including C=O stretching ( $1640\text{ cm}^{-1}$ ), C–O stretching ( $1100\text{ cm}^{-1}$ ), C–H stretching ( $2980\text{ cm}^{-1}$ ), O–H stretching ( $3440\text{ cm}^{-1}$ ) and so on, which indicate the existence of oxygen-containing defects such as carboxylic groups on MWNTs.

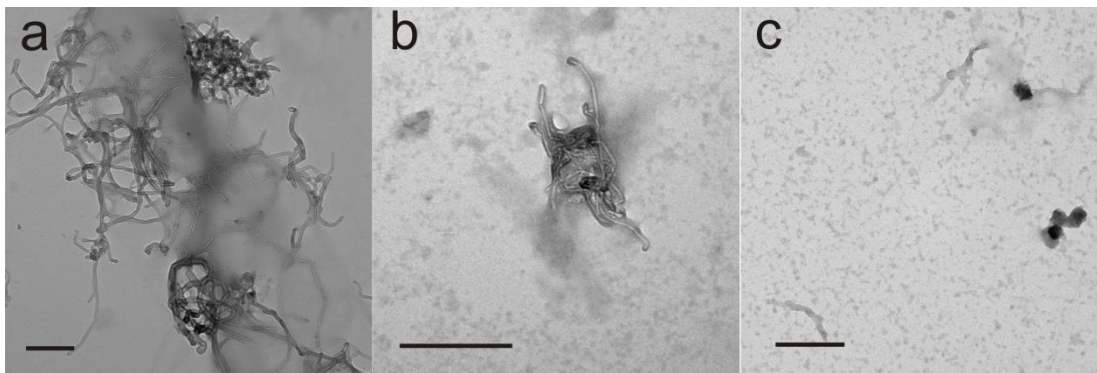


**Figure A2-5.** TEM images for (a) p-MWNT, (b) o-MWNT (5hr), and (c) o-MWNT (8hr) samples incubated with HRP under daily  $\text{H}_2\text{O}_2$  additions for 80 days. The morphology of nanotubes remained similar to samples observed at Day 60, however, the carbonaceous “flakes” were seen to be continuously degraded into even smaller pieces. All scale bars are 200 nm.

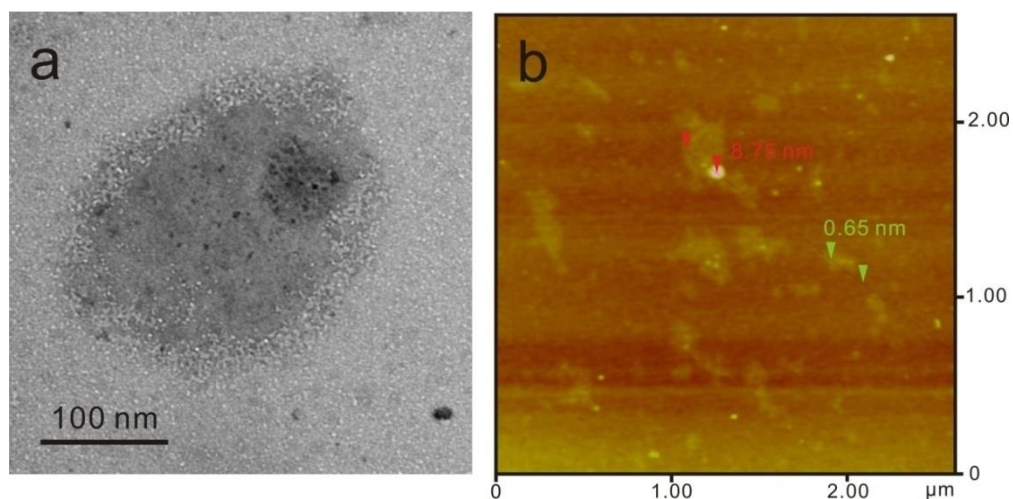


**Figure A2-6.** (a) TEM image of magnified carbonaceous flakes for o-MWNT (8hr) enzymatically degraded with constant H<sub>2</sub>O<sub>2</sub> addition at Day 2. The black dots with diameters around 5 nm adsorbed on the flakes are presumably HRP particles. (b) AFM image for the sample at Day 4. Large amounts of carbonaceous flakes were seen with thickness of about 0.65 nm.

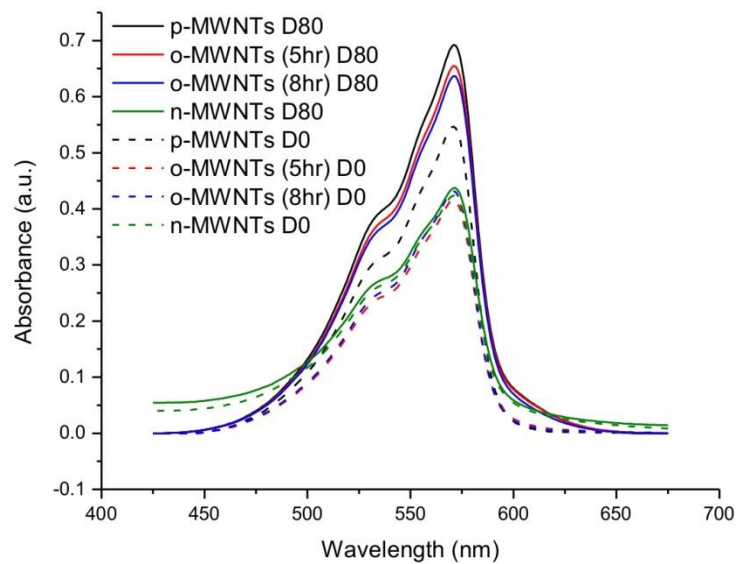


**Figure A2-7.** Visible absorption spectra of HRP activity tested by Amplex Red and  $H_2O_2$  for p-MWNT, o-MWNT (5hr), o-MWNT (8hr) and n-MWNT samples before (dash lines) and after (solid lines) 80 days of degradation process.

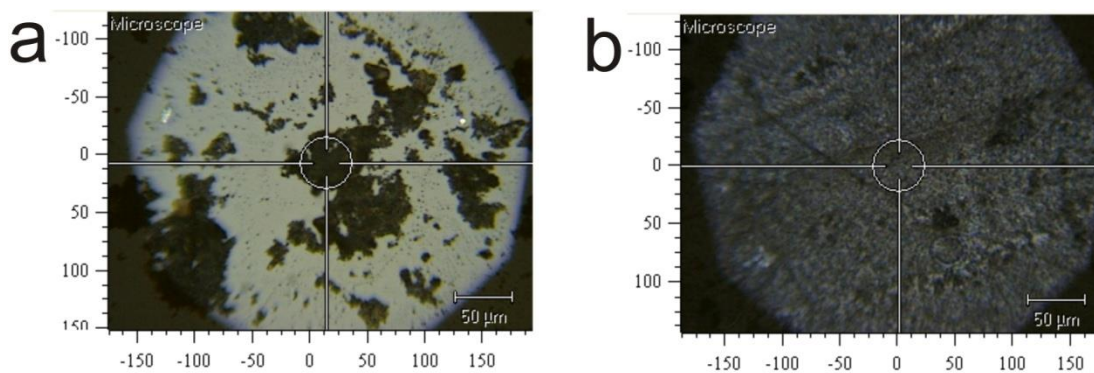


**Figure A2-8.** Images from the optical microscope on the Raman sample stage. (a) Image of o-MWNTs (8hr) before enzymatic degradation, and (b) after enzymatic degradation. The sample before enzymatic degradation tended to aggregate into discrete spots after dried on a sample glass slide, while the sample after degradation formed an even, continuous film. Both samples appeared to be homogeneous as visually observed. 5 spectra were collected and averaged from different spots for both samples.

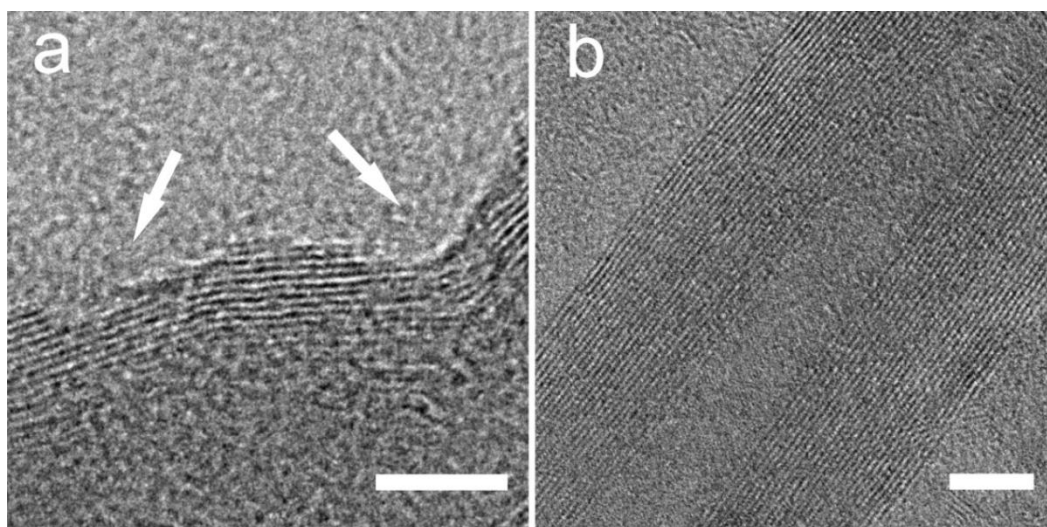


**Figure A2-9.** High-resolution TEM images for o-MWNTs (8hr) (a), and p-MWNTs (b) before enzymatic degradation. All scale bars are 5 nm. The defective sites are shown on the surface of o-MWNT samples as arrowed, in which about 5 – 8 graphitic walls were broken, while the p-MWNTs remain high graphitic integrity with well-defined walls.

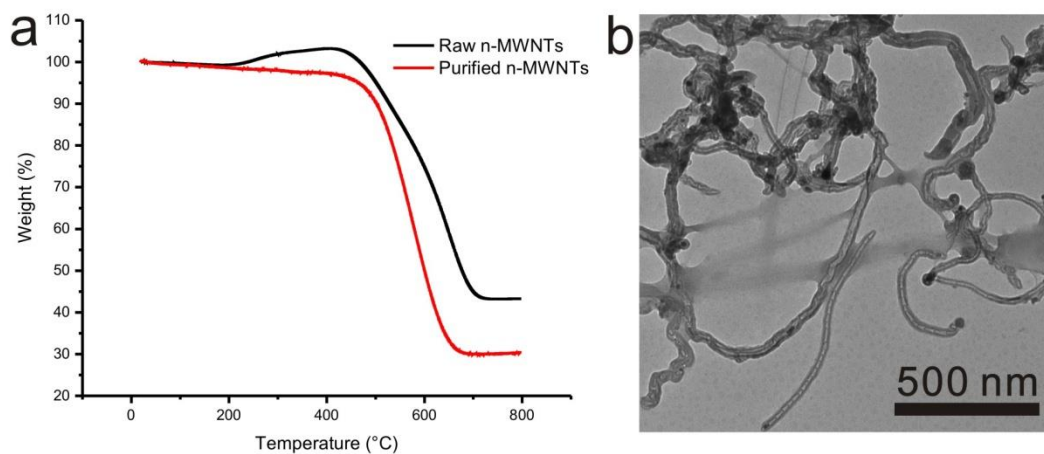


**Figure A2-10.** (a) TGA curves for n-MWNTs before (black) and after (red) purification process in air. (b) TEM image of purified n-MWNT samples after 80 days of incubation in Fenton oxidation environment. The extent of degradation was limited.

### A3. NANO-GOLD CORKING AND ENZYMATIC UNCORKING OF CARBON

#### NANOTUBE CUPS

##### Computational methods

Plane-wave DFT calculations using density functional theory and 3D supercell models were performed using Vienna *ab initio* simulation package (VASP) code. The electron-ion interaction was described by the projector augmented wave (PAW) method of Blöchl and the Perdew, Burke and Ernzerhof (PBE) functional has been used for description of the exchange and correlation. The PBE functional was corrected to include long-range dispersion interactions using the Tkatchenko and Scheffler method as implemented in the VASP code. Calculations were spin-polarized and used a cutoff energy of 400 eV. The graphene flake surface with a zigzag termination running along the Ox axis has been represented using a supercell with Nx=7 and Ny=11 periodic units separating the opposite edges of the graphene flake. These edges were terminated with H atoms or with other functional groups as described in the paper. In order to reduce the lateral interactions for the adsorbed Au<sub>20</sub> clusters on graphene surface, the graphene sheet was separated by vacuum layers up to 13.6 Å and 20.4 Å along Oy and Oz directions, respectively. Given the large dimensions of the supercells used, the sampling of the Brillouin zone was done only at the  $\Gamma$  point. The adsorption energy of the Au<sub>20</sub> cluster on graphene surface was calculated based on equation  $E_{\text{ads}}=(E_{(A)}+E_{(S)}-E_{(A+S)})$  where  $E_{(A)}$  is the energy of the isolated Au<sub>20</sub> cluster,  $E_{(S)}$  is the total energy of the graphene surface and  $E_{(A+S)}$  is the energy of the combined adsorbate-surface system in the optimized configuration. In the sign convention introduced above, positive adsorption energies correspond to stable adsorption configurations. The minimum energy reaction pathways for diffusion of the Au<sub>20</sub> cluster on graphene surface was calculated using the climbing-image nudged elastic band (CI-NEB) method.

**Table A3-1.** Length distribution of as-synthesized nitrogen-doped CNT fibers, oxidized NCNCs, and separated NCNCs obtained from TEM images and DLS analysis.

	TEM <sup>a</sup>	DLS <sup>b</sup>
As-synthesized fiber	4890 ± 2584 nm	5601 ± 3475 nm
Oxidized NCNC	782 ± 585 nm	188 ± 86 nm
Separated NCNC	216 ± 88 nm	148 ± 82 nm

<sup>a</sup> Based on ~300 measurements from TEM images.

<sup>b</sup> DLS analysis of the hydrodynamic volume of nanoparticles based on the assumption of a spherical shape of nanoparticles. The indicated values may not reflect the real lengths

**Table A3-2.** Elemental composition of as-synthesized nitrogen-doped CNTs, separated NCNCs and NCNCs functionalized with GNPs based on energy-dispersive X-ray (EDX) spectroscopy.

Element (Shell)	As-synthesized fiber	Separated NCNC	NCNC+ GNP
	At %	At %	At %
C (K)	97.94	93.34	82.14
O (K)	0.77	6.43	6.07
Fe (K)	1.29	0.23	—
Au (M)	—	—	11.79

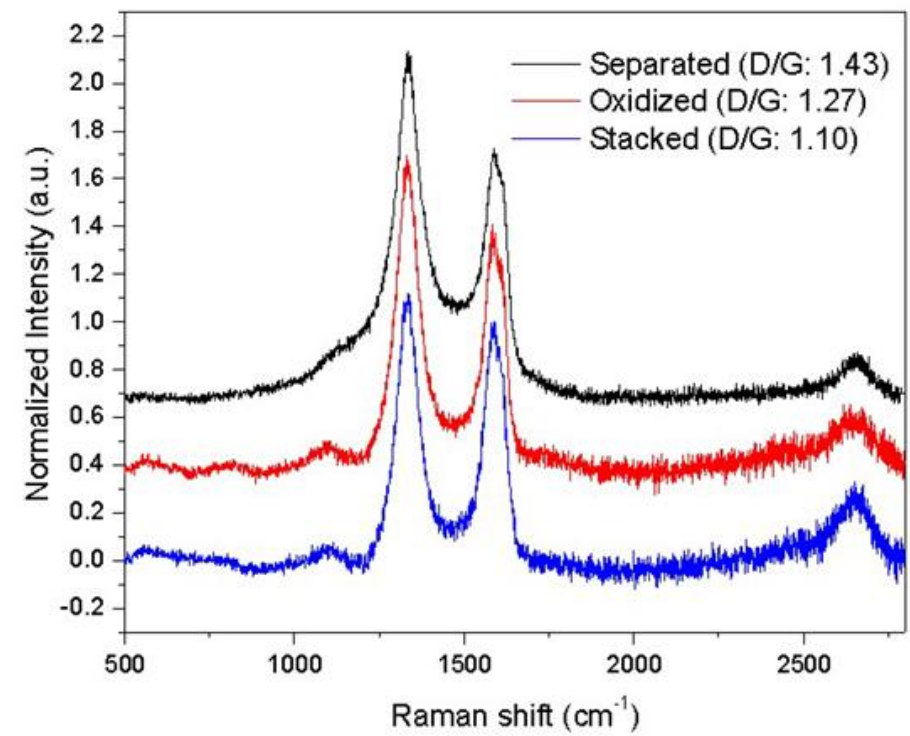


**Figure A3-1.** Raman spectra of as-synthesized stacked NCNCs (blue), oxidized NCNCs (red) and separated NCNCs (black). The corresponding D to G band ratios are shown in the parentheses.

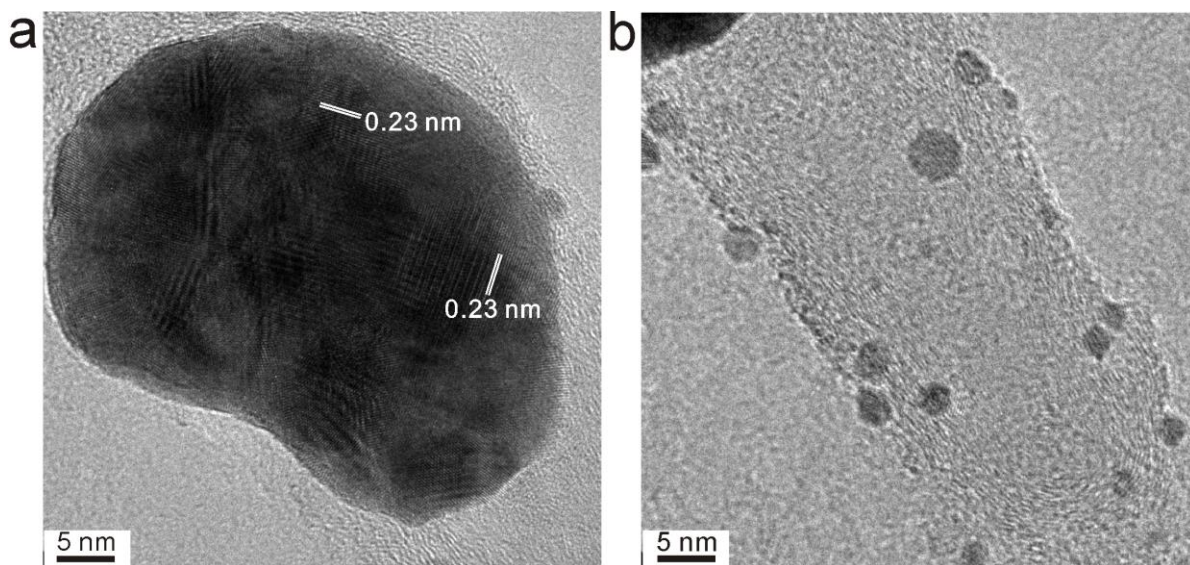


**Figure A3-2.** Magnified high-resolution TEM images of the corked NCNC in Figure 1d, focused on (a) the GNP, and (b) the nanocup. A citrate coating layer was typically observed on the outer surface of GNPs, but not on the inner surface in the cups, suggesting a direct interaction between GNPs and NCNCs. Small gold nanocrystals were also found sparsely bound on the graphitic sidewalls of the nanocups, however, they failed to grow into large nanoparticles, possibly due to the scarcity of functional groups on the sidewalls.

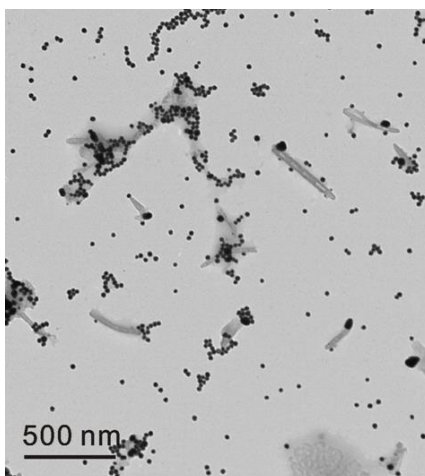


**Figure A3-3.** TEM image of the supernatant solution of the GNP reduction reaction. Free GNPs are somewhat smaller than the GNPs bound to the NCNCs, because of the strong binding of GNPs toward NCNCs, GNPs tend to aggregate on the surface of NCNCs.

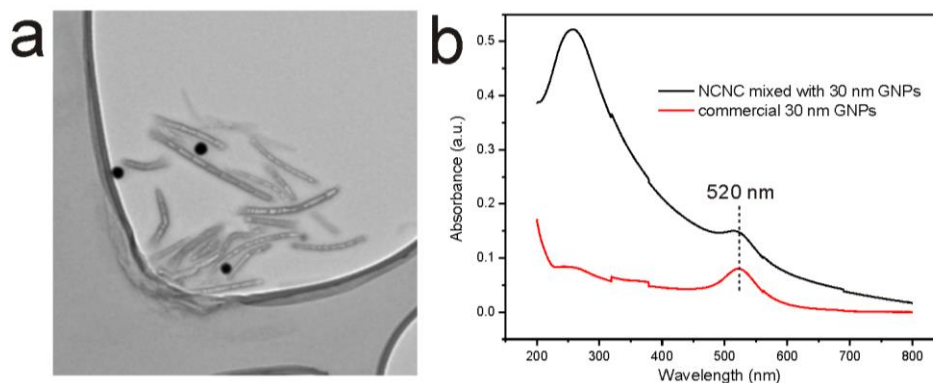


**Figure A3-4.** (a) TEM images of NCNC mixed with commercial 30 nm GNPs. (b) UV-Vis spectra of NCNC mixed with commercial 30 nm GNPs (black) and free commercial GNPs (red). The TEM image shows that the commercial citrate-coated GNPs are not directly attached on the NCNCs, but leaving a gap in between, possibly due to the citrate coating layer. The SPR band of the GNPs did not shift after mixing with NCNCs, indicating the absence of electronic interaction between GNPs and NCNCs.

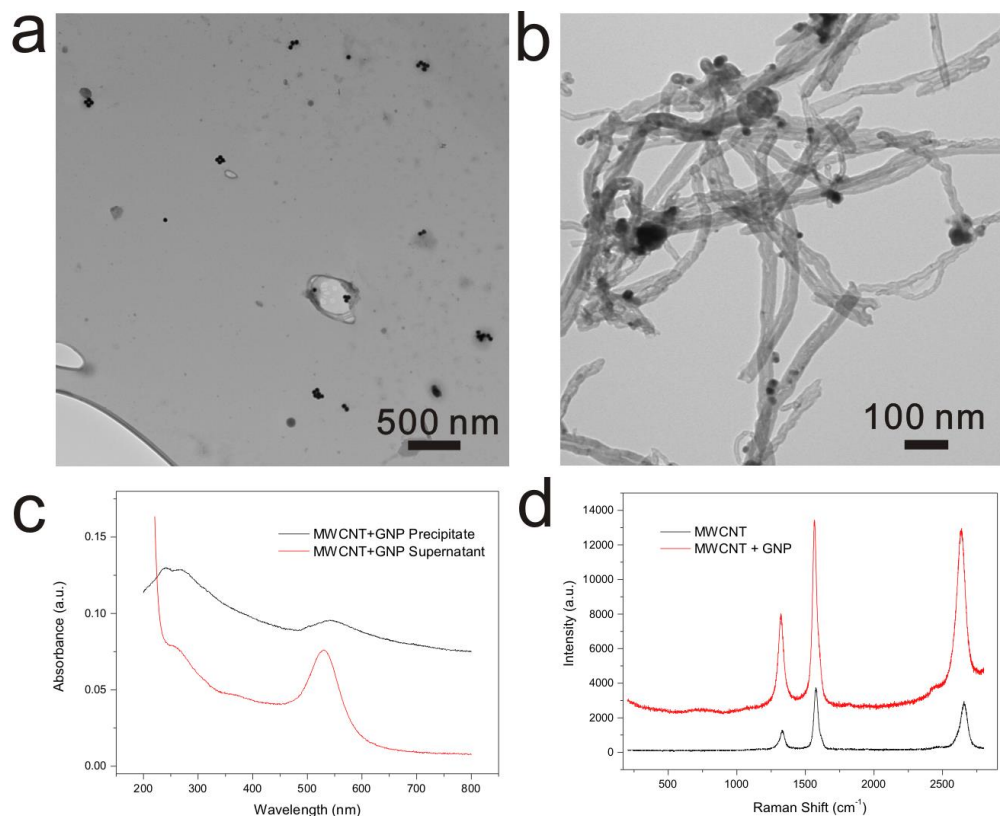


**Figure A3-5.** TEM images of the supernatant (a) and the precipitate (b) of treated MWCNTs decorated with GNPs by reduction. (c) UV-Vis spectra of the supernatant and precipitate of MWCNT+GNP. (d) Raman spectra of MWCNTs decorated with GNPs (red) compared to MWCNTs only.

Undoped MWCNTs were treated following the same procedure as the one used to separate NCNCs: 4 h acid oxidation by 3:1 v/v  $\text{H}_2\text{SO}_4/\text{HNO}_3$  and 8 h of probe-tip sonication. The MWCNTs do not tend to be shortened by the separation procedures. After the GNP formation reaction and the subsequent centrifugation, most of the GNPs were free in the supernatant, only a few GNPs were physically attached on the MWCNTs, causing no red-shift of their SPR bands. The weak physical adsorption of GNPs on MWCNTs did not incur significant SERS effect.

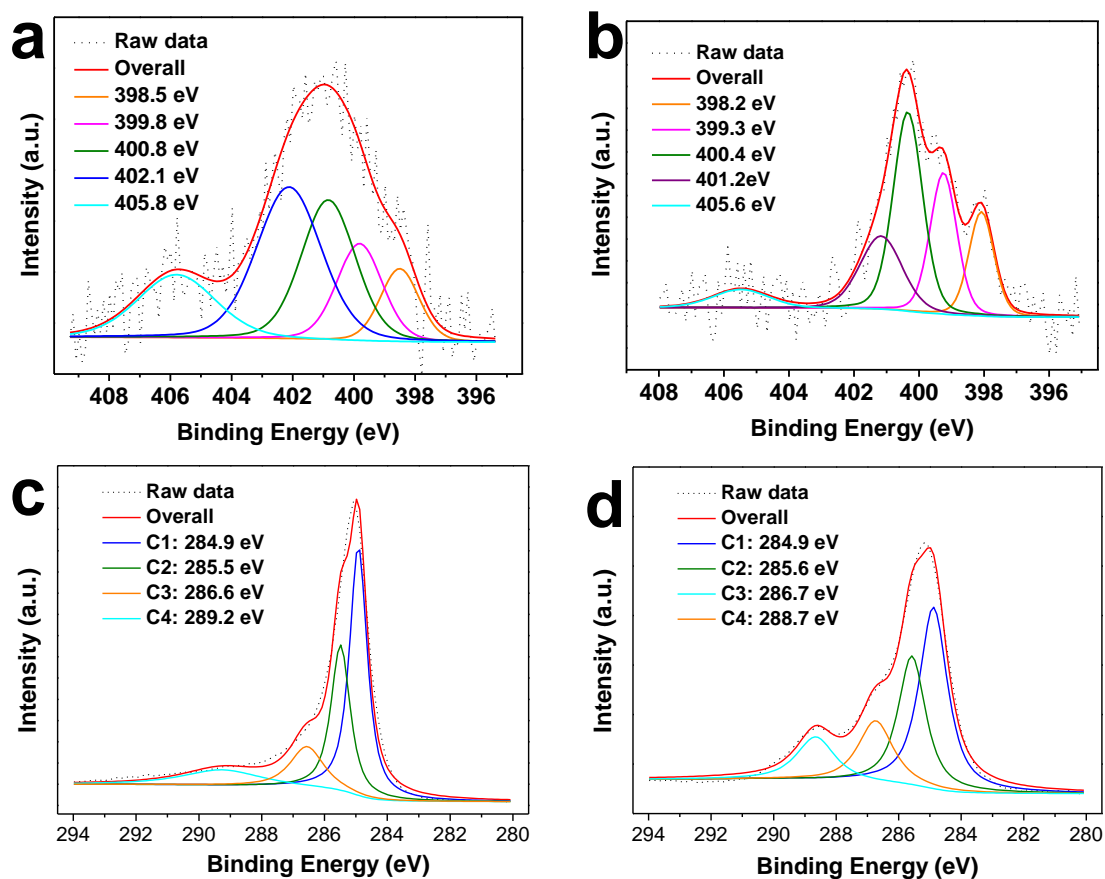


**Figure A3-6.** X-ray photoelectron spectra (XPS) of N1s peak of NCNCs before (a) and after (b) coking with GNPs, and C1s peak of NCNCs before (c) and after (d) functionalization of GNPs. The carbon 1s profile is shown in (c,d). The peaks at 284.9 eV and 285.5 eV were assigned to graphitic  $sp^2$  carbon and C – N structures, respectively. After the GNP functionalization, the peaks corresponding to C – O and C = O structures at 286.7 eV and ~289 eV significantly increased, indicating the oxidation of carbon atoms by chloroauric acid.

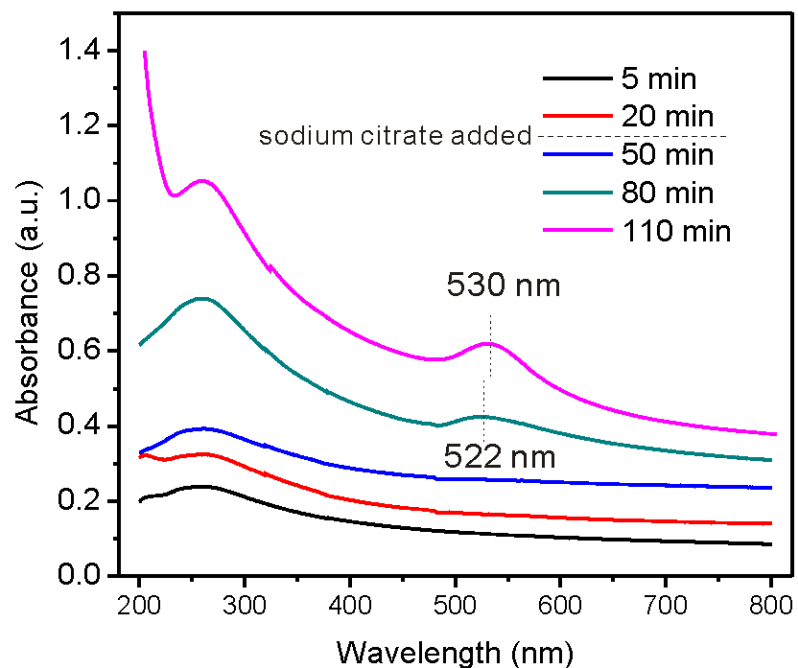


**Figure A3-7.** UV-Vis spectra of NCNCs with GNPs sampled at different reaction times. The sodium citrate was added 20 min after the incubation of NCNCs with  $\text{HAuCl}_4$ .

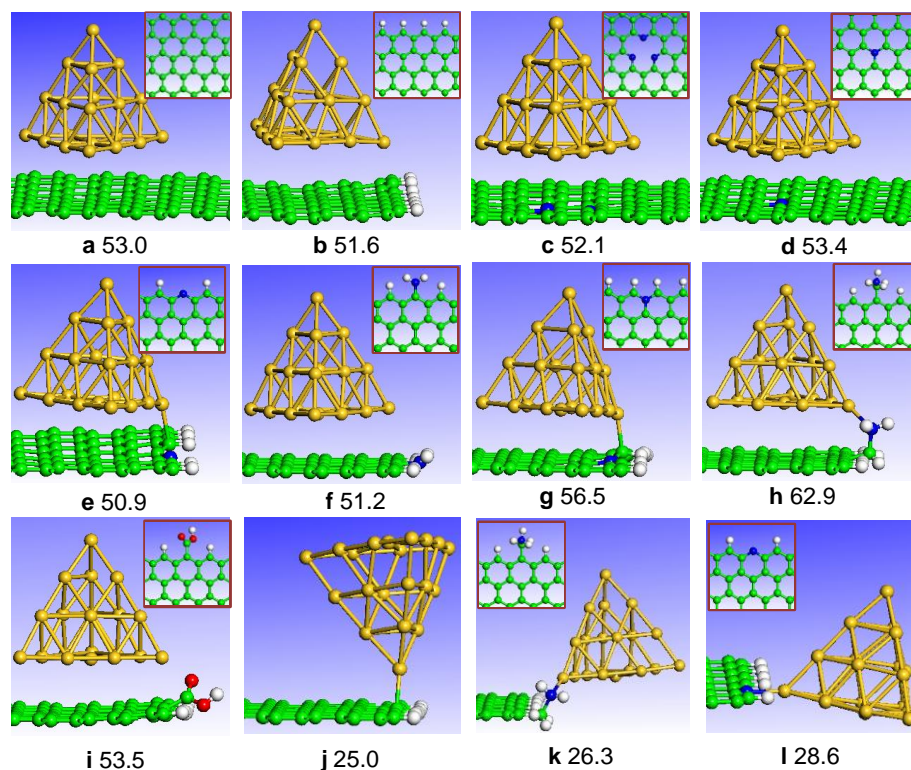


**Figure A3-8.** Pictorial views of the atomic configurations corresponding to adsorption of a  $\text{Au}_{20}$  cluster: (a) on a  $(7 \times 11)$  graphene flake in the central region of the flake; (b) on the graphene flake near the hydrogen terminated zigzag graphene edge; (c) above a graphene defect functionalized with three pyridinic N atoms; (d) above a substitutional N (graphitic N) on the graphene surface; (e) above a pyridinic N on the graphene edge, (f) above an aromatic amine group on the graphene edge; (g) above a graphitic N on the graphene edge; (h) above a  $\text{CH}_2\text{NH}_2$  group on the graphene edge; (i) near the edge of a graphene sheet functionalized with a carboxylic group; (j) attached to the edge of a bare graphene sheet; (k) attached to the amine group on the edge of a graphene sheet; (l) attached to the pyridinic N on the edge of graphene sheet. Insets: top view of the bare graphene sheet with the corresponding bare or functionalized graphene flake. For each configuration the corresponding adsorption energy (in kcal/mol) of the  $\text{Au}_{20}$  cluster is also provided. Legend of atoms: green; N, blue; H, white; O, red; and Au, orange.

Because individual NCNCs have multi-walled structure with diameters of several tens of nanometers, their surface has relatively small curvatures and thus can locally be represented by flat graphene sheets. The Au<sub>20</sub> cluster was placed either at the center or close to the edge of the flake and interactions with different functional groups were probed by evaluation of the corresponding adsorption energies (kcal/mol). Without nitrogen-doping, only the long-range dispersion interactions between the aromatic carbon rings and Au atoms are responsible for the adsorption. As a result there is a slight drop in adsorption energy of Au<sub>20</sub> from the center to the edge of the graphene sheet (a, b). However, when either pyridinic or graphitic nitrogen replaced the carbon atoms in the center, no remarkable difference in adsorption energy was observed (c, d). When Au<sub>20</sub> was adsorbed at the edge of graphene, the adsorption energy varies depending on the edge functional groups. Compared with undoped graphene, the graphene edge functionalized with pyridinic N or aromatic amine does not seem to increase the adsorption energy (e, f). There is a small increase when Au<sub>20</sub> is close to graphitic N on the edge when the apex atom of Au cluster binds with a neighboring C of the graphitic N (g). However, when the graphene edge is functionalized with an aliphatic primary amine (-CH<sub>2</sub>NH<sub>2</sub>), a more significant increase in adsorption energy by over 10 kcal/mol is observed (h). In this case the -CH<sub>2</sub>NH<sub>2</sub> group is extruding out of the graphene plane such that the electron pair from N is unconjugated and forms a covalent bond with Au<sub>20</sub>. By comparison, the carboxylic groups that might exist on the surface from the oxidation process increase only slightly the adsorption energy, even though the oxygen atoms are also located out of graphene plane (i). Besides the binding configuration of Au<sub>20</sub> on the graphitic surface, nitrogen functional groups at the edge can also provide initial or intermediate binding states for the Au<sub>20</sub> cluster. Compared with the bare graphene edge terminated with hydrogen (j), the side interaction of Au<sub>20</sub> can be remarkably enhanced by amine

and pyridinic N groups, with covalent bonds formed between an apex Au atom and N (k,l). Although this side interaction is much weaker than the on-surface interaction due to smaller contributions of Au-C dispersion interactions, the observed enhancement effect from the edge nitrogen groups can be cumulative in the case of the multi-layer graphitic edges at the open rims of NCNCs.

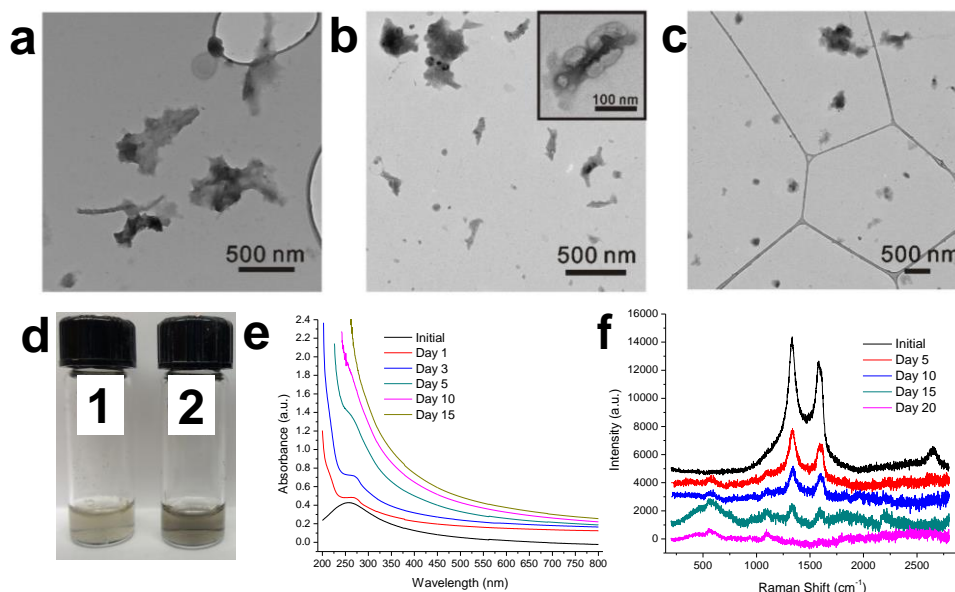


**Figure A3-9.** Degradation of separated NCNCs with hMPO in the presence of H<sub>2</sub>O<sub>2</sub> and NaCl. (a – c) TEM images at (a) Day 5, (b) Day 10 and (c) Day 20. (d) Photograph of (1) the active sample of NCNCs treated with hMPO in the presence of H<sub>2</sub>O<sub>2</sub> and NaCl for 20 days, and (2) the control sample of NCNCs treated only with H<sub>2</sub>O<sub>2</sub> after 20 days; (2) the control sample of NCNCs treated with H<sub>2</sub>O<sub>2</sub> only for 20 days. (e) UV-Vis spectra and (f) Raman spectra of the activated sample during degradation.

TEM images reveal early degradative deformation of tubular structure. At Day 5, amorphous carbonaceous materials were seen surrounding the remaining nanocups. At Day 10, almost all nanocups were deformed, leaving mostly amorphous flakes that roughly retained the shape of original cups. The carbonaceous flakes continued to shrink in their sizes until almost completely degraded after 20 days. Compared to the H<sub>2</sub>O<sub>2</sub> control (at the same initial NCNC concentration incubated without MPO, the brown color of the NCNCs suspension has largely faded, corresponding to the gradual diminishing of the  $\pi$  electron band at 260 nm from UV-Vis spectra. The degradation was confirmed by Raman spectra which showed a complete suppression of D and G bands after 20 days.

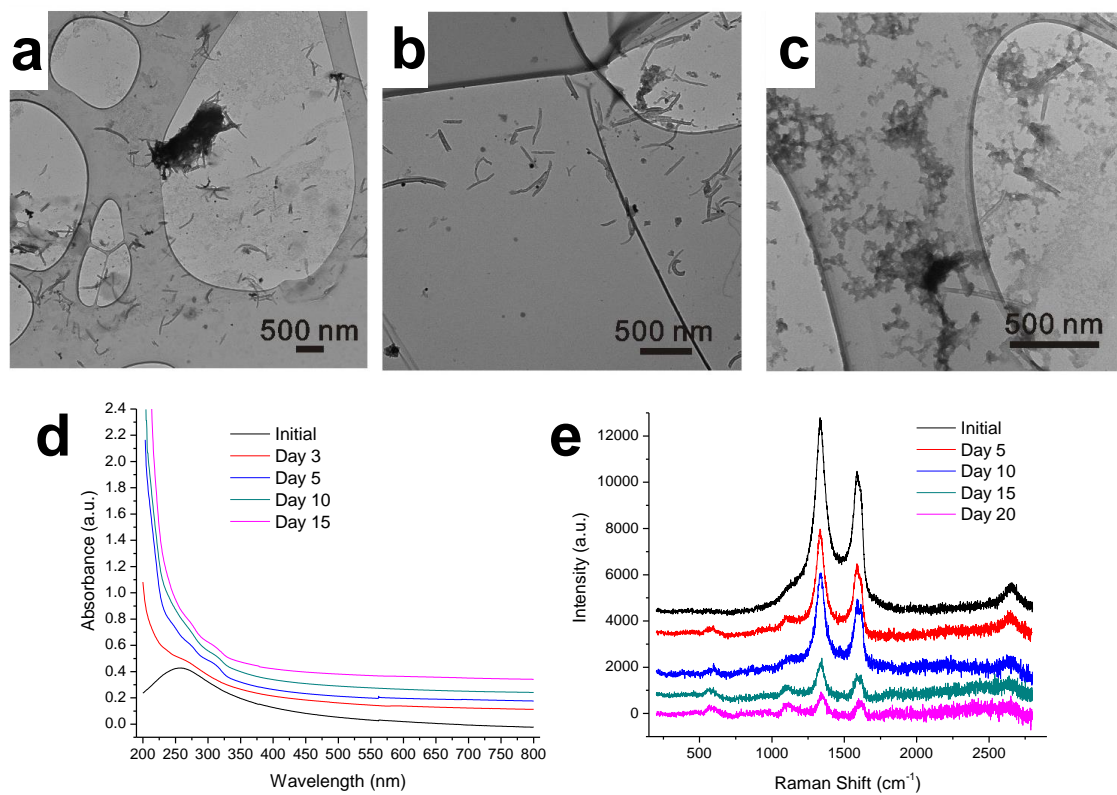


**Figure A3-10.** Degradation of separated NCNCs in the NaClO control, with only NaClO as oxidant. (a – c) TEM images at (a) Day 5, (b) Day 10 and (c) Day 15. (d) UV-Vis spectra and (f) Raman spectra of the sample during degradation. Incomplete degradation was observed on the sample treated with NaClO, the peak at 290 nm indicates the presence of NaClO.

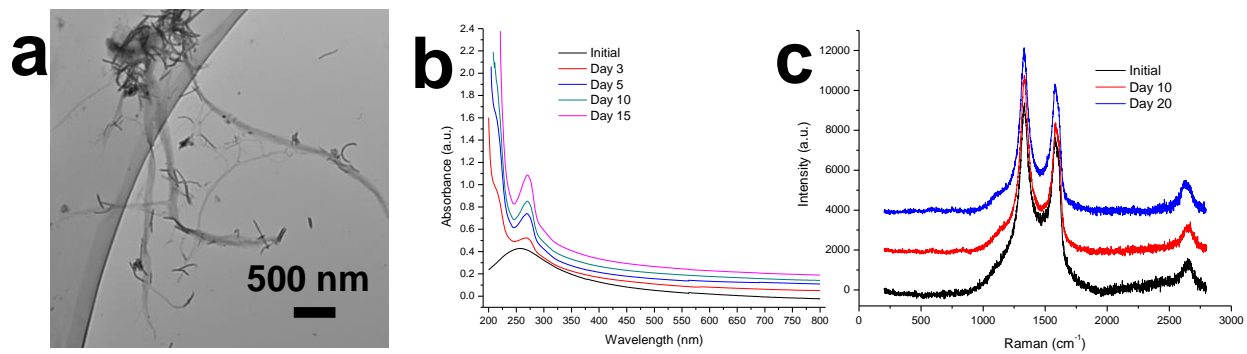


**Figure A3-11.** Separated NCNCs treated only with  $\text{H}_2\text{O}_2$ . (a) TEM image at Day 20; (b) UV-Vis spectra and (c) Raman spectra of the sample during treatment. No significant degradation was observed on the NCNC sample treated only with  $\text{H}_2\text{O}_2$ .

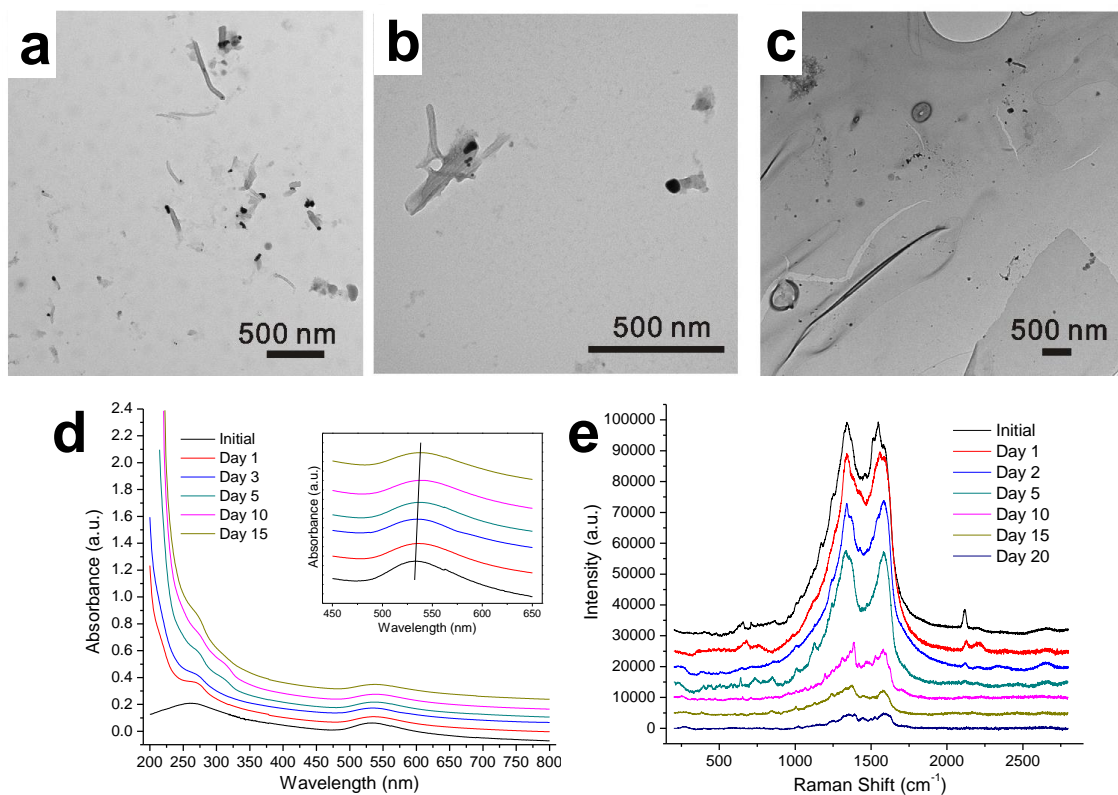


**Figure A3-12.** Degradation of GNP-corked NCNCs with NaClO as oxidant. (a – c) TEM images at (a) Day 5, (b) Day 10 and (c) Day 15. (d) UV-Vis spectra and (f) Raman spectra of the sample during degradation. NaClO only partially degrades the NCNCs by oxidizing the graphitic shells but does not release the GNPs from the nanocups, which is reflected by unchanged SPR bands and a monotonic decrease of D and G Raman bands.

TEM images show that the GNPs were still corking on the remaining NCNCs after 5 and 10 days. Till most of the NCNCs were degraded after 20 days, the GNPs remained isolated without apparent agglomeration, which is also evidenced by UV-Vis spectra showing no red-shift of their SPR bands. The robust binding of GNPs on nanocups induced a lasting surface-enhanced Raman effect that decayed slowly due to only NCNC degradation.

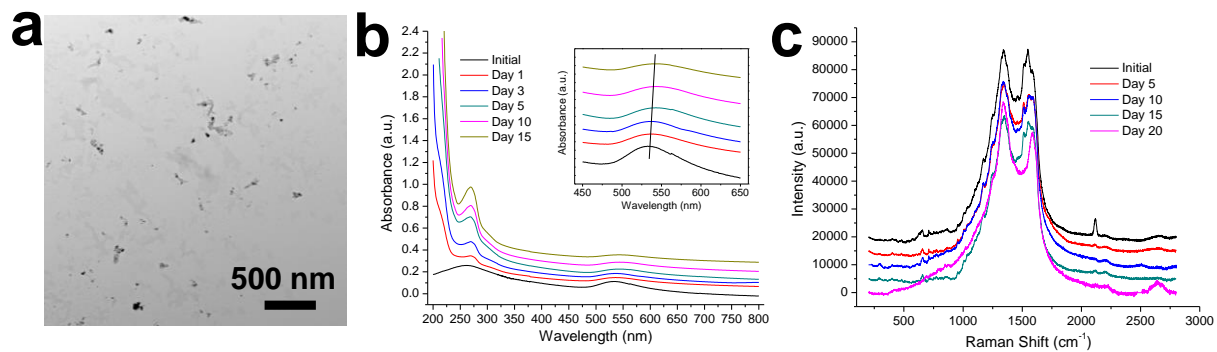


**Figure A3-13.** GNP-corked NCNCs treated with  $\text{H}_2\text{O}_2$  as a control. (a) TEM image at Day 20. The GNPs are still bound to NCNCs showing no apparent degradation. (b) UV-Vis spectra and (c) Raman spectra of the sample during the period of 20 days.

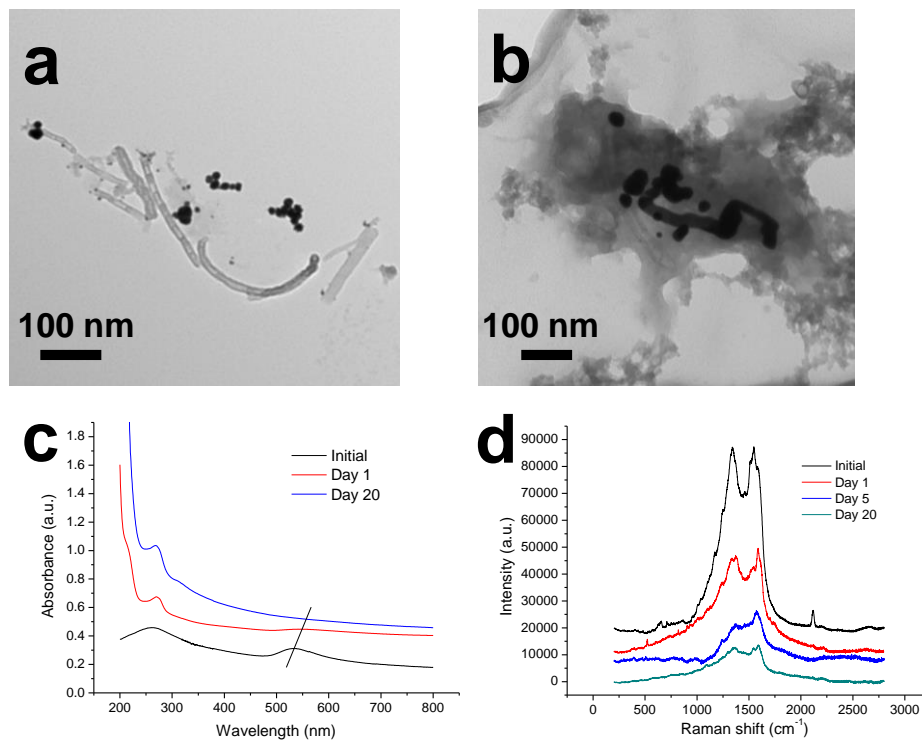


**Figure A3-14.** GNP-corked NCNCs treated with hMPO and  $\text{H}_2\text{O}_2$ . (a,b) TEM image at (a) Day 5 and (b) Day 20. The GNPs were detached from NCNCs forming large agglomerates, but NCNCs were not significantly degraded. (c) UV-Vis spectra and (d) Raman spectra of the sample during the degradation process. The detachment and agglomeration of GNPs are reflected by the red-shift and disappearance of GNPs' surface plasmon resonance (SPR) bands and the loss of the surface-enhanced Raman scattering (SERS) effect.

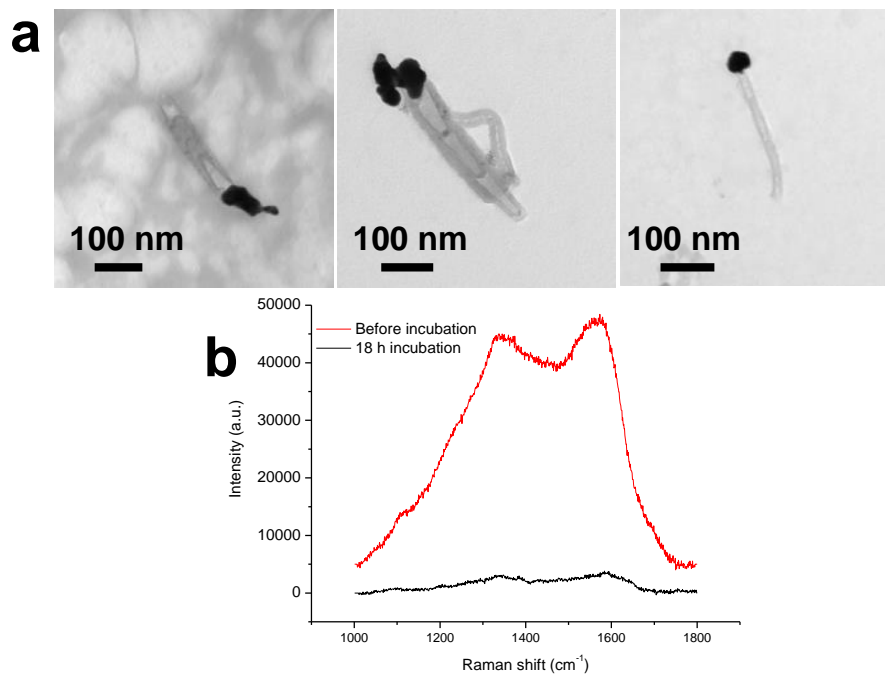


**Figure A3-15.** (a) TEM images showing that most of the GNPs were still attached to NCNCs in the sample treated with neutrophils without incubation. (b) Raman spectra of the NCNC sample treated with neutrophils before incubation (red) and after 18 h incubation (black).

## APPENDIX B

### PUBLICATIONS AND POSTER PRESENTATIONS

#### B1. PUBLICATIONS

- (1) Zhao, Y.; Allen, B. L.; Star, A., Enzymatic degradation of multiwalled carbon nanotubes. *J. Phys. Chem. A* **2011**, *115*, 9536-9544.
- (2) Zhao, Y.; Tang, Y.; Chen, Y.; Star, A., Corking carbon nanotube cups with gold nanoparticles. *ACS Nano* **2012**, *6*, 6912-6921.
- (3) Zhao, Y.; Tang, Y.; Star, A., Synthesis and Functionalization of Nitrogen-doped Carbon Nanotube Cups with Gold Nanoparticles as Cork Stoppers. *J. Vis. Exp.* **2013**, e50383.
- (4) Kotchey, G. P.; Zhao, Y.; Kagan, V. E.; Star, A., Peroxidase-mediated biodegradation of carbon nanotubes in vitro and in vivo. *Adv. Drug Deliv. Rev.* **2013**, *65*, 1921-1932.
- (5) Chiu, C. F.; Barth, B. A.; Kotchey, G. P.; Zhao, Y.; Gogick, K. A.; Saidi, W. A.; Petoud, S.; Star, A., Enzyme-Catalyzed Oxidation Facilitates the Return of Fluorescence for Single-Walled Carbon Nanotubes. *J. Am. Chem. Soc.* **2013**, *135*, 13356-13364.

- (6) Tang, Y.; Burkert, S. C.; Zhao, Y.; Saidi, W. A.; Star, A., The Effect of Metal Catalyst on the Electrocatalytic Activity of Nitrogen-Doped Carbon Nanotubes. *J. Phys. Chem. C* **2013**, *117*, 25213-25221.
- (7) Chen, Y.; Michael, Z. P.; Kotchey, G. P.; Zhao, Y.; Star, A., Electronic Detection of Bacteria Using Holey Reduced Graphene Oxide. *ACS Appl. Mater. Interfaces* **2014**, *6*, 3805-3810.

## **B2. POSTER PRESENTATIONS**

- (1) 245th ACS National Meeting & Exposition – New Orleans, LA, 04/2013  
— Nitrogen-doped carbon nanotube cups corked with gold nanoparticles.
- (2) 8th Annual Conference on Foundation of Nanoscience – Snowbird, UT, 04/2011  
— Exploring the chemical reactivity of nitrogen-doped carbon nanotube cups.

## BIBLIOGRAPHY

1. Novoselov, K. S.; Geim, A. K.; Morozov, S.; Jiang, D.; Zhang, Y.; Dubonos, S.; Grigorieva, I.; Firsov, A., Electric field effect in atomically thin carbon films. *Science* **2004**, *306*, 666-669.
2. Novoselov, K.; Jiang, D.; Schedin, F.; Booth, T.; Khotkevich, V.; Morozov, S.; Geim, A., Two-dimensional atomic crystals. *Proc. Natl. Acad. Sci. U. S. A.* **2005**, *102*, 10451-10453.
3. Geim, A. K.; Novoselov, K. S., The rise of graphene. *Nat. Mater.* **2007**, *6*, 183-191.
4. Iijima, S., Helical microtubules of graphitic carbon. *Nature* **1991**, *354*, 56-58.
5. Iijima, S.; Ichihashi, T., Single-shell carbon nanotubes of 1-nm diameter. *Nature* **1993**, *363*, 603-605.
6. Baughman, R. H.; Zakhidov, A. A.; de Heer, W. A., Carbon nanotubes--the route toward applications. *Science* **2002**, *297*, 787-792.
7. Odom, T. W.; Huang, J.-L.; Kim, P.; Lieber, C. M., Structure and electronic properties of carbon nanotubes. *J. Phys. Chem. B* **2000**, *104*, 2794-2809.
8. Tasis, D.; Tagmatarchis, N.; Bianco, A.; Prato, M., Chemistry of carbon nanotubes. *Chem. Rev.* **2006**, *106*, 1105-1136.
9. Sgobba, V.; Guldi, D. M., Carbon nanotubes—electronic/electrochemical properties and application for nanoelectronics and photonics. *Chem. Soc. Rev.* **2009**, *38*, 165-184.

10. Dai, H., Carbon nanotubes: synthesis, integration, and properties. *Acc. Chem. Res.* **2002**, *35*, 1035-1044.
11. Bachilo, S. M.; Strano, M. S.; Kittrell, C.; Hauge, R. H.; Smalley, R. E.; Weisman, R. B., Structure-assigned optical spectra of single-walled carbon nanotubes. *Science* **2002**, *298*, 2361-2366.
12. Rao, C.; Voggu, R.; Govindaraj, A., Selective generation of single-walled carbon nanotubes with metallic, semiconducting and other unique electronic properties. *Nanoscale* **2009**, *1*, 96-105.
13. Odom, T. W.; Huang, J.-L.; Kim, P.; Lieber, C. M., Atomic structure and electronic properties of single-walled carbon nanotubes. *Nature* **1998**, *391*, 62-64.
14. Wilder, J. W.; Venema, L. C.; Rinzler, A. G.; Smalley, R. E.; Dekker, C., Electronic structure of atomically resolved carbon nanotubes. *Nature* **1998**, *391*, 59-62.
15. Kim, P.; Odom, T. W.; Huang, J.-L.; Lieber, C. M., Electronic density of states of atomically resolved single-walled carbon nanotubes: Van Hove singularities and end states. *Phys. Rev. Lett.* **1999**, *82*, 1225.
16. Kauffman, D. R.; Sorescu, D. C.; Schofield, D. P.; Allen, B. L.; Jordan, K. D.; Star, A., Understanding the sensor response of metal-decorated carbon nanotubes. *Nano Lett.* **2010**, *10*, 958-963.
17. Kiang, C.-H.; Endo, M.; Ajayan, P.; Dresselhaus, G.; Dresselhaus, M., Size effects in carbon nanotubes. *Phys. Rev. Lett.* **1998**, *81*, 1869.
18. Kim, S. N.; Rusling, J. F.; Papadimitrakopoulos, F., Carbon nanotubes for electronic and electrochemical detection of biomolecules. *Adv. Mater.* **2007**, *19*, 3214-3228.
19. Ajayan, P., Nanotubes from carbon. *Chem. Rev.* **1999**, *99*, 1787-1800.

20. Bianco, A.; Wu, W.; Pastorin, G.; Klumpp, C.; Lacerda, L.; Partidos, C. D.; Kostarelos, K.; Prato, M., Carbon Nanotube-based Vectors for Delivering Immunotherapeutics and Drugs. In *Nanotechnologies for the life sciences*, Wiley-VCH Verlag GmbH & Co. KGaA: 2007.
21. Journet, C.; Maser, W.; Bernier, P.; Loiseau, A.; De La Chapelle, M. L.; Lefrant, d. l. S.; Deniard, P.; Lee, R.; Fischer, J., Large-scale production of single-walled carbon nanotubes by the electric-arc technique. *Nature* **1997**, *388*, 756-758.
22. Guo, T.; Nikolaev, P.; Thess, A.; Colbert, D.; Smalley, R., Catalytic growth of single-walled nanotubes by laser vaporization. *Chem. Phys. Lett.* **1995**, *243*, 49-54.
23. Thess, A.; Lee, R.; Nikolaev, P.; Dai, H.; Petit, P.; Robert, J.; Xu, C.; Lee, Y. H.; Kim, S. G.; Rinzler, A. G.; Colbert, D. T.; Scuseria, G. E.; Tománek, D.; Fischer, J. E.; Smalley, R. E., Crystalline ropes of metallic carbon nanotubes. *Science* **1996**, *273*, 483-487.
24. Andrews, R.; Jacques, D.; Qian, D.; Rantell, T., Multiwall carbon nanotubes: synthesis and application. *Acc. Chem. Res.* **2002**, *35*, 1008-1017.
25. Li, X.; Cai, W.; An, J.; Kim, S.; Nah, J.; Yang, D.; Piner, R.; Velamakanni, A.; Jung, I.; Tutuc, E., Large-area synthesis of high-quality and uniform graphene films on copper foils. *Science* **2009**, *324*, 1312-1314.
26. Cassell, A. M.; Raymakers, J. A.; Kong, J.; Dai, H., Large scale CVD synthesis of single-walled carbon nanotubes. *J. Phys. Chem. B* **1999**, *103*, 6484-6492.
27. Kong, J.; Soh, H. T.; Cassell, A. M.; Quate, C. F.; Dai, H., Synthesis of individual single-walled carbon nanotubes on patterned silicon wafers. *Nature* **1998**, *395*, 878-881.
28. Journet, C.; Bernier, P., Production of carbon nanotubes. *Appl. Phys. A-Mater.* **1998**, *67*, 1-9.

29. Kauffman, D. R.; Star, A., Carbon Nanotube Gas and Vapor Sensors. *Angew. Chem. Int. Ed.* **2008**, *47*, 6550-6570.
30. Allen, B. L.; Kichambare, P. D.; Star, A., Carbon Nanotube Field-Effect-Transistor-Based Biosensors. *Adv. Mater.* **2007**, *19*, 1439-1451.
31. Kauffman, D. R.; Shade, C. M.; Uh, H.; Petoud, S.; Star, A., Decorated carbon nanotubes with unique oxygen sensitivity. *Nat. Chem.* **2009**, *1*, 500-506.
32. Chen, Y.; Michael, Z. P.; Kotchey, G. P.; Zhao, Y.; Star, A., Electronic Detection of Bacteria Using Holey Reduced Graphene Oxide. *ACS Appl. Mater. Interfaces* **2014**, *6*, 3805-3810.
33. Vedala, H.; Chen, Y.; Cecioni, S.; Imberty, A.; Vidal, S.; Star, A., Nanoelectronic detection of lectin-carbohydrate interactions using carbon nanotubes. *Nano Lett.* **2010**, *11*, 170-175.
34. Sohn, J. I.; Lee, S.; Song, Y.-H.; Choi, S.-Y.; Cho, K.-I.; Nam, K.-S., Patterned selective growth of carbon nanotubes and large field emission from vertically well-aligned carbon nanotube field emitter arrays. *Appl. Phys. Lett.* **2001**, *78*, 901-903.
35. Bonard, J. M.; Salvétat, J.-P.; Stockli, T.; de Heer, W. A.; Forró L.; Châtelain, A., Field emission from single-wall carbon nanotube films. *Appl. Phys. Lett.* **1998**, *73*, 918-920.
36. Bonard, J.-M.; Croci, M.; Klinke, C.; Kurt, R.; Noury, O.; Weiss, N., Carbon nanotube films as electron field emitters. *Carbon* **2002**, *40*, 1715-1728.
37. Lipomi, D. J.; Vosgueritchian, M.; Tee, B. C.; Hellstrom, S. L.; Lee, J. A.; Fox, C. H.; Bao, Z., Skin-like pressure and strain sensors based on transparent elastic films of carbon nanotubes. *Nat. Nanotechnol.* **2011**, *6*, 788-792.

38. Kang, S. J.; Kocabas, C.; Ozel, T.; Shim, M.; Pimparkar, N.; Alam, M. A.; Rotkin, S. V.; Rogers, J. A., High-performance electronics using dense, perfectly aligned arrays of single-walled carbon nanotubes. *Nat. Nanotechnol.* **2007**, *2*, 230-236.
39. Wu, Z.; Chen, Z.; Du, X.; Logan, J. M.; Sippel, J.; Nikolou, M.; Kamaras, K.; Reynolds, J. R.; Tanner, D. B.; Hebard, A. F., Transparent, conductive carbon nanotube films. *Science* **2004**, *305*, 1273-1276.
40. Blake, R.; Gun'ko, Y. K.; Coleman, J.; Cadek, M.; Fonseca, A.; Nagy, J. B.; Blau, W. J., A generic organometallic approach toward ultra-strong carbon nanotube polymer composites. *J. Am. Chem. Soc.* **2004**, *126*, 10226-10227.
41. Hwang, G. L.; Hwang, K. C., Carbon nanotube reinforced ceramics. *J. Mater. Chem.* **2001**, *11*, 1722-1725.
42. Gong, X.; Liu, J.; Baskaran, S.; Voise, R. D.; Young, J. S., Surfactant-assisted processing of carbon nanotube/polymer composites. *Chem. Mater.* **2000**, *12*, 1049-1052.
43. Liu, T.; Phang, I. Y.; Shen, L.; Chow, S. Y.; Zhang, W.-D., Morphology and mechanical properties of multiwalled carbon nanotubes reinforced nylon-6 composites. *Macromolecules* **2004**, *37*, 7214-7222.
44. Frackowiak, E.; Gautier, S.; Gaucher, H.; Bonnamy, S.; Beguin, F., Electrochemical storage of lithium in multiwalled carbon nanotubes. *Carbon* **1999**, *37*, 61-69.
45. Li, W.; Liang, C.; Zhou, W.; Qiu, J.; Zhou, Z.; Sun, G.; Xin, Q., Preparation and characterization of multiwalled carbon nanotube-supported platinum for cathode catalysts of direct methanol fuel cells. *J. Phys. Chem. B* **2003**, *107*, 6292-6299.

46. Kauffman, D. R.; Tang, Y.; Kichambare, P. D.; Jackovitz, J. F.; Star, A., Long-term performance of Pt-decorated carbon nanotube cathodes in phosphoric acid fuel cells. *Energy & Fuels* **2010**, *24*, 1877-1881.
47. Bianco, A.; Kostarelos, K.; Prato, M., Applications of carbon nanotubes in drug delivery. *Curr. Opin. Chem. Biol.* **2005**, *9*, 674-679.
48. Prato, M.; Kostarelos, K.; Bianco, A., Functionalized carbon nanotubes in drug design and discovery. *Acc. Chem. Res.* **2007**, *41*, 60-68.
49. Liu, Z.; Chen, K.; Davis, C.; Sherlock, S.; Cao, Q.; Chen, X.; Dai, H., Drug delivery with carbon nanotubes for in vivo cancer treatment. *Cancer Res.* **2008**, *68*, 6652-6660.
50. Chen, J.; Chen, S.; Zhao, X.; Kuznetsova, L. V.; Wong, S. S.; Ojima, I., Functionalized Single-Walled Carbon Nanotubes as Rationally Designed Vehicles for Tumor-Targeted Drug Delivery. *J. Am. Chem. Soc.* **2008**, *130*, 16778-16785.
51. Wu, W.; Wieckowski, S.; Pastorin, G.; Benincasa, M.; Klumpp, C.; Briand, J. P.; Gennaro, R.; Prato, M.; Bianco, A., Targeted delivery of amphotericin B to cells by using functionalized carbon nanotubes. *Angew. Chem. Int. Ed.* **2005**, *44*, 6358-6362.
52. Lavan, D. A.; McGuire, T.; Langer, R., Small-scale systems for in vivo drug delivery. *Nat. Biotechnol.* **2003**, *21*, 1184-1191.
53. Kim, B. M.; Qian, S.; Bau, H. H., Filling Carbon Nanotubes with Particles. *Nano Lett.* **2005**, *5*, 873-878.
54. Pastorin, G.; Wu, W.; Wieckowski, S.; Briand, J.-P.; Kostarelos, K.; Prato, M.; Bianco, A., Double functionalisation of carbon nanotubes for multimodal drug delivery. *Chem. Commun.* **2006**, 1182-1184.

55. Wei, Z.; Kondratenko, M.; Dao, L. H.; Perepichka, D. F., Rectifying diodes from asymmetrically functionalized single-wall carbon nanotubes. *J. Am. Chem. Soc.* **2006**, *128*, 3134-3135.
56. Datsyuk, V.; Kalyva, M.; Papagelis, K.; Parthenios, J.; Tasis, D.; Siokou, A.; Kallitsis, I.; Galiotis, C., Chemical oxidation of multiwalled carbon nanotubes. *Carbon* **2008**, *46*, 833-840.
57. Smart, S.; Cassady, A.; Lu, G.; Martin, D., The biocompatibility of carbon nanotubes. *Carbon* **2006**, *44*, 1034-1047.
58. Wepasnick, K. A.; Smith, B. A.; Schrote, K. E.; Wilson, H. K.; Diegelmann, S. R.; Fairbrother, D. H., Surface and structural characterization of multi-walled carbon nanotubes following different oxidative treatments. *Carbon* **2011**, *49*, 24-36.
59. Yang, J. C.; Yen, C. H.; Wang, W. J.; Horng, J. J.; Tsai, Y. P., Assessment of adequate sodium hypochlorite concentration for pre-oxidization of multi-walled carbon nanotubes. *J. Chem. Technol. Biotechnol.* **2010**, *85*, 699-707.
60. Bianco, A.; Kostarelos, K.; Prato, M., Making carbon nanotubes biocompatible and biodegradable. *Chem. Commun.* **2011**, *47*, 10182-10188.
61. Hu, H.; Bhowmik, P.; Zhao, B.; Hamon, M.; Itkis, M.; Haddon, R., Determination of the acidic sites of purified single-walled carbon nanotubes by acid–base titration. *Chem. Phys. Lett.* **2001**, *345*, 25-28.
62. Liu, J.; Rinzler, A. G.; Dai, H.; Hafner, J. H.; Bradley, R. K.; Boul, P. J.; Lu, A.; Iverson, T.; Shelimov, K.; Huffman, C. B.; Rodriguez-Macias, F.; Shon, Y.-S.; Lee, T. R.; Colbert, D. T.; Smalley, R. E., Fullerene Pipes. *Science* **1998**, *280*, 1253-1256.

63. Basiuk, V. A., Reactivity of carboxylic groups on armchair and zigzag carbon nanotube tips: a theoretical study of esterification with methanol. *Nano Lett.* **2002**, *2*, 835-839.
64. Wong, S. S.; Joselevich, E.; Woolley, A. T.; Cheung, C. L.; Lieber, C. M., Covalently functionalized nanotubes as nanometre-sized probes in chemistry and biology. *Nature* **1998**, *394*, 52-55.
65. Valeur, E.; Bradley, M., Amide bond formation: beyond the myth of coupling reagents. *Chem. Soc. Rev.* **2009**, *38*, 606-631.
66. Balasubramanian, K.; Burghard, M., Chemically functionalized carbon nanotubes. *Small* **2005**, *1*, 180-192.
67. Wu, H.-C.; Chang, X.; Liu, L.; Zhao, F.; Zhao, Y., Chemistry of carbon nanotubes in biomedical applications. *J. Mater. Chem.* **2010**, *20*, 1036-1052.
68. Boul, P.; Liu, J.; Mickelson, E.; Huffman, C.; Ericson, L.; Chiang, I.; Smith, K.; Colbert, D.; Hauge, R.; Margrave, J., Reversible sidewall functionalization of buckytubes. *Chem. Phys. Lett.* **1999**, *310*, 367-372.
69. Georgakilas, V.; Kordatos, K.; Prato, M.; Guldi, D. M.; Holzinger, M.; Hirsch, A., Organic functionalization of carbon nanotubes. *J. Am. Chem. Soc.* **2002**, *124*, 760-761.
70. Tagmatarchis, N.; Prato, M., Functionalization of carbon nanotubes via 1, 3-dipolar cycloadditions. *J. Mater. Chem.* **2004**, *14*, 437-439.
71. Bahr, J. L.; Tour, J. M., Highly functionalized carbon nanotubes using in situ generated diazonium compounds. *Chem. Mater.* **2001**, *13*, 3823-3824.
72. Bahr, J. L.; Yang, J.; Kosynkin, D. V.; Bronikowski, M. J.; Smalley, R. E.; Tour, J. M., Functionalization of carbon nanotubes by electrochemical reduction of aryl diazonium salts: a bucky paper electrode. *J. Am. Chem. Soc.* **2001**, *123*, 6536-6542.

73. Kordatos, K.; Da Ros, T.; Bosi, S.; Vázquez, E.; Bergamin, M.; Cusan, C.; Pellarini, F.; Tomberli, V.; Baiti, B.; Pantarotto, D., Novel versatile fullerene synthons. *J. Org. Chem.* **2001**, *66*, 4915-4920.
74. Zhang, W.; Sprafke, J. K.; Ma, M.; Tsui, E. Y.; Sydlik, S. A.; Rutledge, G. C.; Swager, T. M., Modular functionalization of carbon nanotubes and fullerenes. *J. Am. Chem. Soc.* **2009**, *131*, 8446-8454.
75. Zhao, Y.-L.; Stoddart, J. F., Noncovalent functionalization of single-walled carbon nanotubes. *Acc. Chem. Res.* **2009**, *42*, 1161-1171.
76. Nakayama-Ratchford, N.; Bangsaruntip, S.; Sun, X.; Welsher, K.; Dai, H., Noncovalent functionalization of carbon nanotubes by fluorescein-polyethylene glycol: supramolecular conjugates with pH-dependent absorbance and fluorescence. *J. Am. Chem. Soc.* **2007**, *129*, 2448-2449.
77. Liu, Z.; Sun, X.; Nakayama-Ratchford, N.; Dai, H., Supramolecular chemistry on water-soluble carbon nanotubes for drug loading and delivery. *ACS Nano* **2007**, *1*, 50-56.
78. O'Connell, M. J.; Boul, P.; Ericson, L. M.; Huffman, C.; Wang, Y.; Haroz, E.; Kuper, C.; Tour, J.; Ausman, K. D.; Smalley, R. E., Reversible water-solubilization of single-walled carbon nanotubes by polymer wrapping. *Chem. Phys. Lett.* **2001**, *342*, 265-271.
79. Star, A.; Steuerman, D. W.; Heath, J. R.; Stoddart, J. F., Starched carbon nanotubes. *Angew. Chem. Int. Ed.* **2002**, *41*, 2508-2512.
80. Liu, Z.; Davis, C.; Cai, W.; He, L.; Chen, X.; Dai, H., Circulation and long-term fate of functionalized, biocompatible single-walled carbon nanotubes in mice probed by Raman spectroscopy. *Proc. Natl. Acad. Sci.* **2008**, *105*, 1410-1415.

81. Kam, N. W. S.; O'Connell, M.; Wisdom, J. A.; Dai, H., Carbon nanotubes as multifunctional biological transporters and near-infrared agents for selective cancer cell destruction. *Proc. Natl. Acad. Sci. U. S. A.* **2005**, *102*, 11600-11605.
82. Star, A.; Stoddart, J. F.; Steuerman, D.; Diehl, M.; Boukai, A.; Wong, E. W.; Yang, X.; Chung, S. W.; Choi, H.; Heath, J. R., Preparation and properties of polymer-wrapped single-walled carbon nanotubes. *Angew. Chem. Int. Ed.* **2001**, *40*, 1721-1725.
83. Curran, S. A.; Ajayan, P. M.; Blau, W. J.; Carroll, D. L.; Coleman, J. N.; Dalton, A. B.; Davey, A. P.; Drury, A.; McCarthy, B.; Maier, S., A composite from poly (m-phenylenevinylene-co-2, 5-dioctoxy-p-phenylenevinylene) and carbon nanotubes: A novel material for molecular optoelectronics. *Adv. Mater.* **1998**, *10*, 1091-1093.
84. Zheng, M.; Jagota, A.; Semke, E. D.; Diner, B. A.; McLean, R. S.; Lustig, S. R.; Richardson, R. E.; Tassi, N. G., DNA-assisted dispersion and separation of carbon nanotubes. *Nat. Mater.* **2003**, *2*, 338-342.
85. Cao, G.; Wang, Y., *Nanostructures and Nanomaterials: Synthesis, Properties, and Applications*. World Scientific: 2011.
86. Midgley, P.; Weyland, M., 3D electron microscopy in the physical sciences: the development of Z-contrast and EFTEM tomography. *Ultramicroscopy* **2003**, *96*, 413-431.
87. Goldstein, J.; Newbury, D. E.; Echlin, P.; Joy, D. C.; Romig, A. D.; Lyman, C. E.; Fiori, C.; Lifshin, E., *Scanning Electron Microscopy and X-Ray Microanalysis: A Text for Biologists, Materials Scientists, and Geologists*. Springer US: 2011.
88. Binnig, G.; Quate, C. F.; Gerber, C., Atomic force microscope. *Phys. Rev. Lett.* **1986**, *56*, 930.

89. Cappella, B.; Dietler, G., Force-distance curves by atomic force microscopy. *Surf. Sci. Rep.* **1999**, *34*, 1-104.
90. Wang, K.; Ruan, J.; Song, H.; Zhang, J.; Wo, Y.; Guo, S.; Cui, D., Biocompatibility of graphene oxide. *Nanoscale Res Lett* **2011**, *6*.
91. Kotchey, G. P.; Allen, B. L.; Vedala, H.; Yanamala, N.; Kapralov, A. A.; Tyurina, Y. Y.; Klein-Seetharaman, J.; Kagan, V. E.; Star, A., The enzymatic oxidation of graphene oxide. *ACS Nano* **2011**, *5*, 2098-2108.
92. Stankovich, S.; Dikin, D. A.; Piner, R. D.; Kohlhaas, K. A.; Kleinhammes, A.; Jia, Y.; Wu, Y.; Nguyen, S. T.; Ruoff, R. S., Synthesis of graphene-based nanosheets via chemical reduction of exfoliated graphite oxide. *Carbon* **2007**, *45*, 1558-1565.
93. Attal, S.; Thiruvengadathan, R.; Regev, O., Determination of the concentration of single-walled carbon nanotubes in aqueous dispersions using UV-visible absorption spectroscopy. *Anal. Chem.* **2006**, *78*, 8098-8104.
94. Marković, Z.; Jovanović, S.; Kleut, D.; Romčević, N.; Jokanović, V.; Trajković, V.; Todorović-Marković, B., Comparative study on modification of single wall carbon nanotubes by sodium dodecylbenzene sulfonate and melamine sulfonate superplasticiser. *Appl. Surf. Sci.* **2009**, *255*, 6359-6366.
95. Chen, J.; Hamon, M. A.; Hu, H.; Chen, Y.; Rao, A. M.; Eklund, P. C.; Haddon, R. C., Solution properties of single-walled carbon nanotubes. *Science* **1998**, *282*, 95-98.
96. Kim, U. J.; Furtado, C. A.; Liu, X.; Chen, G.; Eklund, P. C., Raman and IR spectroscopy of chemically processed single-walled carbon nanotubes. *J. Am. Chem. Soc.* **2005**, *127*, 15437-15445.

97. Colthup, N. B.; Daly, L. H.; Wiberley, S. E., *Introduction to infrared and Raman spectroscopy*. Elsevier: 1990.
98. Dresselhaus, M. S.; Jorio, A.; Hofmann, M.; Dresselhaus, G.; Saito, R., Perspectives on carbon nanotubes and graphene Raman spectroscopy. *Nano Lett.* **2010**, *10*, 751-758.
99. Moskovits, M.; Suh, J., Surface selection rules for surface-enhanced Raman spectroscopy: calculations and application to the surface-enhanced Raman spectrum of phthalazine on silver. *J. Phys. Chem.* **1984**, *88*, 5526-5530.
100. Li, M.; Cushing, S. K.; Liang, H.; Suri, S.; Ma, D.; Wu, N., Plasmonic nanorice antenna on triangle Nanoarray for surface-enhanced raman scattering detection of hepatitis B virus DNA. *Anal. Chem.* **2013**, *85*, 2072-2078.
101. Chu, H.; Wang, J.; Ding, L.; Yuan, D.; Zhang, Y.; Liu, J.; Li, Y., Decoration of gold nanoparticles on surface-grown single-walled carbon nanotubes for detection of every nanotube by surface-enhanced Raman spectroscopy. *J. Am. Chem. Soc.* **2009**, *131*, 14310-14316.
102. Lee, S. J.; Morrill, A. R.; Moskovits, M., Hot spots in silver nanowire bundles for surface-enhanced Raman spectroscopy. *J. Am. Chem. Soc.* **2006**, *128*, 2200-2201.
103. Fu, X.; Bei, F.; Wang, X.; O'Brien, S.; Lombardi, J. R., Excitation profile of surface-enhanced Raman scattering in graphene-metal nanoparticle based derivatives. *Nanoscale* **2010**, *2*, 1461-1466.
104. Osawa, M.; Matsuda, N.; Yoshii, K.; Uchida, I., Charge transfer resonance Raman process in surface-enhanced Raman scattering from p-aminothiophenol adsorbed on silver: Herzberg-Teller contribution. *J. Phys. Chem.* **1994**, *98*, 12702-12707.

105. Zhao, Y.; Tang, Y.; Chen, Y.; Star, A., Corking carbon nanotube cups with gold nanoparticles. *ACS Nano* **2012**, *6*, 6912-6921.
106. Liu, X.; Romero, H.; Gutierrez, H.; Adu, K.; Eklund, P., Transparent boron-doped carbon nanotube films. *Nano Lett.* **2008**, *8*, 2613-2619.
107. Zhang, G.; Ma, X.; Zhong, D.; Wang, E., Polymerized carbon nitride nanobells. *J. Appl. Phys.* **2002**, *91*, 9324-9332.
108. Allen, B. L.; Kichambare, P. D.; Star, A., Synthesis, characterization, and manipulation of nitrogen-doped carbon nanotube cups. *ACS Nano* **2008**, *2*, 1914-1920.
109. Cruz-Silva, E.; Cullen, D. A.; Gu, L.; Romo-Herrera, J. M.; Muñoz-Sandoval, E.; López-Urías, F.; Sumpter, B. G.; Meunier, V.; Charlier, J.-C.; Smith, D. J., Heterodoped Nanotubes: Theory, Synthesis, and Characterization of Phosphorus– Nitrogen Doped Multiwalled Carbon Nanotubes. *ACS Nano* **2008**, *2*, 441-448.
110. Hernandez, E.; Goze, C.; Bernier, P.; Rubio, A., Elastic properties of C and B x C y N z composite nanotubes. *Phys. Rev. Lett.* **1998**, *80*, 4502.
111. Gao, R.; Wang, Z. L.; Bai, Z.; de Heer, W. A.; Dai, L.; Gao, M., Nanomechanics of individual carbon nanotubes from pyrolytically grown arrays. *Phys. Rev. Lett.* **2000**, *85*, 622.
112. Terrones, M.; Jorio, A.; Endo, M.; Rao, A.; Kim, Y.; Hayashi, T.; Terrones, H.; Charlier, J.-C.; Dresselhaus, G.; Dresselhaus, M., New direction in nanotube science. *Mater. Today* **2004**, *7*, 30-45.
113. Gong, K.; Du, F.; Xia, Z.; Durstock, M.; Dai, L., Nitrogen-doped carbon nanotube arrays with high electrocatalytic activity for oxygen reduction. *Science* **2009**, *323*, 760-764.

114. Allen, B. L.; Keddie, M. B.; Star, A., Controlling the volumetric parameters of nitrogen-doped carbon nanotube cups. *Nanoscale* **2010**, *2*, 1105-1108.
115. Guo, Q.; Xie, Y.; Wang, X.; Zhang, S.; Hou, T.; Lv, S., Synthesis of carbon nitride nanotubes with the C<sub>3</sub>N<sub>4</sub> stoichiometry via a benzene-thermal process at low temperatures. *Chem. Commun.* **2004**, 26-27.
116. Wu, C.; Guo, Q.; Yin, P.; Li, T.; Yang, Q.; Xie, Y., Synthesis of nitrogen-doped carbon nanostructures by the reactions of small molecule carbon halides with sodium azide. *J. Phys. Chem. B* **2005**, *109*, 2597-2604.
117. Venkateswara Rao, C.; Ishikawa, Y., Activity, selectivity, and anion-exchange membrane fuel cell performance of virtually metal-free nitrogen-doped carbon nanotube electrodes for oxygen reduction reaction. *J. Phys. Chem. C* **2012**, *116*, 4340-4346.
118. Matter, P. H.; Wang, E.; Arias, M.; Biddinger, E. J.; Ozkan, U. S., Oxygen reduction reaction catalysts prepared from acetonitrile pyrolysis over alumina-supported metal particles. *J. Phys. Chem. B* **2006**, *110*, 18374-18384.
119. Yang, W.; Fellingner, T.-P.; Antonietti, M., Efficient metal-free oxygen reduction in alkaline medium on high-surface-area mesoporous nitrogen-doped carbons made from ionic liquids and nucleobases. *J. Am. Chem. Soc.* **2010**, *133*, 206-209.
120. Mangun, C. L.; Benak, K. R.; Economy, J.; Foster, K. L., Surface chemistry, pore sizes and adsorption properties of activated carbon fibers and precursors treated with ammonia. *Carbon* **2001**, *39*, 1809-1820.
121. Li, Y.; Zhou, W.; Wang, H.; Xie, L.; Liang, Y.; Wei, F.; Idrobo, J.-C.; Pennycook, S. J.; Dai, H., An oxygen reduction electrocatalyst based on carbon nanotube-graphene complexes. *Nat. Nanotechnol.* **2012**, *7*, 394-400.

122. Schilling, T.; Okunola, A.; Masa, J.; Schuhmann, W.; Bron, M., Carbon nanotubes modified with electrodeposited metal porphyrins and phenanthrolines for electrocatalytic applications. *Electrochim. Acta* **2010**, *55*, 7597-7602.
123. Li, Y.; Zhao, Y.; Cheng, H.; Hu, Y.; Shi, G.; Dai, L.; Qu, L., Nitrogen-doped graphene quantum dots with oxygen-rich functional groups. *J. Am. Chem. Soc.* **2011**, *134*, 15-18.
124. Stephan, O.; Ajayan, P.; Colliex, C.; Redlich, P.; Lambert, J.; Bernier, P.; Lefin, P., Doping graphitic and carbon nanotube structures with boron and nitrogen. *Science* **1994**, *266*, 1683-1685.
125. Suenaga, K.; Johansson, M.; Hellgren, N.; Broitman, E.; Wallenberg, L.; Colliex, C.; Sundgren, J.-E.; Hultman, L., Carbon nitride nanotubulite–densely-packed and well-aligned tubular nanostructures. *Chem. Phys. Lett.* **1999**, *300*, 695-700.
126. Trasobares, S.; Stephan, O.; Colliex, C.; Hsu, W.; Kroto, H.; Walton, D., Compartmentalized CN<sub>x</sub> nanotubes: chemistry, morphology, and growth. *J. Chem. Phys.* **2002**, *116*, 8966-8972.
127. Liu, H.; Zhang, Y.; Li, R.; Sun, X.; D é silets, S.; Abou-Rachid, H.; Jaidann, M.; Lussier, L.-S., Structural and morphological control of aligned nitrogen-doped carbon nanotubes. *Carbon* **2010**, *48*, 1498-1507.
128. Ci, L.; Wei, J.; Wei, B.; Liang, J.; Xu, C.; Wu, D., Carbon nanofibers and single-walled carbon nanotubes prepared by the floating catalyst method. *Carbon* **2001**, *39*, 329-335.
129. Cheung, C. L.; Kurtz, A.; Park, H.; Lieber, C. M., Diameter-controlled synthesis of carbon nanotubes. *J. Phys. Chem. B* **2002**, *106*, 2429-2433.
130. Wu, C.; Li, J.; Dong, G.; Guan, L., Removal of ferromagnetic metals for the large-scale purification of single-walled carbon nanotubes. *J. Phys. Chem. C* **2009**, *113*, 3612-3616.

131. Liu, X.; Guo, L.; Morris, D.; Kane, A. B.; Hurt, R. H., Targeted removal of bioavailable metal as a detoxification strategy for carbon nanotubes. *Carbon* **2008**, *46*, 489-500.
132. Kim, Y.; Luzzi, D. E., Purification of pulsed laser synthesized single wall carbon nanotubes by magnetic filtration. *J. Phys. Chem. B* **2005**, *109*, 16636-16643.
133. Kim, Y.; Torrens, O. N.; Kikkawa, J.; Abou-Hamad, E.; Goze-Bac, C.; Luzzi, D. E., High-purity diamagnetic single-wall carbon nanotube buckypaper. *Chem. Mater.* **2007**, *19*, 2982-2986.
134. Ebbesen, T. W.; Ajayan, P. M.; Hiura, H.; Tanigaki, K., Purification of nanotubes. *Nature* **1994**, *367*, 519.
135. Moon, J.-M.; An, K. H.; Lee, Y. H.; Park, Y. S.; Bae, D. J.; Park, G.-S., High-yield purification process of singlewalled carbon nanotubes. *J. Phys. Chem. B* **2001**, *105*, 5677-5681.
136. Osswald, S.; Havel, M.; Gogotsi, Y., Monitoring oxidation of multiwalled carbon nanotubes by Raman spectroscopy. *J. Raman Spectrosc.* **2007**, *38*, 728-736.
137. Wang, Y.; Shan, H.; Hauge, R. H.; Pasquali, M.; Smalley, R. E., A highly selective, one-pot purification method for single-walled carbon nanotubes. *J. Phys. Chem. B* **2007**, *111*, 1249-1252.
138. Walling, C., Fenton's reagent revisited. *Acc. Chem. Res.* **1975**, *8*, 125-131.
139. Alvizo-Paez, E. R.; Romo-Herrera, J. M.; Terrones, H.; Terrones, M.; Ruiz-Garcia, J.; Hernandez-Lopez, J. L., Soft purification of N-doped and undoped multi-wall carbon nanotubes. *Nanotechnology* **2008**, *19*, 155701.
140. Zhao, Y.; Tang, Y.; Star, A., Synthesis and Functionalization of Nitrogen-doped Carbon Nanotube Cups with Gold Nanoparticles as Cork Stoppers. *J. Vis. Exp.* **2013**, e50383.

141. Wu, C.; Zhu, X.; Wang, C.; Sheng, H.; Yang, J.; Xie, Y., Bamboolike carbon nitride nanotubes (C<sub>9</sub>N<sub>5</sub>H<sub>3</sub>): Atomic-scale construction, synthesis and lithium battery applications. *Appl. Phys. Lett.* **2007**, *90*, 113116.
142. Wang, E., Nitrogen-induced carbon nanobells and their properties. *J. Mater. Res.* **2006**, *21*, 2767.
143. Terrones, M.; Ajayan, P.; Banhart, F.; Blase, X.; Carroll, D.; Charlier, J.-C.; Czerw, R.; Foley, B.; Grobert, N.; Kamalakaran, R., N-doping and coalescence of carbon nanotubes: synthesis and electronic properties. *Appl. Phys. A* **2002**, *74*, 355-361.
144. Jang, J. W.; Lee, C. E.; Lyu, S. C.; Lee, T. J.; Lee, C. J., Structural study of nitrogen-doping effects in bamboo-shaped multiwalled carbon nanotubes. *Appl. Phys. Lett.* **2004**, *84*, 2877-2879.
145. Lin, M.; Tan, J. P. Y.; Boothroyd, C.; Loh, K. P.; Tok, E. S.; Foo, Y.-L., Dynamical observation of bamboo-like carbon nanotube growth. *Nano Lett.* **2007**, *7*, 2234-2238.
146. Mandumpal, J.; Gemming, S.; Seifert, G., Curvature effects of nitrogen on graphitic sheets: structures and energetics. *Chem. Phys. Lett.* **2007**, *447*, 115-120.
147. Zhao, G.; Bagayoko, D.; Wang, E., Electronic structure of short carbon nanobells. *Mod. Phys. Lett. B* **2003**, *17*, 375-382.
148. Bai, X.; Zhong, D.; Zhang, G.; Ma, X.; Liu, S.; Wang, E.; Chen, Y.; Shaw, D. T., Hydrogen storage in carbon nitride nanobells. *Appl. Phys. Lett.* **2001**, *79*, 1552-1554.
149. Zhong, D.; Zhang, G.; Liu, S.; Wang, E.; Wang, Q.; Li, H.; Huang, X., Lithium storage in polymerized carbon nitride nanobells. *Appl. Phys. Lett.* **2001**, *79*, 3500-3502.

150. Tang, Y.; Burkert, S. C.; Zhao, Y.; Saidi, W. A.; Star, A., The Effect of Metal Catalyst on the Electrocatalytic Activity of Nitrogen-Doped Carbon Nanotubes. *J. Phys. Chem. C* **2013**, *117*, 25213-25221.
151. Tang, Y.; Allen, B. L.; Kauffman, D. R.; Star, A., Electrocatalytic Activity of Nitrogen-Doped Carbon Nanotube Cups. *J. Am. Chem. Soc.* **2009**, *131*, 13200-13201.
152. Xu, X.; Jiang, S.; Hu, Z.; Liu, S., Nitrogen-doped carbon nanotubes: high electrocatalytic activity toward the oxidation of hydrogen peroxide and its application for biosensing. *ACS Nano* **2010**, *4*, 4292-4298.
153. Jiang, K.; Schadler, L. S.; Siegel, R. W.; Zhang, X.; Zhang, H.; Terrones, M., Protein immobilization on carbon nanotubes via a two-step process of diimide-activated amidation. *J. Mater. Chem.* **2004**, *14*, 37-39.
154. Carrero-Sanchez, J.; Elias, A.; Mancilla, R.; Arrellin, G.; Terrones, H.; Laclette, J.; Terrones, M., Biocompatibility and toxicological studies of carbon nanotubes doped with nitrogen. *Nano Lett.* **2006**, *6*, 1609-1616.
155. Liu, L.; Yang, C.; Zhao, K.; Li, J.; Wu, H.-C., Ultrashort single-walled carbon nanotubes in a lipid bilayer as a new nanopore sensor. *Nat. Commun.* **2013**, *4*.
156. Chen, Z.; Kobashi, K.; Rauwald, U.; Booker, R.; Fan, H.; Hwang, W.-F.; Tour, J. M., Soluble ultra-short single-walled carbon nanotubes. *J. Am. Chem. Soc.* **2006**, *128*, 10568-10571.
157. Ashcroft, J. M.; Hartman, K. B.; Mackeyev, Y.; Hofmann, C.; Pheasant, S.; Alemany, L. B.; Wilson, L. J., Functionalization of individual ultra-short single-walled carbon nanotubes. *Nanotechnology* **2006**, *17*, 5033.

158. Jia, Z.; Wang, Z.; Liang, J.; Wei, B.; Wu, D., Production of short multi-walled carbon nanotubes. *Carbon* **1999**, *37*, 903-906.
159. Heller, D. A.; Mayrhofer, R. M.; Baik, S.; Grinkova, Y. V.; Usrey, M. L.; Strano, M. S., Concomitant length and diameter separation of single-walled carbon nanotubes. *J. Am. Chem. Soc.* **2004**, *126*, 14567-14573.
160. Ma, X.; Wang, E.; Tilley, R.; Jefferson, D.; Zhou, W., Size-controlled short nanobells: Growth and formation mechanism. *Appl. Phys. Lett.* **2000**, *77*, 4136-4138.
161. Kim, Y.; Hayashi, T.; Fukai, Y.; Endo, M.; Yanagisawa, T.; Dresselhaus, M., Effect of ball milling on morphology of cup-stacked carbon nanotubes. *Chem. Phys. Lett.* **2002**, *355*, 279-284.
162. Shimamoto, D.; Fujisawa, K.; Muramatsu, H.; Hayashi, T.; Kim, Y. A.; Yanagisawa, T.; Endo, M.; Dresselhaus, M. S., A simple route to short cup-stacked carbon nanotubes by sonication. *Carbon* **2010**, *48*, 3643-3647.
163. Wei, J.; Lv, R.; Guo, N.; Wang, H.; Bai, X.; Mathkar, A.; Kang, F.; Zhu, H.; Wang, K.; Wu, D., Preparation of highly oxidized nitrogen-doped carbon nanotubes. *Nanotechnology* **2012**, *23*, 155601.
164. Wang, Y.; Bai, X., High-yield preparation of individual nitrogen-containing carbon nanobells. *Mater. Lett.* **2009**, *63*, 206-208.
165. Allen, B. L.; Shade, C. M.; Yingling, A. M.; Petoud, S.; Star, A., Graphitic Nanocapsules. *Adv. Mater.* **2009**, *21*, 4692-4695.
166. Rosca, I. D.; Watari, F.; Uo, M.; Akasaka, T., Oxidation of multiwalled carbon nanotubes by nitric acid. *Carbon* **2005**, *43*, 3124-3131.

167. Allen, B. L.; Kichambare, P. D.; Gou, P.; Vlasova, I. I.; Kapralov, A. A.; Konduru, N.; Kagan, V. E.; Star, A., Biodegradation of single-walled carbon nanotubes through enzymatic catalysis. *Nano Lett.* **2008**, *8*, 3899-3903.
168. Allen, B. L.; Kotchey, G. P.; Chen, Y.; Yanamala, N. V.; Klein-Seetharaman, J.; Kagan, V. E.; Star, A., Mechanistic investigations of horseradish peroxidase-catalyzed degradation of single-walled carbon nanotubes. *J. Am. Chem. Soc.* **2009**, *131*, 17194-17205.
169. Kotchey, G. P.; Zhao, Y.; Kagan, V. E.; Star, A., Peroxidase-mediated biodegradation of carbon nanotubes in vitro and in vivo. *Adv. Drug Deliv. Rev.* **2013**, *65*, 1921-1932.
170. Lam, C.-W.; James, J. T.; McCluskey, R.; Hunter, R. L., Pulmonary toxicity of single-wall carbon nanotubes in mice 7 and 90 days after intratracheal instillation. *Toxicol. Sci.* **2004**, *77*, 126-134.
171. Mitchell, L. A.; Gao, J.; Vander Wal, R.; Gigliotti, A.; Burchiel, S. W.; McDonald, J. D., Pulmonary and systemic immune response to inhaled multiwalled carbon nanotubes. *Toxicol. Sci.* **2007**, *100*, 203-214.
172. Shvedova, A. A.; Kisin, E. R.; Mercer, R.; Murray, A. R.; Johnson, V. J.; Potapovich, A. I.; Tyurina, Y. Y.; Gorelik, O.; Arepalli, S.; Schwegler-Berry, D., Unusual inflammatory and fibrogenic pulmonary responses to single-walled carbon nanotubes in mice. *Am. J. Physiol. Lung Cell. Mol. Physiol.* **2005**, *289*, L698-L708.
173. Poland, C. A.; Duffin, R.; Kinloch, I.; Maynard, A.; Wallace, W. A.; Seaton, A.; Stone, V.; Brown, S.; MacNee, W.; Donaldson, K., Carbon nanotubes introduced into the abdominal cavity of mice show asbestos-like pathogenicity in a pilot study. *Nat. Nanotechnol.* **2008**, *3*, 423-428.

174. Manna, S. K.; Sarkar, S.; Barr, J.; Wise, K.; Barrera, E. V.; Jejelowo, O.; Rice-Ficht, A. C.; Ramesh, G. T., Single-walled carbon nanotube induces oxidative stress and activates nuclear transcription factor- $\kappa$ B in human keratinocytes. *Nano Lett.* **2005**, *5*, 1676-1684.
175. Bottini, M.; Bruckner, S.; Nika, K.; Bottini, N.; Bellucci, S.; Magrini, A.; Bergamaschi, A.; Mustelin, T., Multi-walled carbon nanotubes induce T lymphocyte apoptosis. *Toxicol. Lett.* **2006**, *160*, 121-126.
176. Cui, D.; Tian, F.; Ozkan, C. S.; Wang, M.; Gao, H., Effect of single wall carbon nanotubes on human HEK293 cells. *Toxicol. Lett.* **2005**, *155*, 73-85.
177. Jia, G.; Wang, H.; Yan, L.; Wang, X.; Pei, R.; Yan, T.; Zhao, Y.; Guo, X., Cytotoxicity of carbon nanomaterials: single-wall nanotube, multi-wall nanotube, and fullerene. *Environ. Sci. Technol.* **2005**, *39*, 1378-1383.
178. Sato, Y.; Yokoyama, A.; Shibata, K.-i.; Akimoto, Y.; Ogino, S.-i.; Nodasaka, Y.; Kohgo, T.; Tamura, K.; Akasaka, T.; Uo, M., Influence of length on cytotoxicity of multi-walled carbon nanotubes against human acute monocytic leukemia cell line THP-1 in vitro and subcutaneous tissue of rats in vivo. *Mol. BioSyst.* **2005**, *1*, 176-182.
179. Kennedy, A. J.; Hull, M. S.; Steevens, J. A.; Dontsova, K. M.; Chappell, M. A.; Gunter, J. C.; Weiss, C. A., Factors influencing the partitioning and toxicity of nanotubes in the aquatic environment. *Environ. Toxicol. Chem.* **2008**, *27*, 1932-1941.
180. Murphy, F. A.; Poland, C. A.; Duffin, R.; Donaldson, K., Length-dependent pleural inflammation and parietal pleural responses after deposition of carbon nanotubes in the pulmonary airspaces of mice. *Nanotoxicology* **2012**, *7*, 1157-1167.

181. Ali-Boucetta, H.; Nunes, A.; Sainz, R.; Herrero, M. A.; Tian, B.; Prato, M.; Bianco, A.; Kostarelos, K., Asbestos-like Pathogenicity of Long Carbon Nanotubes Alleviated by Chemical Functionalization. *Angew. Chem.* **2013**, *125*, 2330-2334.
182. Owens III, D. E.; Peppas, N. A., Opsonization, biodistribution, and pharmacokinetics of polymeric nanoparticles. *Int. J. Pharm.* **2006**, *307*, 93-102.
183. Singh, R.; Pantarotto, D.; McCarthy, D.; Chaloin, O.; Hoebeke, J.; Partidos, C. D.; Briand, J.-P.; Prato, M.; Bianco, A.; Kostarelos, K., Binding and condensation of plasmid DNA onto functionalized carbon nanotubes: toward the construction of nanotube-based gene delivery vectors. *J. Am. Chem. Soc.* **2005**, *127*, 4388-4396.
184. Shi Kam, N. W.; Jessop, T. C.; Wender, P. A.; Dai, H., Nanotube molecular transporters: internalization of carbon nanotube-protein conjugates into mammalian cells. *J. Am. Chem. Soc.* **2004**, *126*, 6850-6851.
185. Schipper, M. L.; Nakayama-Ratchford, N.; Davis, C. R.; Kam, N. W. S.; Chu, P.; Liu, Z.; Sun, X.; Dai, H.; Gambhir, S. S., A pilot toxicology study of single-walled carbon nanotubes in a small sample of mice. *Nat. Nanotechnol.* **2008**, *3*, 216-221.
186. Plata, D.; Gschwend, P.; Reddy, C., Industrially synthesized single-walled carbon nanotubes: Compositional data for users, environmental risk assessments, and source apportionment. *Nanotechnology* **2008**, *19*, 185706.
187. Lee, J.; Mahendra, S.; Alvarez, P. J., Nanomaterials in the construction industry: a review of their applications and environmental health and safety considerations. *ACS Nano* **2010**, *4*, 3580-3590.
188. Hyung, H.; Fortner, J. D.; Hughes, J. B.; Kim, J.-H., Natural organic matter stabilizes carbon nanotubes in the aqueous phase. *Environ. Sci. Technol.* **2007**, *41*, 179-184.

189. Hyung, H.; Kim, J.-H., Natural organic matter (NOM) adsorption to multi-walled carbon nanotubes: Effect of NOM characteristics and water quality parameters. *Environ. Sci. Technol.* **2008**, *42*, 4416-4421.
190. O'Brien, P. J., Peroxidases. *Chem. Biol. Interact.* **2000**, *129*, 113-139.
191. Welinder, K. G., Superfamily of plant, fungal and bacterial peroxidases. *Curr. Opin. Struct. Biol.* **1992**, *2*, 388-393.
192. Davies, M. J.; Hawkins, C. L.; Pattison, D. I.; Rees, M. D., Mammalian heme peroxidases: from molecular mechanisms to health implications. *Antioxid. Redox Signaling.* **2008**, *10*, 1199-1234.
193. Filizola, M.; Loew, G. H., Role of protein environment in horseradish peroxidase compound I formation: Molecular dynamics simulations of horseradish peroxidase-HOOH complex. *J. Am. Chem. Soc.* **2000**, *122*, 18-25.
194. Veitch, N. C., Horseradish peroxidase: a modern view of a classic enzyme. *Phytochemistry* **2004**, *65*, 249-259.
195. Azevedo, A. M.; Martins, V. C.; Prazeres, D. M.; Vojinović, V.; Cabral, J.; Fonseca, L. P., Horseradish peroxidase: a valuable tool in biotechnology. *Biotechnol. Annu. Rev.* **2003**, *9*, 199-247.
196. Chanock, S. J.; El Benna, J.; Smith, R. M.; Babior, B. M., The respiratory burst oxidase. *J. Biol. Chem.* **1994**, *270*, 24519-24519.
197. Nauseef, W. M., How human neutrophils kill and degrade microbes: an integrated view. *Immunol. Rev.* **2007**, *219*, 88-102.
198. Hansson, M.; Olsson, I.; Nauseef, W. M., Biosynthesis, processing, and sorting of human myeloperoxidase. *Arch. Biochem. Biophys.* **2006**, *445*, 214-224.

199. Arnhold, J., Properties, functions, and secretion of human myeloperoxidase. *Biochemistry (Moscow)* **2004**, *69*, 4-9.
200. Farhangrazi, Z. S.; Fossett, M. E.; Powers, L. S.; Ellis Jr, W. R., Variable-temperature spectroelectrochemical study of horseradish peroxidase. *Biochemistry* **1995**, *34*, 2866-2871.
201. Kotchey, G. P.; Gaugler, J. A.; Kapralov, A. A.; Kagan, V. E.; Star, A., Effect of antioxidants on enzyme-catalysed biodegradation of carbon nanotubes. *J. Mater. Chem. B* **2013**, *1*, 302-309.
202. Grätzel, M., Photoelectrochemical cells. *Nature* **2001**, *414*, 338-344.
203. Choi, H. C.; Shim, M.; Bangsaruntip, S.; Dai, H., Spontaneous reduction of metal ions on the sidewalls of carbon nanotubes. *J. Am. Chem. Soc.* **2002**, *124*, 9058-9059.
204. Kotchey, G. P.; Hasan, S. A.; Kapralov, A. A.; Ha, S. H.; Kim, K.; Shvedova, A. A.; Kagan, V. E.; Star, A., A natural vanishing act: the enzyme-catalyzed degradation of carbon nanomaterials. *Acc. Chem. Res.* **2012**, *45*, 1770-1781.
205. Russier, J.; Ménard-Moyon, C.; Venturelli, E.; Gravel, E.; Marcolongo, G.; Meneghetti, M.; Doris, E.; Bianco, A., Oxidative biodegradation of single-and multi-walled carbon nanotubes. *Nanoscale* **2011**, *3*, 893-896.
206. Zhao, Y.; Allen, B. L.; Star, A., Enzymatic degradation of multiwalled carbon nanotubes. *J. Phys. Chem. A* **2011**, *115*, 9536-9544.
207. Vedala, H.; Sorescu, D. C.; Kotchey, G. P.; Star, A., Chemical sensitivity of graphene edges decorated with metal nanoparticles. *Nano Lett.* **2011**, *11*, 2342-2347.
208. Kagan, V. E.; Konduru, N. V.; Feng, W.; Allen, B. L.; Conroy, J.; Volkov, Y.; Vlasova, I. I.; Belikova, N. A.; Yanamala, N.; Kapralov, A.; Tyurina, Y. Y.; Shi, J.; Kisin, E. R.;

- Murray, A. R.; Franks, J.; Stolz, D.; Gou, P.; Klein-Seetharaman, J.; Fadeel, B.; Star, A.; Shvedova, A. A., Carbon nanotubes degraded by neutrophil myeloperoxidase induce less pulmonary inflammation. *Nat. Nanotechnol.* **2010**, *5*, 354-359.
209. Vlasova, I.; Sokolov, A.; Chekanov, A.; Kostevich, V.; Vasilyev, V., Myeloperoxidase-induced biodegradation of single-walled carbon nanotubes is mediated by hypochlorite. *Russ. J. Bioorg. Chem.* **2011**, *37*, 453-463.
210. Hampton, M. B.; Kettle, A. J.; Winterbourn, C. C., Inside the neutrophil phagosome: oxidants, myeloperoxidase, and bacterial killing. *Blood* **1998**, *92*, 3007-3017.
211. Murphy, F. A.; Poland, C. A.; Duffin, R.; Al-Jamal, K. T.; Ali-Boucetta, H.; Nunes, A.; Byrne, F.; Prina-Mello, A.; Volkov, Y.; Li, S., Length-dependent retention of carbon nanotubes in the pleural space of mice initiates sustained inflammation and progressive fibrosis on the parietal pleura. *Am. J. Pathol.* **2011**, *178*, 2587-2600.
212. Yang, S.-T.; Wang, X.; Jia, G.; Gu, Y.; Wang, T.; Nie, H.; Ge, C.; Wang, H.; Liu, Y., Long-term accumulation and low toxicity of single-walled carbon nanotubes in intravenously exposed mice. *Toxicol. Lett.* **2008**, *181*, 182-189.
213. Shvedova, A. A.; Kapralov, A. A.; Feng, W. H.; Kisin, E. R.; Murray, A. R.; Mercer, R. R.; Croix, C. M. S.; Lang, M. A.; Watkins, S. C.; Konduru, N. V.; Allen, B. L.; Conroy, J.; Kotchey, G. P.; Mohamed, B. M.; Meade, A. D.; Volkov, Y.; Star, A.; Fadeel, B.; Kagan, V. E., Impaired clearance and enhanced pulmonary inflammatory/fibrotic response to carbon nanotubes in myeloperoxidase-deficient mice. *PLoS One* **2012**, *7*, e30923.

214. Elgrabli, D.; Floriani, M.; Abella-Gallart, S.; Meunier, L.; Gamez, C.; Delalain, P.; Rogerieux, F.; Boczkowski, J.; Lacroix, G., Biodistribution and clearance of instilled carbon nanotubes in rat lung. *Part Fibre Toxicol* **2008**, *5*, 20.
215. Nunes, A.; Bussy, C.; Gherardini, L.; Meneghetti, M.; Herrero, M. A.; Bianco, A.; Prato, M.; Pizzorusso, T.; Al-Jamal, K. T.; Kostarelos, K., In vivo degradation of functionalized carbon nanotubes after stereotactic administration in the brain cortex. *Nanomedicine* **2012**, *7*, 1485-1494.
216. Sgobba, V.; Guldi, D. M., Carbon nanotubes-electronic/electrochemical properties and application for nanoelectronics and photonics. *Chem. Soc. Rev.* **2009**, *38*, 165-184.
217. Kam, N. W. S.; Liu, Z.; Dai, H., Functionalization of Carbon Nanotubes *via* Cleavable Disulfide Bonds for Efficient Intracellular Delivery of siRNA and Potent Gene Silencing. *J. Am. Chem. Soc.* **2005**, *127*, 12492-12493.
218. Yang, L.; Jiang, S.; Zhao, Y.; Zhu, L.; Chen, S.; Wang, X.; Wu, Q.; Ma, J.; Ma, Y.; Hu, Z., Boron-Doped Carbon Nanotubes as Metal-Free Electrocatalysts for the Oxygen Reduction Reaction. *Angew. Chem. Int. Ed.* **2011**, *50*, 7132-7135.
219. Maldonado, S.; Morin, S.; Stevenson, K. J., Structure, composition, and chemical reactivity of carbon nanotubes by selective nitrogen doping. *Carbon* **2006**, *44*, 1429-1437.
220. Zhao, M. L.; Li, D. J.; Yuan, L.; Yue, Y. C.; Liu, H.; Sun, X., Differences in cytocompatibility and hemocompatibility between carbon nanotubes and nitrogen-doped carbon nanotubes. *Carbon* **2011**, *49*, 3125-3133.
221. Korneva, G.; Ye, H.; Gogotsi, Y.; Halverson, D.; Friedman, G.; Bradley, J.-C.; Kornev, K. G., Carbon Nanotubes Loaded with Magnetic Particles. *Nano Lett.* **2005**, *5*, 879-884.

222. Senthil Kumar, A.; Swetha, P., Electrochemical-Assisted Encapsulation of Catechol on a Multiwalled Carbon Nanotube Modified Electrode. *Langmuir* **2010**, *26*, 6874-6877.
223. Shekunov, B.; Chattopadhyay, P.; Tong, H.; Chow, A., Particle Size Analysis in Pharmaceuticals: Principles, Methods and Applications. *Pharm. Res.* **2007**, *24*, 203-227.
224. Bitter, J. H.; van Dommele, S.; de Jong, K. P., On the virtue of acid–base titrations for the determination of basic sites in nitrogen doped carbon nanotubes. *Catal. Today* **2010**, *150*, 61-66.
225. Castle, A. B.; Gracia-Espino, E.; Nieto-Delgado, C. s.; Terrones, H.; Terrones, M.; Hussain, S., Hydroxyl-Functionalized and N-Doped Multiwalled Carbon Nanotubes Decorated with Silver Nanoparticles Preserve Cellular Function. *ACS Nano* **2011**, *5*, 2458-2466.
226. Cançado, L. G.; Jorio, A.; Ferreira, E. H. M.; Stavale, F.; Achete, C. A.; Capaz, R. B.; Moutinho, M. V. O.; Lombardo, A.; Kulmala, T. S.; Ferrari, A. C., Quantifying Defects in Graphene *via* Raman Spectroscopy at Different Excitation Energies. *Nano Lett.* **2011**, *11*, 3190-3196.
227. Pels, J. R.; Kapteijn, F.; Moulijn, J. A.; Zhu, Q.; Thomas, K. M., Evolution of nitrogen functionalities in carbonaceous materials during pyrolysis. *Carbon* **1995**, *33*, 1641-1653.
228. Crist, B. V., *Handbook of Monochromatic XPS Spectra: The Elements and Native Oxides*. Wiley: Chester: 2000; p 279-282.
229. Kundu, S.; Nagaiah, T. C.; Xia, W.; Wang, Y.; Dommele, S. V.; Bitter, J. H.; Santa, M.; Grundmeier, G.; Bron, M.; Schuhmann, W.; Muhler, M., Electrocatalytic Activity and Stability of Nitrogen-Containing Carbon Nanotubes in the Oxygen Reduction Reaction. *J. Phys. Chem. C* **2009**, *113*, 14302-14310.

230. Casanovas, J.; Ricart, J. M.; Rubio, J.; Illas, F.; Jiménez-Mateos, J. M., Origin of the Large N 1s Binding Energy in X-ray Photoelectron Spectra of Calcined Carbonaceous Materials. *J. Am. Chem. Soc.* **1996**, *118*, 8071-8076.
231. Ramanathan, T.; Fisher, F. T.; Ruoff, R. S.; Brinson, L. C., Amino-Functionalized Carbon Nanotubes for Binding to Polymers and Biological Systems. *Chem. Mater.* **2005**, *17*, 1290-1295.
232. Jansen, R. J. J.; van Bekkum, H., XPS of nitrogen-containing functional groups on activated carbon. *Carbon* **1995**, *33*, 1021-1027.
233. van Dommele, S.; Romero-Izquierdo, A.; Brydson, R.; de Jong, K. P.; Bitter, J. H., Tuning nitrogen functionalities in catalytically grown nitrogen-containing carbon nanotubes. *Carbon* **2008**, *46*, 138-148.
234. Zhou, J.; Wang, J.; Liu, H.; Banis, M. N.; Sun, X.; Sham, T.-K., Imaging Nitrogen in Individual Carbon Nanotubes. *J. Phys. Chem. Lett.* **2010**, *1*, 1709-1713.
235. Chan, L. H.; Hong, K. H.; Xiao, D. Q.; Lin, T. C.; Lai, S. H.; Hsieh, W. J.; Shih, H. C., Resolution of the binding configuration in nitrogen-doped carbon nanotubes. *Phys. Rev. B* **2004**, *70*, 125408.
236. Sarin, V. K.; Kent, S. B.; Tam, J. P.; Merrifield, R. B., Quantitative monitoring of solid-phase peptide synthesis by the ninhydrin reaction. *Anal. Biochem.* **1981**, *117*, 147-57.
237. Love, J. C.; Estroff, L. A.; Kriebel, J. K.; Nuzzo, R. G.; Whitesides, G. M., Self-assembled monolayers of thiolates on metals as a form of nanotechnology. *Chem. Rev.* **2005**, *105*, 1103-69.
238. Malinsky, M. D.; Kelly, K. L.; Schatz, G. C.; Van Duyne, R. P., Chain Length Dependence and Sensing Capabilities of the Localized Surface Plasmon Resonance of

- Silver Nanoparticles Chemically Modified with Alkanethiol Self-Assembled Monolayers. *J. Am. Chem. Soc.* **2001**, *123*, 1471-1482.
239. Storhoff, J. J.; Lazarides, A. A.; Mucic, R. C.; Mirkin, C. A.; Letsinger, R. L.; Schatz, G. C., What Controls the Optical Properties of DNA-Linked Gold Nanoparticle Assemblies? *J. Am. Chem. Soc.* **2000**, *122*, 4640-4650.
240. Hillebrenner, H.; Buyukserin, F.; Kang, M.; Mota, M. O.; Stewart, J. D.; Martin, C. R., Corking Nano Test Tubes by Chemical Self-Assembly. *J. Am. Chem. Soc.* **2006**, *128*, 4236-4237.
241. Hilder, T. A.; Hill, J. M., Modeling the Loading and Unloading of Drugs into Nanotubes. *Small* **2009**, *5*, 300-308.
242. Chen, H.; Yang, Y.; Hu, Z.; Huo, K.; Ma, Y.; Chen, Y.; Wang, X.; Lu, Y., Synergism of C5N Six-Membered Ring and Vapor-Liquid-Solid Growth of CNx Nanotubes with Pyridine Precursor. *J. Phys. Chem. B* **2006**, *110*, 16422-16427.
243. Wang, Z.; Shirley, M. D.; Meikle, S. T.; Whitby, R. L. D.; Mikhalovsky, S. V., The surface acidity of acid oxidised multi-walled carbon nanotubes and the influence of in-situ generated fulvic acids on their stability in aqueous dispersions. *Carbon* **2009**, *47*, 73-79.
244. Flahaut, E.; Bacsa, R.; Peigney, A.; Laurent, C., Gram-scale CCVD synthesis of double-walled carbon nanotubes. *Chem. Commun.* **2003**, 1442-1443.
245. Eklund, P.; Ajayan, P.; Blackmon, R.; Hart, A. J.; Kibng, J.; Pradhan, B.; Bao, A.; Rinzler, A. *International assessment of research and development of carbon nanotube manufacturing and applications*; World Technology Evaluation Center, Inc., Baltimore, MD: 2007; pp 7-17.

246. Hunt, J. P.; Taube, H., The Photochemical Decomposition of Hydrogen Peroxide. Quantum Yields, Tracer and Fractionation Effects. *J. Am. Chem. Soc.* **1952**, *74*, 5999-6002.
247. Mawhinney, D. B.; Naumenko, V.; Kuznetsova, A.; Yates Jr, J. T.; Liu, J.; Smalley, R. E., Surface defect site density on single walled carbon nanotubes by titration. *Chem. Phys. Lett.* **2000**, *324*, 213-216.
248. Ouyang, Y.; Cong, L. M.; Chen, L.; Liu, Q. X.; Fang, Y., Raman study on single-walled carbon nanotubes and multi-walled carbon nanotubes with different laser excitation energies. *Physica E: Low-dimensional Systems and Nanostructures* **2008**, *40*, 2386-2389.
249. Boehm, H. P.; Diehl, E.; Heck, W.; Sappok, R., Surface Oxides of Carbon. *Angewandte Chemie International Edition in English* **1964**, *3*, 669-677.
250. Scheibe, B.; Borowiak-Palen, E.; Kalenczuk, R. J., Oxidation and reduction of multiwalled carbon nanotubes — preparation and characterization. *Mater. Charact.* **2010**, *61*, 185-191.
251. Bahr, J. L.; Mickelson, E. T.; Bronikowski, M. J.; Smalley, R. E.; Tour, J. M., Dissolution of small diameter single-wall carbon nanotubes in organic solvents? *Chem. Commun.* **2001**, 193-194.
252. Dresselhaus, M. S.; Dresselhaus, G.; Jorio, A.; Souza Filho, A. G.; Saito, R., Raman spectroscopy on isolated single wall carbon nanotubes. *Carbon* **2002**, *40*, 2043-2061.
253. Maeda, H.; Wu, J.; Sawa, T.; Matsumura, Y.; Hori, K., Tumor vascular permeability and the EPR effect in macromolecular therapeutics: a review. *J. Control. Release* **2000**, *65*, 271-284.

254. Matsumura, Y.; Maeda, H., A new concept for macromolecular therapeutics in cancer chemotherapy: mechanism of tumor-tropic accumulation of proteins and the antitumor agent smancs. *Cancer Res.* **1986**, *46*, 6387-6392.
255. Allen, T. M.; Cullis, P. R., Drug delivery systems: entering the mainstream. *Science* **2004**, *303*, 1818-1822.
256. O'Neal, D. P.; Hirsch, L. R.; Halas, N. J.; Payne, J. D.; West, J. L., Photo-thermal tumor ablation in mice using near infrared-absorbing nanoparticles. *Cancer Lett.* **2004**, *209*, 171-176.
257. Maeda, H., Macromolecular therapeutics in cancer treatment: the EPR effect and beyond. *J. Control. Release* **2012**, *164*, 138-144.
258. Portney, N. G.; Ozkan, M., Nano-oncology: drug delivery, imaging, and sensing. *Anal. Bioanal. Chem.* **2006**, *384*, 620-630.
259. Emerich, D. F.; Thanos, C. G., Targeted nanoparticle-based drug delivery and diagnosis. *J. Drug Target.* **2007**, *15*, 163-183.
260. Torchilin, V. P., Recent approaches to intracellular delivery of drugs and DNA and organelle targeting. *Annu. Rev. Biomed. Eng.* **2006**, *8*, 343-375.
261. Ren, Y.; Pastorin, G., Incorporation of hexamethylmelamine inside capped carbon nanotubes. *Adv. Mater.* **2008**, *20*, 2031-2036.
262. Guven, A.; Rusakova, I. A.; Lewis, M. T.; Wilson, L. J., Cisplatin@ US-tube carbon nanocapsules for enhanced chemotherapeutic delivery. *Biomaterials* **2012**, *33*, 1455-1461.
263. Yanagi, K.; Miyata, Y.; Kataura, H., Highly Stabilized  $\beta$ -Carotene in Carbon Nanotubes. *Adv. Mater.* **2006**, *18*, 437-441.

264. Lemarchand, C.; Gref, R.; Couvreur, P., Polysaccharide-decorated nanoparticles. *Eur. J. Pharm. Biopharm.* **2004**, *58*, 327-341.
265. Volodkin, D. V.; Skirtach, A. G.; Mohwald, H., Near-IR Remote Release from Assemblies of Liposomes and Nanoparticles. *Angew. Chem. Int. Ed.* **2009**, *48*, 1807-1809.
266. Boateng, J. S.; Matthews, K. H.; Stevens, H. N.; Eccleston, G. M., Wound healing dressings and drug delivery systems: a review. *J. Pharm. Sci.* **2008**, *97*, 2892-2923.
267. Ding, M.; Sorescu, D. C.; Kotchey, G. P.; Star, A., Welding of gold nanoparticles on graphitic templates for chemical sensing. *J. Am. Chem. Soc.* **2012**, *134*, 3472-3479.
268. Ding, M.; Tang, Y.; Star, A., Understanding Interfaces in Metal-Graphitic Hybrid Nanostructures. *J. Phys. Chem. Lett.* **2012**, *4*, 147-160.
269. Sylvestre, J.-P.; Poulin, S.; Kabashin, A. V.; Sacher, E.; Meunier, M.; Luong, J. H., Surface chemistry of gold nanoparticles produced by laser ablation in aqueous media. *J. Phys. Chem. B* **2004**, *108*, 16864-16869.
270. Sheng, Z.-H.; Shao, L.; Chen, J.-J.; Bao, W.-J.; Wang, F.-B.; Xia, X.-H., Catalyst-free synthesis of nitrogen-doped graphene via thermal annealing graphite oxide with melamine and its excellent electrocatalysis. *ACS Nano* **2011**, *5*, 4350-4358.
271. Xie, X.; Long, J.; Xu, J.; Chen, L.; Wang, Y.; Zhang, Z.; Wang, X., Nitrogen-doped graphene stabilized gold nanoparticles for aerobic selective oxidation of benzylic alcohols. *RSC Advances* **2012**, *2*, 12438-12446.
272. Chiu, C. F.; Barth, B. A.; Kotchey, G. P.; Zhao, Y.; Gogick, K. A.; Saidi, W. A.; Petoud, S.; Star, A., Enzyme-Catalyzed Oxidation Facilitates the Return of Fluorescence for Single-Walled Carbon Nanotubes. *J. Am. Chem. Soc.* **2013**, *135*, 13356-13364.

273. Kruusma, J.; Mould, N.; Jurkschat, K.; Crossley, A.; Banks, C. E., Single walled carbon nanotubes contain residual iron oxide impurities which can dominate their electrochemical activity. *Electrochem. Commun.* **2007**, *9*, 2330-2333.
274. Pumera, M.; Miyahara, Y., What amount of metallic impurities in carbon nanotubes is small enough not to dominate their redox properties? *Nanoscale* **2009**, *1*, 260-265.
275. Yu, D.; Zhang, Q.; Dai, L., Highly Efficient Metal-Free Growth of Nitrogen-Doped Single-Walled Carbon Nanotubes on Plasma-Etched Substrates for Oxygen Reduction. *J. Am. Chem. Soc.* **2010**, *132*, 15127-15129.
276. Novoselov, K. S.; Geim, A. K.; Morozov, S. V.; Jiang, D.; Zhang, Y.; Dubonos, S. V.; Grigorieva, I. V.; Firsov, A. A., Electric Field Effect in Atomically Thin Carbon Films. *Science* **2004**, *306*, 666-669.
277. Castro Neto, A. H.; Guinea, F.; Peres, N. M. R.; Novoselov, K. S.; Geim, A. K., The electronic properties of graphene. *Rev. Mod. Phys.* **2009**, *81*, 109-162.
278. Chen, H.; Müller, M. B.; Gilmore, K. J.; Wallace, G. G.; Li, D., Mechanically Strong, Electrically Conductive, and Biocompatible Graphene Paper. *Adv. Mater.* **2008**, *20*, 3557-3561.
279. Berger, C.; Song, Z.; Li, X.; Wu, X.; Brown, N.; Naud, C.; Mayou, D.; Li, T.; Hass, J.; Marchenkov, A. N.; Conrad, E. H.; First, P. N.; de Heer, W. A., Electronic Confinement and Coherence in Patterned Epitaxial Graphene. *Science* **2006**, *312*, 1191-1196.
280. Choi, S.-M.; Jhi, S.-H.; Son, Y.-W., Effects of strain on electronic properties of graphene. *Phys. Rev. B* **2010**, *81*, 081407.

281. Novoselov, K. S.; Jiang, D.; Schedin, F.; Booth, T. J.; Khotkevich, V. V.; Morozov, S. V.; Geim, A. K., Two-dimensional atomic crystals. *Proc. Natl. Acad. Sci. U. S. A.* **2005**, *102*, 10451-10453.
282. Kim, K. S.; Zhao, Y.; Jang, H.; Lee, S. Y.; Kim, J. M.; Kim, K. S.; Ahn, J.-H.; Kim, P.; Choi, J.-Y.; Hong, B. H., Large-scale pattern growth of graphene films for stretchable transparent electrodes. *Nature* **2009**, *457*, 706-710.
283. Reina, A.; Jia, X.; Ho, J.; Nezich, D.; Son, H.; Bulovic, V.; Dresselhaus, M. S.; Kong, J., Large area, few-layer graphene films on arbitrary substrates by chemical vapor deposition. *Nano Lett.* **2008**, *9*, 30-35.
284. Hummers Jr, W. S.; Offeman, R. E., Preparation of graphitic oxide. *J. Am. Chem. Soc.* **1958**, *80*, 1339-1339.
285. Marcano, D. C.; Kosynkin, D. V.; Berlin, J. M.; Sinitskii, A.; Sun, Z.; Slesarev, A.; Alemany, L. B.; Lu, W.; Tour, J. M., Improved synthesis of graphene oxide. *ACS Nano* **2010**, *4*, 4806-4814.
286. Kosynkin, D. V.; Higginbotham, A. L.; Sinitskii, A.; Lomeda, J. R.; Dimiev, A.; Price, B. K.; Tour, J. M., Longitudinal unzipping of carbon nanotubes to form graphene nanoribbons. *Nature* **2009**, *458*, 872-876.
287. Rao, C. V.; Cabrera, C. R.; Ishikawa, Y., In Search of the Active Site in Nitrogen-Doped Carbon Nanotube Electrodes for the Oxygen Reduction Reaction. *J. Phys. Chem. Lett.* **2010**, *1*, 2622-2627.
288. Forster, S.; Thumser, A. E.; Hood, S. R.; Plant, N., Characterization of Rhodamine-123 as a Tracer Dye for Use In In vitro Drug Transport Assays. *PLoS One* **2012**, *7*, e33253.

289. Smith, B. W.; Monthieux, M.; Luzzi, D. E., Encapsulated C60 in carbon nanotubes. *Nature* **1998**, *396*, 323-324.
290. Kataura, H.; Maniwa, Y.; Abe, M.; Fujiwara, A.; Kodama, T.; Kikuchi, K.; Imahori, H.; Misaki, Y.; Suzuki, S.; Achiba, Y., Optical properties of fullerene and non-fullerene peapods. *Appl. Phys. A* **2002**, *74*, 349-354.
291. Yudasaka, M.; Ajima, K.; Suenaga, K.; Ichihashi, T.; Hashimoto, A.; Iijima, S., Nano-extraction and nano-condensation for C60 incorporation into single-wall carbon nanotubes in liquid phases. *Chem. Phys. Lett.* **2003**, *380*, 42-46.